Investigation of the Factors Influencing Magnetic Flux Leakage and Magnetic Barkhausen Noise

Yujue Wang

Wolfson Centre for Magnetics
School of Engineering
Cardiff University

A thesis submitted for the degree of
Doctor of Philosophy

June 2021

Abstract

Magnetic Nondestructive methods, including Magnetic Flux Leakage (MFL) and Magnetic Barkhausen Noise (MBN), are widely used to evaluate the structural integrity, mechanical properties, and microstructures of ferromagnetic materials. The MFL method is commonly applied to nondestructively evaluate the damage in ferromagnetic materials due to its reliability, high efficiency, and cost-saving. The MBN method is applicable in nondestructive evaluation (NDE) of mechanical and material properties due to the high sensitivity of Barkhausen jumps to residual (or applied) stress and microstructure of ferromagnetic material. The recognized research and successful applications helped these methods to be feasible NDE tools. However, there are still several important factors that may have noticeable influences on the experimental results of these NDE methods and usually are ignored in applications.

In this thesis, the effects of the factors of stress and temperature on the MFL method, as well as the influences of temperature and microstructure on the MBN method are analysed via analytical and numerical modelling.

A new finite element model for evaluating the effect of stress on the MFL amplitude is proposed and validated in defective steel under various stresses. Moreover, the new models describing the direct effect of temperature and the combined effects of temperature and thermal stress on the MFL signals are presented. The direct and combined effects are verified in an environmental temperature range from -40°C to 60°C by experimental results of a single lamination steel and multilayer structure, respectively.

A set of newly derived equations modelling the effect of temperature on the MBN signals are given. Both the direct effect of temperature and the combined effects of temperature and thermal stress are considered in these equations, which are further simplified to linear functions consistent with the measured results in an environmental temperature range from -40°C to 40°C. Furthermore, the microstructure factors, including the microstructure induced anisotropy in non-oriented silicon steel and the metallographic phases changing with carbon content in steel, are theoretically and experimentally investigated, respectively. For the factor of anisotropy, a new model describing the dependency of Barkhausen emission on the angle between measurement and rolling directions is proposed. It allows the deduction of a trigonometric function to evaluate the effect of directional anisotropy. The agreement of simulated and measured results of MBN signals indicates the feasibility of the presented model. In the investigation of the influence of carbon content in steel on MBN signals, an optimisation method for MBN pick-up coil is proposed, and a multifunctional measurement system is presented. The correlations of the MBN signals and hysteresis loops related to the carbon content in steel are experimentally observed. The method for the quantitative evaluation of the carbon content using MBN signals and hysteresis loops are discussed.

Table of Contents

CHAPTER 3

Nondestructive Evaluation Techniques and the Important Factors Influencing Magnetic NDE Methods 42

CHAPTER 4

Evaluation of the Effect of Stress on Magnetic Flux Leakage 100

CHAPTER 5

CHAPTER 6

Nomenclature

Greek symbol

α	Interdomain coupling
β_1, β_2, β_3, β_4	Temperature coefficients
γ	Coefficient of the stochastic behaviour of MBN
γ_0, γ_{11}, γ_{12}	Coefficients of magnetostriction
ζ_T, ζ_{T1}, ζ_{T2}	Coefficients of thermal expansion
ε	Mechanical strain
ε_0	Permittivity of free space (8.85 × 10^{-12} F/m)
ε_r	Relative permittivity
θ	Angle between directions of stress and magnetisation or Angle between measurement direction and rolling direction
λ	Magnetostriction
μ	Permeability
μ_0	Permeability of free space ($4\pi \times 10^{-7}$ H/m)
μ_r	Relative permeability
μ_r'	Differential relative permeability
ν	Poisson’s ratio
ρ	Magnetic charge density
ρ_E	Electric charge density
σ	Mechanical stress
Φ	Magnetic flux
χ	Magnetic susceptibility
χ'	Differential susceptibility
χ'_{H_C}	Maximum differential susceptibility at coercivity

χ'_{an}	Maximum differential anhysteresis susceptibility

Other symbols

a	Domain density
b	Coefficient of magnetostriction
B	Magnetic flux density
B_r	Remanence
c	Reversibility factor
d	Atomic lattice spacing
E	Young’s modulus or Electric field
E_a	Magnetocrystalline anisotropy energy
E_{ex}	Exchange energy
E_m	Magnetostatic energy
E_λ	Magnetoelastic energy
E_Z	Zeeman energy
H	Magnetic field
H_e	Effective magnetic field
H_σ	Stress equivalent magnetic field
H_c	Coercive field
I	Current
J	Current density
k	Domain wall pinning factor
k_B	Boltzmann constant (1.380649×10^{-23} J/K)
N_d, N_y	Demagnetising factors
m	Magnetic moment

M	Magnetisation
M_{an}	Anhystersis magnetisation
M_{irr}	Irreversible magnetisation
M_{rev}	Reversible magnetisation
M_s	Spontaneous magnetisation
M_{st}	Saturation magnetisation
t	time
T	Temperature
T_c	Curie temperature
T_r	Reference temperature
V	Voltage

Acronyms

ABBM	Alessandro, Beatrice, Bertotti and Montorsi
EC	Eddy current
EMAT	Electromagnetic Acoustic Transducer.
FEM	Finite Element Method
IR	Infrared
J-A	Jiles-Atherton
JSW	Jiles, Sipahi and Williams
MFL	Magnetic Flux Leakage
MBN	Magnetic Barkhausen noise
NDE	Nondestructive evaluation
XRD	X-ray diffraction

Acknowledgements

I would like to express my gratitude to everyone who has assisted me during my PhD study at Cardiff University. I appreciate the funding from CSC and Cardiff University.

I would like to express my heartfelt appreciation to my supervisor Dr Turgut Meydan for giving me the opportunity to pursue research at Cardiff University and for his consistent advice, supervision, support and encouragement. Also, special thanks to my second supervisor Dr Yevgen Melikhov for his invaluable support, motivation, and contribution from the start of this research.

I would like to thank Dr Paul Williams, my friends Sahar, Greg, Hafeez, Shuaichao, Seda, and work colleagues from Wolfson Centre for Magnetics for the technical help, brilliant ideas, conversations and the wonderful time spent.

Finally, I dedicate this thesis to my family for their constant support and encouragement. My deepest thanks go to my mum Jieqiong for standing by and loving me through all of my ups and downs.

List of Publications

Journal publications

[1] **Yujue Wang**, Turgut Meydan and Yevgen Melikhov. Quantitative Evaluation of the Effect of Temperature on Magnetic Barkhausen Noise. *Sensors*, vol. 21, no. 3, pp. 898 (1-18), 2021.

[2] **Yujue Wang**, Yevgen Melikhov, Turgut Meydan, Zengchong Yang, Donghang Wu, Bin Wu, Cunfu He and Xiucheng Liu. Stress-Dependent Magnetic Flux Leakage: Finite Element Modelling Simulations Versus Experiments. *Journal of Nondestructive Evaluation*, vol.39, no.1, pp.1-9, 2020.

Conference presentation

[1] **Yujue Wang**, Yevgen Melikhov, Turgut Meydan, Bin Wu, Cunfu He and Xiucheng Liu. Analytical and numerical modelling of stress-dependent magnetic flux leakage. *IEEE Magnetics Society Summer School*, Quito, Ecuador, poster presentation, 2018.

Chapter 1

Introduction

This chapter provides the outline of the thesis, the aims and the contribution of the investigation.

1.1 Research Background

Ferromagnetic materials have been used in a wide range of industrial applications and modern technologies. The development of material science gives ferromagnetic materials a significant role in load-bearing structures and implementing special functions, such as the seamless track used in high-speed railway, the silicon steel employed in transformer, the thick-walled seamless steel pipes used in ultra-supercritical thermal power generator and the main-shaft bearing of a wind-driven generator. The evaluation of mechanical properties and health status of these ferromagnetic structures is vital to ensure the safe and reliable operation of the crucial equipment.

There are several commonly used magnetic NDE techniques that are well-suited for evaluating the integrity and mechanical properties of ferromagnetic materials, including Magnetic Flux Leakage (MFL) and Magnetic Barkhausen Noise (MBN). However, using these NDE techniques to evaluate ferromagnetic components accurately is a great challenge. The ferromagnetic NDE methods usually consider single factor influence only. For example, MFL method focuses on the effect of defect and MBN method only consider stress influence during residual stress inspection. However, those ferromagnetic components generally work in complicated conditions. Stress and temperature are the most common factors that could have noticeable influences on the measured results of these NDE methods. Stress can alter the magnetisation of ferromagnetic material due to the magnetomechanical effect, but also it will induce stress concentration near a discontinuous geometry. Temperature can also change the magnetisation due to the magnetothermal effect. It may cause thermal stress, which will further influence the magnetisation of ferromagnetic materials. In addition, the microstructure of ferromagnetic material is another important factor influencing the results of NDE techniques. For example, the grains in non-oriented grain silicon steel are heavily deformed and elongated after rolling, resulting in magnetocrystalline anisotropy. The amount of carbon in the form of ferrite and pearlite in steel could alter the mechanical and magnetic properties of the material. These factors will eventually alter the inspection results of the ferromagnetic NDE techniques. Therefore, the traditional magnetic NDE methods used for isotropic and single-factor influential inspection are far from qualified to solve practical engineering problems.

1.2 Research Aims

This thesis focuses on contributing to two commonly used magnetic NDE methods affected by multifactor: the factors of stress and temperature affecting the magnetic flux leakage generated in the vicinity of defects (MFL method); the effects of temperature and microstructure on the Barkhausen emissions (MBN method).

The research aims to

1) Propose a universal numerical method to simulate the effect of mechanical stress on the magnetic flux leakage measurement
2) Develop analytical models for evaluation of the effect of temperature on MFL and MBN signals
3) Develop a theoretical method for determining the dependence of MBN on the angle between measurement and rolling directions in anisotropic ferromagnetic material
4) Experimentally investigate the correlation between the amount of carbon in steels and magnetic NDE methods.

To meet the above purposes, both theoretical and experimental work are carried out, which involved various magnetic measurements, as well as analytical and numerical modelling.

1.3 Organisation of the Thesis

This thesis is organised into nine chapters, which cover theoretical and experimental aspects of the effects of stress, temperature and microstructure on magnetic NDE methods.

Chapter 2 introduces the fundamental theories of magnetism, ferromagnetic material and the analytical methods in modelling magnetic hysteresis and magnetic Barkhausen noise (MBN).

Chapter 3 presents a general review of NDE techniques and a detailed description of the magnetic NDE methods. Also, it provides insight into industrial motivations for this research related to the evaluation of integrity and mechanical properties of ferromagnetic materials.

Chapter 4 describes an analytical model and a finite element model to evaluate the effect of stress on magnetic flux leakage. The analytical model extends the dipole model by considering the stress concentration, which leads to a heterogeneous distribution of magnetisation along the defect surface. The finite element model uses solid mechanics and magnetic modules to simulate the stress-induced magnetisation distribution in a defective dog-bone tensile rod. MFL signal induced by the defect along the sensor scanning line is extracted from the converged solution. Both models are verified by experiments, and the measured peak-to-peak normalised amplitudes are consistent with the results predicted by two models.

Chapter 5 proposes an analytical model to investigate the effect of temperature on magnetic flux leakage. The effect of temperature involves two conditions: the thermal effect itself and the combined effect of temperature and thermal stress. In the first case, the proposed model is based on the modified temperature-dependent J-A model. In the second case, where the combined effects of temperature and thermal stress are considered, the proposed model further introduces the magnetomechanical J-A model. The thermal stress distribution around the defect of a cylindrical through-hole is solved by thermodynamics and solid mechanics theories. The magnetomechanical mechanism is employed to analyse the stress-dependent magnetisation distribution, the crucial parameter in the magnetic dipole model. The verified experiments are conducted on an M250-50A non-oriented (NO) grain silicon steel specimen with a cylindrical through-hole defect. The MFL signals predicted by both modified models well agree with the experimental results.

In **Chapter 6**, a new model relating the MBN amplitude and temperature is proposed and validated. The effect of temperature on magnetic Barkhausen noise (MBN) is divided into two types: the direct effect of temperature itself and the indirect effect of thermally induced stress. The theoretical model is proposed for describing the effects of temperature on the MBN signal. For the case considering the direct effect of temperature only, the analytical model allows predicting the effect of temperature on MBN profile. Based on the model, a simple linear calibration curve is presented to evaluate the effect of temperature on MBN amplitude quantitatively. For the case where the indirect effect of thermal stress is taken into account in addition to the direct effect, the proposed theoretical model allows the deduction of parabolic function for quantitative evaluation of the combined effects on MBN. The direct only and combined effects of temperature on MBN have been studied experimentally on M250-50A NO silicon steel and the adhesive structure of NO steel and ceramic glass, respectively. The reciprocal of the measured MBN peak amplitude (1/*MBNp*) in the first case shows a linear function of temperature, which agrees with the proposed linear calibration curve. In the experiments considering the combined effects, 1/MBNp shows parabolic dependence on temperature, which is further simplified as piecewise functions for practical applications.

In **Chapter 7**, magnetic anisotropy correlated with the crystallographic structure in NO silicon steel on the Magnetic Barkhausen Noise (MBN) technique is studied. The theoretical model is proposed for describing the effect of anisotropy on the MBN signal. Meanwhile, the effect of excitation frequency is also considered in the model. The proposed model predicts the amplitude increasing and envelope broadening with the increase of excitation frequency. Besides, it calculates the decrease in amplitude and increases the MBN envelope width with the increasing angle between the tested direction and rolling direction (RD). The analytical model allows the deduction of a trigonometric function for quantitative evaluation of the anisotropic effect on MBN. The effect of anisotropy on MBN has been investigated experimentally on M330-35A NO electrical steel under excitation frequencies of 50 Hz and 100 Hz, respectively. Under both excitation frequencies, the measured MBN peak amplitudes (MBNp) show cosine dependences on the angle, which approach the proposed trigonometric calibration curves.

Chapter 8 proposes a method for optimising the MBN pick-up coil and experimentally investigates the effect of carbon content in steel on the MBN signals and magnetic hysteresis loops. The MBN pick-up coil is optimised using analytical models of inductance and parasitic capacitance for the hexagonal winding coaxial coil. A multifunctional measurement system using the optimised coil is employed to measure magnetic hysteresis loops and MBN signals. The measured peak-to-peak value of MBN envelope, coercive field and remanence on hysteresis loop are used to characterise the carbon content in various steels.

Chapter 9 concludes the findings and contributions of the investigation regarding the effects of stress, temperature and microstructure on magnetic NDE methods. Also, the possible future directions for this work are presented with respect to the multiphysics simulation and deep learning in magnetic flux leakage and Barkhausen noise techniques.

Chapter 2

Ferromagnetism

This chapter describes the fundamental theories of magnetic field and mechanisms of magnetisation. In addition, the theoretical aspects of micromagnetics, including the domain theory, the different micromagnetic energies, are introduced. It provides insight into the cause of hysteresis in ferromagnetic materials by explaining the domain structures and domain wall motion. And finally, analytical models of hysteresis and magnetic Barkhausen noise are introduced.

2.1 Magnetic field

One of the most fundamental concepts in magnetism is magnetic field (***H***), which is a vector field that describes the magnetic influence on a magnetised material or a moving electric charge. A magnetic field can be produced by a permanent magnet or a moving electric charge. A magnetic field generated by an electric current has been solved by Ampère and expanded by Maxwell [1]:

$$\nabla\times\boldsymbol{H}=\boldsymbol{J}_f+\frac{\partial\boldsymbol{D}}{\partial t} \tag{2.1}$$

where $\boldsymbol{J}_f$ is a free current density, $\boldsymbol{D}$ is the electric displacement field.

When a magnetic field is generated in a medium, the response of the medium is its magnetic induction $\boldsymbol{B}$, also usually called the magnetic flux density. The relation between magnetic induction and magnetic field is called the permeability of the medium. In particular, the permeability of free space or vacuum is a universal constant represented as μ_0 ($\mu_0 = 4\pi\times10^{-7}$ H/m). The magnetic induction in free space is written as

$$\boldsymbol{B}=\mu_0\boldsymbol{H} \tag{2.2}$$

However, in other media, particularly in a ferromagnetic material, $\boldsymbol{B}$ is no longer proportional to $\boldsymbol{H}$. They are found following the regularity of a more complicated relation named magnetic hysteresis. But their relation can also be represented by the permeability of the medium μ through the equation

$$\boldsymbol{B} = \mu(H) \cdot \boldsymbol{H} \tag{2.3}$$

where μ is no longer a constant. It is the product of μ_0 and dimensionless quantity μ_r, where μ_r is relative permeability varying with the strength of magnetic field.

As mentioned above, an electric current can generate a magnetic field. Conversely, a changing magnetic field can induce an electric field. According to Faraday's law and Lenz's law [1,2], a spatially varying electric field ($\boldsymbol{E}$) always accompanies a time-varying magnetic field:

$$\nabla \times \boldsymbol{E} = -\frac{\partial \boldsymbol{B}}{\partial t} \tag{2.4}$$

Together with Gauss's law, which describes the relation between static electric field and the electric charges, and Gauss's law for magnetism, which states there is no magnetic monopole, Maxwell formulated a few partial differential equations now called Maxwell's equations [2]:

$$\begin{cases} \nabla \cdot \boldsymbol{E} = \frac{\rho_E}{\varepsilon_0} \\ \nabla \cdot \boldsymbol{B} = 0 \\ \nabla \times \boldsymbol{E} = -\frac{\partial \boldsymbol{B}}{\partial t} \\ \nabla \times \boldsymbol{B} = \mu_0 (\boldsymbol{J} + \varepsilon_0 \frac{\partial \boldsymbol{E}}{\partial t}) \end{cases} \tag{2.5}$$

where ρ_E is the electric charge density and $\boldsymbol{J}$ is the current density. The publication of the equations marked the unification of previously separated theories. The equations provide one of the most important mathematic models for electric, magnetic, optical and radio technologies.

In addition to the permanent magnets, which have constant residual magnetisation, solenoids or electromagnets are widely used to produce magnetic fields. The Biot-Savart law is one of the fundamental laws to calculate the magnetic field generated by an electric current [1]:

$$\boldsymbol{H} = \frac{I}{4\pi}\int_C \frac{\boldsymbol{dl}\times\boldsymbol{r}}{|\boldsymbol{r}|^3} \tag{2.6}$$

where I is electric current, $\boldsymbol{dl}$ is a vector along with path C, and $\boldsymbol{r}$ is the displacement vector from wire element ($\boldsymbol{dl}$) to the calculated point. This equation can be used relatively straightforward to calculate a magnetic field generated by a solenoid made by winding numbers of turns enamelled copper wire. For a long thin solenoid that is used to produce a uniform magnetic field, the magnetic field strength at the centre of it will be

$$H = \frac{NI}{L} \tag{2.7}$$

where N is the turns of the solenoid and L is its length. Another widely used coil to produce a uniform field is Helmholtz coils, which consists of two coaxial coils with the same turns and carrying current. When the Helmholtz coils consist of N turns of wire carrying constant current I, the magnetic field strength at the axis of symmetry can be given by

$$H = \frac{NIR^2}{2(R^2+x^2)^{3/2}} \tag{2.8}$$

where R is the coil radius and x is the coil distance on-axis, as shown in Fig. 2.1.

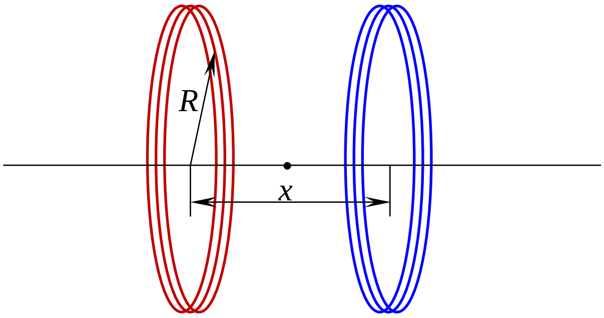

Figure 2.1. Two coaxial coils configuration of Helmholtz pair

Although the Biot-Savart law and Maxwell equations can be applied to compute the magnetic field in various simple situations, there is not always an analytical solution (e.g., the magnetic field in a shaped solenoid coil with a soft material core). One of the advantages of numerical techniques over analytical methods is the ability to simulate a wide range of physics and geometry. Besides, the numerical methods are superior to analytical models in solving time-stepping problems [1,3,4]. Furthermore, the numerical modelling methods are more furnished to better fit the nonlinear problems by discretizing the problem properties and geometries [3,4]. Hence, in general cases, it is necessary to resort to numerical techniques to obtain a solution.

One of the widely used numerical techniques, Finite Element Modelling (FEM), is based on the concept of dividing the original problem domain into an equivalent system (mesh) of numerous smaller subdomains called finite elements and applying a numerical formulation based on interpolation theory to these elements [3,4]. The FEM simulation packages commercially available are COMSOL Multiphysics, MagNet by Infolytica, ANSYS, *etc*. Compared to the Finite Difference Method, the FEM method can significantly improve the solution accuracy [3,4]. Besides, numerical methods such as the Boundary Element Method and Finite Difference Method are not appropriate to solve nonlinear problems [4]. Hence, FEM is preferred for solving electromagnetic field problems. The FEM model created using COMSOL Multiphysics software and the FEM simulations to investigate the stress-dependent magnetic flux leakage field will be presented in Chapter 4.

2.2 Magnetisation

2.2.1 Magnetic materials

According to Ampère's theorem [1], current in an electrical circuit will produce a field so that a current loop carrying an electric current will generate the magnetic dipole moment $\boldsymbol{m}$, which can be considered the most elementary unit of magnetism. The torque on a magnetic dipole moment in a magnetic induction follows the equation

$$\boldsymbol{\tau} = \boldsymbol{m} \times \boldsymbol{B} \tag{2.9}$$

It means that magnetic induction $\boldsymbol{B}$ tries to align the dipole such that the moment $\boldsymbol{m}$ will lie parallel to the induction.

To consider the effect of magnetic material on magnetic induction $\boldsymbol{B}$, it is necessary to define a quantity, magnetisation $\boldsymbol{M}$, which represents magnetic moments per unit volume ($\boldsymbol{m}/V$) in a magnetic material. When an external field $\boldsymbol{H}$ is applied, there are two contributions to form the magnetic induction $\boldsymbol{B}$: one from the magnetic field and the other from the magnetisation so that Equation (2.3) can be rewritten as

$$\boldsymbol{B}=\mu_0(\boldsymbol{H}+\boldsymbol{M}) \tag{2.10}$$

Another quantity linking magnetisation with the external field is called magnetic susceptibility χ and can be expressed as

$$\boldsymbol{M}=\chi\boldsymbol{H} \tag{2.11}$$

The various magnetic materials can be generally classified into three groups according to their susceptibilities: diamagnetic, paramagnetic and ferromagnetic. As its name suggests, the susceptibility value of a diamagnetic material is negative, while the other two groups are positive. To state clearly, in the diamagnetic group, χ is relatively small and of order -10^{-5}, in the paramagnetic group, χ is relatively small as well and of order 10^{-3} to 10^{-5} [1], and χ is much greater than 1 in the ferromagnetic group. In this thesis, the research objects are ferromagnetic materials.

2.2.2 Demagnetising field

When an external field magnetises a ferromagnetic material with finite dimensions, the directions of magnetisation and the magnetic field generated by the magnetised sample are opposite inside the sample. According to the theory of magnetic dipole moment, the magnetisation is considered as being the effect of aligning the magnetic dipoles within the magnetic material, and the dipoles create magnetic "poles" near the ends of the finite sample giving rise to a magnetic field opposing the applied field.

The demagnetising field is only related to the magnetisation in the material and the geometry of the specimen. The demagnetising field $\boldsymbol{H_d}$ is proportional to the magnetisation $\boldsymbol{M}$ but points in the opposite direction so that it can be given by

$$\boldsymbol{H_d} = -N_d\boldsymbol{M} \tag{2.12}$$

where N_d is the demagnetising factor dependent on the shape of the specimen and $0 \leq N_d \leq 1$. The accurate analytic solutions for N_d can only be obtained in geometries with second-order differential equations, such as ellipsoids [1,5].

In ellipsoidal bodies, which are uniformly magnetised, the demagnetising field is in turn also uniform. If the three principal axes (assumed as a, b and c) of the ellipsoidal body coincide with the x, y and z axes and $a \geq b \geq c \geq 0$, the axial components of demagnetising factor are [5]

$$N_{dx} + N_{dy} + N_{dz} = 1 \tag{2.13}$$

And the exact formulas give as

$$N_{dx} = \frac{cos\varphi cos\vartheta}{sin^3\vartheta sin^2\theta}[F(\psi,\vartheta) - E(\psi,\vartheta)] \tag{2.14}$$

$$N_{dy} = \frac{cos\varphi cos\vartheta}{sin^3\vartheta sin^2\theta cos^2\theta}[E(\psi,\vartheta) - cos^2\theta \cdot F(\psi,\vartheta) - \frac{sin^2\theta sin\vartheta cos\vartheta}{cos\varphi}] \tag{2.15}$$

$$N_{dz} = \frac{cos\varphi cos\vartheta}{sin^3\vartheta cos^2\theta}[\frac{sin\vartheta cos\varphi}{cos\vartheta} - E(\psi,\vartheta)] \tag{2.16}$$

where

$$cos\varphi = b/a, \quad (0 \le \varphi \le \pi/2) \tag{2.17}$$

$$cos\vartheta = c/a, \quad (0 \le \varphi \le \pi/2) \tag{2.18}$$

$$sin\theta = \frac{sin\varphi}{sin\vartheta} = \psi, \quad (0 \le \psi \le \pi/2) \tag{2.19}$$

and $F(\psi,\vartheta)$ and $E(\psi,\vartheta)$ are elliptic integrals of the first and second kinds. ψ is the modulus and ϑ is the amplitude of these integrals. The Equations (2.14) to (2.16) given above allow us to calculate the demagnetising factor of an ellipsoid, but the calculation will not be an easy task. For some special and simple geometries, the factors are easy to obtain, for example, the demagnetising factors of a toroid and a long cylinder are 0 and that of a sphere is 1/3.

In general cases, the demagnetising factor is hard to solve analytically. Therefore, to avoid the error caused by calculating the demagnetising factor, for specimens with the same geometry and subject to the same external magnetic field, the analytical results can apply the normalisation method to eliminate demagnetising effect in this thesis. Besides, concerning complex geometry, FEM is preferred to numerically compute magnetic field including the demagnetising field, which will be presented in Chapter 4.

2.2.3 Magnetisation process

The relation between magnetic induction ***B*** and magnetic field ***H*** has been given in Equations (2.2), (2.3) and (2.10). For free space and paramagnetic material, magnetic induction is linear to the magnetic field, while the relationship is much more complicated in the case of ferromagnetic material. Besides, the one-to-one correspondence between states of induction and the applied field can be seen in free space and paramagnetic material, but it is absent in ferromagnetic material. The most common way to represent the bulk magnetic properties of a ferromagnetic material is by a plot of a *B-H* hysteresis curve or *M-H* hysteresis curve.

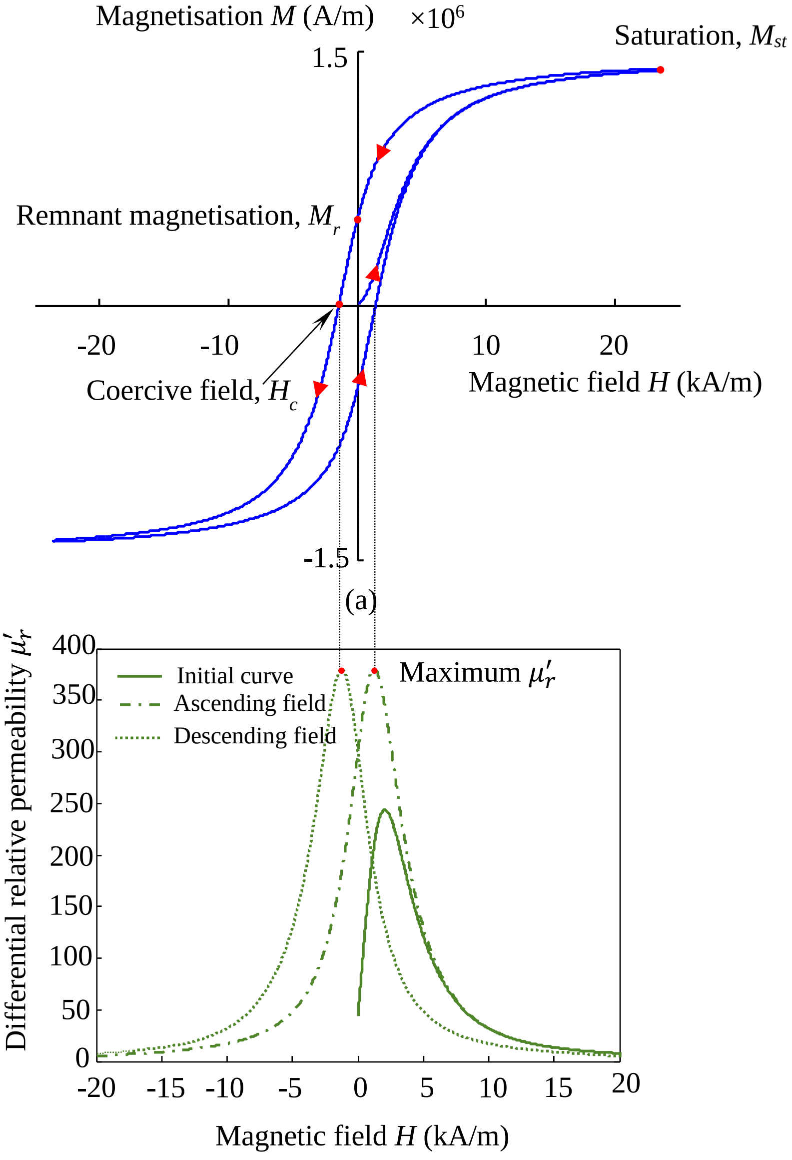

(b)

Figure 2.2. Graphical illustration of the magnetisation process in a specimen of 1.0 wt % C carbon steel. [6] **(a)** The initial magnetisation curve and hysteresis loop of the specimen; **(b)** The differential relative permeability as a function of applied field in the carbon steel.

Fig. 2.2a shows a typical *M-H* curve including an initial magnetisation process and a major hysteresis loop. The initial magnetisation process starts after the demagnetisation, where the net magnetisation is zero. When applying an external magnetic field, the magnetic dipoles or domains are trying to align to the field until the material is magnetically saturated. When all domains are aligned parallel to the field direction, it is named saturation magnetisation M_{st}. The magnetic domain is a region where the magnetic moments point in the same direction will be introduced in the next section.

When the external field is reducing, more and more domains are no longer parallel to the field. However, when the field reduces to zero, there are still numerous domains aligned so that the ferromagnetic specimen retains considerable net magnetisation, which is the remnant magnetisation M_r (in B-H curve, it is remnant flux density B_r).

If the field is reducing further, the direction of the applied field will be reversed, and the magnetisation keeps decreasing. When the magnetisation reaches zero, the amount of magnetic field corresponds to the coercive field, marked as H_c in Fig. 2.2a. After this point, with the increase of reverse field, domains are trying to align to the reverse field until saturation.

Then reversing the external field, the magnetisation will experience remnant magnetisation and coercive point again. Their values are the same as the aforementioned decreasing part of the hysteresis loop, but the signs are the opposite. Continuous applying and reversing the external magnetic field results in repetition of the magnetisation cycle pattern where the magnetisation M changes with the magnetic field H along the hysteresis loop.

When analysing the response of the carbon steel to the applied field, the relative permeability μ_r can become infinite and even negative along the hysteresis loop. Therefore, it is more reliable to use the term of differential relative magnetic permeability to describe the dynamic magnetisation process along the hysteresis loop and it is defined as

$$\mu_r' = \frac{1}{\mu_0}\frac{dB}{dH} \tag{2.20}$$

As an example, Fig. 2.2b shows the differential magnetic relative permeability varies as a nonlinear function of the applied field, along the initial magnetisation curve and hysteresis loop of the carbon steel.

2.3 Micromagnetic Theory

In the previous sections, the important macroscopic magnetic properties of ferromagnets, represented on a *B-H* curve or hysteresis loop, have been discussed. This section will explain the magnetic phenomena on the microscopic scale of magnetic domain and magnetic energies. In addition, the domains' behaviour and their related magnetic energies will be introduced. Furthermore, the hysteresis and magnetic Barkhausen noise models related to the domain motion and magnetisation will be discussed in the following Sections.

2.3.1 Magnetic domain

Weber assumed the ferromagnetic material should already have magnetic moments which were randomly oriented in a demagnetised state and became aligned under the action of the applied field [1]. Ewing inherited this hypothesis to explain the hysteresis on the basis of the interactions between atomic dipole moments [1]. But they did not realize that the demagnetised ferromagnet was already in an ordered state as there were numerous atomic magnetic moments oriented locally in parallel, which rarely exist in paramagnet. The region in a ferromagnet where all the dipole moments point along the same direction is called a magnetic domain [1,7]. Domains are separated by domain walls. The directions of domains are aligned randomly in the demagnetisation state so that the ferromagnet does not present bulk magnetisation in macroscopy.

In a domain, all magnetic moments are pointed parallel to each other, giving rise to a spontaneous magnetisation M_s, according to Weiss mean-field theory [7]. It is an interatomic interaction that causes neighbouring atomic magnetic moments to align parallel to minimise the exchange energy. The spontaneous magnetisation equals the saturation magnetisation at 0 K (i.e., absolute zero) but decreases with the temperature increase and becomes zero at the Curie point.

With the observations of domains by the Bitter colloid method [8] and magneto-optic Kerr effect method [9], the hypothesis of the magnetic domain was verified. Fig. 2.3 shows the domain configuration of a nanostructured Permalloy specimen during one cycle magnetisation process [10,11]. At the beginning (H = 0 A/m), the domains constitute the flux closure domain pattern where the net magnetisation shows zero. The flux closure domains are usually the last domains to flip over in the magnetising process as shown in Fig. 2.3e and 2.3f. They, in reverse, emerge at the beginning of the demagnetising process to provide return paths for the spontaneous magnetisation of the main domains.

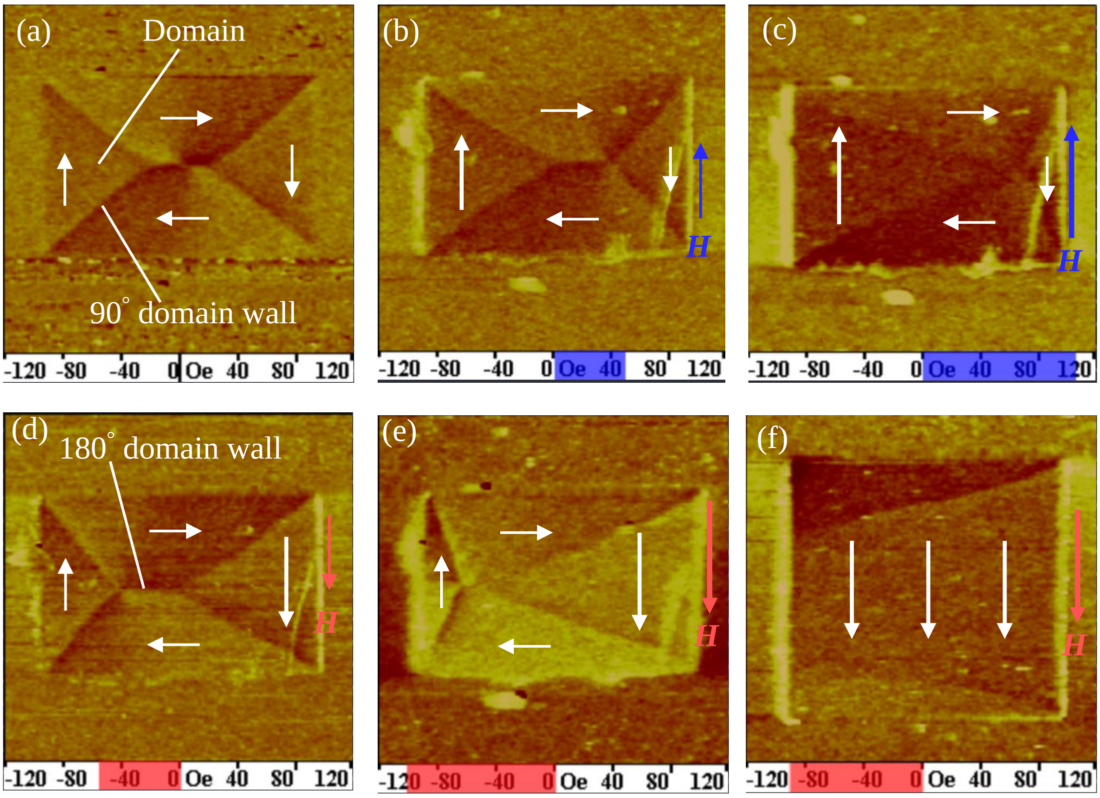

Figure 2.3. Domain configurations of Permalloy elements. **(a)** ~ **(e)** show the domain motion during a 2μm×2μm×26nm Permalloy specimen in a magnetisation cycle and **(f)** shows the saturation condition of a 3μm×3μm×26nm Permalloy specimen (1Oe = 79.58 A/m). [10,11]

2.3.2 Domain wall

It can be seen in Fig. 2.3 that the domains are separated by layers which are called domain walls. The domain walls between two antiparallel domains are 180° domain walls as marked in Fig. 2.3d. The domain walls between the main and perpendicular domains are 90° domain walls marked in Fig. 2.3a. The domain wall is not infinitesimal in width. Bloch [13] first suggested that the domain walls should be transition layers between domains, so they were named after him (Bloch walls). The widths of domain walls are determined by minimizing domain wall energy. For example, the thickness of a domain wall of iron is approximately 160 atomic layers

[1]. The magnetic moments reorient within domain wall and the directions of the moments change gradually over numbers of atomic layers as shown in Fig. 2.4 [12].

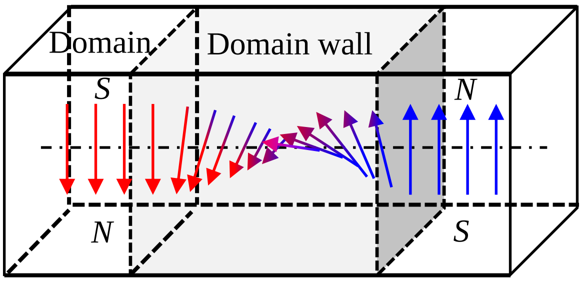

Figure 2.4. Illustration of the domain, 180° domain wall and the alignment of magnetic moments within them [12].

In a bulk specimen, the realigning magnetic moments lead to magnetisation normal to the plane of the material, while in a thin film specimen that the ferromagnetic domain can extend across the whole width of the specimen, the moments will rotate within the plane of the material which is known as Néel wall [1] (as shown in Fig. 2.5).

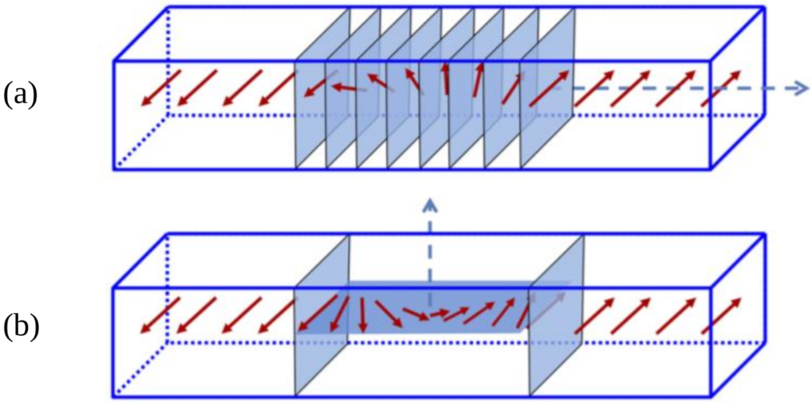

Figure 2.5. The typical **(a)** Bloch wall and **(b)** Néel wall [1,14].

As mentioned above, there are different kinds of domain walls including 180° and 90° walls. In cubic material, when anisotropic constant $K > 0$, only 180° and 90° domain walls exist. There are some other non-180° walls, for example, in nickel when $K < 0$, the easy axes are all the <111> directions so that the non-180° walls are either 71° or 109° [1].

2.3.3 Behaviour of domains

The behaviour of domains has been briefly introduced previously. In this section, the changes inside domains under the action of a changing magnetic field and the mechanism behind them are discussed.

In a ferromagnetic material, when a small increment of the applied field is removed, the magnetisation will return to the original value. It is called reversible magnetisation. By contrast, during irreversible magnetisation, the magnetisation does not return to its initial value on removing the field. More often, both reversible and irreversible processes occur together during the magnetisation cycle. The corresponding changes of the domain are classified as the reversible and the irreversible change of domain.

In a reversible process at a relatively weak applied field, the domain wall bows like an elastic membrane. When the field is removed, the wall will resile to its initial position. The bowing of the domain wall will become irreversible once the wall is adequately deformed. It may also become irreversible if the wall encounters further pinning sites to prevent its resilience when removing the field. In an irreversible process, the domain wall motion usually performs the effect of translation. The wall displacement caused by pinning sites can give rise to energy loss.

At low field amplitude, the direction of magnetic moments slightly deflects from easy axes to the field direction resulting in the reversible rotation of moments within the domain. In this stage, the energetically favourable domain closest to the field direction expands at the expense of neighbouring domains. With the field amplitude increase, when the field energy overcomes the anisotropy energy, the moments will rotate from the original easy axis to the new one closest to the irreversible field direction. Similar to the previous stage, the magnetisation process is accompanied by the domain wall motion and volume growth of energetically favourable domains. At the high field, the magnetisation process is continued by domain rotating towards the field direction. In this case, there is a reversible mechanism within the domain as the energy minimum of the easy axis closest to the field can be perturbed by the field energy so that the rotation of moments into the field direction can be reversible. And finally, at a very high field, the ferromagnetic material reaches its saturation with all moments aligning to the field direction. These processes are diagrammatically shown in Fig. 2.6.

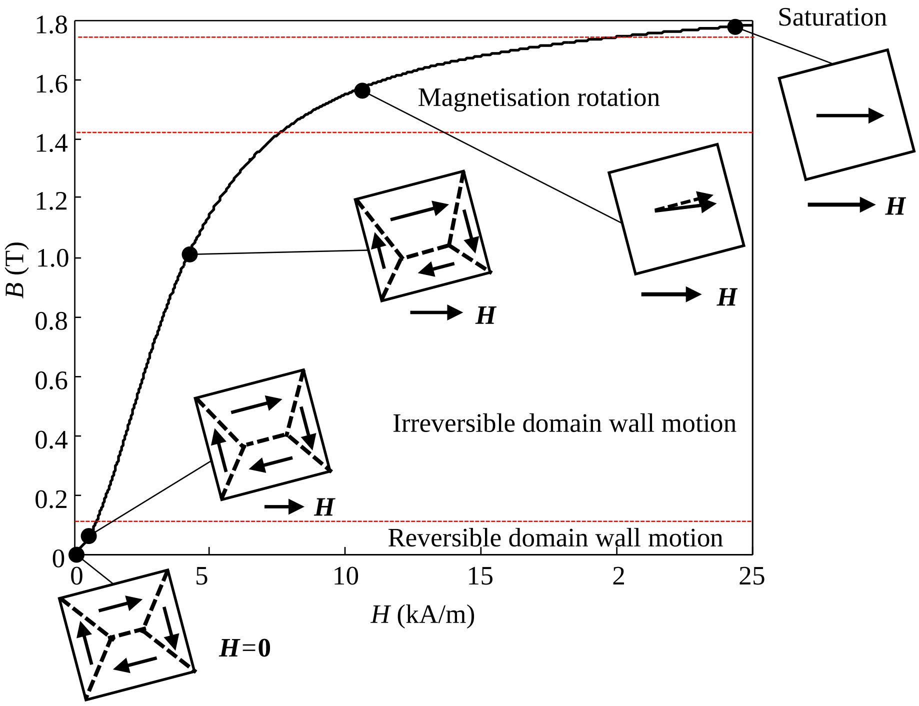

Figure 2.6. Changes of domain structures during the magnetisation process in a ferromagnetic material [1].

The modern theory of magnetic domain is based on the total magnetic free energy [15-17]. There are several main contributions to the total free energy including exchange energy, magnetocrystalline anisotropy energy and magnetostatic energy, which are discussed as follows.

2.3.4 Magnetic energies

As discussed previously, a ferromagnetic material consists of a number of domains in the absence of an external magnetic field and in each of them, all magnetic moments are aligned parallel. During the magnetisation process, the domain rotation and domain wall motion occur according to the minimum energy theory. The static total magnetic free energy E_{tot} is contributed by exchange energy E_{ex}, magnetocrystalline anisotropy energy E_a, magnetostatic energy E_m, magnetoelastic energy E_λ, Zeeman energy E_z and domain wall energy E_{dw}. Hence, the total magnetic free energy can be written as

$$E_{tot} = E_{ex} + E_a + E_m + E_\lambda + E_z + E_{dw} \tag{2.21}$$

I. **Exchange energy**

Exchange energy derived from a quantum mechanical effect of the exchange interaction is closely related to the coupling of adjacent atomic magnetic moments and their tendency to align parallel to each other. If the nearest-neighbour interaction is considered exclusively, the exchange energy of two nearest-neighbour spins is written as [1]

$$E_{ex} = -2J_{ex}\boldsymbol{S_i} \cdot \boldsymbol{S_j} \tag{2.22}$$

where J_{ex} is the exchange constant, $\boldsymbol{S_i}$ and $\boldsymbol{S_j}$ are the nearest-neighbour spin angular momenta. According to Equation (2.22), to minimise the exchange energy all the neighbouring magnetic moments within a ferromagnet should be aligned parallel, i.e., the ferromagnet is uniformly magnetised.

II. **Magnetocrystalline anisotropy energy**

The combination of crystal structure and spin-orbit interaction gives rise to the contribution to the magnetocrystalline anisotropy energy. The anisotropy energy favours magnetic configurations where the magnetic moments tend to align along energetically favourable crystallographic directions. For example, the cubic 3d transition material such as iron and nickel, their magnetic moments align preferentially along their easy axes, i.e., <100> and <111> axes, respectively.

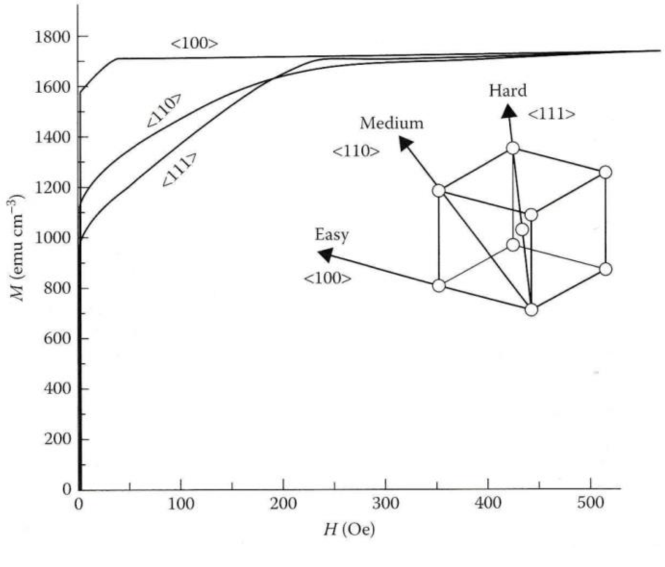

Figure 2.7. Magnetisation curves for iron along axes <100>, <110> and <111> (1Oe = 79.58 A/m, 1 emu·cm^{-3} = 1000 A/m) [1].

The magnetisation curves along various axes in iron are shown in Fig. 2.7. It can be seen that the highest low-field susceptibility of iron is along axis <100> which is called 'easy axis'. It is easiest to magnetise iron along the easy axis while it is more and more difficult to magnetise iron along axes <110> and <111> which are called 'medium axis' and 'hard axis', respectively.

In a cubic crystal such as iron, the anisotropy energy is given by:

$$E_a = K_1(cos^2\theta_1 cos^2\theta_2 + cos^2\theta_2 cos^2\theta_3 + cos^2\theta_1 cos^2\theta_3) +$$

$$K_2(cos^2\theta_1 cos^2\theta_2 cos^2\theta_3) \tag{2.23}$$

where θ_1, θ_2 and θ_3 are angles of the magnetisation vectors relative to the three principal crystal axes, K_1 and K_2 are the first and second-order anisotropy coefficients. For example, K_1 and K_2 of iron at room temperature are 48 kJ/m^3 and 5 kJ/m^3 respectively [1]. If neglecting the second term on the right hand of Equation 2.23, the one-constant equation that only retains the first item can be used as an approximation

$$E_a = K_1(cos^2\theta_1 cos^2\theta_2 + cos^2\theta_2 cos^2\theta_3 + cos^2\theta_1 cos^2\theta_3) \tag{2.24}$$

For $K_1 > 0$, the easy axes are <100> directions such as iron, while $K_1 < 0$, the easy axes are <111> directions such as nickel.

III. **Magnetostatic energy**

The magnetostatic energy E_m is the potential energy of magnetic moments that are subjected to the magnetic field. The magnetostatic energy can be expressed as an integral over the body volume. For a single domain crystal as shown in Fig. 2.8a, the energy per unit volume is given by

$$E_m = -\mu_0 \int \boldsymbol{H_d} d\boldsymbol{M_s} = \frac{\mu_0}{2} N_d \boldsymbol{M}_s^2 \tag{2.25}$$

where $\boldsymbol{H_d}$ is the demagnetising field, N_d is the demagnetising factor and $\boldsymbol{M_s}$ is the spontaneous magnetisation within a domain. In the case where the ferromagnetic crystal is a single domain, all magnetic moments align along the easy axis so that it results in a large demagnetising field at the ends as shown in Fig. 2.8a. The energy will be reduced by nearly half, if the crystal is divided into two domains where the magnetic moments align antiparallel as shown in Fig. 2.8b, since the new south and north poles created by magnetic moments are closer, reducing the demagnetising field. Similarly, when the domain is split into four individuals as shown in Fig. 2.8c, the energy will be reduced by about one-fourth of the initial one. The magnetostatic energy is minimized by creating the closure domain where the magnetic flux is enclosed and the magnetic poles are eliminated as shown in Fig. 2.8d.

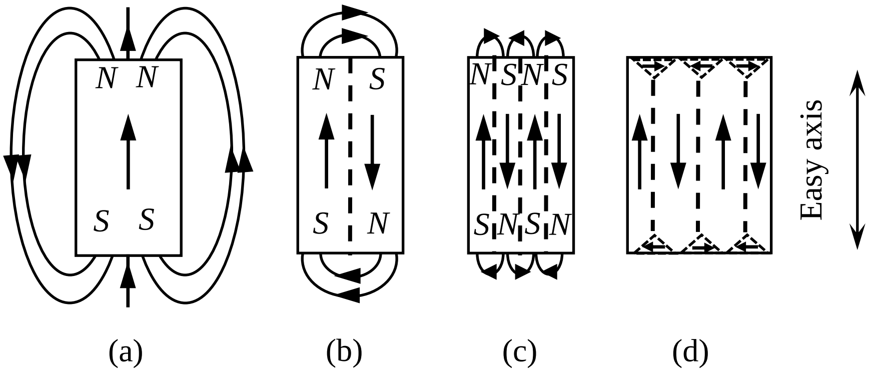

Figure 2.8. Diversion ferromagnetic crystal into domains [18].

IV. **Magnetoelastic energy**

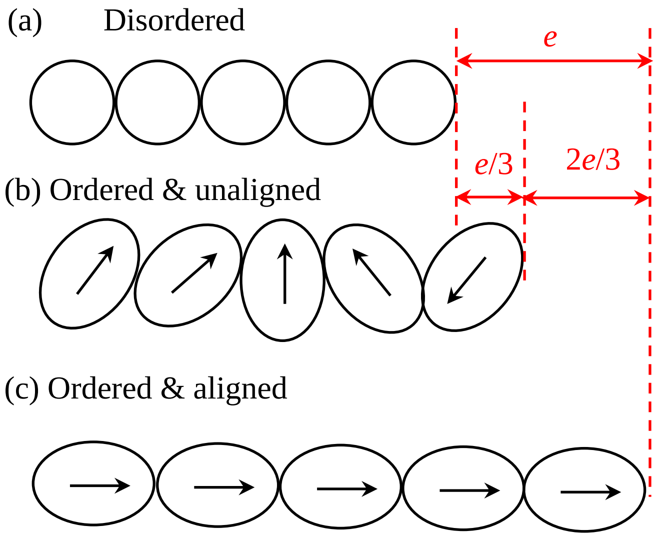

Figure 2.9. A schematic diagram illustrating the magnetostriction in **(a)** the disordered (paramagnetic) state, **(b)** the unmagnetized ferromagnetic state, **(c)** saturate magnetisation ferromagnetic state (image reproduced from [1])

Magnetoelastic energy describes the energy caused by elastic lattice distortion. The distortion or strain is called magnetostriction (λ). There are two main types of magnetostriction: (1) spontaneous strain arising from the ordering of the magnetic moments when the ferromagnetic material is cooled from its Curie temperature, and (2) field-induced strain caused by the realignment of domains.

In case of the temperature cooling down from the Curie point of the ferromagnetic material, the previously disordered magnetic moments due to random alignment become ordered within domains. The spontaneous magnetisation M_s appears within domains and orients variously from domain to domain to ensure that the bulk magnetisation is zero. With the spontaneous magnetisation appearance, the spontaneous strain e or magnetostriction λ_0 is generated along a particular direction as shown in Fig. 2.9b. The relation of spontaneous magnetostriction can be given as

$$\lambda_0 = \frac{e}{3} \tag{2.26}$$

When the material is magnetised to saturation, all the magnetic moments align parallel within domains as shown in Fig. 2.9c. The relation between spontaneous strain e and saturation magnetostriction λ_s is expressed as

$$\lambda_s = \frac{2e}{3} \tag{2.27}$$

If the material is isotropic, its saturation magnetostriction λ_s at any angle θ to the applied field direction can be given as

$$\lambda_s(\theta) = \frac{3}{2}\lambda_s\left(cos^2\theta - \frac{1}{3}\right) \tag{2.28}$$

While if the material is anisotropy, the saturation magnetostriction needs to be defined concerning the crystal axis where the magnetisation lies. The saturation magnetostriction in a single domain, single crystal cubic material is given by [1,18]

$$\lambda_s = \frac{3}{2}\lambda_{100}\left(\alpha_1^2\beta_1^2 + \alpha_2^2\beta_2^2 + \alpha_3^2\beta_3^2 - \frac{1}{3}\right) + \\ 3\lambda_{111}(\alpha_1\alpha_2\beta_1\beta_2 + \alpha_2\alpha_3\beta_2\beta_3 + \alpha_1\alpha_3\beta_1\beta_3) \tag{2.29}$$

where λ_{100} is the saturation magnetostriction along the <100> direction, λ_{111} is the saturation magnetostriction along the <111> direction, α_1, α_2 and α_3 are the direction cosine of the spontaneous magnetisation vector with respect to the crystal axes, β_1, β_2 and β_3 are the direction cosines of measured magnetostriction relative to the crystal axes as shown in Fig. 2.10. The equation validates a crystal having either <100> or <111> as the easy axis.

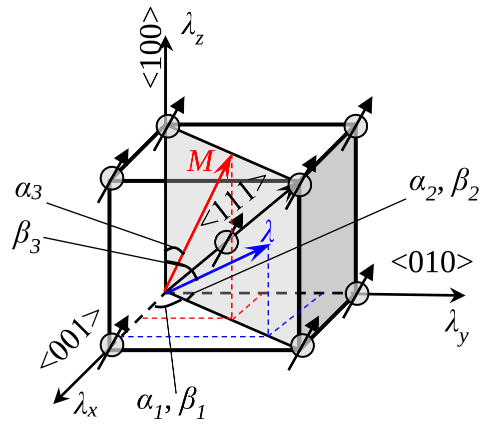

Figure 2.10. A schematic diagram showing the principal crystal axes and the magnetostriction measurement directions [1].

Most commonly, the strain is usually measured in the same direction of magnetisation, and hence, Equation (2.29) can be further simplified to [1]

$$\lambda_s = \lambda_{100} + 3(\lambda_{111} - \lambda_{100})(\alpha_1^2\alpha_2^2 + \alpha_2^2\alpha_3^2 + \alpha_3^2\alpha_1^2) \tag{2.30}$$

When applied additional stress to a ferromagnetic material, the magnetisation direction will change, and the relation between the direction of magnetisation *M* within a domain and the direction of stress σ should be considered. It has been known that the direction of *M* can be influenced by magnetocrystalline anisotropy in the absence of stress. While with the action of stress, the direction of *M* will be combinedly controlled by stress and anisotropy. By considering the contribution of stress, the magnetoelastic energy E_λ for an iron-based material can be approximated as [16]

$$E_\lambda = -\frac{3}{2}\lambda_{100}\sum_{i=1}^{3}\sigma_{ii}\alpha_i^2 - \frac{3}{2}\lambda_{111}\sum_{i\neq j}\sigma_{ij}\alpha_i\alpha_j \tag{2.31}$$

where α_i and α_{ij} are the direction cosines of magnetisation *M* aforementioned, and σ_{ii} and σ_{ij} are the tensor components corresponding to applied stress σ.

And when uniaxial σ stress that may be caused by residual strain or an external force is applied, the magnetoelastic energy in an isotropic material is shown below

$$E_\lambda = -\frac{3}{2}\sigma\lambda_s cos^2\theta \tag{2.32}$$

where the θ is the angle between directions of stress and magnetisation. This equation has a similar format to uniaxial anisotropy energy, so it is called stress-induced anisotropy, where the effect of applied stress can be considered as the introduction of an extra easy axis of magnetization in addition to the magnetocrystalline easy axis.

For ferromagnetic material with positive magnetostriction, the magnetoelastic energy is minimum when the direction of magnetisation is parallel to the unidirectional tensile stress, while for the negative one, the energy is minimised when the magnetisation is perpendicular to the unidirectional tensile stress. The mechanism of magnetomechanical will be further discussed in Section 2.4.

V. **Zeeman energy**

After Pieter Zeeman [15-17], the Zeeman energy is the interaction energy between the magnetisation $\boldsymbol{M}$ and the externally applied field $\boldsymbol{H}$. It is written as:

$$E_Z = -\mu_0 \int_V \boldsymbol{M} \cdot \boldsymbol{H} dV \tag{2.33}$$

According to the equation, in a unit volume the Zeeman energy favours the alignment of magnetic moments parallel to the direction of the externally applied field.

VI. **Domain wall energy**

In the previous discussion, the transition region that separates domains has been defined as the domain wall (see Fig. 2.4). And the total energy of the Bloch domain wall per unit area E_{dw} is given by [1]:

$$E_{dw} = \frac{\mu_0 \xi \boldsymbol{m}^2 \pi^2}{l_{dw} S_{la}} + K_1 l_{dw} \tag{2.34}$$

where ξ is the interaction between nearest magnetic moments, $\boldsymbol{m}$ is the individual magnetic moments, S_{la} is the lattice spacing, l_{dw} is the thickness of the domain wall and K_1 is the first order of anisotropy constant. From the equation, the energy is the sum of the exchange (the first item) and anisotropy (the second item) energies of domain wall, which can determine the thickness of domain wall in dynamic balance. When the exchange energy is the dominant term, the total energy is minimized at a thick domain wall. While the anisotropy energy is prominent, the domain wall energy is minimized at a thin domain wall.

2.4 Theory of Ferromagnetic Hysteresis

2.4.1 Magnetic hysteresis

The effective domain structure of a material is the one minimizing the sum of those energies mentioned previously called the magnetic Gibbs free energy of the material. Assuming all imperfections are absent in an isotropic ferromagnetic material, according to the classical thermodynamic of reversible system, the Gibbs energy per unit volume is given by [1,19]

$$G = U - TS + \frac{3}{2}\sigma\lambda \tag{2.35}$$

where:
G is the Gibbs energy density,
U is the internal energy density,
T is the thermodynamic temperature,
S is the entropy
σ is the stress and λ is the bulk magnetostriction.

Here, if the stress is not considered. The Helmholtz energy density A is given by

$$A = G + \mu_0 \boldsymbol{H} \cdot \boldsymbol{M} = U - TS + \mu_0 \boldsymbol{H} \cdot \boldsymbol{M} \tag{2.36}$$

The internal energy density U due to magnetisation is given by [1,19]

$$U = \frac{1}{2}\alpha\mu_0 \boldsymbol{M}^2 \tag{2.37}$$

The energy in a domain is influenced by other neighbour domains. The effect of interaction between domains can be represented as an effective contribution to the magnetic field. The effective filed is given by [19]

$$\boldsymbol{H}_e = \frac{1}{\mu_0}\left(\frac{dA}{d\boldsymbol{M}}\right)_T \tag{2.38}$$

So that the effective field $\boldsymbol{H}_e$ is expressed as [20]

$$\boldsymbol{H}_e = \boldsymbol{H} + \alpha \boldsymbol{M} \tag{2.39}$$

where α is a mean field parameter representing interdomain coupling.

Applying Maxwell-Boltzmann statistics, in the case of $\alpha \neq 0$, the anhysteresis magnetisation $\boldsymbol{M_{an}}$ as a function of the effective field for isotropic material can be described by the modified Langevin equation [20]:

$$\boldsymbol{M_{an}} = M_{st}\left[\coth\left(\frac{\boldsymbol{H}+\alpha\boldsymbol{M}}{a}\right) - \frac{a}{\boldsymbol{H}+\alpha\boldsymbol{M}}\right] \tag{2.40}$$

where M_{st} is the saturation magnetisation and the coefficient of domain density

$$a = \frac{k_B T}{\mu_0 m} \tag{2.41}$$

where k_B is Boltzmann constant and m are magnetic moments. The anhysteresis magnetisation curve is shown in Fig. 2.11a.

The anhysteretic magnetisation assumes the case where there is no hysteresis loss. In this case, moment rotation within domains is considered exclusively rather than the energy losses in domains. Then, by considering the domain wall motion, which is irreversible, the energy will be dissipated while overcoming the pinning sites. Under the assumption of uniform pinning sites and each of them having the mean pinning energy, the total energy consumption on pinning is proportional to the change in magnetisation. The irreversible magnetisation energy is assumed to be the difference between the energy obtained in the lossless case and the energy due to the losses induced by domain wall motions. Consequently, after differentiating operations, the irreversible magnetisation M_{irr} can be written as [21-23]

$$\boldsymbol{M}_{irr} = \boldsymbol{M}_{an} - k\delta\frac{d\boldsymbol{M}_{irr}}{d\boldsymbol{H}_e} \tag{2.42}$$

where k is the pinning coefficient and δ is +1 when $dH/dt > 0$ and -1 when $dH/dt < 0$. The coefficient k may vary with magnetisation rather than constant. It can be adjusted as $k[1 - k_a(\frac{\boldsymbol{M}}{\boldsymbol{M}_{st}})^2]$, where k_a is the adjustment amount [24].

In most cases, irreversible magnetisation is accompanied by reversible magnetisation. In the Jiles-Atherton (J-A) model, the reversible due to reversible domain wall bowing, translation and rotation is given as

$$\boldsymbol{M}_{rev} = c(\boldsymbol{M}_{an} - \boldsymbol{M}_{irr}) \tag{2.43}$$

where c is the reversibility coefficient.

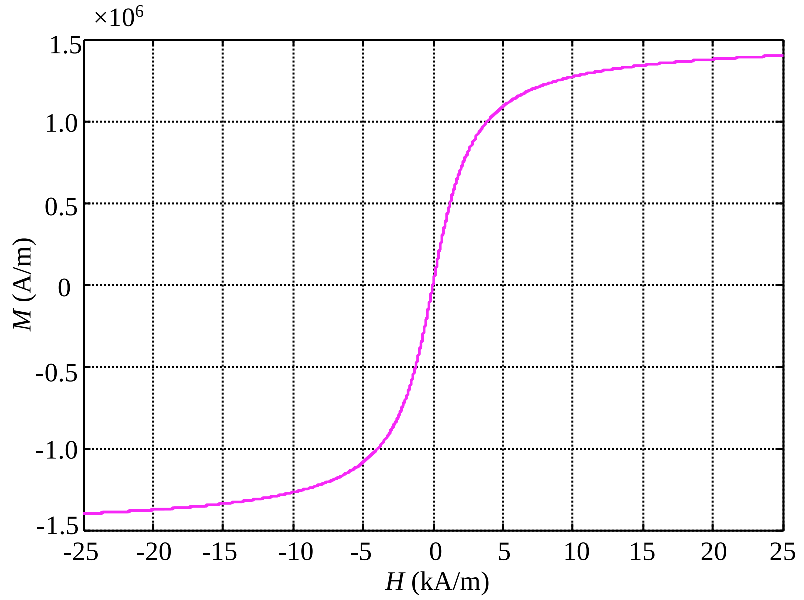

(a)

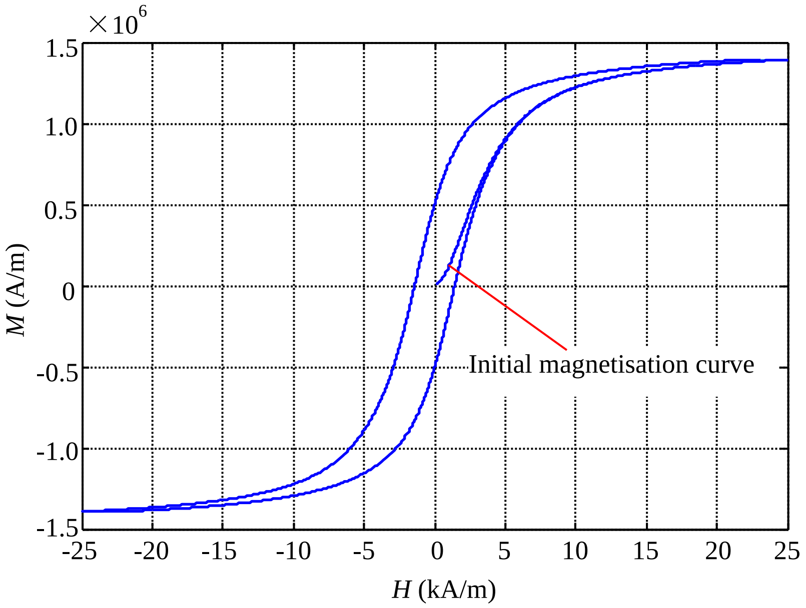

(b)

Figure 2.11. The typical anhysteresis **(a)** and hysteresis **(b)** magnetisation curves of ferromagnetic material ($M_{st} = 1.5\times10^6$, $a = 1800$, $k = 1800$, $\alpha = 1.4\times10^{-3}$, $c = 0.14$) [6].

The total hysteresis magnetisation ($\boldsymbol{M}$) should meet the following formula:

$$\boldsymbol{M} = \boldsymbol{M}_{rev} + \boldsymbol{M}_{irr} \tag{2.44}$$

Then, by differentiating the equation with respect to $\boldsymbol{H}$, the total differential magnetisation of ferromagnetic material is given by the following expression [21-23]

$$\frac{d\boldsymbol{M}}{d\boldsymbol{H}} = \frac{\chi_M}{k\delta - \alpha\chi_M} \tag{2.45}$$

where

$$\boldsymbol{\chi_M} = \delta_m[\boldsymbol{M}_{an} - \boldsymbol{M}] + k\delta c\frac{d\boldsymbol{M}_{an}}{d\boldsymbol{H}_e} \tag{2.46}$$

To eliminate the unphysical negative susceptibility dM/dH in the original J-A model, δ_m is introduced as

$$\delta_m = \begin{cases} 0: \frac{dH}{dt} < 0 \; and \; M_{an}(H_e) - M(H) > 0 \\ 0: \frac{dH}{dt} > 0 \; and \; M_{an}(H_e) - M(H) < 0 \\ 1: otherwise \end{cases} \tag{2.47}$$

Here the matrixial expresses of magnetisation are given. Generally, in an isotropic material magnetised unidirectionally, the expressions can be simplified as scalar ones. The typical hysteresis curve is shown in Fig. 2.11b.

2.4.2 The effect of stress on hysteresis

According to the previous discussion, it can be concluded that when a cubic crystal and isotropic material, such as iron, is demagnetised, the magnetic moments within magnetic domains, which are separated by 90° and 180° domain walls, are aligned along with one of the energetically favourable crystallographic directions due to magnetocrystalline anisotropy. When external stress is applied, the domain structure gains additional magnetoelastic energy that has been quantitatively described in Equation (2.32).

The magnetoelastic energy E_λ is related to the magnetostriction λ and external stress σ. If the external stress is uniaxial and parallel to the direction of magnetisation, the energy is proportional to the product of magnetostriction and stress, which is either positive or negative. Based on the different signs, there are two situations: (1) the sign of $\lambda\sigma$ is positive where the ferromagnet with positive magnetostriction is subjected to tensile stress or the negative one is subjected to compressive stress. (2) the sign of $\lambda\sigma$ is negative where the compressive stress is applied to the ferromagnet with positive magnetostriction or the tensile stress is applied to the negative one.

For example, Fig. 2.12 shows the situations of magnetomechanical effect by taking material with positive and isotropic magnetostriction. In the demagnetised state, the four flux-closure domains can be assumed as an analysing unit that consists of two antiparallel domains separated by 180° domain walls and two domains perpendicular to and separated from the antiparallel domains by 90° domain walls as shown in Fig. 2.12a.

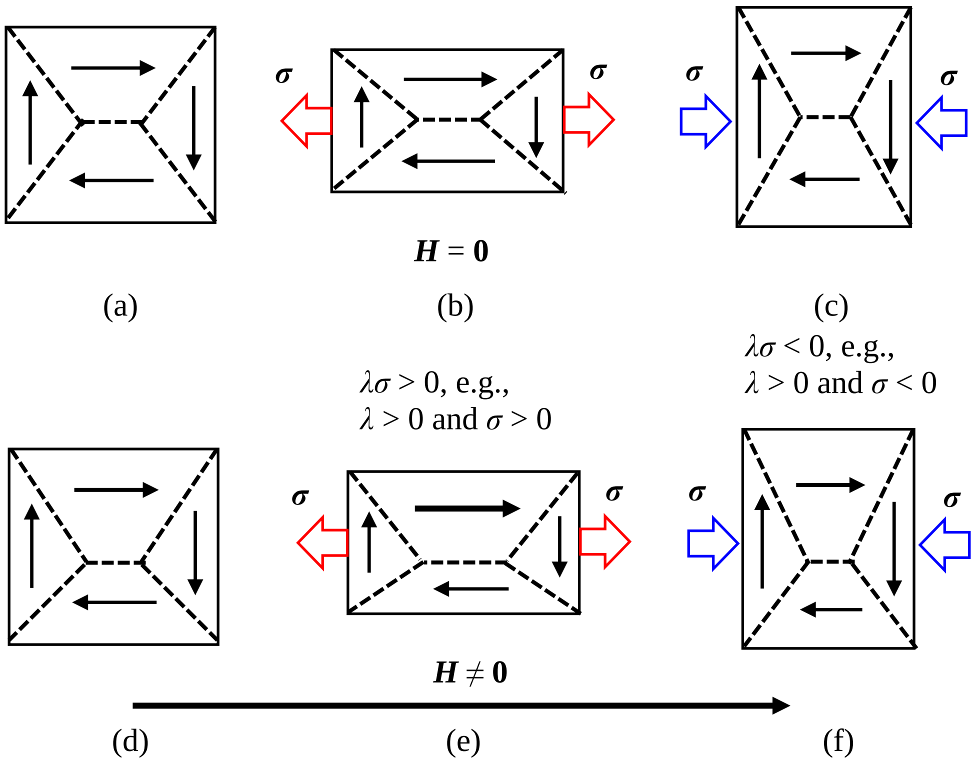

Figure 2.12. Magnetic field and stress affecting the movement of magnetic domains in the microstructure. **(a)** to **(c)** Schematic drawing the domain structure of cubic crystal ferromagnets subjected to various stress states but no external field. **(d)** to **(f)** Schematic drawing the domain structure subjected to an external field and various stress states. [25]

When the magnetic field $\boldsymbol{H} = \mathbf{0}$ A/m, the flux-closure domains are symmetric and after applying external stress the symmetric structure remains so that the mechanical stress will not affect the magnetic properties of the sample as shown in Figs. 2.12b and 2.12c. While $\boldsymbol{H} \neq \mathbf{0}$ A/m (see Figs. 2.12d~2.12f), the symmetric structure is destroyed due to the asymmetric extension of the domain within which the magnetic moments are parallel to the direction of $\boldsymbol{H}$. If the unidirectional tensile stress ($\sigma > 0$) is applied to the material along the direction of the magnetic field which means $\lambda\sigma > 0$, this gives rise to the further growth in the volume of the domain that is parallel to the magnetic field (see Fig. 2.12e). While if the compressive stress ($\sigma < 0$) is applied along the magnetic field, i.e., $\lambda\sigma < 0$, the stress would restrain the extension of the domain. It can be observed by comparing Figs. 2.12d and 2.12f.

To theoretically analyse the magnetoelastic effect, by taking the stress into account, the Helmholtz energy density A and the effective field $\boldsymbol{H}_e$ in Equations (2.36) and (2.38) are rewritten as

$$A = U - TS + \tfrac{3}{2}\sigma\lambda + \mu_0 \boldsymbol{H} \cdot \boldsymbol{M} \tag{2.48}$$

$$\boldsymbol{H}_e = \boldsymbol{H} + \alpha\boldsymbol{M} + \boldsymbol{H}_{\boldsymbol{\sigma}} \tag{2.49}$$

where $\boldsymbol{H}_{\boldsymbol{\sigma}}$ is the stress equivalent field. And if the direction of stress $\boldsymbol{\sigma}$ is parallel to that of magnetic field $\boldsymbol{H}$,

$$\boldsymbol{H}_{\boldsymbol{\sigma}} = \frac{3}{2\mu_0}\boldsymbol{\sigma}\left(\frac{d\lambda}{dM}\right)_{\sigma,T} \tag{2.50}$$

The equation of stress equivalent field is determined by $\frac{d\lambda}{dM}$. In a low magnetisation region, the magnetostriction is assumed as a parabolic function of magnetisation approximately [26,27]:

$$\lambda = bM^2 \tag{2.51}$$

where b is the magnetostriction coefficient which can be obtained from the parabolic fitting of experimental magnetostriction values as shown in Fig. 2.13. The coefficient of quadratic term in the symmetric parabola can either be positive or negative.

In a high magnetisation region, the magnetostriction curves may display more complicated characteristics as shown in Figs. 2.14a and 2.14b. Besides, by considering the effect of stress, the magnetostriction curves would be far different from each other under different applied stresses as illustrated in Figs. 2.14c and 2.14d. Jiles [28] proposed an empirical model to describe the relation between magnetostriction and magnetisation under stress as

$$\lambda(\sigma, M) = \sum_{i=0}^{\infty} \gamma_i(\sigma)\, M^{2i} \tag{2.52}$$

where

$$\gamma_i(\sigma) = \gamma_i(0) + \sum_{i=0}^{\infty} \frac{\sigma^n}{n!} \gamma_i^n(0) \tag{2.53}$$

where $\gamma_i^n(0)$ is the nth derivative of γ_i with respect to stress at σ = 0 MPa. And generally, we can ignore the high order and remain the second-order item so that the Equation (2.52) can be approximately simplified as

$$\lambda(\sigma, M) \approx \gamma_0 + (\gamma_{11} + \gamma_{12}\sigma) M^2 \tag{2.54}$$

where γ_0, γ_{11}, and γ_{12} are stress-dependent coefficients and can be determined through fitting the measured magnetostriction curves.

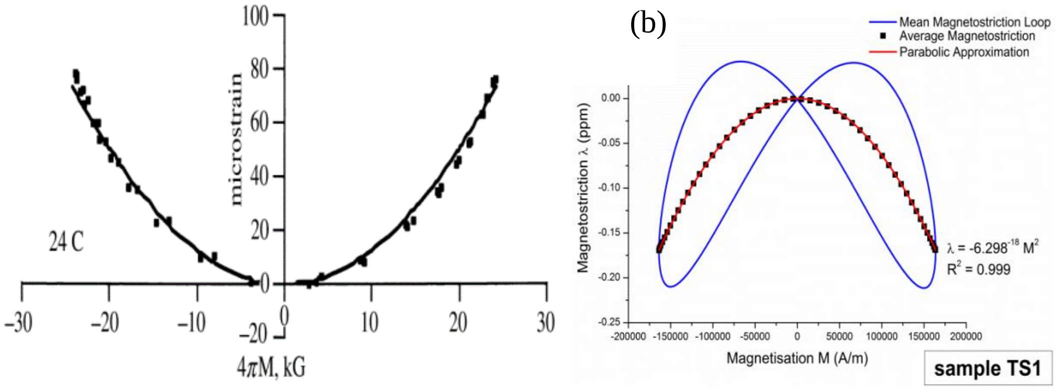

(a) (b)

Figure 2.13. Magnetostriction as function of magnetisation with parabolic fitting in **(a)** polycrystalline iron cobalt (FeCo+2%V, 4πM is magnetisation expressed in Gaussian unit, 1G = 0.1mT and in free space 1G = 79.577A/m) [29], **(b)** nitrided SAE6481 steel (sample TS1) [30].

Consequently, if the direction of stress $\boldsymbol{\sigma}$ is parallel to that of magnetic field $\boldsymbol{H}$, by substituting Equations (2.51) and (2.54) into Equation (2.50) respectively the stress equivalent field can be further written as

$$\boldsymbol{H_\sigma} = \frac{3b}{\mu_0} \boldsymbol{\sigma} M \tag{2.55}$$

$$\boldsymbol{H_\sigma} = \frac{3(\gamma_{11} + \gamma_{12}\sigma)}{\mu_0} \boldsymbol{\sigma} M \tag{2.56}$$

The different forms of stress equivalent field can meet different conditions. For example, when analytically evaluating the stress-dependent magnetic Barkhausen noise [30], Equation (2.55) is preferable since at relative low magnetisation the parabolic fitting is more approximate to the measured magnetostriction curve.

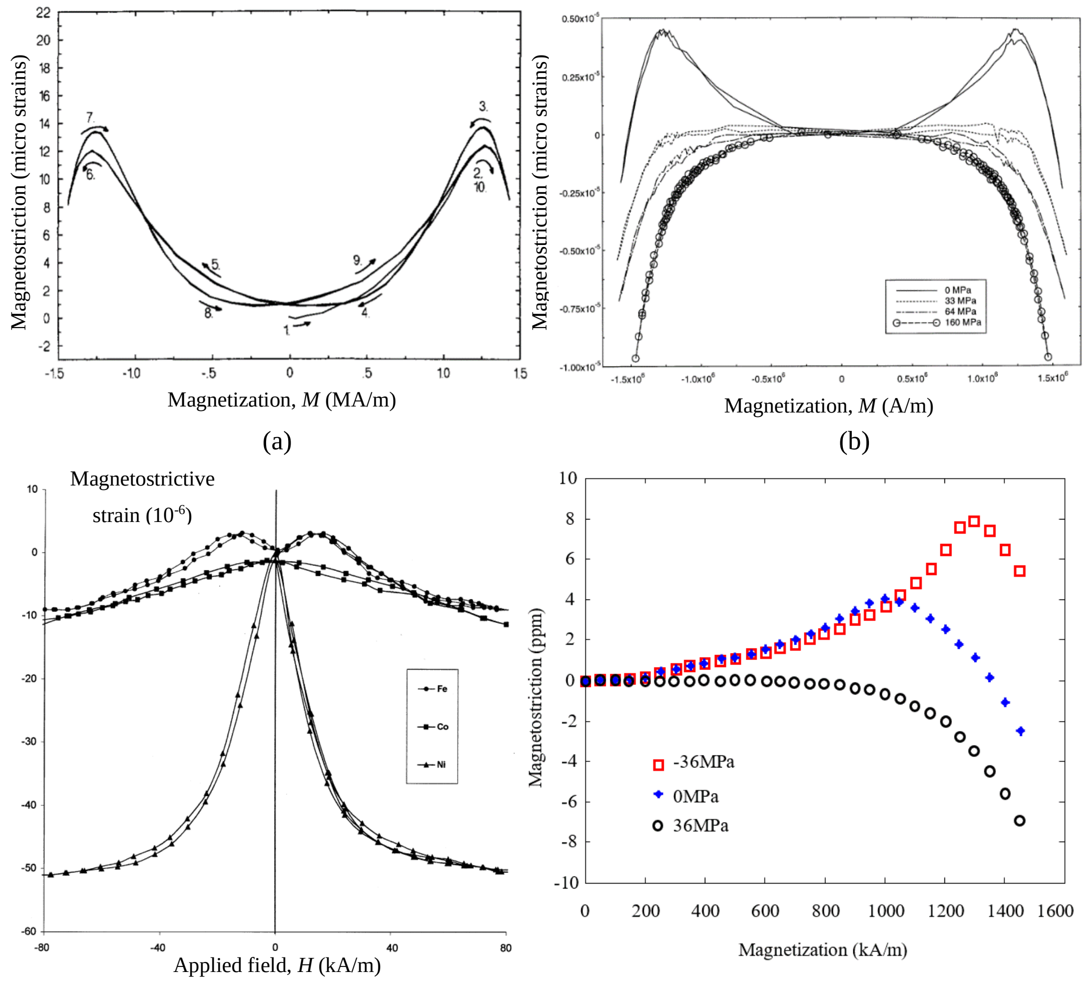

(a) (b)

(c) (d)

Figure 2.14. **(a)** Magnetostriction of 2% Mn pipeline steel as a function of magnetisation [31], **(b)** Magnetostriction of 0.003% wt carbon steel as a function of magnetisation obtained from various stresses [32], **(c)** Magnetostriction as a function of the field in polycrystalline iron, cobalt and nickel [33], and **(d)** The Magnetostriction in iron obtained from different stresses [34].

To further simplify the effective field by combining the item of M, $\boldsymbol{H_e}$ arrives at

$$\boldsymbol{H_e} = \boldsymbol{H} + \tilde{\alpha}\boldsymbol{M} \tag{2.57}$$

where

$$\tilde{\alpha} = \alpha + \frac{3}{2\mu_0}\frac{1}{M}\left(\frac{d\lambda}{dM}\right)_{\sigma,T} \tag{2.58}$$

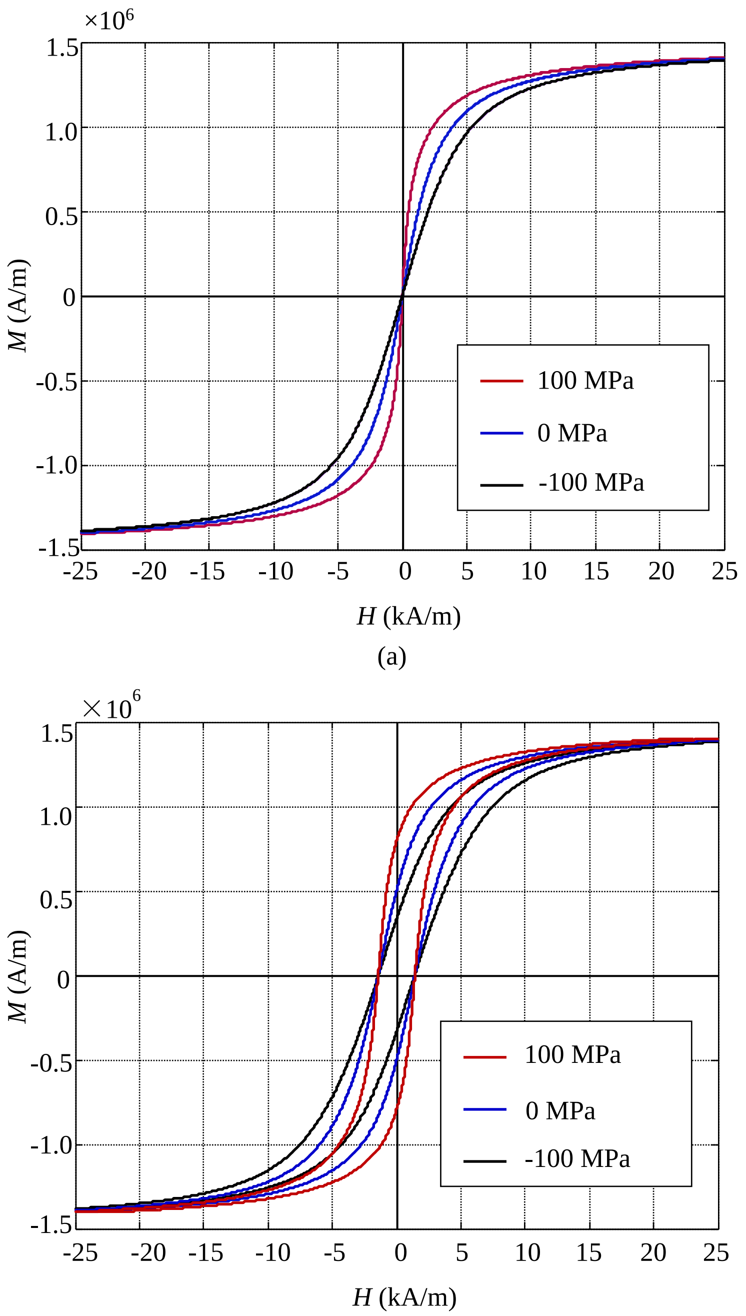

(a)

(b)

Figure 2.15. The typical anhysteresis curves **(a)** and hysteresis curves **(b)** for a ferromagnetic material with positive magnetostriction under tensile, compressive and free stresses.

And further, the Equations (2.40) and (2.45) that describe the anhysteresis and hysteresis magnetisation are rewritten as

$$\boldsymbol{M}_{an} = M_{st}\left[\coth\left(\frac{\boldsymbol{H}+\tilde{\alpha}\boldsymbol{M}}{a}\right) - \frac{a}{\boldsymbol{H}+\tilde{\alpha}\boldsymbol{M}}\right] \tag{2.59}$$

$$\frac{dM}{dH} = \frac{\chi_M}{k\delta - \tilde{\alpha}\chi_M} \tag{2.60}$$

The typical anhysteresis and hysteresis curves for a ferromagnetic material with positive magnetostriction under tensile, compressive and free stresses are shown in Fig. 2.15. The relation between stress and hysteresis loop can be further used to develop the models of magnetic flux leakage and magnetic Barkhausen noise.

2.5 Magnetic Barkhausen Noise

The Barkhausen effect is the phenomenon of the discontinuous stepwise jumps within a ferromagnetic material subjected to a changing magnetic field. These discontinuities are greatly ascribed to the discontinuous domain wall motion. The domain process during magnetisation has been discussed previously. The irreversible domain wall motion, including irreversible discontinuous domain wall bowing, rotation and especially translation, mainly contributes to the Barkhausen noise and magnetoacoustic emission [1].

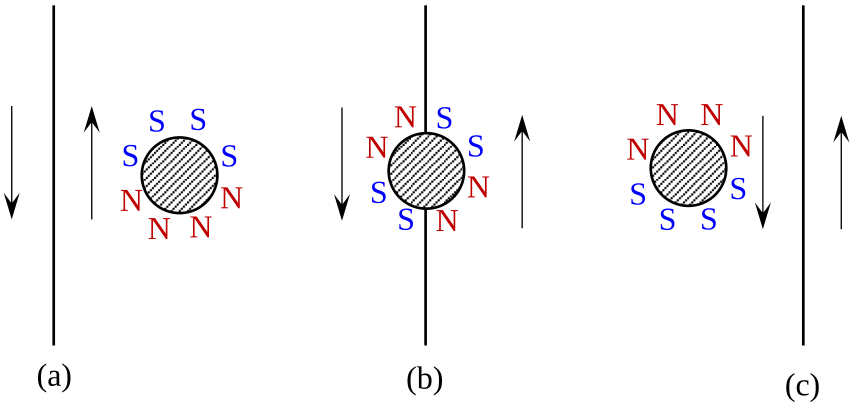

Figure 2.16. Interaction of domain wall and inclusion. **(a)** Free poles distribution on an inclusion. **(b)** Free poles redistribution on the inclusion when intersected by the domain wall. **(c)** Free poles rebalance after the domain wall passing across the inclusion. [1]

During irreversible magnetisation, the domain walls suddenly break away from the pinning sites related to the presence of “inclusions”, including carbide oxide and microcracks. An “inclusion” can be viewed as an isolated region of the second phase within a domain with different spontaneous magnetisation from surrounding moments or no magnetised at all. The inclusion enclosed within a domain would have magnetic free poles as shown in Fig. 2.16a with attendant magnetostatic energy. When the domain wall bisects the inclusion, the free poles occur a change of distribution to reduce the magnetostatic energy as shown in Fig. 2.16b. After the domain wall passing across the inclusion, the free poles finally redistribute as shown in Fig. 2.16c to reduce the magnetostatic energy. The redistribution of free poles would generate flux pulses which are detected by search coils and named Barkhausen noise.

In soft ferromagnetic materials with weak pinning sites such as iron and electrical steels, the irreversible domain wall motion mainly contributes to the magnetic Barkhausen Noise (MBN) and the required critical strength of the magnetic field to induce domain wall to break through pinning sites is relatively low. Therefore, within the relatively low magnetisation range, the domain walls move with a high velocity, resulting in a relatively high differential susceptibility dM/dH and intensive Barkhausen Effect. The strongest MBN can be observed at the coercive field due to the largest value of differential susceptibility. Compared with the effect of domain wall motion on MBN, the other contributions like domain rotation are relatively lower. The relation between the magnitude of MBN and the magnetisation processes is plotted in Fig. 2.17. It can be seen that the highest MBN is generated at the coercive field of the M-H curve with the highest value of differential susceptibility. The MBN pulses concentrate in the steep range of M-H curve where the magnetisation takes place predominantly by irreversible domain wall motion, while the MBN emissions, due to irreversible domain wall bowing and domain rotation which occur at the lower and higher levels of magnetic field, respectively, are shown to be relatively low.

The quantitative description of the Barkhausen noise using mathematic equations is difficult due to its random nature. After development in decades, the most notable attempt to mathematically describe the MBN emission was made by Alessandro, Beatrice, Bertotti and Montorsi (ABBM) [35] who proposed a model of the stochastic domain wall motion under the action of an applied field and subject to a random coercive field $\boldsymbol{H_c}$ inside the material. In their model, the coercive field fluctuates as a function of magnetic flux Φ and the features of the coercive field are given by

$$\frac{d\boldsymbol{H_c}}{d\boldsymbol{\phi}} + \frac{\boldsymbol{H_c} - <\boldsymbol{H_c}>}{\xi} = \frac{dW_n}{d\boldsymbol{\phi}} \tag{2.61}$$

where ξ is the finite length corresponding to the finite interaction range of the domain wall with pinning sites and $W_n(\xi)$ is a white noise function with zero mean value but a finite variance proportional to the intensity of pinning.

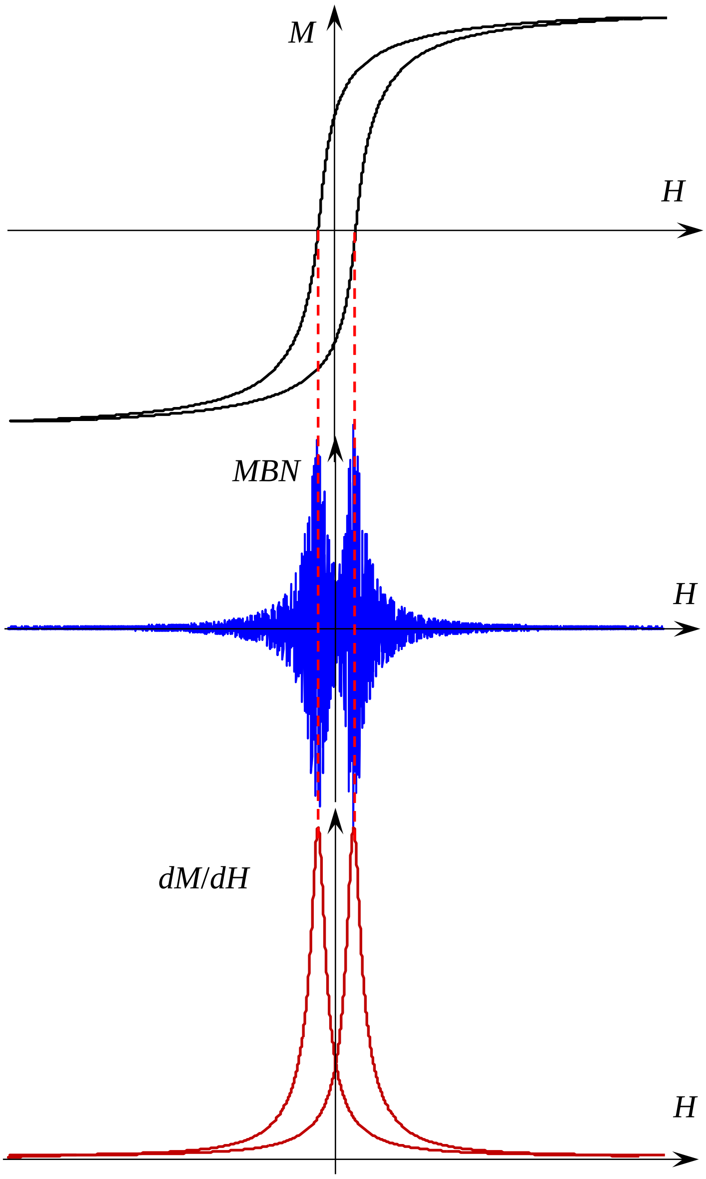

Figure 2.17. The relation between magnetisation, MBN and susceptibility [1].

By considering the generic local field influenced by applied field $\boldsymbol{H_a}$ and magnetostatic field $\boldsymbol{H_m}$, the time derivative of magnetic flux is described as

$$\frac{d\dot{\boldsymbol{\phi}}}{dt} = \frac{1}{C_g}\left(\frac{d\boldsymbol{H_a}}{dt} - \frac{d\boldsymbol{H_m}}{dt} - \frac{d\boldsymbol{H_c}}{dt}\right) \tag{2.62}$$

where C_g is a coefficient produced by electrical conductivity and a dimensionless coefficient. The Barkhausen activity generated with magnetic flux $\boldsymbol{\Phi}$, magnetisation

M (or magnetostatic field $\boldsymbol{H_m}$) and coercive field $\boldsymbol{H_c}$ fluctuation within a given time interval is correlated with the activity in the previous time interval but varies by a stochastic amount.

This model has restricted the rates of changes of applied field $d\boldsymbol{H_a}/dt$ and magnetisation $d\boldsymbol{M}/dt$ as constant values. The model was extended to the entire hysteresis loop by Jiles, Sipahi and Williams (JSW) [36]. In the extended model, it is assumed that the Barkhausen activity in a given time interval is proportional to the rate of change of magnetisation

$$\frac{dM_{BN}}{dt} \propto \frac{dM}{dt} = \chi' \frac{dH}{dt} \tag{2.63}$$

where M_{BN} represents the Barkhausen activity and χ' is the differential susceptibility dM/dH. The M_{BN} with regard to the Barkhausen jumps is assumed to be the product of a number of events N and the average Barkhausen jump size $<M_{\overline{BN}}>$ within a time interval Δt

$$M_{BN}\Delta t = N\langle M_{\overline{BN}}\rangle \Delta t \tag{2.64}$$

To reveal the random nature of Barkhausen activity, the number of events over a given time interval $N(t_n)$ is assumed to follow a Poisson distribution and is related to the number in the previous period $N(t_{n-1})$, which is expressed as

$$N(t_n) = N(t_{n-1}) + \delta_{rand}\sqrt{N(t_{n-1})} \tag{2.65}$$

where δ_{rand} is a random number in range $-1.47 \leq \delta_{rand} \leq +1.47$ [37] (originally the range was ±1 [36]).

Consequently, the Equation (2.63) of the rate of change of Barkhausen activity can be rewritten as

$$\frac{dM_{BN}(t_n)}{dt} = \langle M_{\overline{BN}}\rangle\, \chi' \frac{dH(t_n)}{dt}\left[N(t_{n-1}) + \delta_{rand}\sqrt{N(t_{n-1})}\right] \tag{2.66}$$

Subsequently, Jiles *et al.* [37], [38] modified the differential susceptibility dM/dH as dM_{irr}/dH to eliminate the influence of reversible magnetisation that rarely induce Barkhausen activity. The Barkhausen activity produced by the number of Barkhausen events N and the average size of events $<M_{\overline{BN}}>$ is further modified as differential with the irreversible magnetisation. And hence, Equation (2.66) is further rewritten as

$$\frac{dM_{BN}}{dt} = \frac{dM_{irr}}{dH}\frac{dH}{dt}\frac{d(N\langle M_{\overline{BN}}\rangle)}{dM_{irr}} \tag{2.67}$$

The simulated results using ABBM and JSW models are shown in Fig. 2.18 (a) and (b). The advantage of the JSW models, including its modified models, is that they extend the Barkhausen activity from limited magnetisation regions to the entire hysteresis loop. Besides, by using the proportional relation between the differential irreversible susceptibility dM_{irr}/dH and Barkhausen activity, it is possible to predict the effects of temperature and stress on the amplitude of MBN and the correlated work for quantitative evaluation of the effects of temperature and thermal stress on MBN will be presented in Chapter 6.

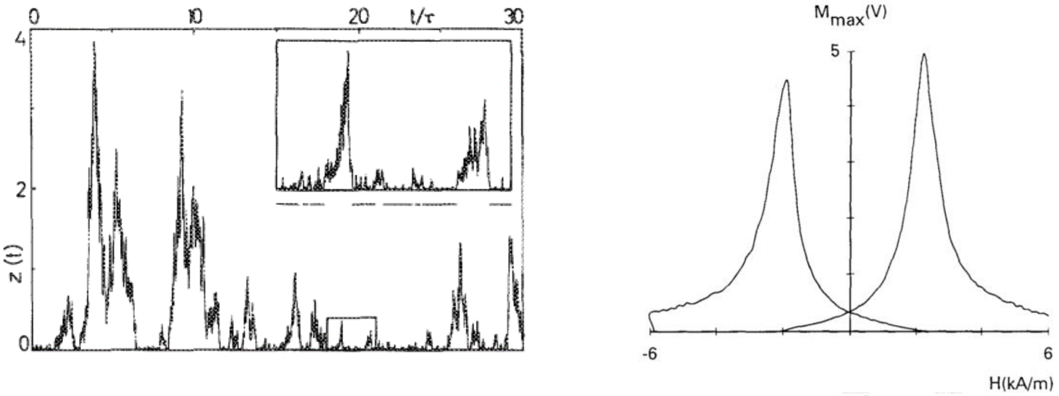

(a) (b)

Figure 2.18. **(a)** The simulated Barkhausen activity using the ABBM model [35]. **(b)** The calculated Barkhausen emission voltage with the applied field using the JSW model [39].

2.6 Chapter Summary

This chapter has described the basic theories of macroscopical and microscopical magnetics. The magnetic field and magnetisation processes were introduced in macroscopical magnetics. Subsequently, the micromagnetic theories including the domain, domain wall and micromagnetic energies were introduced. It further discussed the hysteretic magnetisation processes as well as the model of ferromagnetic hysteresis. The effect of stress on hysteresis was analysed via the concept of stress equivalent field. Finally, the magnetic Barkhausen effect phenomenon was discussed. These theories and relations will be later used in the development of magnetic flux leakage and magnetic Barkhausen noise models in the following chapters.

2.7 References for Chapter 2

[1] D. C. Jiles. Introduction to magnetism and magnetic materials. *CRC press*, 2015.

[2] T. Bécherrawy. Electromagnetism: Maxwell equations, wave propagation and emission. *John Wiley & Sons*, 2013.

[3] C. W. Trowbridge. Computing electromagnetic fields for research and industry: major achievements and future trends. *IEEE Trans. Magn.*, vol. 32, no. 3, pp. 627–630, 1996.

[4] I. Zainal Abidin. Modelling and experimental investigation of eddy current distribution for angular defect characterisation. *Doctoral dissertation, Newcastle University*, 2011.

[5] J. A. Osborn. Demagnetising factors of the general ellipsoid. *Phys. Rev.*, vol. 67, no. 11–12, pp. 351-357, 1945.

[6] D. C. Jiles, J. B. Thoelke, and M. K. Devine. Numerical determination of hysteresis parameters for the modelling of magnetic properties using the theory of ferromagnetic hysteresis. *IEEE Trans. Magn.*, vol. 28, no. 1, pp. 27–35, 1992.

[7] P. Weiss. Molecular field and ferromagnetic property. *J. Phys. Theor. Appl.*, vol. 6, pp. 661–690, 1907.

[8] F. Bitter. On inhomogeneities in the magnetisation of ferromagnetic materials. *Phys. Rev.*, vol. 38, no. 10, pp. 1903-1905, 1931.

[9] R. Carey and E. D. Isaac. Magnetic domains and techniques for their observation. 1966.

[10] R. D. Gomez, T. V Luu, A. O. Pak, K. J. Kirk, and J. N. Chapman. Domain configurations of nanostructured Permalloy elements. *J. Appl. Phys.*, vol. 85, no. 8, pp. 6163–6165, 1999.

[11] R. D. Gomez, T. V Luu, A. O. Pak, I. D. Mayergoyz, K. J. Kirk, and J. N. Chapman. Domain wall motion in micron-sized permalloy elements. *J. Appl. Phys.*, vol. 85, no. 8, pp. 4598–4600, 1999.

[12] C. Kittel. Physical theory of ferromagnetic domains. *Rev. Mod. Phys.*, vol. 21, no. 4, pp. 541-583, 1949.

[13] F. Bloch. Zur theorie des austauschproblems und der remanenzerscheinung der ferromagnetika. *Springer*, 1932, pp. 295–335.

[14] E. Bhatia, Z. H. Barber, I. J. Maasilta, and K. Senapati. Domain wall induced modulation of low field HT phase diagram in patterned superconductor-ferromagnet stripes. *AIP Adv.*, vol. 9, no. 4, pp. 045107 (1-5), 2019.

[15] W. F. Brown. Micromagnetics. *Interscience publishers*, no. 18, 1963.

[16] L. Vandenbossche. Magnetic Hysteretic Characterization of Ferromagnetic

Materials with Objectives towards Non-Destructive Evaluation of Material Degradation. *Doctoral dissertation, Ghent University*, 2009.

[17] C. Abert. Micromagnetics and spintronics: models and numerical methods. *Eur. Phys. J. B*, vol. 92, no. 6, pp. 1-45, 2019.

[18] B. D. Cullity and C. D. Graham. Introduction to magnetic materials. *John Wiley & Sons*, 2011.

[19] D. C. Jiles. Coupled Magnetoelastic Theory of Magnetic and Magnetostrictive Hysteresis. *IEEE Trans. Magn.*, vol. 29, no. 4, pp. 2113–2123, 1993.

[20] D. C. Jiles and D. L. Atherton. Theory of ferromagnetic hysteresis. *J. Magn. Magn. Mater.*, vol. 61, no. 1–2, pp. 48–60, 1986.

[21] S. E. Zirka, Y. I. Moroz, R. G. Harrison, and K. Chwastek. On physical aspects of the Jiles-Atherton hysteresis models. *J. Appl. Phys.*, vol. 112, no. 4, pp. 043916 (1-7), 2012.

[22] K. Chwastek and J. Szczygłowski. An alternative method to estimate the parameters of Jiles–Atherton model. *J. Magn. Magn. Mater.*, vol. 314, no. 1, pp. 47–51, 2007.

[23] A. Benabou, S. Clénet, and F. Piriou. Comparison of Preisach and Jiles-Atherton models to take into account hysteresis phenomenon for finite element analysis. *J. Magn. Magn. Mater.*, vol. 261, no. 1–2, pp. 139–160, 2003.

[24] U. D. Annakkage, P. G. McLaren, E. Dirks, R. P. Jayasinghe, and A. D. Parker. A current transformer model based on the Jiles-Atherton theory of ferromagnetic hysteresis. *IEEE Trans. power Deliv.*, vol. 15, no. 1, pp. 57–61, 2000.

[25] Z. Wang, Y. Gu, and Y. Wang. A review of three magnetic NDT technologies. *J. Magn. Magn. Mater.*, vol. 324, no. 4, pp. 382–388, 2012.

[26] P. Garikepati, T. T. Chang, and D. C. Jiles. Theory of ferromagnetic hysteresis: evaluation of stress from hysteresis curves. *IEEE Trans. Magn.*, vol. 24, no. 6, pp. 2922–2924, 1988.

[27] L. Mierczak, D. C. Jiles, and G. Fantoni. A new method for evaluation of mechanical stress using the reciprocal amplitude of magnetic Barkhausen noise. *IEEE Trans. Magn.*, vol. 47, no. 2, pp. 459–465, 2011.

[28] D. C. Jiles and M. K. Devine. The law of approach as a means of modelling the magnetomechanical effect. *J. Magn. Magn. Mater.*, vol. 140, pp. 1881–1882, 1995.

[29] B. E. Lorenz and C. D. Graham. Magnetostriction Versus Magnetisation of Hiperco 50 From 20 ^{o}C to 700 ^{o}C. *IEEE Trans. Magn.*, vol. 42, no. 12, pp. 3886–3888, 2006.

[30] L. Mierczak. Evaluation of structural integrity of steel components by non-destructive magnetic methods. *Doctoral dissertation, Cardiff University*, 2015.

[31] J. M. Makar and D. L. Atherton. Effects of stress on the magnetostriction of 2% Mn pipeline steel. *IEEE Trans. Magn.*, vol. 30, no. 4, pp. 1388–1394, 1994.

[32] J. M. Makar and B. K. Tanner. The in situ measurement of the effect of plastic deformation on the magnetic properties of steel: Part I–Hysteresis loops and magnetostriction. *J. Magn. Magn. Mater.*, vol. 184, no. 2, pp. 193–208, 1998.

[33] Y. Chen, B. K. Kriegermeier-Sutton, J. E. Snyder, K. W. Dennis, R. W. McCallum, and D. C. Jiles. Magnetomechanical effects under torsional strain in iron, cobalt and nickel. *J. Magn. Magn. Mater.*, vol. 236, no. 1–2, pp. 131–138, 2001.

[34] M. E. Kuruzar and B. D. Cullity. The magnetostriction of iron under tensile and compressive stress. *Int. J. Magn.*, vol. 1, no. 14, pp. 323–325, 1971.

[35] B. Alessandro, C. Beatrice, G. Bertotti, and A. Montorsi. Domain-wall dynamics and Barkhausen effect in metallic ferromagnetic materials. I. Theory. *J. Appl. Phys.*, vol. 68, no. 6, pp. 2901–2907, 1990.

[36] D. C. Jiles, L. B. Sipahi, and G. Williams. Modelling of micromagnetic Barkhausen activity using a stochastic process extension to the theory of hysteresis. *J. Appl. Phys.*, vol. 73, no. 10, pp. 5830–5832, 1993.

[37] D. C. Jiles. Dynamics of domain magnetisation and the Barkhausen effect. *Czechoslov. J. Phys.*, vol. 50, no. 8, pp. 893–924, 2000.

[38] T. W. Krause, L. Clapham, A. Pattantyus, and D. L. Atherton. Investigation of the stress-dependent magnetic easy axis in steel using magnetic Barkhausen noise. *J. Appl. Phys.*, vol. 79, no. 8, pp. 4242–4252, 1996.

[39] D. C. Jiles and L. Suominen. Effects of surface stress on Barkhausen effect emissions: Model predictions and comparison with X-ray diffraction studies. *IEEE Trans. Magn.*, vol. 30, no. 6, pp. 4924–4926, 1994.

Chapter 3

Nondestructive Evaluation Techniques and the Important Factors Influencing Magnetic NDE Methods

In this chapter, the nondestructive evaluation (NDE) techniques and their applications to material characterisation are introduced. The NDE techniques are classified into nonmagnetic, including optical, ultrasonics and radiography NDE, and magnetic techniques, which are further subdivided into macromagnetic and micromagnetic. The macromagnetic techniques, including magnetic flux leakage and hysteresis loop, the micromagnetic NDE techniques, especially magnetic Barkhausen noise, and the effects of stress, temperature and microstructure on these magnetic NDE methods, are emphatically discussed.

3.1 Nondestructive Test and Evaluation

Nondestructive testing (NDT) is a broad and interdisciplinary field for assuring the integrity of structural components and the performance of systems. It plays a critical role in locating defects of structures and characterising the conditions of materials. Compared with the destructive test, its most significant advantage is that it allows inspection without damaging the tested objects and interfering with subsequent use.

Nondestructive evaluation (NDE) is usually interchangeable with NDT. But the measurements of NDE are more quantitative. For example, it requires the quantitative characterisation of defects such as length and depth rather than just the defect location. In this thesis, the focus will be on the research of NDE techniques.

The development of NDE technology depends on the discoveries of physics. For example, the vibration mechanics bred the ultrasonic NDE technique, and the magnetics gave rise to the hysteresis NDE technique. According to different physics branches, various NDE techniques can be classified into nonmagnetic NDE techniques and magnetic NDE techniques.

The nonmagnetic NDE techniques include visual NDE, ultrasonic NDE and radiography NDE, *etc*. Visual or optical NDE initially relied on an operator's eyes to find defects and now is a fast-evolving NDE technique by combining machine vision and artificial intelligence (AI). Ultrasonics NDE is widely used to detect flaws in a long pipeline and broad plate by propagating the high frequency mechanical wave within the structures. Radiography NDE uses the penetration of X-ray or gamma-ray to examine the imperfection of material and evaluate the properties of a material. These NDE techniques will be introduced in detail in the following section.

The magnetic NDE techniques in this thesis are subdivided into macroscopic magnetic (i.e., macromagnetic) NDE and microscopic magnetic (i.e., micromagnetic) NDE techniques. The macromagnetic NDE techniques are widely used to inspect defects and magnetic properties of ferromagnetic material. The defects are usually detected by eddy current (EC) and magnetic flux leakage (MFL) using the different magnetic properties between defects and adjacent material on a scale much larger than a micrometre. The magnetic properties of ferromagnetic bulk are widely measured by the magnetic hysteresis loop method. The previous chapter has introduced that micromagnetics was a branch of magnetic physics dealing with the behaviour of ferromagnetic material at sub-micrometre length scales. The micromagnetic NDE techniques employ the behaviours of microscale magnetic structure such as domain wall motion to evaluate the properties and imperfections of material. It includes magnetic Barkhausen noise (MBN) and magnetoacoustic emission (MAE) techniques. The macromagnetic and micromagnetic NDE techniques will be presented in sections 3.3 and 3.4, respectively.

3.2 Non-magnetic NDE Techniques

3.2.1 Optical NDE technique

The optical test relied on the operator's eyes to find defects on the surface of a sample may be the first technique used in NDT. It has developed from original and straightforward to complex and elaborate by employing optical aids such as microscopy and optical fibre device. It should be noted that ocular inspection is rarely used in the industrial field other than the medical field due to the large scale of objects and long-term monitoring. To monitor structures in the long term and inspect large structures like pipeline, the widely used optical NDE techniques include optical fibre, infrared thermography, and endoscopy.

The optical fibre method uses the optical fibre to collect and sense the light signals from the tested object. It is known that the light properties in fibre system such as intensity, phase wavelength and transit time can be quantitatively impacted by strain, temperature, and pressure. It is most successfully used in the field of civil engineering [1-3]. Another successful application is the embedded fibre in composite material for monitoring the health of composite material [4-6]. To monitor the health of a large object, multiple discrete optical fibre sensors are distributed at various locations of the object to form a monitoring network which is a hot NDE research area.

The infrared thermography (IR) technique uses the invisible infrared light emitted by an object to inspect flaws on the surface or sub-surface due to the temperature difference. There are two kinds of IR: passive and active [1]. Passive IR measures the temperature difference between the object and ambient with different temperatures. In comparison, active IR differs the object from the surrounding by heating up or cooling down the object. The active IR is commonly used in NDE due to its controllability. Various active IR methods have been developed in recent years, such as pulsed thermography [7], pulsed eddy current thermography [8] and ultrasonic lock-in thermography [9].

Endoscopy was first used for medical examination and currently can be used to nondestructively evaluate defects on the internal surface of a sealed object. The endoscopic NDE technique has rapidly improved with the development of computer and charge-coupled device (CCD) image sensors [1,10,11]. Combined with state-of-the-art information techniques (IT), the endoscopy and other optical NDE techniques can implement remote control and intelligent identification of defects or lesions [10,11].

3.2.2 Ultrasonic NDE technique

Ultrasonic inspection, which uses ultrahigh frequency mechanical wave to locate and identify defects in a structure is one of the most important NDE techniques. Unlike optical NDE techniques, the ultrasonic NDE technique can detect both surface and internal discontinuities and is preferable to long or large structures like pipeline and storage tank [12,13,14].

Ultrasonic testing is based on rapidly time-varying deformations in solid materials, which is generally referred to as high frequency acoustics. There are four principal modes of sonic waves based on the ways of vibrations, i.e., longitudinal waves, shear waves, Rayleigh waves and Lamb waves [12]. In longitudinal waves, the particles oscillate along the longitudinal direction or the direction of wave propagation since expansion and compression forces are applied on the particles of solid as shown in Fig. 3.1a. For shear waves, the oscillations occur in the direction transverse to that of propagation as illustrated in Fig. 3.1b. The waves that travel on the surface of solid material and penetrate to a depth of one wavelength are called Rayleigh waves or surface waves as seen in Fig. 3.1c. Lamb waves propagate parallel to the tested surface throughout the thickness of the material, and there are two most common vibratory modes of Lamb waves: symmetrical and asymmetrical modes (see Fig. 3.1d).

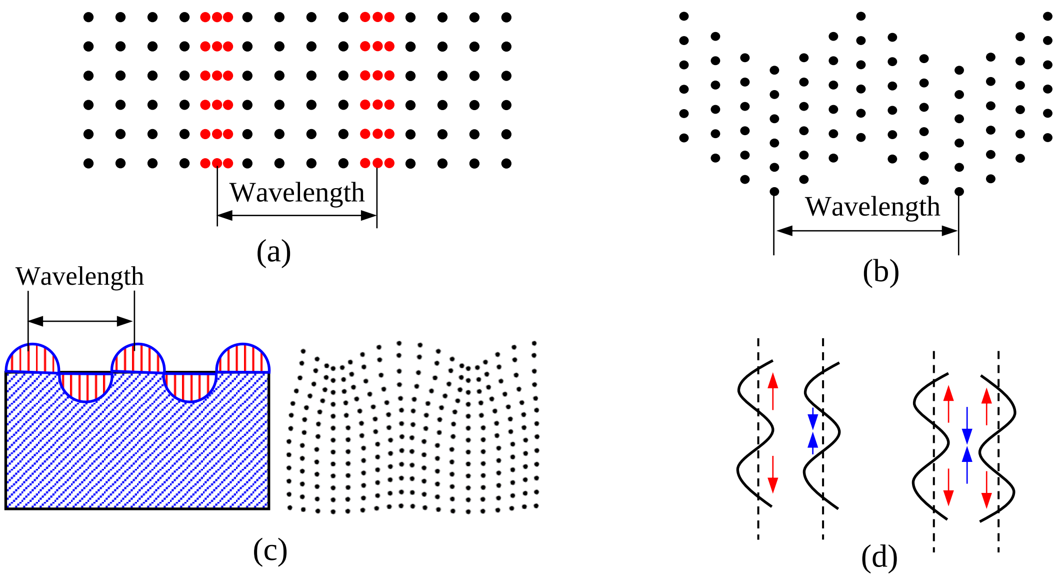

Figure 3.1. Four principle modes of ultrasonic waves. **(a)** Longitudinal wave, **(b)** Shear wave, **(c)** Rayleigh wave, **(d)** symmetric and asymmetric Lamb waves. [12]

The ultrasonic waves are excited from electrical pulses, and the reflected mechanical vibrations are transformed back to electrical signals. This is the basic mechanism of ultrasonic testing. The conversions between electrical pulses and mechanical vibration need an active medium to convert the electrical energy to acoustic energy and *vice versa*. The various acoustic transducers based on their active elements can be classified into two main kinds: piezoelectric transducers (PZTs) and electromagnetic acoustic transducers (EMATs).

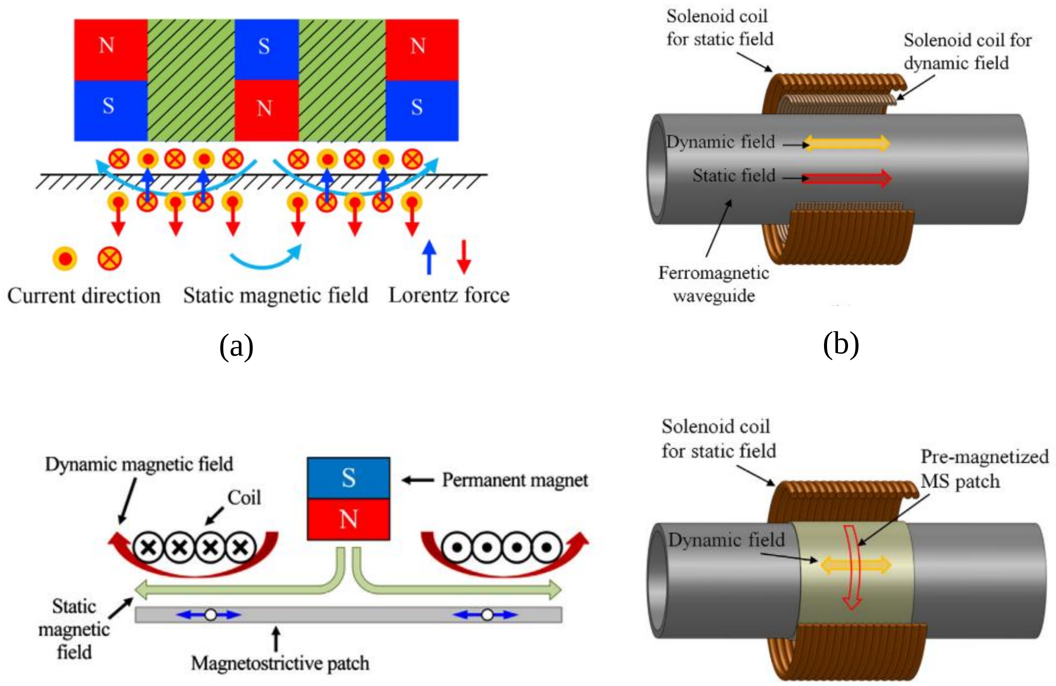

(a) (b)

(c) (d)

Figure 3.2. Various configurations of EMATs. **(a)** Lorentz force EMAT [22], **(b)** Magnetostrictive EMAT generation and sensing of a longitudinal wave in a ferromagnetic pipe directly [21], **(c)** Magnetostrictive patch transducer for generating omnidirectional Lamb waves in a plate [23], **(d)** Magnetostrictive patch transducer for generating shear waves in a pipe [21].

Piezoelectric transducers (PZTs) use the piezoelectric effect of a polarized material such as quartz crystal and piezoelectric ceramic to excite and receive ultrasonic waves [15]. The sonic beams produced by PZTs straight emitting into a solid material to detect flaws that are parallel to the surface of the material are called straight beams [12,16]. The angle beam transducers reduce the concentrated energy and expand the inspection range. For example, in an angle welding structure test, the straight beam is hard to arrive at the testing area [17]. Nowadays, the popular studies of PZTs are inspection fatigue cracks using the non-collinear shear wave mixing method [18,19] and building of transducer arrays [14].

Analogous to PZTs, Electromagnetic acoustic transducers (EMATs) transduce the electrical energy to mechanical vibration and converse the received mechanical vibration to electrical pulses. But the EMATs are based on different physical principles from PZTs, and they can act without couplant. When a meander coil is placed near the surface of an electrically conducting metallic material and fed into a current with designed frequency, eddy current will be induced in the surface region of the material. The dynamic eddy current in the material will experience Lorentz force when a static magnetic field is present [20,21,22]. This kind EMATs are Lorentz force EMATs as shown in Fig. 3.2a.

The other type of EMATs is magnetostrictive. The phenomenon that the shape of ferromagnetic material changes with an applied magnetic field is called magnetostriction. Inversely, the change in dimension of a magnetised ferromagnetic material caused by external stress will change the status of magnetisation of the material, which is the Villari effect. Besides, when a ferromagnetic material is subject to a static field and a dynamic field orthogonal to the static field direction, a shearing deformation will be generated in the material, i.e., the Wiedemann effect. A number of EMATs have used these magnetostrictive phenomena to directly generate and receive ultrasonic waves in ferromagnetic materials [24,25]. The other magnetostrictive EMATs use thin magnetostrictive patches which are adhered to on the surface of a tested object [21,23,26]. The different configurations of magnetostrictive EMATs are shown in Fig. 3.2b ~ 3.2d. As EMATs are easy to tailor-make for a specific purpose and have several advantages such as good sensitivity, long range inspection, contactless potential, and the capability to generate high-powered shear waves, the use and design of EMATs have drawn more and more researchers' attention.

3.2.3 Radiographic NDE technique

Roentgen first discovered X-rays in 1895, and the international unit of exposure dose for X-ray is named after him. X-rays and gamma rays (γ-rays) are part of the electromagnetic spectrum but invisible. They are electromagnetic waves but act somewhat like particles with no charge and mass, referred to as photons. These rays can travel straight regardless of the influence of electrical and magnetic fields but can be absorbed to different extents by different materials. The radiographic NDE technique uses the different penetrations of X-rays or γ-rays in the materials of a tested object and defect to evaluate the health of the structure [27].

The main principle of radiographic NDE is using the radiation emitting towards a test specimen in front of a photographic film and recording the image of the specimen's internal structure on the film due to the penetrating ability of X-ray. The mental or solid specimen can absorb some of the radiation. The amount of energy absorbed by a material depends on its thickness and density. Thus, a greater proportion of the absorption will occur at the thicker and denser materials [28]. The energy not absorbed by the material will cause exposure to the film. Since the absorption magnitude of the radiation depends on the thickness and density of the material, the air in discontinuities such as holes and cracks present in the mental or solid specimen will cause variations in the radiation intensity transmitted, which are recorded in films [27,28].

To reduce the test time especially the lag time between the specimen exposed to radiation and the resulting image, a real-time radiographic NDE technique has been developed to display results on a screen rather than on a film [29]. The real-time radiographic NDE significantly increases the inspection efficiency and allows engineers to inspect entirely and automatically [30,31].

In addition to defect inspection, X-rays can also be used to evaluate the properties of materials such as chemical composition and residual stress [32]. The X-ray diffraction (XRD) technique for evaluating the properties of materials is based on the diffraction of collimated X-rays from periodic atomic planes or crystal lattice and the angle of the diffracted signal as shown in Fig. 3.3a. The conditions that are essential for the diffraction to occur via constructive interference is given by Bragg [33]

$$n\lambda_X = 2d_0 \sin(\theta_0) \tag{3.1}$$

where n is the order of diffraction, λ_X is the X-ray wavelength, d_0 is the lattice spacing and θ_0 is the angle of the diffracted beam. Different lattice planes are obeyed different diffracting conditions and varying intensities of the diffracted signal according to the crystal structures and phases. Consequently, each phase could produce a characteristic diffraction pattern that allows quantitative identification [32].

Residual stress is a type of mechanical stress that remains in the material even free of external stress and changing temperature. As residual stress is self-equilibrated, the tensile stress in an area is always equilibrated by compressive stress nearby. It results in zero net stress shown in the bulk material [34]. It is not easy to be nondestructively evaluated. XRD is one of the most successful methods to identify residual stresses. It is based on the change of the angles caused by the alteration of the atomic lattice spacing to determine the strain inside the material as shown in Fig. 3.3. The strain ε defined by the stress-free lattice spacing d_0 and lattice spacing residual stress d_σ is given as

$$\varepsilon = \frac{d_\sigma - d_0}{d_0} \tag{3.2}$$

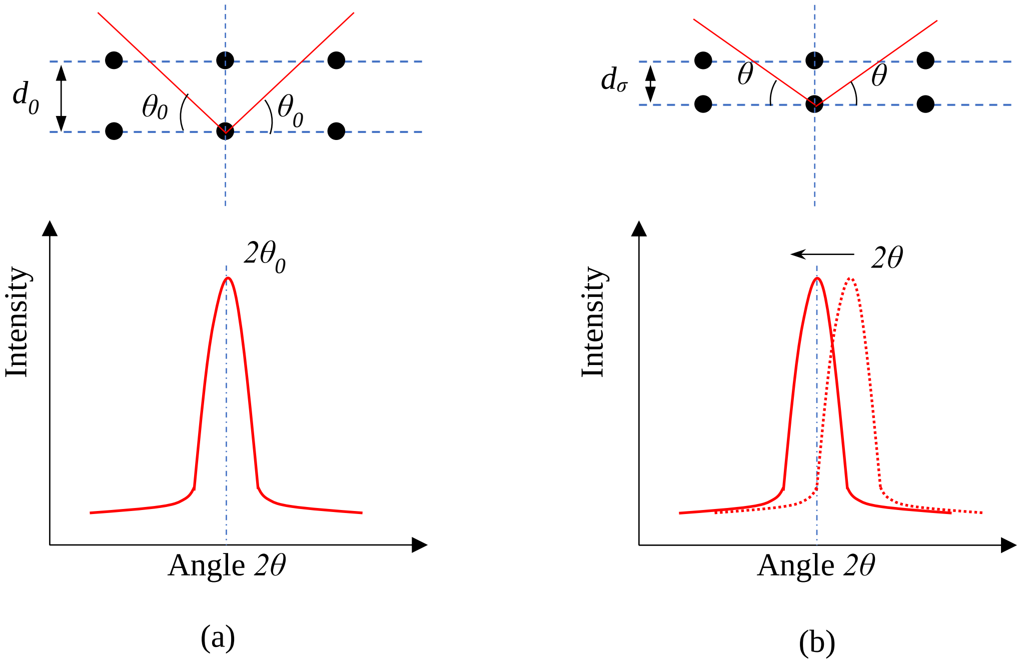

Figure 3.3. Diffraction of X-ray in a crystal lattice for **(a)** stress free condition and **(b)** residual stress condition [32].

The XRD method requires the precise measurement of lattice spacing for stress-free material. When the evolution of the lattice spacing d is plotted as a function of $\sin^2\psi$ (ψ is the angle between scattering vector and the normal to the specimen surface), a linear relation is resulting for simple cases, for example, a case of shot-peened 5056-0 aluminium [35] as shown in Fig. 3.4. This is the widely used $\sin^2\psi$ method [36], which allows the calculation of residual stress by measuring the lattice spacing in at least two different ψ_i angles.

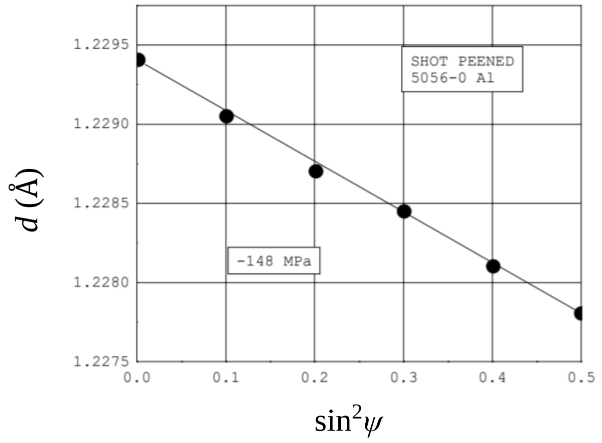

Figure 3.4. Linear relation between lattice spacing and $\sin^2\psi$ for shot-peened 5056-0 aluminium [35]

In addition to the previously discussed phase and stress, the XRD is sensitive to texture and grain size, which usually introduce measurement errors to the results. Besides, the small spatial resolution of XRD leads to time consumption for broad specimen testing. But XRD is a commonly accepted and time proved NDE technique for phase analysis and residual stress measurement.

3.3 Macromagnetic NDE Techniques

3.3.1 Eddy current

A time-varying current feeding into an excitation coil will create an alternating magnetic field when an electrically conducting material is placed in the alternating magnetic affected region. An eddy current (EC) will be induced in the material according to Faraday’s Law as discussed in Chapter 2. Meanwhile, the induced eddy current generates a magnetic field opposite the primary one generated by the coil per Lenz’s Law as shown in Fig. 3.5. The interaction between the secondary field generated by the eddy current and the primary magnetic field is sensed by pick-up coils or other magnetic sensors such as a Hall effect sensor. The presence of defect will result in a change in the impedance of pick-up coil and output voltage of the magnetic sensor. EC technique uses the interaction of these magnetic fields, which can be affected by the lift-off of the coil, the geometry of the specimen surface, the conductivity and the permeability of the material.

In practice, the magnetic flux generated by the coil is perpendicular to the surface of the tested specimen, and the induced circulating current is parallel to the surface as illustrated in Fig. 3.5. The circulating current density decreases exponentially with the depth, known as the skin effect [37]. The effect indicates that the eddy current will concentrate near the surface adjacent to the coil as the impediment of the opposing field will decrease with depth. The standard penetration depth of eddy current δ_{ec} in a conductive material is generally defined as a depth where the current density reduces to 1/e (around 37%) of the density at the surface of the material. It is determined by the exciting frequency f, the conductivity σ_E and permeability μ of the material

$$\delta_{ec} = \sqrt{\frac{1}{\pi f \sigma_E \mu}} \tag{3.3}$$

Hence, the excitation frequency should be carefully selected for a given material to assure the defects can be detected. The single frequency eddy current is widely used for surface flaws inspection. To obtain the best sensor response, the sensor needs to properly design for inducing the greatest eddy current density near the defect [38]. The single frequency EC method is easy to operate. Still, its limitation is apparent as well, i.e., its effectiveness is limited since it is well-designed to evaluate only one or two kinds of defects [37].

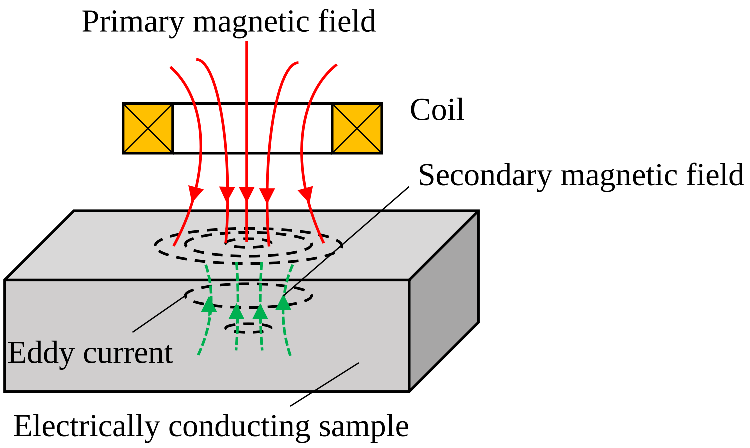

Figure 3.5. The eddy current induced in electrically conducting sample [39].

To improve the efficiency of the EC technique, the multifrequency eddy current technique has been proposed and used to analyse flaws with complex shapes and identify defects in the presence of various conductivity, permeability, geometry and lift-off [40]. As there are a few discrete frequencies carrying by the excitation current, it is difficult to perform quantitative measurements and generate visualisations of the data. Therefore, the combination of neural network and artificial intelligence have been popular recently [41,42].

Pulsed eddy current (PEC) is another popular NDE technique and has developed rapidly in recent years [39,44,45]. PEC uses a large pulsed current feeding into the excitation coil. The transient change of excitation current will induce an eddy current in the tested material. It consists of a continuum of frequencies in broadband that improves the multifrequency eddy current. The transient pulse is rich in the low frequency components, which are preferable to detect subsurface flaws. Different frequency components carrying the information of different depths facilitates the possibility of quantitative evaluation of the cracks inside the material.

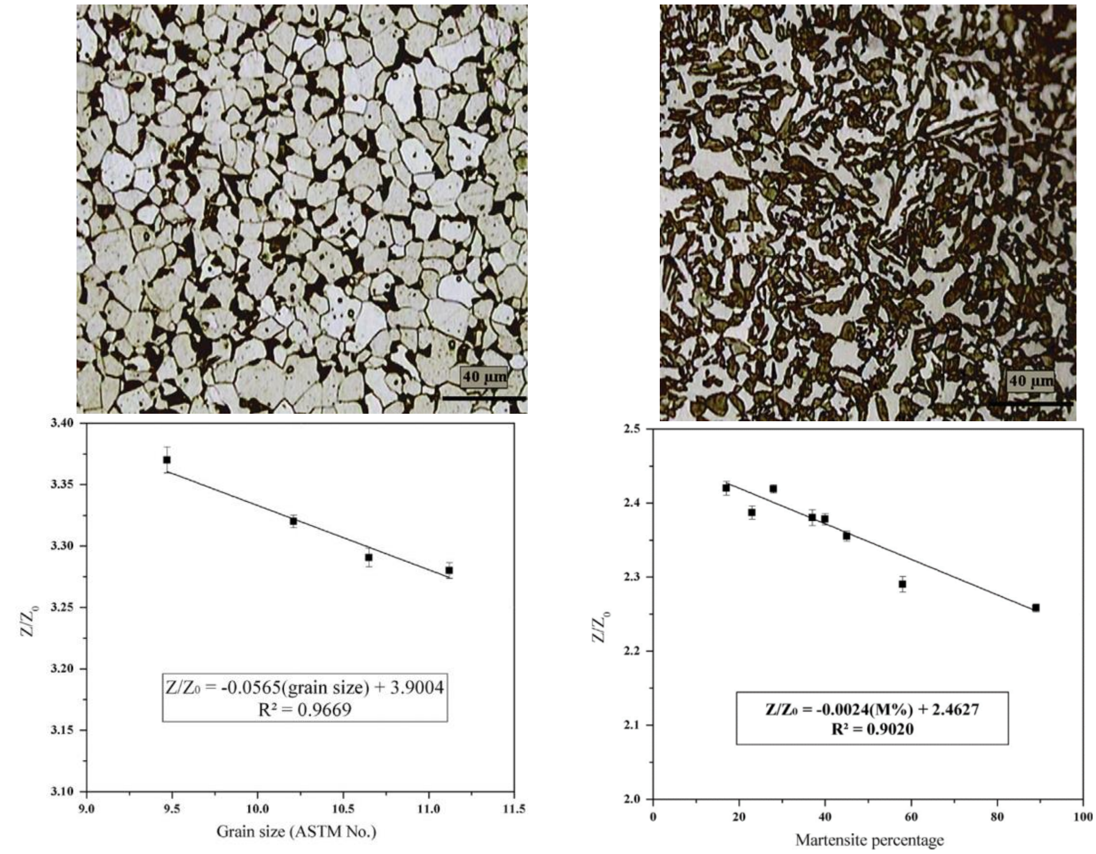

(a) (b)

Figure 3.6. **(a)** Optical microscopic image of a sample etched with Nital solution (the bright region is ferrite) and the relation between the ferrite grain size in DP steel and the normalised impedance. **(b)** Optical microscopic image of a sample etched with sodium metabisulfite solution (the dark region is martensite) and the relation between the percentage of martensite and the normalised impedance [43].

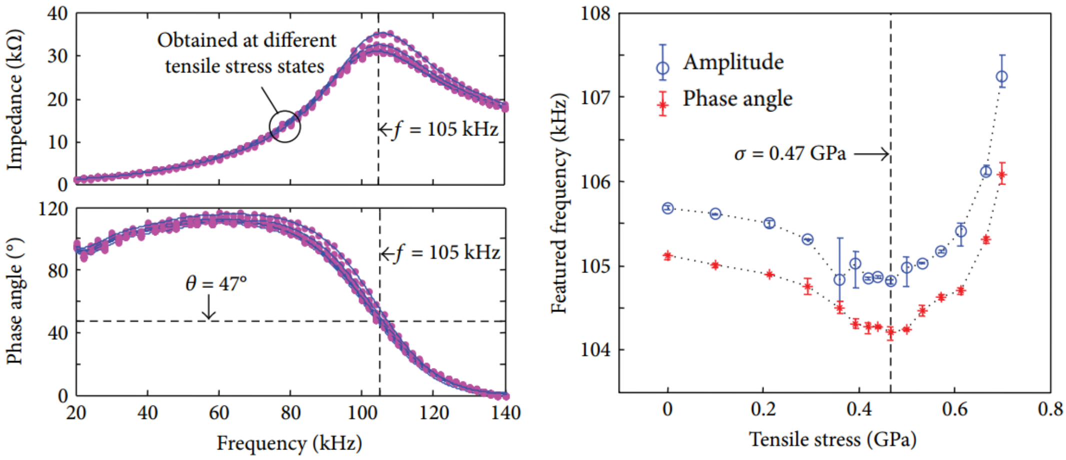

Figure 3.7. The impedance and phase angle curves *vs* various tensile stresses [47].

EC has a strong potential for evaluating the microstructure and residual stress due to its sensitivity to the properties of materials [43,46,47]. The change of the microstructure of material could directly affect the electromagnetic properties of the material, such as permeability, which would further influence the response of the EC signal. Fig. 3.6 gives examples of EC measurements on the grain sizes of dual-phase steel and the percentage of martensite phase [43]. When external stress is applied on a tested specimen, according to the magnetomechanical theory discussed in the previous chapter, the magnetic properties such as permeability will change so that the EC signal will be altered subsequently. The features of EC, such as impedance and phase angle used to evaluate the stress applied on the tested specimen, are shown in Fig. 3.7 [47].

3.3.2 Magnetic flux leakage

Magnetic Flux Leakage (MFL) is one of the most economical, reliable, efficient and widely used NDE techniques for examining the presence of defects in a ferromagnetic material. When a ferromagnetic specimen is applied to an external magnetic field, it will be magnetised along the direction of the applied field. Suppose there is no defect in the sample. In that case, the magnetic flux is concentrated in the material, and it forms a closure-flux with a magnet or electromagnet used to supply magnetic field. When a magnetic sensor is scanning the surface of the specimen, a healthy signal will be detected as shown in Fig. 3.8a. If there is a defect or discontinuity in the surface or subsurface, the magnetic flux will leak out the material near the defect due to the sudden permeability change. The sensor scanning result shows a pulse signal as shown in Fig. 3.8b.

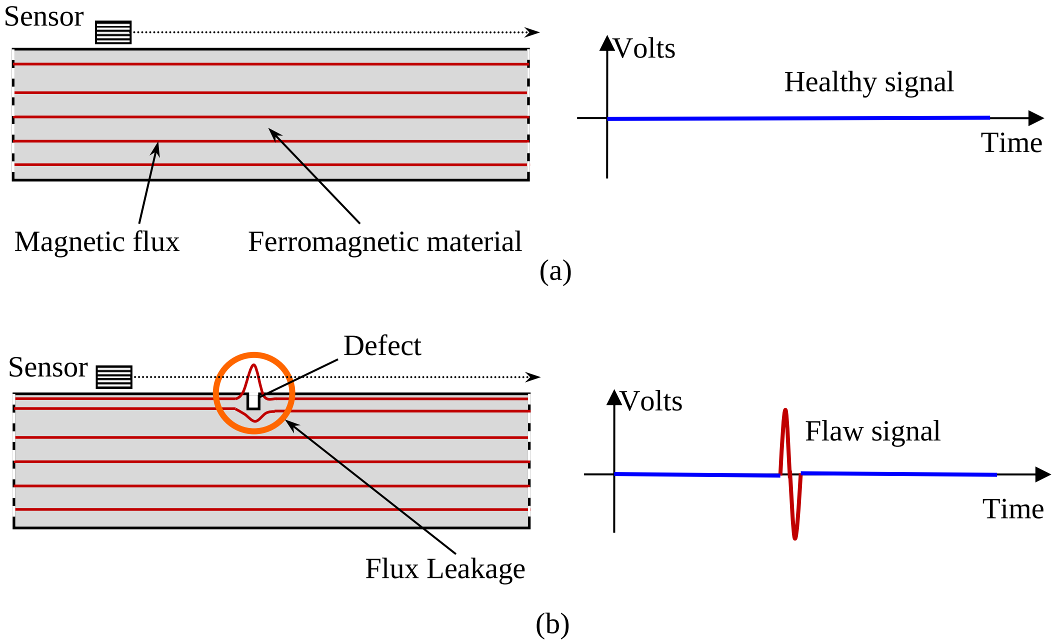

Figure 3.8. The principle of magnetic flux leakage technique. **(a)** Healthy condition, **(b)** defective condition.

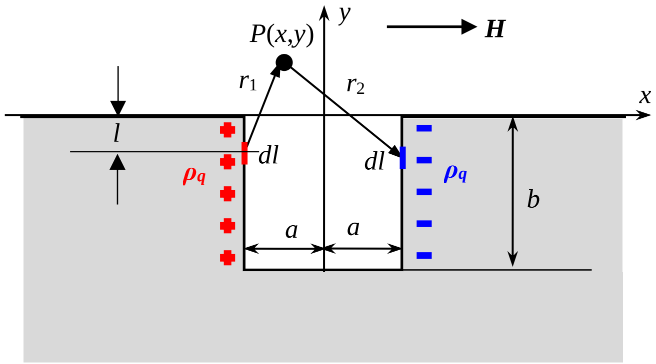

Figure 3.9. The schematic diagram of the dipole model of magnetic flux leakage presented by Zatsepin and Shcherbinin for a notch defect [48].

To analyse and interpret the measured signal, Zatsepin and Shcherbinin (Z-S dipole model) [48] presented an analytical model based on the assumption of magnetic dipole charges for a notch defect as shown in Fig. 3.9. The cross-section of the defect is in the *xy*-plane, and the defect is symmetric about the *yz*-plane. The *z*-axis does not show in the schematic diagram due to the simplification of the 2-dimensional (2D) model. According to the assumption of magnetic dipole, one of the defect walls is assigned with the positive magnetic charge density (north polarity) while the other wall possesses the negative one (south polarity). The width and depth of the defect are 2*a* and *b*, respectively.

Infinitesimal element with a length of *dl* along the defect wall carries a positive magnetic charge of $d\rho$ ($dl \times \rho_q$), which produces a magnetic field of $d\boldsymbol{H_1}$ at a point $P(x,y)$ in the free space. The leakage magnetic field $d\boldsymbol{H_1}$ is given as

$$d\boldsymbol{H_1} = \frac{1}{4\pi}\frac{\boldsymbol{r_1}}{r_1^3}d\rho \tag{3.4}$$

where $\boldsymbol{r_1}$ is a vector pointing from the element of *dl* to point *P* and r_1 is the norm of the vector or the distance between *dl* and *P*. similarly, $d\boldsymbol{H_2}$ produced by the negative charges on the other defect wall is expressed as

$$d\boldsymbol{H_2} = \frac{1}{4\pi}\frac{\boldsymbol{r_2}}{r_2^3}d\rho \tag{3.5}$$

where $\boldsymbol{r_2}$ and r_2 are the vector pointing from *dl* to point *P* and the distance between *dl* and *P*.

Besides, the differential forms of axial (H_x) and radial (H_y) components of the leakage field are

$$dH_x = \frac{\rho_q}{4\pi}\left[\frac{(x+a)}{[(x+a)^2+(y-l)^2]^{\frac{3}{2}}} - \frac{(x-a)}{[(x-a)^2+(y-l)^2]^{\frac{3}{2}}}\right]dl \tag{3.6}$$

$$dH_y = \frac{\rho_q}{4\pi}\left[\frac{(y-l)}{[(x+a)^2+(y-l)^2]^{\frac{3}{2}}} - \frac{(y-l)}{[(x-a)^2+(y-l)^2]^{\frac{3}{2}}}\right]dl \tag{3.7}$$

where $-b \le l \le 0$ and the magnetic charge density ρ_q can be determined by the equation [49]

$$\rho_q = H\frac{\pi n(\mu_r - 1)}{(n+\mu_r)tan^{-1}n} \tag{3.8}$$

where *n* is related to the demagnetising factor and $n=b/a$. The typical leakage flux distribution obtained using Equations (3.6) ~ (3.8) has been proved adequate to describe experimental results as shown in Fig. 3.10.

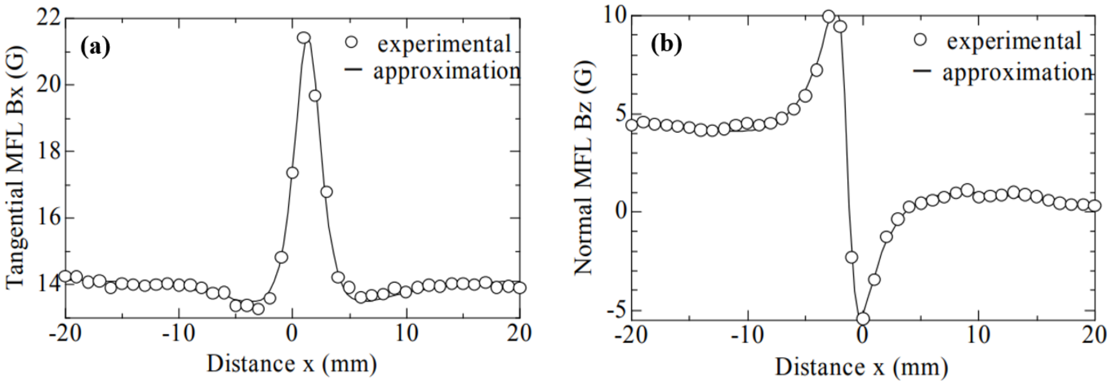

Figure 3.10. The simulated **(a)** axial and **(b)** radial components of MFL signal using Z-S dipole model to approximate the experimental results [50]

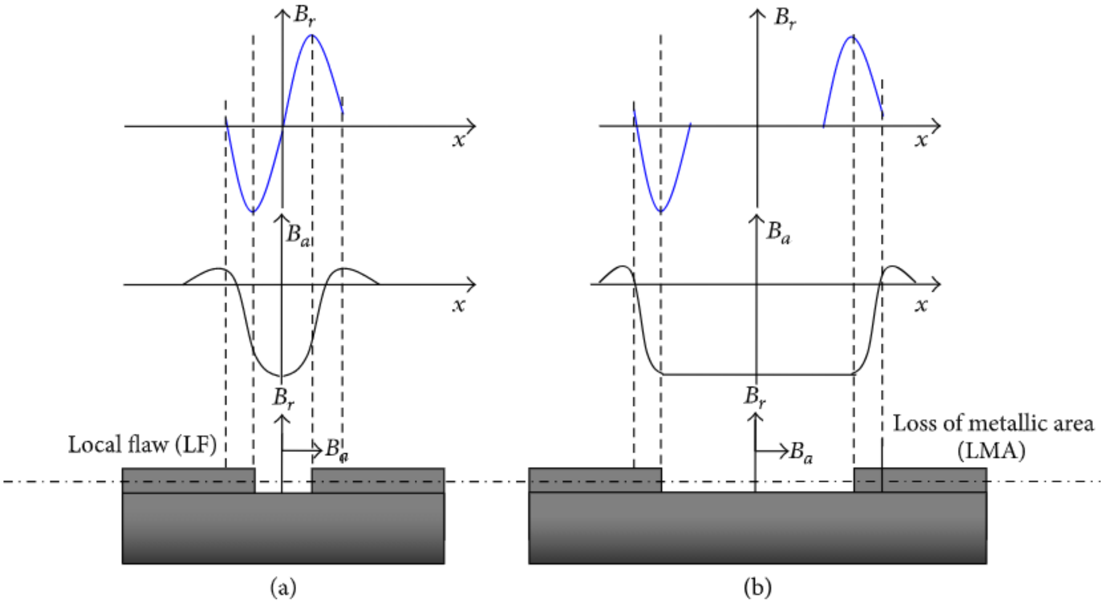

Figure 3.11. The tangential and normal components of the MFL signal induced by local flaws and loss of metallic area defects [51].

There are two main types of defects: local flaw (LF), such as broken wire and pitting defect, and loss of metallic area (LMA), such as wear damage and corrosion. Fig. 3.11 shows the axial and radial components of the leakage flux density induced by local flaws and the loss of metallic area defects [51,52]. The width between two peaks of the radial component or the half peak of the axial component is used to identify the width of defect inversely. The peak-to-peak values of the radial or axial components are employed to assess the depth of defect inversely.

The Z-S dipole model has been improved to 3D for a cylindrical surface breaking defect in a magnetised ferromagnetic material [53,54]. The material is magnetically saturated by an external magnetic field, and the magnetisation in the material is assumed to be locally constant. Fig. 3.12a shows a small cylindrical defect on the surface of the material. Its radius and depth are R and b, respectively. Compared with the 2D model, the arbitrary point $P(x,y,h)$ has an additional coordinate h along the z-axis known as lift-off. The magnetic charge on the infinitesimal element dS is given by

$$d\rho = \rho_q dS = \boldsymbol{M} \cdot \boldsymbol{n} dS = M sin\theta dS \tag{3.9}$$

where $\boldsymbol{M} = M\boldsymbol{j}$ is the surface magnetisation vector and $\boldsymbol{n}$ is the unit normal vector going into the defect. Then, the leakage magnetic field at point P due to the elemental charge $d\rho$ is given by

$$d\boldsymbol{H} = \frac{d\rho}{4\pi r^3}\boldsymbol{r} = \frac{M sin\theta dS}{4\pi r^3}\boldsymbol{r} \tag{3.10}$$

where

$$dS = R dz d\theta \tag{3.11}$$

$$\boldsymbol{r} = (x - R con\theta)\boldsymbol{i} + (y + R sin\theta)\boldsymbol{j} + (h - z)\boldsymbol{k} \tag{3.12}$$

$$M = \left[\frac{\mu}{\mu - N_y(\mu - 1)}\right] H \tag{3.13}$$

The precondition for the establishment of Equation (3.13) is that the defect is shaped as an oblate spheroid with major axis and minor axis, and N_y is the demagnetising factor along the y-axis [55]

$$N_y = \frac{1}{2(m^2-1)}\left[\frac{m^2}{\sqrt{m^2-1}} sin^{-1}\left(\frac{\sqrt{m^2-1}}{m}\right) - 1\right] \tag{3.14}$$

The radial MFL signal computed using Equations (3.10) ~ (3.14) is compared with the experimental one as shown in Fig. 3.12b. These signals show good agreement, which indicates the feasibility of this model.

In practical cases, the analytical models would not meet the requirement of MFL simulation due to the complex geometry and the imponderable demagnetising factor. The finite element method (FEM) is a preferable technique to simulate the magnetic field for the design of the MFL system and the selection of sensor [56,57]. FEM has been used to find and verify a few methods and phenomena, such as the magnetic compressive effect [58] and velocity effect [59] on MFL.

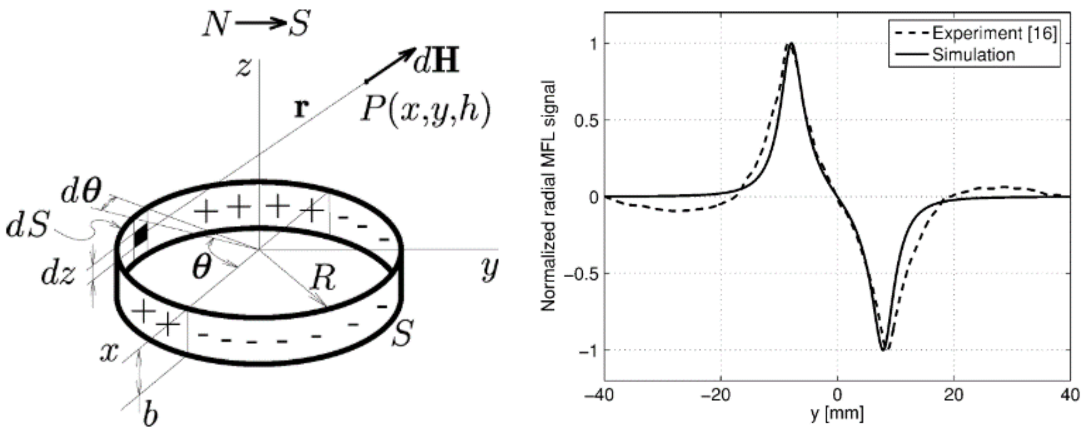

(a) (b)

Figure 3.12. **(a)** The schematic diagram of 3D dipole model of magnetic flux leakage for a cylindrical defect [53]. **(b)** The comparison of computed and experimental radial MFL signals [54].

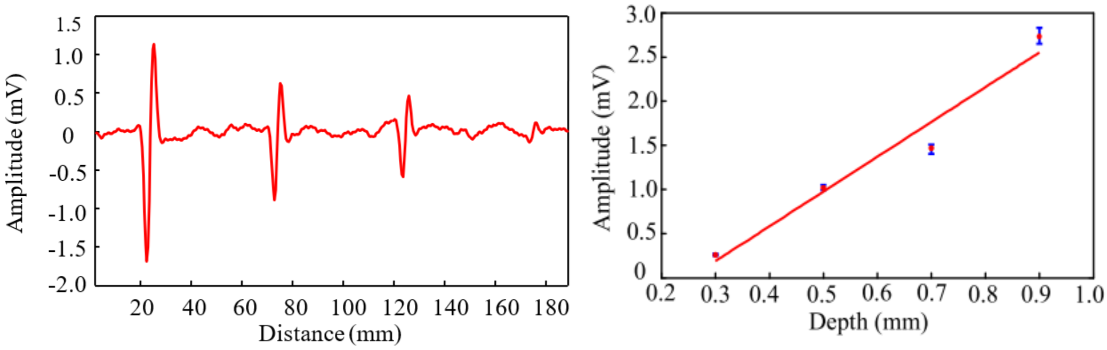

(a) (b)

Figure 3.13. **(a)** The MFL signal detected by TMR sensor. **(b)** The linear relation between depth of pitting defect and amplitude of MFL signal [57].

One of the factors that plays a critical role in quantitative MFL inspection is the magnetic sensor. Conventional MFL systems employ permanent magnets to provide high-intensity magnetic fields and pick-up coils to sense the MFL signal [52]. However, the intensity of the flux leakage field may be very weak in the μT range [60,61] that is undetectable by the traditional pick-up coil. Hall effect sensors and magnetoresistive (MR) sensors have propelled the significant improvement of the MFL technique. Okolo *et al.* [61] used a Hall effect sensor to detect a hairline crack successfully. Pelkner *et al.* [62] used a giant magnetoresistance (GMR) based magnetometer to sense a crack with a depth less than 50 μm. The ongoing development of MR elements offers a new kind of MR that has superior performances over GMR, namely tunnel magnetoresistance (TMR) [63]. It has been used in MFL inspections recently [51,57]. Fig. 3.13 shows the ability of TMR sensor in detecting tiny pitting defects and the linear relation between depth and amplitude of MFL signal.

3.3.3 The effect of stress on magnetic flux leakage

The magnetic flux leakage profiles simulated by the analytical models have been validated and proved to be in good agreement with measured results. According to the theoretical models, the main parameters impacting the amplitudes of detected MFL signals are the sensor lift-off [64], the size of defect [57,64], and the magnetic properties [65] of the tested specimen. These factors and another inspection parameter, namely scanning velocity [59], have been studied by numbers of investigators. For a specific inspection system and specimen, these parameters are determined except for the magnetic properties, which could be further influenced by stress.

As discussed in the previous chapter, the applied stress could significantly vary the magnetic hysteresis loop, consequently, the magnetic properties. Langman [68] has observed the decrease of the flux density by a factor of about six as the increase of 120 MPa tension perpendicular to the magnetic field reduces in mild steels at lower field strengths (~400 A/m). Therefore, the action of stress on MFL is necessary to investigate for the accurate evaluation of the shapes and sizes of the defect. To improve estimating the sizes of pit defects on a hydraulic pressure vessel, Mandal *et al.* [69] have experimentally investigated the influence of hoop stress on MFL signals induced by pits. It has experimentally shown that the hoop pressure in the pipelines could decrease the amplitude of the MFL signals by more than 40% as shown in Fig. 3.14a. To further evaluate the effect of stress on MFL signals, the experimental results were fitted with the analytical Z-S model as shown in Fig. 3.14b. Since the stress parameter was not involved in the model, only the fitting value of the linear density of magnetic charges in the model was used for qualitative discussion [69], [70].

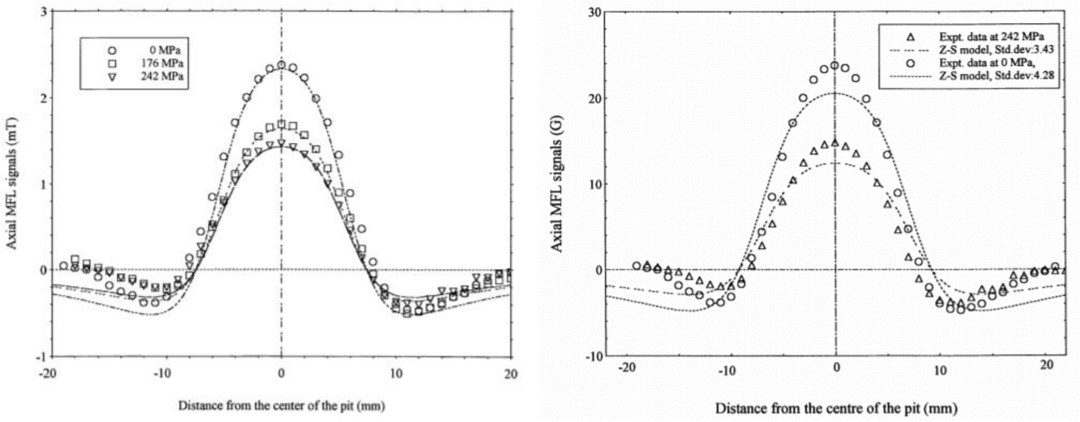

(a) (b)

Figure 3.14. **(a)** Axial component MFL signals for 0 MPa, 176 MPa and 242 MPa hoop pressure [66]. **(b)** A fitting of the Z-S model for the axial field with the axial MFL data for 0 MPa and 242 MPa by using the magnetic charge density 62.7 and 37.72, respectively [67].

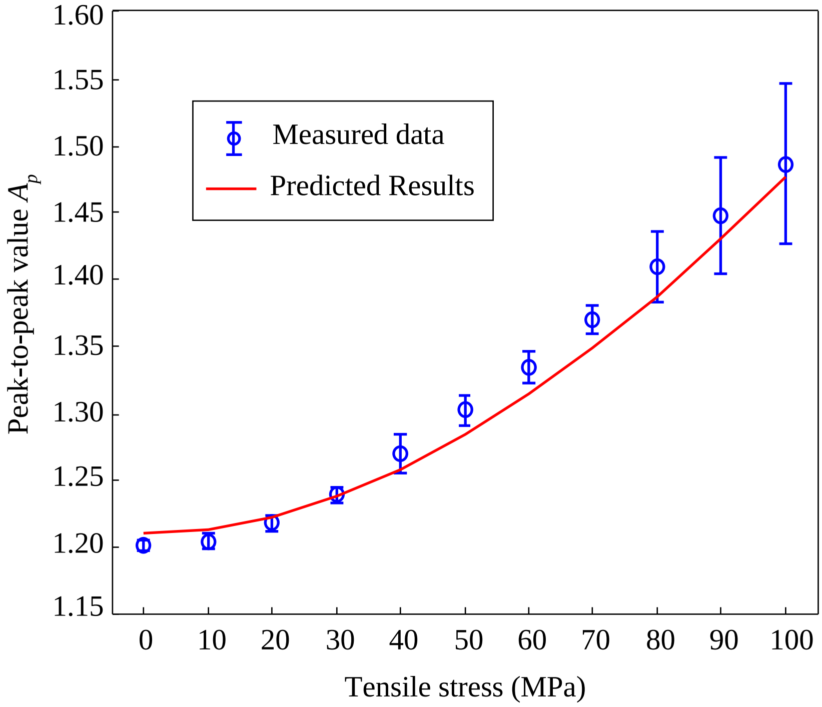

Figure 3.15. Measured and predicted peak-to-peak amplitudes of the normalised MFL signals obtained from various tensile stresses [71].

The stress-dependent J-A model was combined with the magnetic dipole model through magnetisation in [71]. The extended model has successfully predicted the effect of the tensile stress on the MFL signal induced by a cylindrical through-hole defect on a tensioned dog-bone specimen. The peak-to-peak amplitude of MFL

(MFL_{pp}) has been experimentally shown to increase by 24% when applying 100 MPa stress in tension as seen in Fig. 3.15. Besides, the predicted dependency of MFL_{pp} on the applied tensile stress could well fit the measured data with a coefficient of determination higher than 0.99. The details of the improved model will be presented in Chapter 4. Nevertheless, the analytical formulas are limited to simple geometries where the stress concentration can be analysed. Therefore, in more complicated situations, the leakage fields need to be calculated using numerical methods, such as finite element modelling.

The pioneering finite element modelling of the MFL field by Hwang and Lord [72] paved the way for the numerical analysis of defect-induced MFL signals. Significant progress has been made in this area with improvements in computational capabilities by considering non-linear material properties [67,73] and coupling them with stress [66,74,75]. Ivanov *et al.* [74] incorporated stress distributions into the magnetic FEM model by varying the permeability in the region under stress. Babbar *et al.* [66] introduced stress information into the magnetic FEM model by adjusting the permeability variable. Zhong *et al.* [75] built a FEM model to simulate the metal magnetic memory (MMM), which operated in the reversible magnetisation region. The MMM method could qualitatively evaluate defects rather than quantitatively identify defects due to relatively large errors.

FEM simulations of stress-induced MFL signals are more challenging to achieve than situations without stress since the magnetic permeability, magnetisation, and demagnetisation are stress dependent and nonlinear functions of the applied field. In order to solve the coupled magnetomechanical problem in defect reconstruction from MFL signals, a Multiphysics FEM model will be presented in Chapter 4 by interlinking the physics of mechanics and magnetics.

3.3.4 Magnetic hysteresis loop

The magnetic hysteresis B-H or M-H loop is the fundamental characteristic of a ferromagnetic material. The hysteresis properties such as differential relative magnetic permeability μ_r', coercive field H_c and remanence M_r or B_r (see Fig. 2.2) are sensitive to factors like stress, grain size, heat treatment and the microstructure.

It is a proven technique to use hysteresis loops for evaluating the microstructures and performance of ferromagnets. Raghunathan *et al.* [76] extended the typical J-A hysteresis model to two phase materials using the Boltzmann function. The measurement in [77] verified the hysteresis curve of the composite, which was mixed by cobalt manganese ferrite (soft phase) and barium hexaferrite (hard phase) powders, was magnetically coupled by the hysteresis loops of soft and hard phases (see Fig. 3.16). The heat treatment evaluation using magnetic parameters of hysteresis loops having been reported in various papers [78–80]. Besides, the magnetic hysteresis loops are a vital characteristic to evaluate the performance of a permanent magnet [81].

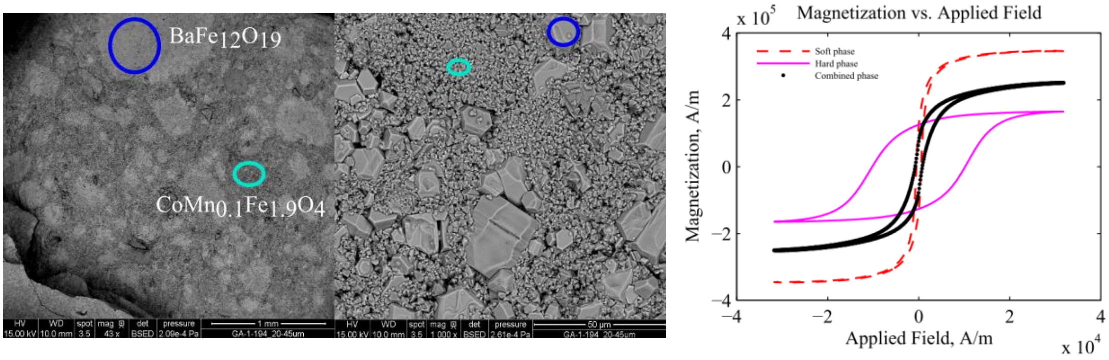

(a) (b)

Figure 3.16. **(a)** Microstructure of the two-phase composite sample including soft phase cobalt manganese ferrite (green circle) and hard phase barium hexaferrite (blue circle). **(b)** Hysteresis loops for soft phase, hard phase and two-phase materials [77].

Evaluation of the carbon content of steel components using hysteresis loops is a feasible area in NDE. Batista *et al.* [82] employed various magnetic properties of hysteresis loops such as coercive field, relative permeability and saturation magnetisation to investigate the carbon content in steels. Jiles [83] also investigated the carbon content in AISI 1000 series carbon steels using hysteresis loop characteristics such as initial permeability, coercive field, and anhysteresis permeability. The evaluation of carbon content in steel will be further discussed in the applications of MBN.

3.3.5 The effect of stress on hysteresis loop

The effect of stress or magnetomechanical effect characterises the change of magnetic properties of ferromagnetic material when subjected to external stress. A number of investigators have reported the effect of stress on hysteresis loops. In

Langman's measurements [68], the shapes of hysteresis loops of mild steel changed considerably under stress. Kwun and Burkhardt [84] experimentally showed the significant influence of stress on hysteresis loops of steels. Atherton and Jiles [85] found that the anhysteresis and hysteresis curves were both sensitive to stress and theoretically interpreted the effect of stress on magnetisation. Attempts to develop a mathematical model for explaining the effect of stress on hysteresis has been made. But it was not an easy task as there was no direct hysteresis parameter such as coercive field, remanence and permeability uniquely related to the effect of stress. Hence, the theory based on the ideas of domain process and domain wall motion [85,86] had a hope to interpret the results of the effect of stress. Szpunar *et al.* [87] empirically determined the magnetic parameters changing with stress. And Sablik *et al.* [88] were the first ones to theoretically proposed the mathematic model of magnetomechanical hysteresis.

Evaluation of stress in ferromagnetic material using the properties of hysteresis loop is of interest in NDE. When a ferromagnetic material is subjected to uniaxial applied stress, the effect of stress can be equivalent to an effective magnetic field H_σ, which leads to changes in the magnetic properties such as coercivity and permeability. The stress equivalent magnet field H_σ is given as [88]

$$H_\sigma = \frac{3}{2\mu_0}\sigma\left(\frac{\partial\lambda}{\partial M}\right)_{\sigma,T} \tag{3.15}$$

The effects of stress on anhysteresis and hysteresis parameters such as susceptibilities of anhysteresis at the origin χ'_{an}, susceptibilities of hysteresis at coercive field χ'_{H_c} and the coercivity field H_c have been reported by investigators, including Langman [68], Kwun *et al.* [84], Jiles *et al.* [85] and Sablik *et al.* [88]. And Garikepati *et al.* [89] combined the anhysteresis magnetisation with Equation (3.15) to obtain an equation for the dependence of the reciprocal of the susceptibilities at the origin χ'_{an} on stress

$$\frac{1}{\chi'_{an}(0)} - \frac{1}{\chi'_{an}(\sigma)} = \frac{3b\sigma}{\mu_0} \tag{3.16}$$

where b is a proportional coefficient of magnetostriction λ and magnetisation M based on the parabolic approximation $\lambda = bM^2$. The prediction using Equation (3.16) was proven to be in good agreement with experimental data for AISI 4130 steel subjected to various stresses shown in Fig. 3.17.

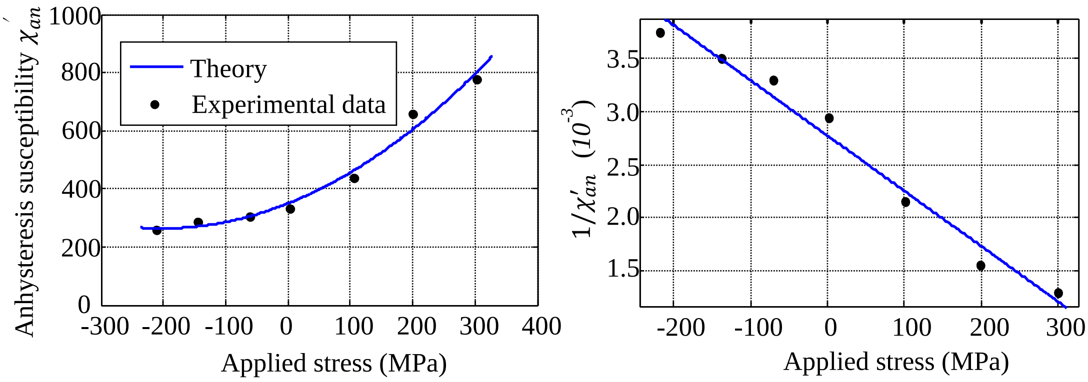

(a) (b)

Figure 3.17. **(a)** Anhysteresis susceptibility at the origin as a function of stress. **(b)** Reciprocal anhysteresis susceptibility at the origin as a function of stress [89].

However, it should be noted that the approximated coefficient *b* is only constant within a limited range of stresses and the relation between magnetostriction λ and magnetisation *M* is only parabolic at low levels of *M*. Consequently, the dependence of maximum magnetisation M_{max}, the anhysteresis susceptibility χ'_{an} and relative permeability at coercive field μ'_{rH_c} on the applied stress may fail in prediction according to the sign of $\partial\lambda/\partial M$.

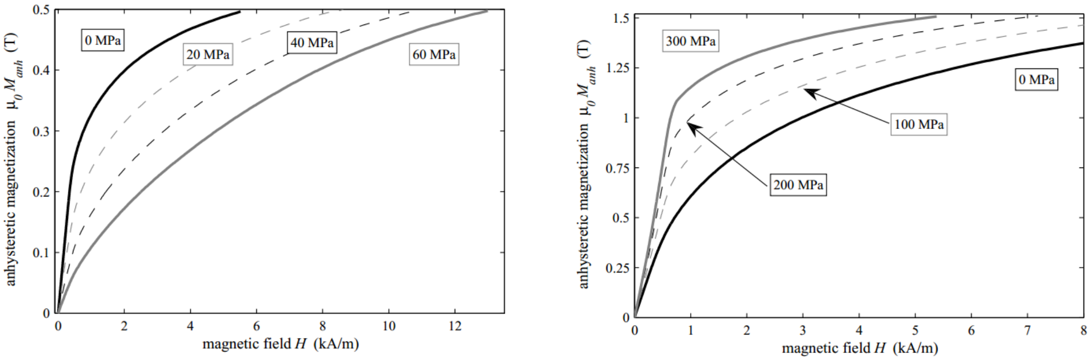

(a) (b)

Figure. 3.18. **(a)** Anhysteresis magnetisation curves measured for a nickel sample under various tensile loads. **(b)** Anhysteresis magnetisation curves obtained for 18%-Ni maraging steel under various tensile stresses [91].

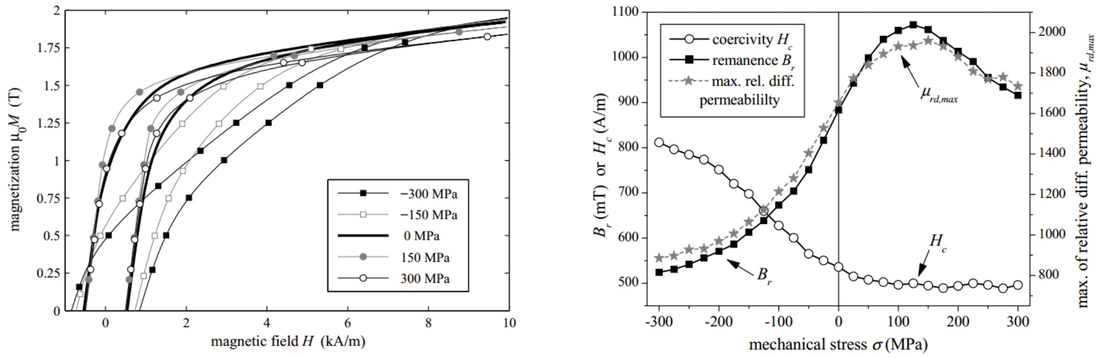

(a) (b)

Figure 3.19. **(a)** The hysteresis loops obtained for low carbon steel under various stresses. **(b)** The hysteresis loop parameters as a function of the applied static elastic stress [91].

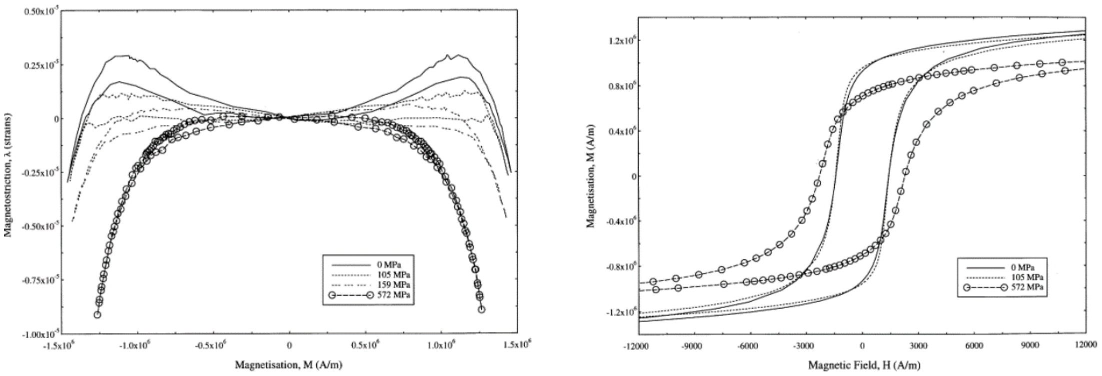

(a) (b)

Figure 3.20. **(a)** Magnetostriction curves for 0.86wt% carbon steel subjected to various tensile stresses. **(b)** Hysteresis loops for 0.86wt% carbon steel under different tensile loads [92].

Fig. 3.18 shows that the anhysteresis magnetisation increases with the increasing tensile stress when the sign of $\partial\lambda/\partial M$ remains positive while decreasing in the case of negative coefficient b. But for most steels, there is an occurrence of local extremum of H_σ at some critical intermediate value according to the following equation [90]

$$H_\sigma = \frac{3(\gamma_{11}+\gamma_{12}\sigma)}{\mu_0}\sigma M \tag{3.17}$$

Therefore, the magnetic properties may also present local extrema, for example, the remanence and maximum relative differential permeability as functions of stress for low carbon steel shown in Fig. 3.19. Besides, as discussed in the previous chapter, the $\partial\lambda/\partial M$ is positive at low-level magnetisation but may become negative at the high magnetisation region. For example, the magnetostriction measurements for 0.86 wt % carbon steel are shown in Fig. 3.20a. In this case, the stress equivalent field H_σ reduces the total effective field and decreases the magnetic properties of the hysteresis loop, as seen in Fig. 3.20b.

3.3.6 The effect of temperature on hysteresis loop

In addition to the effect of stress, the effect of temperature on hysteresis loop is a critical factor that should be considered in hysteretic NDE. It is known that the lower the temperature (≥ 0K) is, the higher the spontaneous magnetisation. According to Weiss theory [78], an exchange field where individual magnetic moments interact with each other could lead to the existence of critical temperature (i.e., Curie temperature) below which the thermal energy of the electronic moments is insufficient to cause random paramagnetic alignment. The temperature dependence of spontaneous magnetisation is approximately given as [93,94]

$$M_s(T) = M_s(0)\left(\frac{T_c - T}{T_c}\right)^{\beta_1} \tag{3.18}$$

where $M_s(0)$ is the spontaneous magnetisation at 0 K, T_c is the Curie temperature of the ferromagnetic material and β_1 is the critical exponent that depends on the representative mean field interaction.

Following an analogous way of spontaneous magnetisation, other parameters of the J-A model, including the pinning coefficient k, the domain density a, the domain coupling α and the reversibility coefficient c, have been extended as a function of temperature.

As the first approximation, the pinning coefficient is approximately equal to the coercivity. Since the coercivity field exponentially decreases with the increase of temperature in a ferromagnetic material, the pinning factor k is expected to vary exponentially with temperature as

$$k(T) = k(0)e^{\frac{-T}{\beta_2 T_c}} \tag{3.19}$$

where $k(0)$ is the pinning coefficient at 0 K, and β_2 is the critical exponent for the pinning factor and is approximated to be $\beta_1/2$.

Similarly, the domain density, a, exponentially decays with temperature as

$$a(T) = a(0)e^{\frac{-T}{\beta_3 T_c}} \tag{3.20}$$

where $a(0)$ is the domain density at 0 K and β_3 is the critical exponent for domain density, which is approximated to be $\beta_1/2$.

The domain coupling, α, which represents the strength of magnetic interaction between domains in isotropic material can be expressed as [95]

$$\alpha = \frac{3a}{M_s} - \frac{1}{\chi'_{an}} \tag{3.21}$$

At higher anhysteretic susceptibilities, χ'_{an}, the contribution of the second term to domain coupling is negligible and hence substituting the expression for scalar M_s and a from (3.18) and (3.20) respectively yields as a first approximation

$$\alpha(T) = \alpha(0)e^{(\frac{-T}{\beta_3 T_c})}(\frac{T_c - T}{T_c})^{-\beta_1} \tag{3.22}$$

where $\alpha(0)$ is the domain coupling at 0 K.

And the reversibility factor, c, is treated in an analogous way to that of domain coupling, α, and, for isotropic materials, is expressed as [95]

$$c = \frac{3a}{M_s}\chi'_{in} \tag{3.23}$$

where χ'_{in} is the initial susceptibility which is assumed as constant. By substituting the expression for M_s and a from (3.18) and (3.20), respectively, gives

$$c(T) = c(0)e^{(\frac{-T}{\beta_2 T_c})}(\frac{T_c - T}{T_c})^{-\beta_1} \tag{3.24}$$

where $c(0)$ is the reversibility factor at 0 K.

Furthermore, as the values at absolute zero such as $M_s(0)$ and $k(0)$ are impossible to be measured, Li *et al.* [96] has extended the model to normal temperature by given a fiducial temperature T_0 (298K) and given the corrected formulas as follows

$$M_s(T) = M_s(T_0)\left(\frac{T_c - T}{T_c - T_0}\right)^{\beta_1}, T < T_c \tag{3.25}$$

$$k(T) = k(T_0)e^{\frac{2(T_c - T)}{\beta_1 T_c}}, T < T_c \tag{3.26}$$

$$\alpha(T) = \alpha(T_0)e^{\frac{2(T_0 - T)}{\beta_1 T_c}}, T < T_c \tag{3.27}$$

$$\alpha(T) = \alpha(T_0)e^{\frac{2(T_0 - T)}{\beta_1 T_c}}\left(\frac{T_c - T}{T_c - T_0}\right)^{-\beta_1}, T < T_c \tag{3.28}$$

$$c(T) = c(T_0)e^{\frac{2(T_0 - T)}{\beta_1 T_c}}\left(\frac{T_c - T}{T_c - T_0}\right)^{-\beta_1}, T < T_c \tag{3.29}$$

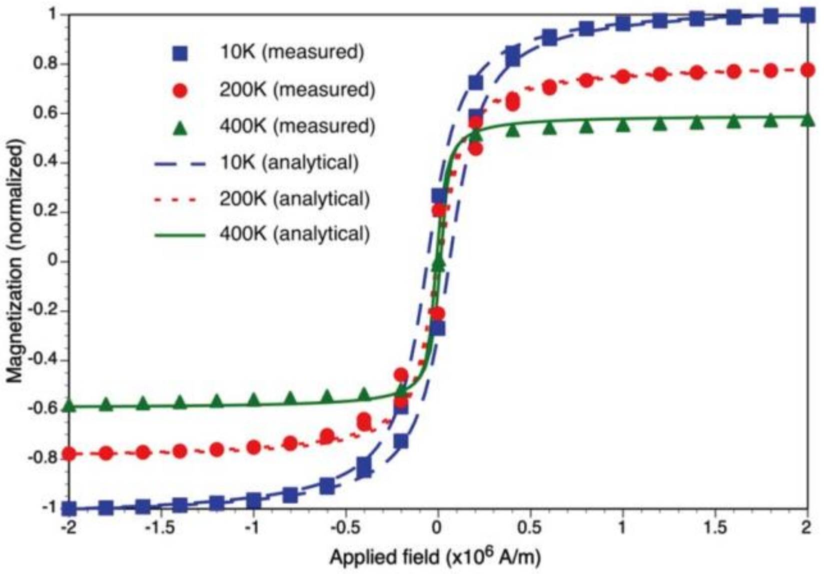

Figure 3.21. Temperature dependence of magnetisation curves in a substituted cobalt ferrite material [94].

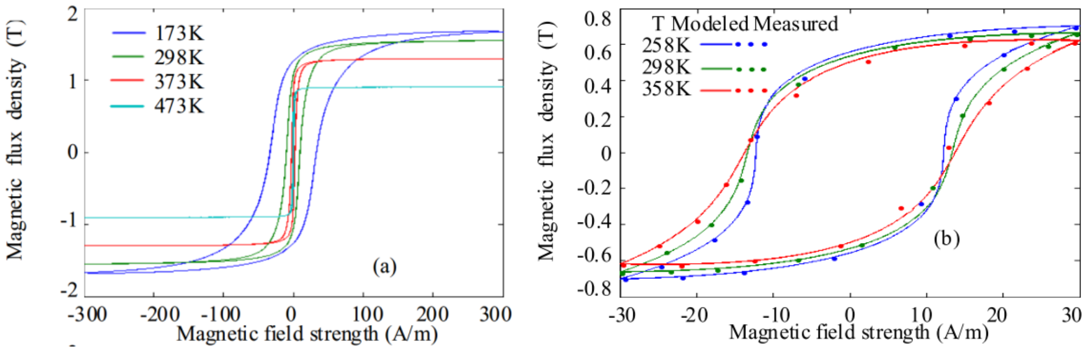

(a) (b)

Figure 3.22. (a)The major hysteresis loops for Fe-Si non-oriented steel measured at different temperatures, (b) the minor hysteresis loops for Fe-Si non-oriented steel measured at different temperatures [96].

The example plots of measured and simulated hysteresis loops using Equations (3.18) ~ (3.24) for substituted cobalt ferrite (with Curie point at 550K) at 10 K, 200 K and 400 K are compared in Fig. 3.21. The modelled hysteresis loops using Equations (3.25) ~ (3.29) and the corresponding measured results are shown in Fig. 3.22b. It can be found in Figs. 3.21 and 3.22 that the maximum values of magnetic flux density decreased with the increase of temperature for both materials at various applied magnetic field strengths. The coercive fields of the major hysteresis loops were observed to decrease with temperature (see Figs. 3.21 and 3.22a), but for the minor hysteresis loops, the reverse happened (see Fig. 3.22b). A few investigators have further computed the maximum permeability of hysteresis loops for non-oriented steel under various temperatures [97,98]. Their results showed that the permeability at low flux density increased with temperature while the opposite applied at high flux density. This phenomenon has also been found in other ferromagnetic materials, such as carbon steels [99,100]. Therefore, before applying the temperature-dependent hysteresis model, it is important to determine the magnetic flux density range of magnetic NDE methods. In this thesis, the magnetic flux leakage and Barkhausen noise will work in relatively high magnetic fields. Hence, the temperature-dependent hysteresis model used to analyse the thermal effect on magnetic flux leakage and magnetic Barkhausen noise will be modelled for the major hysteresis loop and presented in chapters 5 and 6.

3.3.7 Commercially available system for macromagnetic measurement

In addition to the laboratory sensors/systems mentioned above, there are several commercially available electromagnetic systems for macromagnetic measurement. They use various macromagnetic properties extracted from eddy current and hysteresis loop to characterise the microstructural and mechanical parameters of samples. The representative systems include the Impulse Magnetic Process Online Controller (IMPOC), Harmonic Analysis Coil Online Measuring (HACOM) system and EMspec® sensor system.

The IMPOC system is based on two identically constructed measuring sensors arranged on the top and bottom sides of the strip. Each measuring sensor comprises a magnetising coil and a measuring coil. The magnetising coil excites a pulsed magnetic field to magnetise the steel strip and the measuring coil inspects the gradient of the residual magnetic field strength on the upper and lower side of the strip. The measured residual magnetisation gradient is then correlated to mechanical properties of the steel strip (i.e. tensile strength and yield strength) using a mathematical model [101-103]. The system could measure moving strips up to a speed of 900 m/s. The measuring error of IMPOC system could be less than 10% [101]. But it should be noted that the IMPOC system is sensitive to lift-off changes between the material surface and sensor. In practice, especially in monitoring hot strips, it would be difficult to control lift-off at the head and tail of steel strips, which would cause further error in IMPOC reading [103].

HACOM is a type of hysteresis measurement system that could provide a non-destructive determination of direction-dependent mechanical properties (e.g. tensile stress and yield strength) as well as material properties (e.g. anisotropy and strain hardening) [102,103]. The system uses relatively low sinusoidal magnetic field at four different frequencies between 20Hz and 5kHz to magnetise samples. The magnetisation of the sample runs through hysteresis loops exciting induction signals in a receiving coil which is further analysed using fast Fourier transform (FFT) to gain the harmonic spectrum. Due to symmetry reasons, only odd harmonics will appear in the sine and cosine terms. The system is sensitive to external EM noise. Hence, the environment where many sources of external EM noise exist could lead to errors in HACOM measurement. Thus, the HACOM system requires magnetic shielding when deployed online. The system is also sensitive to lift-off. Therefore, the lift-off effect may also influence HACOM measurement.

EMspec® (Electromagnetic Spectroscopy) sensor array system has been developed for monitoring steel phase transformation. EMspec® sensor consists of an H-shaped ferrite yoke, one excitation coil, one active sensing coil and one dummy sensing coil [104,105]. The excitation coil runs simultaneously at multiple frequencies ranging from a few Hz to tens of kHz and the magnetic field experienced by the target steel is low, which corresponds to the Rayleigh region. The active sensing coil detects the voltage induced in the steel by the exciting coil, while the dummy coil combined with the sensing coil zeros the signal when there is no sample present. The inductance versus frequency spectrum, which is affected by the target steel sample permeability and resistivity, is calculated by a digital signal processor (DSP) based on an FFT of the excitation current and the induced voltage [104,105].

The basic principle of measuring the amount of transformation phase fraction is that each inductance spectrum corresponds to a microstructure of a certain amount of ferrite phase statistically mixed with the austenite phase. A zero-crossing frequency (ZCF), which is the frequency where the inductance goes to zero, is characterised by the effective electrical resistivity and low field magnetic permeability of the steel strip under measurement [104,105]. The advantage of using the ZCF to determine the low field magnetic permeability is that it is relatively insensitive to the variation of lift-off distance compared to the inductance itself [105].

3.4 Micromagnetic NDE Techniques

Micromagnetics is a field of physics dealing with the behaviour of ferromagnetic magnetic at sub-micrometre length scales [106–108], which are much larger than the atomic structure of the material, whereas small enough to resolve magnetic structures such as magnetic domain and domain walls. Micromagnetic NDE techniques are based on the micromagnetics theories to evaluate the macroscopic material properties and mechanical properties. The well-known micromagnetic NDE technologies are magnetoacoustic emission (MAE) and magnetic Barkhausen noise (MBN)

3.4.1 Magnetoacoustic emission and magnetic Barkhausen noise

Magnetoacoustic emission (MAE) is closely related to the magnetic Barkhausen emission. MAE is an effect of the generation of low level acoustic bursts due to sudden discontinuous changes in magnetisation involving localized strains or magnetostriction. A broadband ultrasonic transducer could detect these acoustic bursts. Microscopic magnetostrictive pulses cause these bursts via the creation, motion, and annihilation of non-180^o domain walls during the magnetisation process. MAE was first observed by Lord [78] and applied by other investigators [109,110]. Since the number and volume of non-180^o domain walls are affected by uniaxial stress, the amplitude of MAE for ferromagnetic materials is stress-dependent. It was observed by Gorkunov *et al.* [111].

The magnetic Barkhausen Noise (MBN) is generated by the irreversible motion of magnetic domain walls when they break away from pinning sites in the ferromagnetic materials subjected to a changing magnetic field. During the domain walls motion and transition, pinning sites, local microstructural defects, stress, and so on jointly contribute to the discontinuous stepwise jumps [112], which can be detected by the search coil near the surface of the sample. Therefore, the MBN technique is capable of various NDE fields, such as residual stress [113], hardness [112], and anisotropy [114]. The frequency range of MBN for NDE applications is usually 10-500kHz, so according to Equation (3.3) for penetration depth, the obtained emissions originate from the surface layer.

Traditionally, MBN measurement systems consist of a computer, electronic components such as an amplifier and filter, a magnetising unit, and a sensor or probe consisting of a pickup coil and a ferrite core. The magnetising unit used to excite the magnetic field can be formed by an open loop solenoid or a close loop electromagnetic yoke wound by enamelled wire [115]. In applications, a close loop electromagnet is popularly chosen [116]. In some cases, a flux sensing coil or feedback coil for controlling the currents can also be placed in the magnetising leg [117].

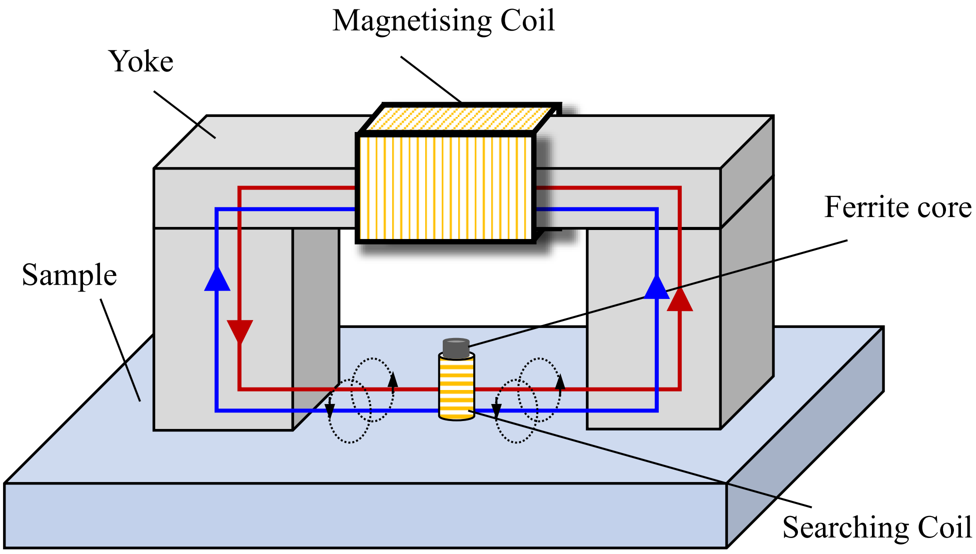

Figure 3.23. The schematic diagram of a typical Barkhausen noise measurement setup.

For the sensing unit used to detect Barkhausen emissions, the main component is a cylindrical coil that can pick up the pulse change of flux density generated by the domain walls suddenly passing through pinning sites. Since the air coil has relatively low sensitivity, a soft ferromagnet core such as ferrite core is usually inserted into the air coil to increase the sensitivity of the sensing unit [118]. The sensing unit is generally positioned between electromagnet legs at the magnetised region of the surface of a sample. The typical MBN measurement system is shown in Fig. 3.23.

The original signal measured by the MBN sensor contains the low frequency component derived from the magnetising current and the high frequency Barkhausen emissions. To obtain the MBN signal only as illustrated in Fig. 3.24a, a band-pass filter within a few kHz to around 100kHz is used to eliminate the low frequency component and the super high frequency noise. There are various methods to analyse the MBN signal, such as the pulse numbers and frequency spectrum. Due to the stochastic nature of the Barkhausen emissions, the widely used method is the root mean square (RMS or MBN$_{rms}$) voltage as shown in Fig. 3.24b.

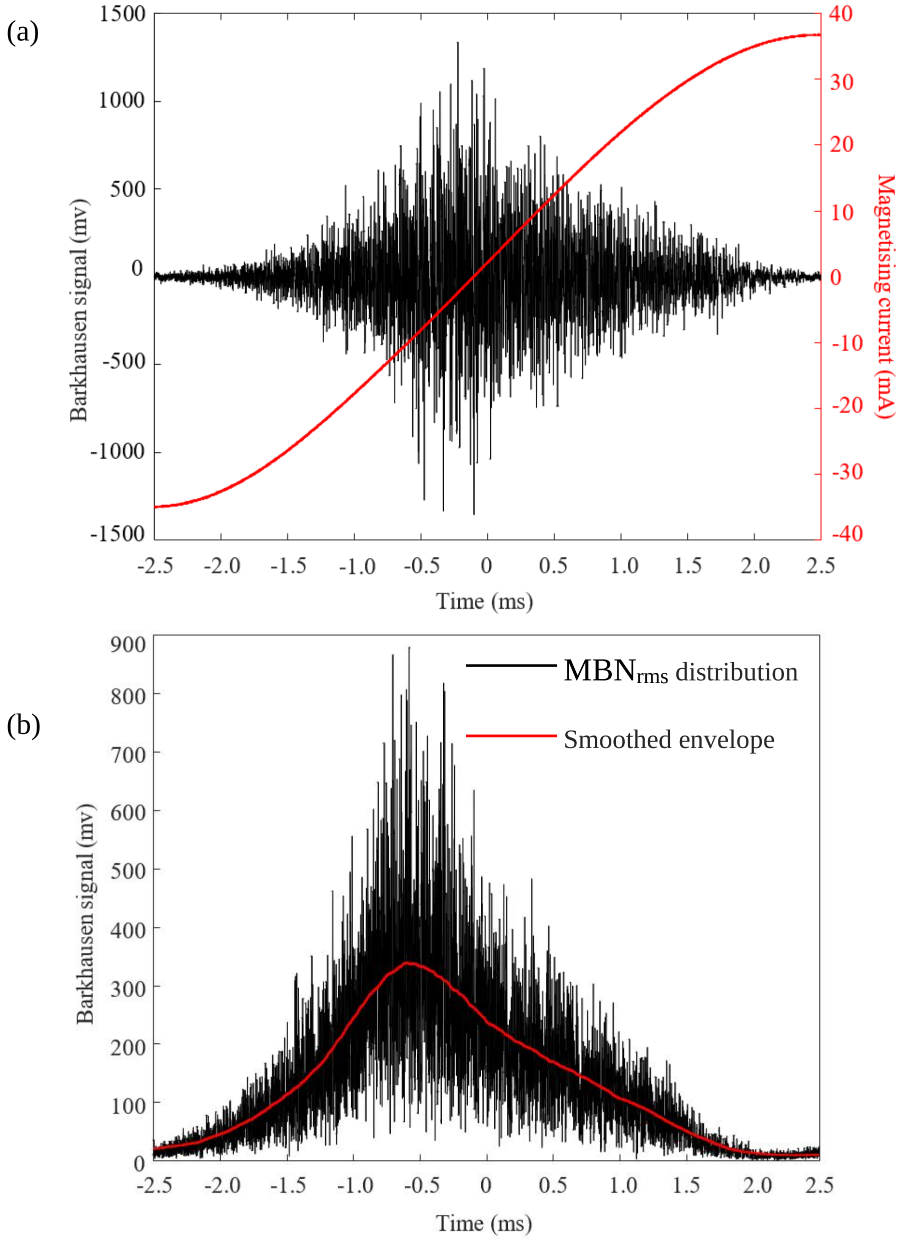

Figure 3.24. **(a)** Raw Barkhausen emissions obtained for carbon steel. **(b)** Extraction of the smoothed envelope of MBN$_{rms}$ distribution.

It has been proven that the MBN is a potential NDE technique for the evaluation of material properties, such as residual stress [113], hardness [112], and anisotropy [114]. In comparison, these studies were made with different magnetising currents and frequencies. The MBN profile could significantly be affected by the magnetising currents since the magnetic properties related to the MBN signal would change. The measurement and the analysis of high magnetising current, i.e., saturation magnetisation, would provide more information about different phase features and gradients in properties. In the case of a low magnetising current, the applied voltage could correspond to the magnetising current with less hysteresis distortion. It is well known the peak value of MBN increases with the increase of applied current or voltage as shown in Fig. 3.25 [115,119]. Fig. 3.25a shows that the higher current could provide more information as it could supply enough energy to excite two peaks of the MBN profile.

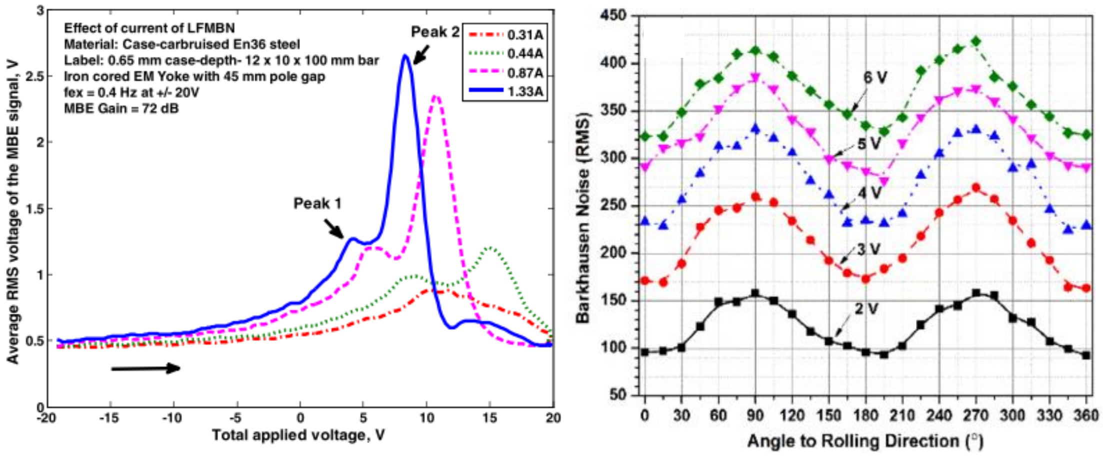

(a)

(b)

Figure 3.25. **(a)** The MBN profile measured on the case-carburized bar sample with different magnetising currents [115]. **(b)** The MBN$_{rms}$ measured on the hot-rolled non-oriented electrical steel with different magnetising voltages [119].

Besides, it was experimentally shown that the shape of the MBN signal depended on the frequency of magnetisation and the resonant frequency of the pick-up coil [115,119–121]. The most intuitive change of MBN profile is the peak value of MBN$_{rms}$ increasing with the excitation frequency increase as shown in Fig.3.26 [119-121]. It is known that the MBN signal level is related to the number of domain walls and their extent of displacement at a given instantaneous magnetisation field [122]. The increase in excitation frequency contributes to the increase in the number of domain walls, which leads to the increase in MBN level [123]. Since the MBN_{rms} is obtained by averaging Barkhausen emission pulses over a suitable time interval, the overall increase in MBN_{rms} with the excitation frequency shown in Fig. 3.26 could be attributed to the increase in domain wall activity due to the increasing rate of change of magnetisation in the material. However, the excitation frequency would influence the peak height of MBN_{rms} and affect the magnetisation by adding classical and excess eddy current losses [124]. Therefore, in addition to the increase in height, the increase of excitation frequency would result in broadening the MBN_{rms} but reducing the features of MBN profile, as shown in Fig. 3.27 [115].

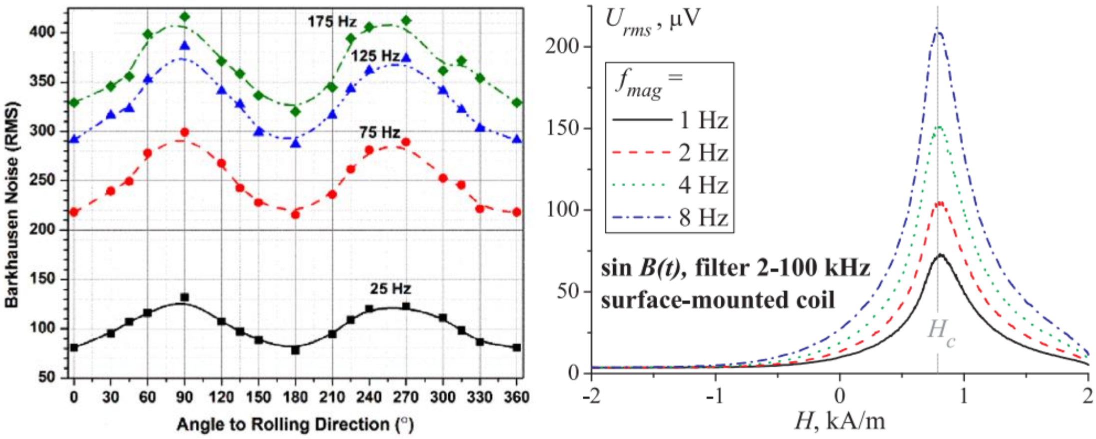

(a) (b)

Figure 3.26. **(a)** The MBN_{rms} measured on the hot-rolled non-oriented electrical steel with different magnetising frequencies [119]. **(b)** The MBN envelopes measured on TRIP steel with various magnetising frequencies [121].

It is also well known that the MBN_{rms} profile strongly depends on the resonant frequency characteristics of the pick-up coil. The pick-up coil with a larger number of turns will have better sensitivity and better response in the lower frequency range, while the lower number turns coil will shift its resonant frequency to a higher frequency range with worse sensitivity [115,120]. Moorthy [119] has experimentally shown (see Fig. 3.28) that for the case-carburized sample with a gradient in material properties along with the depth, it became increasingly challenging to detect MBN signal caused in the deeper subsurface due to the shift in the resonant frequency of pick-up coil to the higher frequency range. Hence, the pick-up coil with a resonant frequency in a low frequency range can be used to detect the MBN signal from the deep subsurface, while the higher frequency resonant coil can be useful for detecting the near-surface properties by minimizing the influence of deeper subsurface.

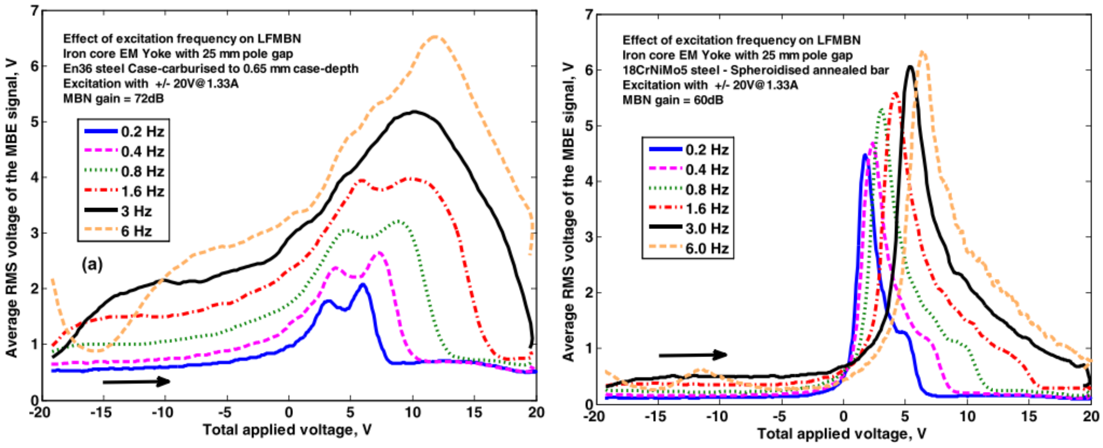

(a) (b)

Figure 3.27. The MBN$_{rms}$ profile measured on the surfaces of **(a)** case-carburized sample and **(b)** spheroidized annealed sample under various excitation frequencies [115].

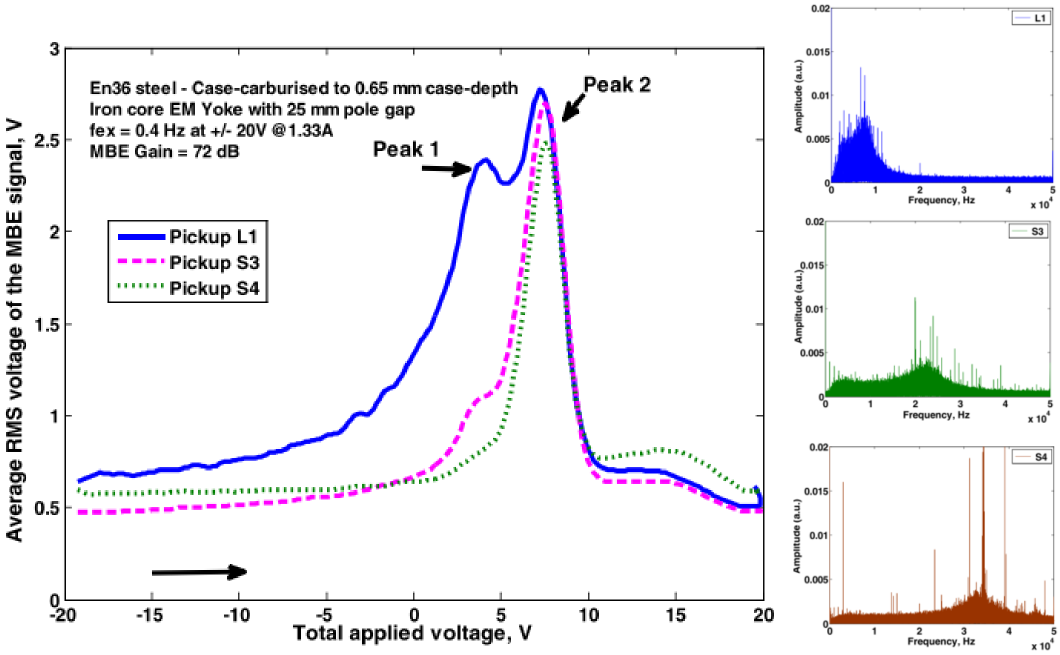

(a) (b)

Figure 3.28. **(a)** The MBN$_{rms}$ profiles measured on the surface of case-carburized sample by different pick-up coils. **(b)** Frequency response characteristics of the pick-up coils [115].

Since MBN is sensitive to microstructure (such as texture, grain size, composition), it has been proven that the microstructure of ferromagnetic material could significantly influence MBN signals. And in turn, MBN is a considerable potential NDE technique for characterising the microstructure of ferromagnetic materials. Most MBN applications are conducted on isotropic material, whereas it is also a promising method for characterisation of the microstructure-induced anisotropy of ferromagnetic materials, *e.g.*, grain-oriented (GO) electrical steel [114,125] and non-oriented (NO) electrical steel [119]. The magnetic anisotropy of ferromagnetic materials is originated from the dependency of magnetic properties on the direction of the magnetic field. There is a preferred direction called the easy axis, which is more easily magnetised at a certain magnetic field. The main reasons that cause the magnetic anisotropy in steel are attributed to the magnetocrystalline structure, grain shape and stress [78,126]. In industrial applications, to obtain specific materials, annealing and the rolling process would be used. For example, in GO steel, the unique Goss texture ({110}<001>) results in the alignment of the easy axis (<001>) to the rolling direction, which leads to a strong MBN signal in this direction as shown in Fig.3.29.

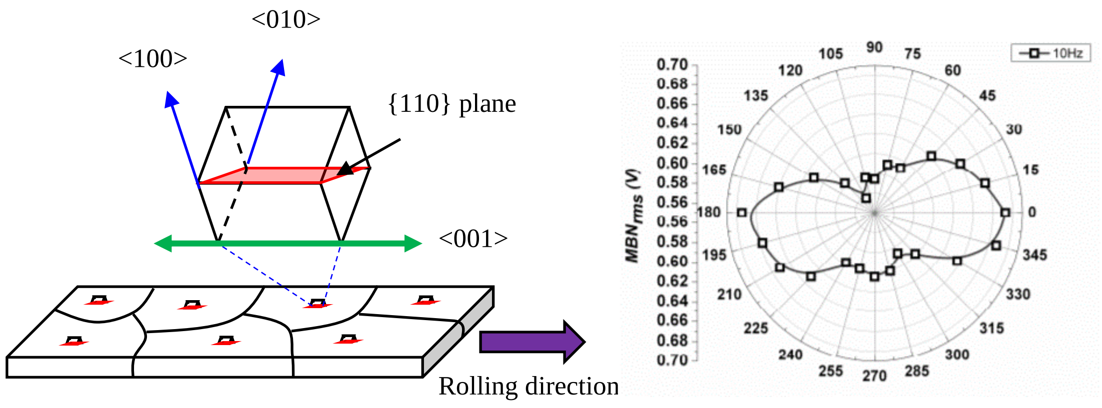

(a)

(b)

Figure 3.29. **(a)** Goss texture of GO electrical steel. **(b)** Polar plot of the MBN$_{\mathrm{rms}}$ for the GO electrical steel [125].

The non-oriented electrical steel usually consists of mixed texture, which has weakly magnetic anisotropy on macroscopic scale. But the NO steels are usually manufactured under two-stage cold rolling with intermediate annealing. After the first cold rolling, the annealing could recrystallize and decarburize the steel, and the annealing after the second cold rolling can remove residual stress and obtain the desired random orientation of grain growth [127]. During the process, there is still inherent anisotropy in its magnetic properties at angles to the rolling direction due to the heavy deformation and elongation, but much less pronounced than in GO steel, which has been experimentally verified as shown in Fig. 3.30 [119]. The simulation of the anisotropic MBN is a difficult task due to the change of magnetic properties at the angles to the rolling direction. But attempts have been made to model the anisotropic materials [128,129]. Upadhaya *et al.* [129] identified the parameters of J-A model in different measurement directions and gave the direction-dependent anisotropic parameters by fitting the measured results. This model has been experimentally verified in their study. The effect of microstructure-induced anisotropic on MBN signal and the directional MBN model will be presented in Chapter 7.

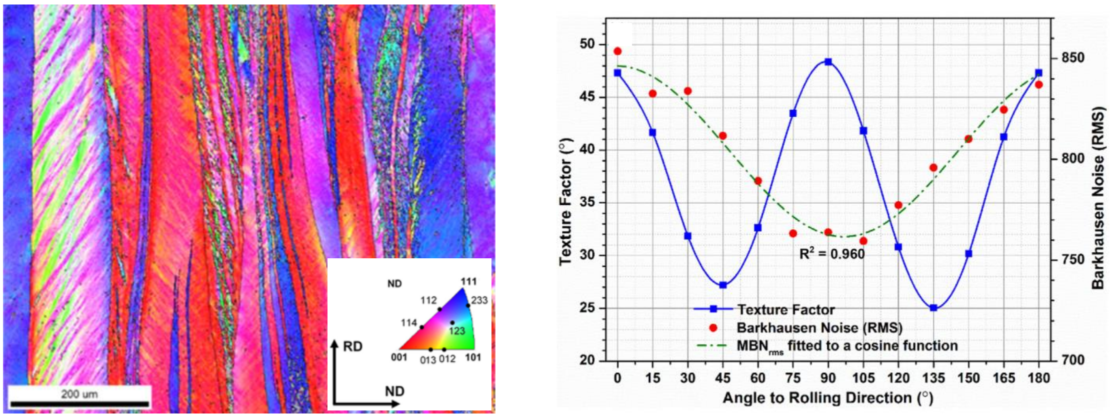

(a) (b)

Figure 3.30. **(a)** The microstructure and texture of the NO steel after cold rolling. **(b)** The measured MBN_{rms} and texture factor as a function of angle to the rolling direction [119].

MBN is originated from the magnetic domain walls motion during the magnetisation process. Its correlation to the microstructural properties is evident. In carbon steel, its characteristics and distribution are governed by the microstructures, including single and multiple iron-carbon metallurgical phases. According to the Iron-Carbon phase diagram, the common types of phases present in carbon steel at room temperature are ferrite, cementite (Fe_3C_{III}, Fe_3C_{II} and Fe_3C_I) and pearlite, whose grain size, iron crystalline structure and amount of carbon atoms in the lattice are different from each other as shown in Fig. 3.31. Therefore, they would perform different magnetic properties.

Ferrite is iron containing an extremely minimal amount of carbon. At room temperature, ferrite is a relatively soft magnetic material, and it comprises iron atoms organised in a body centred crystalline structure. Its solid solubility or the amount of carbon dissolved in ferrite is practically zero at room temperature, and the solubility increases to only a maximum of 0.02% at 723℃. The right-hand side of the diagram represents cementite, also known as iron carbide, which is formed by the combination of iron and carbon containing 6.67% carbon. Compared with the low mechanical (high ductility and low strength) and magnetically soft (in terms of coercivity) ferrite, cementite shows high mechanical and magnetic hardness. Thus, the relative volume fraction of the ferrite and cementite phases gives rise to the final mechanical and magnetic properties of the steel. In carbon steel, which generally contains less than 2% carbon in weight, the mixture of ferrite and cementite turns to a lamellar (thin plate like layers) microstructure referred to as pearlite.

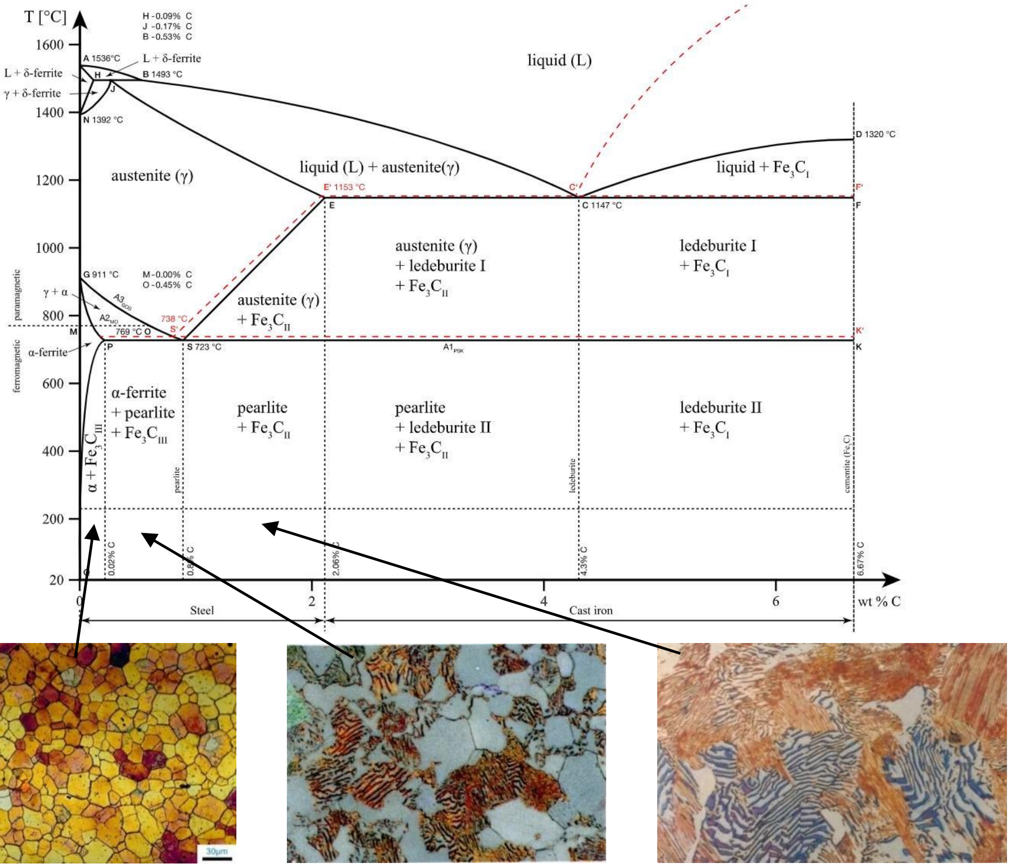

Figure 3.31. The Iron-Carbon phase diagram [130].

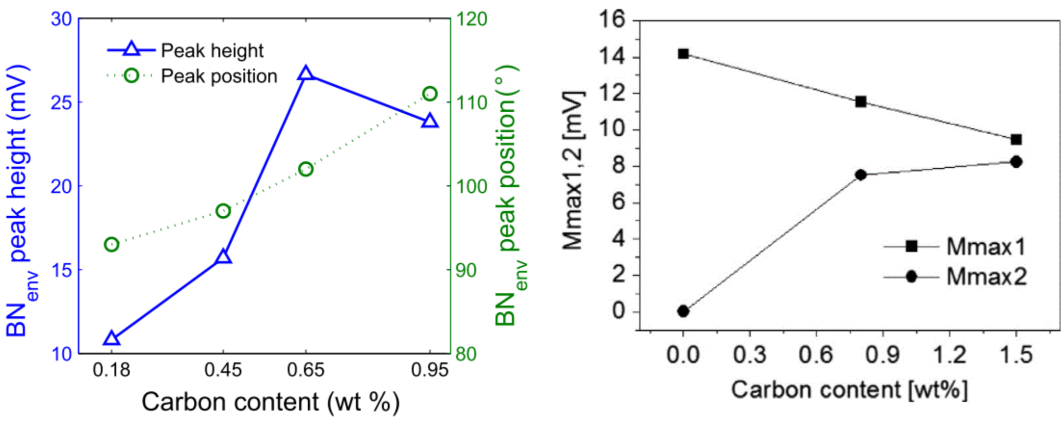

(a) (b)

Figure 3.32. **(a)** MBN envelop peak height and position as a function of carbon content [131]. **(b)** Maximum MBN amplitude as a function of carbon content [82].

With the increase of the carbon content, the soft phase ferrite decreases while the harder phases pearlite and cementite increase proportionally. Therefore, the carbon content in steel corresponds to the volume fraction of phases and further refers to the mechanical properties of steel. Since Barkhausen noise and hysteresis loop are sensitive to the microstructure of ferromagnetic material, they have been used to evaluate the carbon content in steel [82,83,131,132]. Jiles [83] has experimentally shown that the coercivity and hysteresis loss increased while the initial permeability decreased with carbon content. The different types of cementite, i.e., the normal lamellar pearlite and the dispersed spheroidised structure were analysed and demonstrated that the pearlite is more effective in blocking the movement of magnetic domain walls. The correction between MBN envelope peak amplitude and carbon content of steel has also been investigated [131]. The measured results illustrated that the peak height of MBN envelopes increased with carbon content until they reached 0.65% carbon in weight and then abruptly decreased beyond this point (see Fig. 3.32a). While the measurements of Batista et al. [82] shown that the MBN envelopes had two peaks either increasing or decreasing with carbon content from 0% to 1.5% carbon in weight (see Fig. 3.32b). To avoid the contradiction of MBN peak value, Zhang *et al.* [132] extracted parameters with two fitted Gaussian curves to MBN profiles, and the gaps between two peaks of Gaussian fitted curves presented a linear dependence on carbon content. But it may only be feasible for low carbon steel since when the percent of the carbon in weight higher than 0.26%, it could be predicted that the gap would increase again. Therefore, to combine a few magnetic techniques and a few features of a NDE technique is a potential method to quantitatively evaluate the carbon content of steel, which will be discussed in Chapter 8.

3.4.2 The effect of stress on magnetic Barkhausen noise

In early applications of MBN, it was found that the peak amplitude of MBN in steel increased with the increase of stress in tension, while decreased with the increase of stress in compression [133,134]. The previous chapter has discussed the origin of MBN on the microscale. When applying a sufficient magnetic field, the domain walls were forced to overcome the local pinning sites such as inclusion, dislocations, and precipitates. The discontinuous and irreversible domain wall motion was one of the most important mechanisms by which the MBN was caused. The other mechanisms included the discontinuous rotation within a domain and the inversion of magnetisation in single domain particles [78]. Among them, the discontinuous domain motion and rotation contributed to the Barkhausen effect largely. The domain motion and rotation would be significantly influenced by stress as discussed in the previous chapter. Hence, the level of Barkhausen emission could have a noticeable change with stress.

As aforementioned in Section 3.3, the stress was treated as an equivalent field H_σ, which depended on the type of stress (compression and tension) and the differential function value of magnetostriction *vs* magnetisation ($\partial\lambda/\partial M$). When external stress was applied to the magnetised material, the domain structure changed to a new optimal configuration due to the additional magnetoelastic energy. The magnetoelastic energy E_λ was related to the magnetostriction λ and external stress σ. If the external stress was uniaxial and parallel to the direction of magnetisation, the energy was proportional to the product of magnetostriction and stress, which was either positive or negative as expressed in Equation (2.32).

Following an analogous argument to hysteresis, when analysing the stress-dependent MBN, the following conditions could be considered: (1) The sign of $\sigma \cdot \frac{\partial\lambda}{\partial M}$ is positive, and the direction of the applied magnetic field is parallel to the direction of stress. The stress equivalent field H_σ further enhances the effective field H_e and consequently increases the velocity of domain wall motion to pass the pinning sites allowing larger Barkhausen jumps than those in stress free condition. Therefore, in this case, the higher stress leads to the higher MBN amplitude as shown in Fig. 3.33a. (2) The sign of $\sigma \cdot \frac{\partial \lambda}{\partial M}$ is negative, and the direction of the applied magnetic field is parallel to the direction of stress. The stress equivalent field H_σ further weakens the effective field H_e and consequently decreases the velocity of domain wall motion to pass the pinning sites resulting in lower Barkhausen jumps than that in stress free condition. Therefore, in this case, the higher stress leads to the lower MBN amplitude as shown in Fig. 3.33b.

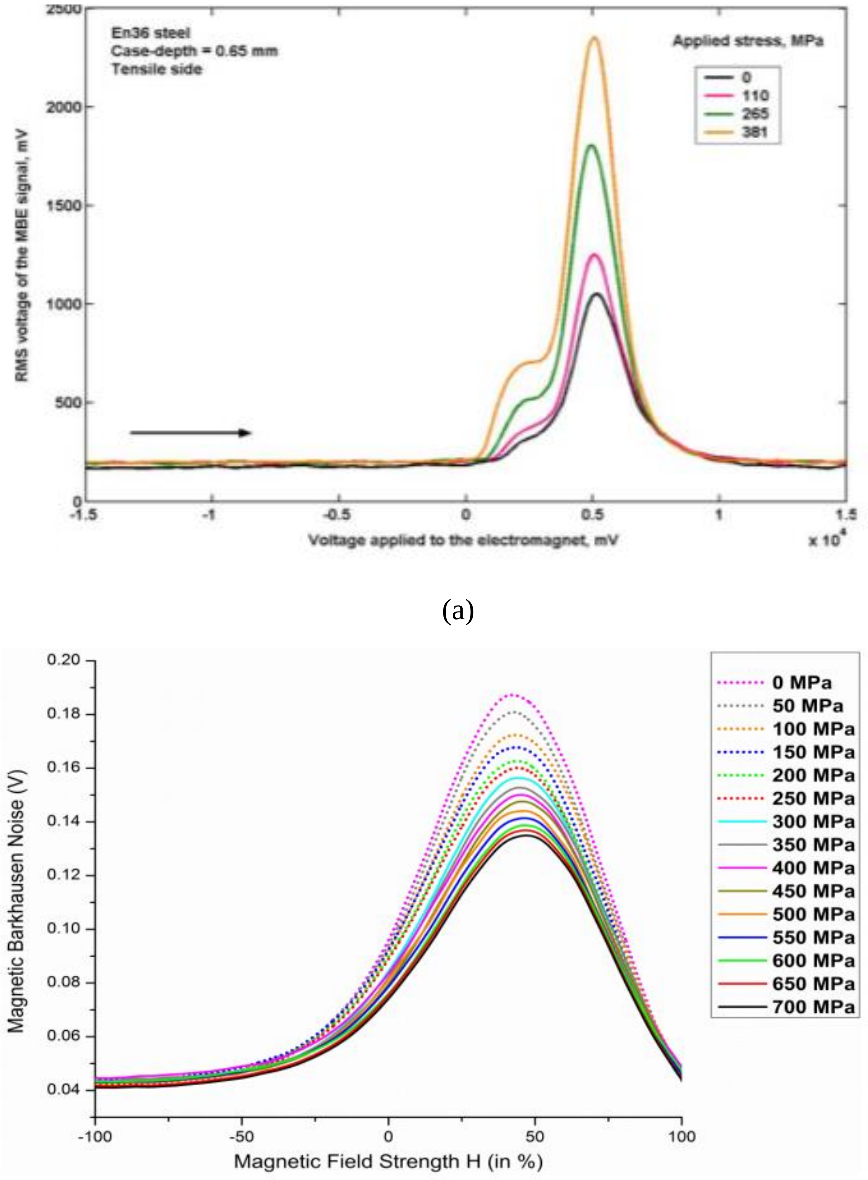

(a)

(b)

Figure 3.33. **(a)** The effect of tensile stress on Barkhausen noise in EN36 steel [135]. **(b)** Barkhausen noise signal envelopes obtained for TS2 sample under various applied tensile stresses [136].

The Barkhausen activity usually occurs near the coercive field H_c, where the differential susceptibility dM/dH arrives at its maximum value. If the rate of change of magnetic field dH/dt is fixed, the rate of change of magnetisation with time dM/dt reaches a maximum at the coercive point, resulting in the maximum Barkhausen jumps in a given interval. Generally, the maximum value of the $\mathrm{MBN_{rms}}$ envelope is proportional to the intense extent of Barkhausen jumps. Therefore, the trends of the peak values of $\mathrm{MBN_{rms}}$ are analogous to the maximum Barkhausen jumps. Lo *et al.* [137] incorporated the effect of applied stress into the differential irreversible susceptibility χ'_{irr} by altering the effective interdomain coupling parameter α_{eff} and the pinning coefficient k_{eff}. The differential irreversible susceptibility χ'_{irr} deduced from magnetomechanical hysteresis model was given as

$$\chi'_{irr} = \frac{M_{an}-M_{irr}}{\left(\frac{k_{eff}\delta}{\mu_0}\right)-\left[\alpha_{eff}+\left(\frac{3\sigma}{2\mu_0}\right)\cdot\left(\frac{\partial^2\lambda}{\partial M^2}\right)\right]\cdot(M_{an}-M_{irr})} \tag{3.30}$$

where M_{an} and M_{irr} were the anhysteretic and irreversible magnetisations, respectively. The k_{eff} was given as

$$k_{eff} = k_0 - n_0 \frac{\langle\frac{3}{2}\lambda_s\sigma\langle 1-cos^2\theta\rangle\rangle}{2m} \tag{3.31}$$

where k_0 was the pinning coefficient in the case of stress free, n_0 was the pinning sites density, θ was the angle between stress σ and the domain magnetisation, m was magnetic moment, and λ_s was the saturation magnetostriction. And α_{eff} was given as

$$\alpha_{eff} = \alpha + \frac{3b\sigma}{\mu_0} \tag{3.32}$$

where α was the mean field interdomain coupling parameter and b was the magnetostriction coefficient from the parabolic approximation of the measured magnetostriction curves.

The differential irreversible susceptibility χ'_{irr} was subsequently used to simulate the Barkhausen emission signal based on the stress-dependent hysteretic-stochastic process model of domain wall dynamics. The extended model rewritten in terms of rate of irreversible changes in magnetisation M_{irr} was governed by

$$\frac{d(\mu_0\dot{M_{irr}})}{dt} = \frac{1}{\sigma GS}\left(\frac{dH_a}{dt} - \frac{dH_p}{dt}\right) - \frac{\mu_0\dot{M_{irr}}}{\sigma GS\chi'_{irr}} \tag{3.33}$$

where dH_a/dt and dH_p/dt were the rate of change of applied field and the local pinning field, respectively. The stress dependence of the values of $\mathrm{MBN_{rms}}$ envelope (normalised with respect to the values at 0 MPa) together with the simulated ones were shown in Fig. 3.34a.

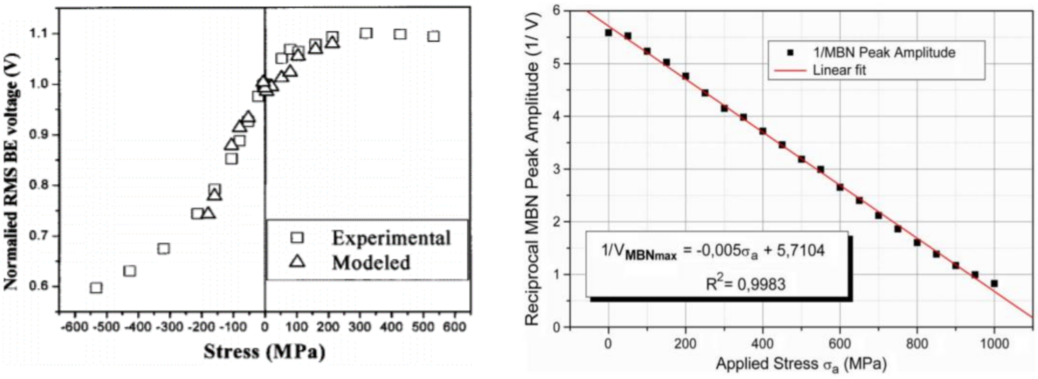

(a) (b)

Figure 3.34. **(a)** Comparison of measured and modelled $\mathrm{MBN_{rms}}$ (normalised) for AISI 410 stainless steel as a function of applied stress [137]. **(b)** Reciprocal of MBN peak amplitude for the Carburized SAE 9310 sample as a function of applied stress [138].

Mierczak *et al*. [129] proposed an alternative and much simpler method of stress evaluation using the reciprocal of the Barkhausen signal amplitude. It was known that in soft magnetic materials the maximum anhysteretic differential susceptibility χ'_{an} was approximately equal to the maximum differential susceptibility at the coercive point χ'_{H_c} [78,138,139]. The maximum differential susceptibility was proportional to the peak value of MBN signal. Therefore, the dependency of the reciprocal of Barkhausen peak amplitude on stress was given by

$$\frac{1}{MBN_{pk}(\sigma)} = \frac{1}{MBN_{pk}(0)} - \frac{3b'\sigma}{\mu_0} \tag{3.34}$$

where $MBN_{pk}(0)$ and $MBN_{pk}(\sigma)$ were the peak MBN voltage under stresses of zero and σ, and b' was an adjustable empirical model parameter with respect to the magnetostriction coefficient b and the parameters of ABBM model [140]. This relation had been verified experimentally as shown in Fig. 3.34b.

3.4.3 The effect of temperature on magnetic Barkhausen noise

It has discussed the thermal effect on hysteresis loop related to magnetic properties above. It has been known that the Barkhausen emission was originated from the magnetic properties of ferromagnetic material. Thus, the change of temperature would give rise to the alternation of MBN. It has been experimentally verified that the MBN_{rms} decreased with the increase in temperature [141-144]. Altpeter [141] observed that the MBN_{rms} amplitude of the compact cementite specimen disappeared at its Curie temperature. Wang *et al.* [142] and Guo *et al.* [143] found the decrease in the MBN_{rms} as the increasing temperature under free of applied stress for A3 and Q235 steels, respectively. Ding *et al.* [144] also experimentally showed the decrease in both longitudinal and transversal MBNrms as the increasing temperature plotted in Fig. 3.35a.

However, the temperature rarely independently affects the MBN signal. The environmental temperature may lead to a thermally induced stress where, for example, tens or even hundreds of MPa of stress values can be reached in a seamless track of high-speed railway [144,145]. Since the MBN is sensitive to stress [137-139], thermal stress could result in a noticeable MBN_{rms} change. Hence, it is necessary to understand and distinguish the mechanism of the effects caused by temperature and thermal stress and evaluate these effects on MBN quantitatively.

To the best knowledge, few attempts have been made to theoretically describe the combined effects of temperature and thermal stress on the MBN measurement. However, the process has been made in recent years. The most notable attempt to mathematically describe the Barkhausen emission was made by Alessandro, Beatrice, Bertotti and Montorsi (ABBM) [140], who proposed a model of the effect based on a stochastic process. The model was extended to the entire hysteresis loop by Jiles, Sipahi and Williams (JSW) [146], who assumed the Barkhausen activity in a given time interval was proportional to the rate of change of magnetisation. Subsequently, Jiles [147] modified the differential susceptibility dM/dH as dM_{irr}/dH to eliminate the influence of reversible magnetisation that rarely induces Barkhausen activity. Lo *et al.* [137] used an extended hysteretic stochastic model, introducing the magneto-mechanical effect, to simulate the influence of stress on Barkhausen emission. Mierczak *et al.* [138] found the linear dependency of the reciprocal peak amplitude of

MBN signal on stress and proposed a method for evaluating the effect of stress. Wang *et al.* [142] and Guo *et al.* [143] investigated the temperature effect of stress detection using MBN and proposed an analytical model base on the average volume of Barkhausen jump as shown in Fig. 3.35b and 3.35c.

(a)

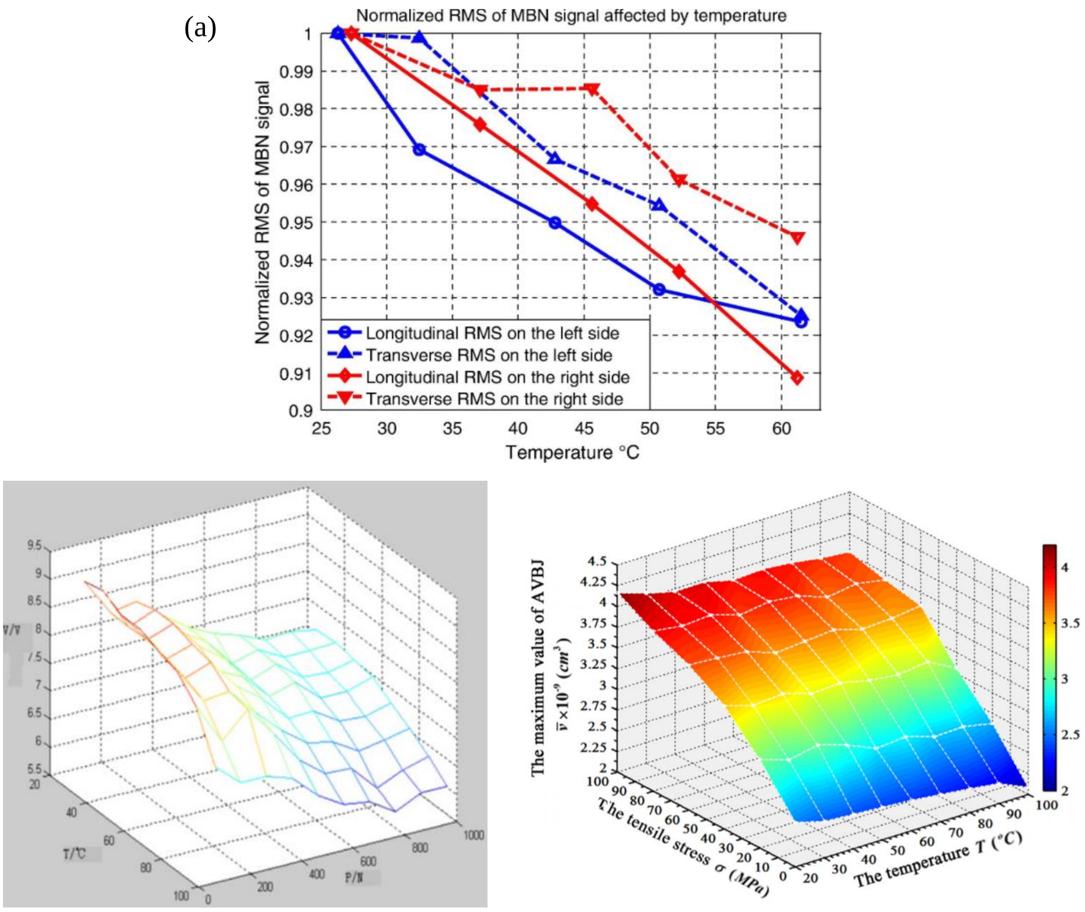

(b) (c)

Figure 3.35. **(a)** The thermal effect on MBNrms for rail [135]. The thermal effect on stress detection using MBN for **(b)** EN36 steel [142] and **(c)** Q235 steel [143].

To theoretically describe the relation between Barkhausen emission and temperature, the J-A hysteresis model that has exerted latent capacity to introduce the effects of stress [148] and temperature [93,94] is adopted. The methods to quantitatively evaluate the direct temperature effect and the combined effect of temperature and thermal stress on MBN will be presented in Chapter 6.

3.4.4 Commercially available system for micromagnetic measurement

There are several commercially available Barkhausen measurement systems that are being used to measure mechanical properties and material microstructures. The widely used systems are the micromagnetic multiparameter microstructure and stress analysis (3MA) system and Microscan 600 system.

3MA system previously based on magnetic Barkhausen noise and magnetic tangential field analysis has further integrated incremental permeability and eddy current impedance measurements [149,150]. By using an electromagnetic sensor step by step in a time-multiplexing mode, these NDE techniques are selected, and the different measurement quantities are measured and digitised. These techniques are sensitive to mechanical properties since the relevant microstructure governs the magnetic behaviours of material under mechanical change, such as tensile load and hardness [149,150]. However, the application of the multiple-parameter approach is not an easy task. Each magnetic parameter is associated with several mechanical properties such as hardness, tensile stress and yield stress. Therefore, the magnetic parameters need the calibration process where the material characteristics of interest are expressed in terms of polynomials of the measurement quantities. After decades of development, the unknown expansion coefficients in the model have been estimated by using calibration specimens with well-proven and destructively determined reference values [150]. Since the new materials emerge one after another, the calibration work will be continuous.

The Microscan 600 system supplied by Stresstech Ltd. is based on the Barkhausen effect to evaluate variation in stress and microstructure in a wide range of ferromagnetic materials as well as control surface quality and test near-surface defects [151]. It mainly includes the Barkhausen noise analyser (Rollscan series), which comprises the power supply and data acquisition card, and the Barkhausen sensor, which contains the magnetising and probing circuits. The analyser is a full-featured, self-contained unit but also can be connected to the PC via LAN port using the Ethernet cable. The sensor is coupled to the analyser via the LEMO multi-pin interface [136]. There are many sensors making Microscan 600 systems flexible such as the flat sensor for plate surface inspection.

During measurement, the sinusoidal voltage feeding in the primary coil generated a magnetic flux in the ferrite yoke, which was enclosed via ferrite pole pieces and the magnetised volume of the tested specimen underneath the sensor. The Barkhausen emissions from the magnetised section of the tested sample were detected in the form of voltage pulses induced in the pick-up coil wound on a ferrite probe. The output voltage from the pick-up coil is subsequently amplified with the low noise AD797 operational amplifier and digitised by data acquisition card with sampling frequency of 2.5 MHz. The digitised data are recorded in PC hard disk for post-processing, such as yielding the RMS value of MBN [119,136]. The system provides a wide range of magnetising frequencies from 1 Hz to 1000 Hz and the magnetising voltage from 0 Vpp (peak-to-peak voltage) to 16 Vpp. It also provides 10 kHz to 70 kHz band-pass filter and 70 kHz to 200 kHz filter [151]. In addition to the aforementioned features, the Microscan 600 system possesses good stability and resists electromagnetic interference [136]. Therefore, Microscan 600 system is used to detect Barkhausen emission in this thesis. Its schematic diagram will be depicted in chapter 6 and its applications for evaluation of the effects of temperature and anisotropy will be introduced in chapters 6 and 7, respectively.

3.5 Chapter Summary

This chapter has introduced the main NDE techniques, including non-magnetic and magnetic, to evaluate the integrity, microstructure, and mechanical properties of ferromagnetic material. The applications, advantages, and disadvantages of various NDE methods were discussed. Details of magnetic NDE techniques, especially MFL hysteresis loop and MBN, and the previous work on the investigations of the effects of stress, temperature and microstructure on these magnetic techniques were introduced.

3.6 References for Chapter 3

[1] Y. Zhu, G. Tian, R. Lu, and H. Zhang. A review of optical NDT technologies. *Sensors*, vol. 11, no. 8, pp. 7773–7798, 2011.

[2] D. Garcia-Sanchez, A. Fernandez-Navamuel, D. Z. Sánchez, D. Alvear, and D. Pardo. Bearing assessment tool for longitudinal bridge performance. *J. Civ. Struct. Heal. Monit.*, vol. 10, no. 5, pp. 1023–1036, 2020.

[3] T. Chan, L. Yu, H. Tam, Y. Ni, S. Liu, W. Chung and L. Cheng. Fiber Bragg grating sensors for structural health monitoring of Tsing Ma bridge: Background and experimental observation. *Eng. Struct.*, vol. 28, no. 5, pp. 648–659, 2006.

[4] A. K. Tay, D. A. Wilson, A. C. Demirdogen, J. R. Houghton, and R. L. Wood. Microdamage and optical signal analysis of impact-induced fracture in smart

structures. *Fiber Optic Smart Structures and Skins III*, vol. 1370, pp. 328–343, 1990.

[5] V. M. Murukeshan, P. Y. Chan, L. S. Ong, and A. Asundi. Effects of different parameters on the performance of a fiber polarimetric sensor for smart structure applications. *Sensors Actuators A Phys.*, vol. 80, no. 3, pp. 249–255, 2000.

[6] G. Thursby, B. Sorazu, F. Dong, D. C. Betz, and B. Culshaw. Damage detection in structural materials using a polarimetric fiber optic sensor. *Smart Structures and Materials 2003: Smart Sensor Technology and Measurement Systems*, vol. 5050, pp. 61–70, 2003.

[7] S. Sfarra, C. Ibarra-Castanedo, N.P. Avdelidis, M. Genest, L. Bouchagier, D. Kourousis, A. Tsimogiannis, A. Anastassopoulous, A. Bendada, X. Maldague, and D. Ambrosini. A comparative investigation for the nondestructive testing of honeycomb structures by holographic interferometry and infrared thermography. *Journal of Physics: Conference Series*, vol. 214, no. 1, pp. 012071 (1-4), 2010.

[8] J. Wilson, G. Tian, I. Mukriz, and D. Almond.PEC thermography for imaging multiple cracks from rolling contact fatigue. *NDT&E Int.*, vol. 44, no. 6, pp. 505–512, 2011.

[9] D. Palumbo, R. Tamborrino, U. Galietti, P. Aversa, A. Tatì, and V. A. M. Luprano. Ultrasonic analysis and lock-in thermography for debonding evaluation of composite adhesive joints. *NDT&E Int.*, vol. 78, pp. 1–9, 2016.

[10] S. M. Anouncia. Digital interferometry with image processing and computational techniques for NDT of composite materials. *Insight-Non-Destructive Test. Cond. Monit.*, vol. 60, no. 12, pp. 685–696, 2018.

[11] J. Yang, C. Favazza, R. Chen, J. Yao, X. Cai, K. Maslov, Q. Zhou, K. Shung and L. Wang. Simultaneous functional photoacoustic and ultrasonic endoscopy of internal organs in vivo. *Nat. Med.*, vol. 18, no. 8, pp. 1297–1302, 2012.

[12] W. M. Alobaidi, E. A. Alkuam, H. M. Al-Rizzo, and E. Sandgren. Applications of ultrasonic techniques in oil and gas pipeline industries: A review. *Am. J. Oper. Res.*, vol. 5, no. 04, pp. 274-287, 2015.

[13] B. Dutton, A. R. Clough, M. H. Rosli, and R. S. Edwards. Non-contact ultrasonic detection of angled surface defects. *NDT&E Int.*, vol. 44, no. 4, pp. 353–360, 2011.

[14] B. W. Drinkwater and P. D. Wilcox. Ultrasonic arrays for non-destructive evaluation: A review. *NDT&E Int.*, vol. 39, no. 7, pp. 525–541, 2006.

[15] J. A. Gallego-Juarez. Piezoelectric ceramics and ultrasonic transducers. *J. Phys. E.*, vol. 22, no. 10, pp. 804-816, 1989.

[16] J. Yang, X. Zhao, Y. Zhang, and Z. Cao. A new type of wheeled intelligent ultrasonic thickness measurement system. *2013 Symposium on Piezoelectricity,*

Acoustic Waves, and Device Applications, pp. 1–4, 2013.

[17] A. Lhémery, P. Calmon, I. Lecœur-Taıbi, R. Raillon, and L. Paradis. Modeling tools for ultrasonic inspection of welds. *NDT&E Int.*, vol. 33, no. 7, pp. 499–513, 2000.

[18] H. Lv, J. Jiao, B. Wu, and C. He. Evaluation of fatigue crack orientation using non-collinear shear wave mixing method. *J. Nondestruct. Eval.*, vol. 37, no. 4, pp. 1-16, 2018.

[19] H. Lv, J. Zhang, J. Jiao, and A. Croxford. Fatigue crack inspection and characterisation using non-collinear shear wave mixing. *Smart Mater. Struct.*, vol. 29, no. 5, pp. 055024 (1-14), 2020.

[20] Y. Xie, W. Yin, Z. Liu, and A. Peyton. Simulation of ultrasonic and EMAT arrays using FEM and FDTD. *Ultrasonics*, vol. 66, pp. 154–165, 2016.

[21] Y. Y. Kim and Y. E. Kwon. Review of magnetostrictive patch transducers and applications in ultrasonic nondestructive testing of waveguides. *Ultrasonics*, vol. 62, pp. 3–19, 2015.

[22] Z. Liu, Y. Hu, M. Xie, B. Wu, and C. He. Development of omnidirectional A0 mode EMAT employing a concentric permanent magnet pairs with opposite polarity for plate inspection. *NDT&E Int.*, vol. 94, pp. 13–21, 2018.

[23] J. K. Lee, H. W. Kim, and Y. Y. Kim. Omnidirectional Lamb waves by axisymmetrically-configured magnetostrictive patch transducer. *IEEE Trans. Ultrason. Ferroelectr. Freq. Control*, vol. 60, no. 9, pp. 1928–1934, 2013.

[24] X. Zhang, X. Liu, B. Wu, C. He, T. Uchimoto, and T. Takagi. An improved analytical model of the magnetostriction-based EMAT of SH0 mode guided wave in a ferromagnetic plate. *Ultrasonics*, vol. 108, pp. 106213 (1-7), 2020.

[25] P. W. Tse, X. Liu, Z. Liu, B. Wu, C. He, and X. Wang. An innovative design for using flexible printed coils for magnetostrictive-based longitudinal guided wave sensors in steel strand inspection. *Smart Mater. Struct.*, vol. 20, no. 5, pp. 055001 (1-12), 2011.

[26] Z. Liu, J. Fan, Y. Hu, C. He, and B. Wu. Torsional mode magnetostrictive patch transducer array employing a modified planar solenoid array coil for pipe inspection. *NDT&E Int.*, vol. 69, pp. 9–15, 2015.

[27] G. Wang and T. Liao. Automatic identification of different types of welding defects in radiographic images. *NDT&E Int.*, vol. 35, no. 8, pp. 519–528, 2002.

[28] C. Hayes. The ABC's of nondestructive weld examination. *Weld. J.*, vol. 76, no. 5, pp. 46–51, 1997.

[29] A. Gayer, A. Saya, and A. Shiloh. Automatic recognition of welding defects in real-time radiography. *NDT&E Int.*, vol. 23, no. 3, pp. 131–136, 1990.

[30] Y. Zou, D. Du, B. Chang, L. Ji, and J. Pan. Automatic weld defect detection method based on Kalman filtering for real-time radiographic inspection of

spiral pipe. *NDT&E Int.*, vol. 72, pp. 1–9, 2015.

[31] T. Liao and J. Ni. An automated radiographic NDT system for weld inspection: part I—weld extraction. *NDT&E Int.*, vol. 29, no. 3, pp. 157–162, 1996.

[32] J. Epp. X-ray diffraction (XRD) techniques for materials characterization. *Materials characterization using nondestructive evaluation (NDE) methods*, *Elsevier*, pp. 81–124, 2016.

[33] W. L. Bragg. The diffraction of short electromagnetic waves by a crystal. *Proc. Cambridge Phil. Soc.*, 1929.

[34] P. J. Withers and H. Bhadeshia. Residual stress. Part 1–measurement techniques. *Mater. Sci. Technol.*, vol. 17, no. 4, pp. 355–365, 2001.

[35] P. S. Prevéy. Current applications of X-ray diffraction residual stress measurement. *Dev. Mater. Charact. Technol.*, pp. 103–110, 1996.

[36] V. Hauk. Structural and residual stress analysis by nondestructive methods: Evaluation-Application-Assessment. *Amsterdam*, *Elsevier*, 1997.

[37] A. Sophian, G. Tian, D. Taylor, and J. Rudlin. Electromagnetic and eddy current NDT: a review. *Insight*, vol. 43, no. 5, pp. 302–306, 2001.

[38] F. Thollon and N. Burais. Geometrical optimization of sensors for eddy currents nondestructive testing and evaluation. *IEEE Trans. Magn.*, vol. 31, no. 3, pp. 2026–2031, 1995.

[39] I. Zainal Abidin. Modelling and experimental investigation of eddy current distribution for angular defect characterisation. *Doctoral dissertation*, *Newcastle University*, 2011.

[40] Z. Liu, K. Tsukada, and K. Hanasaki. One-dimensional eddy current multi-frequency data fusion: A multi-resolution analysis approach. *Insight* (*Northampton*), vol. 40, no. 4, pp. 286–289, 1998.

[41] C. Glorieux, J. Moulder, J. Basart, and J. Thoen. The determination of electrical conductivity profiles using neural network inversion of multi-frequency eddy-current data. *J. Phys. D. Appl. Phys.*, vol. 32, no. 5, pp. 616-622, 1999.

[42] B. P. C. Rao, B. Raj, T. Jayakumar, and P. Kalyanasundaram. An artificial neural network for eddy current testing of austenitic stainless steel welds. *NDT&E Int.*, vol. 35, no. 6, pp. 393–398, 2002.

[43] S. Ghanei, M. Kashefi, and M. Mazinani. Comparative study of eddy current and Barkhausen noise nondestructive testing methods in microstructural examination of ferrite-martensite dual-phase steel. *J. Magn. Magn. Mater.*, vol. 356, pp. 103–110, 2014.

[44] T. Clauzon, F. Thollon, and A. Nicolas. Flaws characterization with pulsed eddy currents NDT. *IEEE Trans. Magn.*, vol. 35, no. 3, pp. 1873–1876, 1999.

[45] A. Sophian, G. Tian, D. Taylor, and J. Rudlin. A feature extraction technique based on principal component analysis for pulsed Eddy current NDT. *NDT &E*

Int., vol. 36, no. 1, pp. 37–41, 2003.

[46] M. Kashefi, A. Rafsanjani, S. Kahrobaee, and M. Alaee. Magnetic nondestructive technology for detection of tempered martensite embrittlement. *J. Magn. Magn. Mater.*, vol. 324, no. 23, pp. 4090–4093, 2012.

[47] F. Meng, X. Liu, H. Wang, C. He, and B. Wu. Characterization of elastic and plastic behaviors in steel plate based on eddy current technique using a portable impedance analyzer. *J. Sensors*, vol. 2017, pp. 1-12, 2017.

[48] N. N. Zatsepin. Calculation of the magnetic field of surface defects. I. Field topography of defect models. *Sov, J. NDT*, vol. 2, pp. 50–59, 1966.

[49] C. Edwards and S. B. Palmer. The magnetic leakage field of surface-breaking cracks. *J. Phys. D. Appl. Phys.*, vol. 19, no. 4, pp. 657-673, 1986.

[50] M. Abe, S. Biwa, and E. Matsumoto. Three dimensional evaluation of parallelepiped flaw using amorphous MI sensor and neural network in biaxial MFLT. *2008 3rd International Conference on Sensing Technology*, pp. 238–241, 2008.

[51] X. Liu, Y. Wang, B. Wu, Z. Gao, and C. He. Design of tunnel magnetoresistive-based circular MFL sensor array for the detection of flaws in steel wire rope. *J. Sensors*, vol. 2016, pp. 1-8, 2016.

[52] C. Jomdecha and A. Prateepasen. Design of modified electromagnetic main-flux for steel wire rope inspection. *NDT&E Int.*, vol. 42, no. 1, pp. 77–83, 2009.

[53] S. M. Dutta, F. H. Ghorbel, and R. K. Stanley. Simulation and analysis of 3-D magnetic flux leakage. *IEEE Trans. Magn.*, vol. 45, no. 4, pp. 1966–1972, 2009.

[54] S. M. Dutta, F. H. Ghorbel, and R. K. Stanley. Dipole modeling of magnetic flux leakage. *IEEE Trans. Magn.*, vol. 45, no. 4, pp. 1959–1965, 2009.

[55] J. A. Osborn. Demagnetising factors of the general ellipsoid. *Phys. Rev.*, vol. 67, no. 11–12, pp. 351-357, 1945.

[56] F. I. Al-Naemi, J. P. Hall, and A. J. Moses.FEM modelling techniques of magnetic flux leakage-type NDT for ferromagnetic plate inspections. *J. Magn. Magn. Mater.*, vol. 304, no. 2, pp. 790–793, 2006.

[57] B. Wu, Y. Wang, X. Liu, and C. He. A novel TMR-based MFL sensor for steel wire rope inspection using the orthogonal test method. *Smart Mater. Struct.*, vol. 24, no. 7, pp. 075007 (1-12), 2015.

[58] Y. Sun and Y. Kang. A new MFL principle and method based on near-zero background magnetic field. *NDT&E Int.*, vol. 43, no. 4, pp. 348–353, 2010.

[59] Z. Du, J. Ruan, Y. Peng, S. Yu, Y. Zhang, Y. Gan, and T. Li. 3-D FEM simulation of velocity effects on magnetic flux leakage testing signals. *IEEE Trans. Magn.*, vol. 44, no. 6, pp. 1642–1645, 2008.

[60] J. Aguila-Munoz, J. H. Espina-Hernandez, J. A. Perez-Benitez, F. Caleyo, and J. M. Hallen. Crack detection in steel using a GMR-based MFL probe with

radial magnetisation. *23rd Int. Conf. Electron. Commun. Comput. CONIELECOMP 2013*, pp. 104–108, 2013.

[61] C. K. Okolo and T. Meydan. Pulsed magnetic flux leakage method for hairline crack detection and characterization. *AIP Adv.*, vol. 8, no. 4, p. 047207 (1-12), 2018.

[62] M. Pelkner, M. Blome, V. Reimund, H. M. Thomas, and M. Kreutzbruck. Flux leakage measurements for defect characterization using a high precision 3-axial GMR magnetic sensor. *AIP Conf. Proc.*, vol. 1335, pp. 380–387, 2011.

[63] P. P. Freitas, R. Ferreira, S. Cardoso, and F. Cardoso. Magnetoresistive sensors. *J. Phys. Condens. Matter*, vol. 19, no. 16, pp. 165221 (1-21), 2007.

[64] Z. Huang, P. Que, and L. Chen. 3D FEM analysis in magnetic flux leakage method. *NDT&E Int.*, vol. 39, no. 1, pp. 61–66, 2006.

[65] Z. Deng, Y. Sun, Y. Kang, K. Song, and R. Wang. A permeability-measuring magnetic flux leakage method for inner surface crack in thick-walled steel pipe. *J. Nondestruct. Eval.*, vol. 36, no. 4, pp. 1-14, 2017.

[66] V. Babbar, B. Shiari, and L. Clapham. Mechanical damage detection with magnetic flux leakage tools: modeling the effect of localized residual stresses. *IEEE Trans. Magn.*, vol. 40, no. 1, pp. 43–49, 2004.

[67] D. L. Atherton and M. G. Daly. Finite element calculation of magnetic flux leakage detector signals. *NDT&E Int.*, vol. 20, no. 4, pp. 235–238, 1987.

[68] R. Langman. The effect of stress on the magnetisation of mild steel at moderate field strengths. *IEEE Trans. Magn.*, vol. 21, no. 4, pp. 1314–1320, 1985.

[69] K. Mandal, D. Dufour, T. W. Krause, and D. L. Atherton. Investigations of magnetic flux leakage and magnetic Barkhausen noise signals from pipeline steel. *J. Phys. D. Appl. Phys.*, vol. 30, no. 6, pp. 962-973, 1997.

[70] K. Mandal and D. L. Atherton. A study of magnetic flux-leakage signals. *J. Phys. D. Appl. Phys.*, vol. 31, no. 22, pp. 3211-3217, 1998.

[71] Y. Wang, X. Liu, B. Wu, J. Xiao, D. Wu, and C. He. Dipole modeling of stress-dependent magnetic flux leakage. *NDT&E Int.*, vol. 95, pp. 1–8, 2018.

[72] J. H. Hwang and W. Lord. Finite element modeling of magnetic field/defect interactions. *J. Test. Eval.*, vol. 3, no. 1, pp. 21–25, 1975.

[73] E. Altschuler and A. Pignotti. Nonlinear model of flaw detection in steel pipes by magnetic flux leakage. *NDT&E Int.*, vol. 28, no. 1, pp. 35–40, 1995.

[74] P.A. Ivanov, V. Zhang, C.H. Yeoh, H. Udpa, Y. Sun, S.S. Udpa and W. Lord. Magnetic flux leakage modeling for mechanical damage in transmission pipelines. *IEEE Trans. Magn.*, vol. 34, no. 5, pp. 3020–3023, 1998.

[75] L. Zhong, L. Li, and X. Chen. Simulation of magnetic field abnormalities caused by stress concentrations. *IEEE Trans. Magn.*, vol. 49, no. 3, pp. 1128–1134, 2012.

[76] A. Raghunathan, Y. Melikhov, J. E. Snyder, and D. C. Jiles. Modeling of two-phase magnetic materials based on JilesAtherton theory of hysteresis. *J. Magn. Magn. Mater.*, vol. 324, no. 1, pp. 20–22, 2012.

[77] N. P. Gaunkar, O. Kypris, I. C. Nlebedim, and D. C. Jiles. Analysis of Barkhausen noise emissions and magnetic hysteresis in multi-phase magnetic materials. *IEEE Trans. Magn.*, vol. 50, no. 11, pp, 1-4, 2014.

[78] D. C. Jiles. Introduction to magnetism and magnetic materials. *CRC press*, 2015.

[79] W. Xie, E. Polikarpov, J.P. Choi, M. E. Bowden, K. Sun, and J. Cui. Effect of ball milling and heat treatment process on MnBi powders magnetic properties. *J. Alloys Compd.*, vol. 680, pp. 1–5, 2016.

[80] J. Y. Law, J. Rial, M. Villanueva, N. López, J. Camarero, L.G. Marshall, J.S. Blázquez, J.M. Borrego, V. Franco, A. Conde and L.H. Lewis. Study of phases evolution in high-coercive MnAl powders obtained through short milling time of gas-atomized particles. *J. Alloys Compd.*, vol. 712, pp. 373–378, 2017.

[81] H. Nakamura, K. Hirota, M. Shimao, T. Minowa, and M. Honshima. Magnetic properties of extremely small Nd-Fe-B sintered magnets. *IEEE Trans. Magn.*, vol. 41, no. 10, pp. 3844–3846, 2005.

[82] L. Batista, U. Rabe, I. Altpeter, S. Hirsekorn, and G. Dobmann. On the mechanism of nondestructive evaluation of cementite content in steels using a combination of magnetic Barkhausen noise and magnetic force microscopy techniques. *J. Magn. Magn. Mater.*, vol. 354, pp. 248–256, 2014.

[83] D. C. Jiles. Magnetic properties and microstructure of AISI 1000 series carbon steels. *J. Phys. D. Appl. Phys.*, vol. 21, no. 7, pp. 1186–1195, 1988.

[84] H. Kwun and G. L. Burkhardt. Effects of grain size, hardness, and stress on the magnetic hysteresis loops of ferromagnetic steels. *J. Appl. Phys.*, vol. 61, no. 4, pp. 1576–1579, 1987.

[85] D. C. Jiles and D. L. Atherton. Theory of the magnetisation process in ferromagnets and its application to the magnetomechanical effect. *J. Phys. D. Appl. Phys.*, vol. 17, no. 6, pp. 1265-1281, 1984.

[86] D. C. Jiles and D. L. Atherton. Theory of ferromagnetic hysteresis. *J. Magn. Magn. Mater.*, vol. 61, no. 1–2, pp. 48–60, 1986.

[87] B. Szpunar and J. Szpunar. Influence of stresses on the hysteresis curve in constructional steel. *IEEE Trans. Magn.*, vol. 20, no. 5, pp. 1882–1884, 1984.

[88] M. J. Sablik, H. Kwun, G. L. Burkhardt, and D. C. Jiles. Model for the effect of tensile and compressive stress on ferromagnetic hysteresis. *J. Appl. Phys.*, vol. 61, no. 8, pp. 3799–3801, 1987.

[89] P. Garikepati, T. Chang, and D. C. Jiles. Theory of ferromagnetic hysteresis: Evaluation of stress from hysteresis curves. *IEEE Trans. Magn.*, vol. 24, no. 6,

pp. 2922–2924, 1988.

[90] D. C. Jiles and M. K. Devine. The law of approach as a means of modelling the magnetomechanical effect. *J. Magn. Magn. Mater.*, vol. 140–144, no. PART 3, pp. 1881–1882, 1995.

[91] L. Vandenbossche. Magnetic Hysteretic Characterization of Ferromagnetic Materials with Objectives towards Non-Destructive Evaluation of Material Degradation. *Doctoral dissertation*, *Ghent University*, 2009.

[92] J. M. Makar and B. K. Tanner. The in situ measurement of the effect of plastic deformation on the magnetic properties of steel: Part I–Hysteresis loops and magnetostriction. *J. Magn. Magn. Mater.*, vol. 184, no. 2, pp. 193–208, 1998.

[93] A. Raghunathan, Y. Melikhov, J. E. Snyder, and D. C. Jiles. Modeling the temperature dependence of hysteresis based on Jiles-Atherton theory. *IEEE Trans. Magn.*, vol. 45, no. 10, pp. 3954–3957, 2009.

[94] A. Raghunathan, Y. Melikhov, J. E. Snyder, and D. C. Jiles. Theoretical model of temperature dependence of hysteresis based on mean field theory. *IEEE Trans. Magn.*, vol. 46, no. 6, pp. 1507–1510, 2010.

[95] D. C. Jiles, J. B. Thoelke, and M. K. Devine. Numerical determination of hysteresis parameters for the modeling of magnetic properties using the theory of ferromagnetic hysteresis. *IEEE Trans. Magn.*, vol. 28, no. 1, pp. 27–35, 1992.

[96] C. Li, Z. Tang, G. Lin, S. Lin, and Q. Huang. Modeling the temperature dependence of minor hysteresis loops in ferromagnetic materials. *Proc. 2016 IEEE Int. Conf. Electron. Inf. Commun. Technol. ICEICT 2016*, pp. 505–508, 2016.

[97] J. Wilson, L. Zhou, C. Davis and A.J. Peyton. High temperature magnetic characterisation of structural steels using Epstein frame. *Measurement Science and Technology*, vol. 32, pp. 125601 (1-9), 2021.

[98] N. Takahashi, M. Morishita, D. Miyagi and M. Nakano. Examination of magnetic properties of magnetic materials at high temperature using a ring specimen. IEEE *Trans. Magn.*, vol.46, no. 2, pp.548-551, 2010.

[99] L. Zhou, R. Hall, and C. Davis. Measured and modelled low field relative permeability for dual phase steels at high temperature. *J. Magn. Magn. Mater.*, vol. 475, pp.38-43, 2019.

[100] S. Kahrobaee, and M. Kashefi. Assessment of retained austenite in AISI D2 tool steel using magnetic hysteresis and Barkhausen noise parameters. *Journal of Materials Engineering and Performance*, vol.24, no. 3, pp.1192-1198, 2015.

[101] IMPOC brochure. Available online: https://www.emg-automation.com /fileadmin/content/automation/qualitaetssichernde_systeme/dokumente/IMPOC_brochure_EN_Rev00_01-2018.pdf (accessed on 22 September 2021).

[102] W. Jacobs. Quantification of Microstructure During the Phase Transformation of Dynamically Cooled Steels Using the EMspec® Sensor. Doctoral dissertation, *University of Warwick*, 2020.

[103] A. Peyton, N. Karimian, J. Wilson, M. Stolzenberg, R. Schmidt, C. Davis, P. Lombard, P. Meilland, A. Martinez-de-Guerenu and K. Gurruchaga. The application of electromagnetic measurements for the assessment of skin passed steel samples, *19th World Conference on Non-Destructive Testing*, 2016.

[104] J. Shen, L. Zhou, W. Jacobs, P. Hunt and C. Davis. Real-time in-line steel microstructure control through magnetic properties using an EM sensor. *J. Magn. Magn. Mater.*, vol. 490, p.165504 (1-8), 2019.

[105] H. Yang, F. Van Den Berg, C. Bos, A. Luinenburg, J. Mosk, P. Hunt, M. Dolby, J. Hinton, A. Peyton and C. Davis. EM sensor array system and performance evaluation for in-line measurement of phase transformation in steel. *Insight-Non-Destructive Testing and Condition Monitoring*, vol. 61, no. 3, pp.153-157, 2019.

[106] L. Landau and E. Lifshitz. On the theory of the dispersion of magnetic permeability in ferromagnetic bodies. *Perspectives in Theoretical Physics, Elsevier*, pp. 51–65, 1992.

[107] W. F. Brown. Micromagnetics. *Interscience publishers*, no. 18, 1963.

[108] C. Abert. Micromagnetics and spintronics: models and numerical methods. *Eur. Phys. J. B*, vol. 92, no. 6, pp. 1-45, 2019.

[109] M. Guyot and V. Cagan. The magneto-acoustic emission. *J. Appl. Phys.*, vol. 73, no. 10, pp. 5348–5353, 1993.

[110] A. Stupakov, R. Farda, M. Neslušan, A. Perevertov, and T. Uchimoto. Evaluation of a Nitrided Case Depth by the Magnetic Barkhausen Noise. *J. Nondestruct. Eval.*, vol. 36, no. 4, pp. 1–9, 2017.

[111] E. S. Gorkunov, Y. N. Dragoshanskii, and V. A. Khamitov. Magnetoelastic acoustic emission in ferromagnetic materials. II. Effect of elastic and plastic strains on parameters of magnetoelastic acoustic emission. *Russ. J. Nondestruct. Test.*, vol. 37, no. 12, pp. 835–858, 2001.

[112] X. Liu, R. Zhang, B. Wu, and C. He. Quantitative prediction of surface hardness in 12CrMoV steel plate based on magnetic Barkhausen noise and tangential magnetic field measurements. *J. Nondestruct. Eval.*, vol. 37, no. 2, pp. 1-8, 2018.

[113] J. Capó-Sánchez, J. Pérez-Benitez, and L. R. Padovese. Analysis of the stress dependent magnetic easy axis in ASTM 36 steel by the magnetic Barkhausen noise. *NDT&E Int.*, vol. 40, no. 2, pp. 168–172, 2007.

[114] M. Maciusowicz and G. Psuj. Time-Frequency Analysis of Barkhausen Noise for the Needs of Anisotropy Evaluation of Grain-Oriented Steels. *Sensors*, vol.

20, no. 3, pp. 768 (1-16), 2020.

[115] V. Moorthy. Important factors influencing the magnetic Barkhausen noise profile. *IEEE Trans. Magn.*, vol. 52, no. 4, pp. 1–13, 2015.

[116] S. Santa-aho, A. Laitinen, A. Sorsa, and M. Vippola. Barkhausen Noise Probes and Modelling: A Review. *J. Nondestruct. Eval.*, vol. 38, no. 4, pp. 1–11, 2019.

[117] S. White, T. Krause, and L. Clapham. Control of flux in magnetic circuits for Barkhausen noise measurements. *Meas. Sci. Technol.*, vol. 18, no. 11, pp. 3501-3510, 2007.

[118] S. Tumanski. Induction coil sensors - A review. *Meas. Sci. Technol.*, vol. 18, no. 3, pp. R31-R37, 2007.

[119] Y. He, M. Mehdi, E. J. Hilinski, and A. Edrisy. Through-process characterization of local anisotropy of Non-oriented electrical steel using magnetic Barkhausen noise. *J. Magn. Magn. Mater.*, vol. 453, pp. 149–162, 2018.

[120] M. Vashista and V. Moorthy. Influence of applied magnetic field strength and frequency response of pick-up coil on the magnetic Barkhausen noise profile. *J. Magn. Magn. Mater.*, vol. 345, pp. 208–214, 2013.

[121] A. Stupakov. Dynamic normalization of the Barkhausen noise signal. *J. Magn. Magn. Mater.*, vol. 482, pp. 135–147, 2019.

[122] V. Moorthy, S. Vaidyanathan, T. Jayakumar, and B. Raj. On the influence of tempered microstructures on magnetic Barkhausen emission in ferritic steels. *Philos. Mag. A*, vol. 77, no. 6, pp. 1499–1514, 1998.

[123] J. A. Pérez-Benítez, J. H. Espina-Hernández, P. Martínez-Ortiz, A. F. Chávez-González, and J. M. De La Rosa. Analysis of the influence of some magnetising parameters on magnetic Barkhausen noise using a microscopic model. *J. Magn. Magn. Mater.*, vol. 347, pp. 51–60, 2013.

[124] S. E. Zirka, Y. I. Moroz, R. G. Harrison, and K. Chwastek. On physical aspects of the Jiles-Atherton hysteresis models. *J. Appl. Phys.*, vol. 112, no. 4, pp. 043916 (1-7), 2012.

[125] M. F. De Campos, M. A. Campos, F. J. G. Landgraf, and L. R. Padovese. Anisotropy study of grain oriented steels with Magnetic Barkhausen Noise. *Journal of Physics: Conference Series*, vol. 303, no. 1, pp. 012020 (1-6), 2011.

[126] B. D. Cullity and C. D. Graham. Introduction to magnetic materials. *John Wiley & Sons*, 2011.

[127] A. J. Moses. Electrical steels: past, present and future developments. *IEE Proc. A* (*Physical Sci. Meas. Instrumentation, Manag. Educ.*), vol. 137, no. 5, pp. 233–245, 1990.

[128] J. V Leite, N. Sadowski, P. Kuo-Peng, N. J. Batistela, J. P. A. Bastos, and A. A. De Espindola. Inverse Jiles-Atherton vector hysteresis model. *IEEE Trans.*

Magn., vol. 40, no. 4, pp. 1769–1775, 2004.

[129] B. Upadhaya, L. Perkkiö, P. Rasilo, A. Belahcen, P. Handgruber, and A. Arkkio. Representation of anisotropic magnetic characteristic observed in a non-oriented silicon steel sheet. *AIP Adv.*, vol. 10, no. 6, pp. 065222 (1-10), 2020.

[130] H. Okamoto. The C-Fe (carbon-iron) system. *J. Phase Equilibria*, vol. 13, no. 5, pp. 543–565, 1992.

[131] A. A. Samimi, T. W. Krause, and L. Clapham. Multi-parameter Evaluation of Magnetic Barkhausen Noise in Carbon Steel. *J. Nondestruct. Eval.*, vol. 35, no. 3, pp. 1–8, 2016.

[132] S. Zhang, X. Shi, L. Udpa, and Y. Deng. Micromagnetic measurement for characterization of ferromagnetic materials' microstructural properties. *AIP Adv.*, vol. 8, no. 5, pp. 056614 (1-7), 2018.

[133] S. Tiitto. On the mechanism of magnetisation transitions in steel. *IEEE Trans. Magn.*, vol. 14, no. 5, pp. 527–529, 1978.

[134] R. W. Leep. The Barkhausen effect and its application in nondestructive testing. *Proceedings of the Symposium on Physics and Nondestructive Testing*, 1968.

[135] V. Moorthy, B. A. Shaw, and S. Day. Evaluation of applied and residual stresses in case-carburised En36 steel subjected to bending using the magnetic Barkhausen emission technique. *Acta Mater.*, vol. 52, no. 7, pp. 1927–1936, 2004.

[136] L. Mierczak. Evaluation of structural integrity of steel components by non-destructive magnetic methods. *Doctoral dissertation*, *Cardiff University*, 2015.

[137] C. C. H. Lo, S. J. Lee, L. Li, L. C. Kerdus, and D. C. Jiles. Modeling stress effects on magnetic hysteresis and Barkhausen emission using a hysteretic-stochastic model. *IEEE Trans. Magn.*, vol. 38, no. 5, pp. 2418–2420, 2002.

[138] L. Mierczak, D. C. Jiles, and G. Fantoni. A new method for evaluation of mechanical stress using the reciprocal amplitude of magnetic Barkhausen noise. *IEEE Trans. Magn.*, vol. 47, no. 2, pp. 459–465, 2010.

[139] D. C. Jiles. The effect of stress on magnetic Barkhausen activity in ferromagnetic steels. *IEEE Trans. Magn.*, vol. 25, no. 5, pp. 3455–3457, 1989.

[140] B. Alessandro, C. Beatrice, G. Bertotti, and A. Montorsi. Domain-wall dynamics and Barkhausen effect in metallic ferromagnetic materials. I. Theory. *J. Appl. Phys.*, vol. 68, no. 6, pp. 2901–2907, 1990.

[141] I. Altpeter. Nondestructive evaluation of cementite content in steel and white cast iron using inductive Barkhausen noise. *J. Nondestruct. Eval.*, vol. 15, no. 2, pp. 45–60, 1996.

[142] P. Wang, X. Ji, X. Yan, L. Zhu, H. Wang, G. Tian and E. Yao. Investigation of temperature effect of stress detection based on Barkhausen noise. *Sensors*

Actuators A Phys., vol. 194, pp. 232–239, 2013.

[143] L. Guo, D. Shu, L. Yin, J. Chen, and X. Qi. The effect of temperature on the average volume of Barkhausen jump on Q235 carbon steel. *J. Magn. Magn. Mater.*, vol. 407, pp. 262–265, 2016.

[144] S. Ding, P. Wang, Y. Lin, and D. Zhu. Reduction of thermal effect on rail stress measurement based on magnetic Barkhausen noise anisotropy. *Measurement*, vol. 125, pp. 92–98, 2018.

[145] V. Damljanović and R. L. Weaver. Laser vibrometry technique for measurement of contained stress in railroad rail. *J. Sound Vib.*, vol. 282, no. 1–2, pp. 341–366, 2005.

[146] D. C. Jiles, L. B. Sipahi, and G. Williams. Modeling of micromagnetic Barkhausen activity using a stochastic process extension to the theory of hysteresis. *J. Appl. Phys.*, vol. 73, no. 10, pp. 5830–5832, 1993.

[147] D. C. Jiles. Dynamics of domain magnetisation and the Barkhausen effect. *Czechoslov. J. Phys.*, vol. 50, no. 8, pp. 893–924, 2000.

[148] D. C. Jiles. Theory of the magnetomechanical effect. J. Phys. D. Appl. Phys., vol. 28, no. 8, pp. 1537-1546, 1995.

[149] G. Dobmann, I. Altpeter, R. Becker, M. Lang, R. Kern, A. Yashan and W. Theiner. Electromagnetic and micro-magnetic non-destructive characterization (NDC) for material mechanical property determination and prediction in steel industry and in lifetime extension strategies of NPP steel components. *International Journal of Applied Electromagnetics and Mechanics*, vol. 15, no. 1-4, pp.269-274, 2002.

[150] G. Dobmann, I. Altpeter, B. Wolter and Kern, R. Industrial applications of 3MA–micromagnetic multiparameter microstructure and stress analysis. *Electromagn. Nondestr. Eval. (XI)*, vol. 31, pp.18-25, 2008.

[151] Barkhausen Noise Signal Analysers. https://www.stresstech.com/products /barkhausen-noise-equipment/barkhausen-noise-signal-analyzers/ (accessed on 22 September 2021)

Chapter 4

Evaluation of the Effect of Stress on Magnetic Flux Leakage

Evaluation of the effect of stress on magnetic flux leakage (MFL) signals caused by a defect is a complicated task due to the nonlinear coupling of magnetics and mechanics. In this chapter, an analytical model to facilitate the evaluation is introduced, and a finite element model to solve more complex defects is proposed. The analytical model extends the dipole model for a tensioned sample with a cylindrical through-hole defect by considering the stress concentration, which leads to the heterogeneous distribution of magnetisation along the defect surface. Classic Timoshenko's theory is used to solve the localized compressive stress and tensile stress around the defect. The J-A model is employed to determine the stress-dependent magnetisation distribution. In comparison, the finite element model uses solid mechanics and magnetic modules to simulate the stress-induced magnetisation distribution in a dog-bone like rod with a cylindrical square-notch defect. MFL signal induced by the defect along the sensor scanning line is extracted from the converged solution. The analytical and numerical models are verified by experiments on a tension plate with cylindrical through-hole and a tension rod with cylindrical square-notch, respectively. The measured peak-to-peak normalised amplitudes are consistent with the results predicted by both models. In the analytical model, the peak-to-peak amplitude of the normalised MFL signal demonstrates the parabolic dependency on the applied tensile stress. In the finite element model, both the simulated and measured results show a similar linear dependency of the peak-to-peak amplitudes of the normalised MFL signals on the applied stress.

4.1 Introduction

The magnetic flux leakage (MFL) method is commonly used to nondestructively evaluate the damage in ferromagnetic materials due to its reliability, high efficiency, and cost-saving. In MFL applications, specimens are magnetised, and magnetic flux leaks due to sudden changes in magnetic permeability of the materials near geometric discontinuities. The leakage flux is detected by an MFL sensor, and the detected signal is then used for the inverse problem of assessment of the sizes of defects. The inverse problem has, however, many challenges. For example, stress, which is a common condition, affects the MFL signal considerably as discussed in Chapter 3. In this case, if applied hastily, the inverse problem will lead to a significant error in defect sizing.

Mandal *et al.* [1,2] have experimentally shown that circumferential hoop stress generated by in-service pipelines could decrease the amplitude of MFL signals by more than 40%. Wang *et al.* [3] found that tensile stress of 100MPa applying on a dog-bone specimen with a cylindrical through-hole could cause an increase of 24% in peak-to-peak amplitude of MFL signal. Therefore, to accurately evaluate the sizes of defects, it is necessary to consider the effects of stress on the MFL signals.

To accurately evaluate the effect of the stress on MFL signal, a few researchers have made attempts to fit analytical outcomes to experimental results mathematically. Mandal *et al.* [2] used analytical models of Zatsepin-Shcherbinin (Z-S model) [4] and Edwards-Palmer [5] to fit experimental data under different stresses by altering the densities of magnetic charges. However, the values of magnetic charge densities were changed deliberately rather than varied as a function of stress. Hence, this method might not be appropriate to size defects quantitatively under stress. Inspired by the Z-S model, several dipole models [6-8] were proposed to predict the MFL signal induced by defect considering the nonlinear magnetic behaviours of ferromagnetic material. Furthermore, Wang *et al.* [3] proposed the improved dipole model by introducing the magnetomechanical Jiles-Atherton (J-A) model into the traditional dipole model. The improved dipole model will be introduced in the following section. The model could accurately predict the effect of stress on MFL signal induced by the regularly geometric defect.

However, for a defect with a complex geometry that a fully analytical description of the stress concentration around the defect is virtually impossible as well as the calculation of its demagnetising factor, the analytical model will no longer be applicable. Besides, the analytical model only considered the stress distribution along the surface of the defect rather than the whole stress concentration area. There might be interactions between regions near the defect. In addition, even small stress applied to a defect with a regular and simple geometry may transform the defect into one with a (much) more complex geometry due to deformation.

Compared with mathematical models, the finite element method (FEM) can compete with analytical methods due to its flexibility in simulation and reveal the overall perspective of stress-dependent magnetisation. The pioneering finite element modelling of the MFL field by Hwang and Lord [9] paved the way to the numerical analysis of defect-induced MFL signal. Subsequently, significant progress has been made in this area by considering non-linear material properties [10] and coupling with stress [11] due to the improvements in computational capabilities. Ivanov *et al.* [11] incorporated stress distribution into the magnetic FEM model varying the permeability in the region under stress. Babbar *et al.* [12] introduced stress information into the magnetic FEM model by adjusting the permeability variable. In these studies, adjustments of simulation results aimed to fit the measured were performed by changing one or more magnetic properties [10-13], which may not correspond to reality. FEM of stress-induced MFL is far more difficult since stress varies a number of magnetic properties of ferromagnetic material, including magnetic permeability, magnetisation, and demagnetisation. Zhong *et al.* [14] built a FEM model that coupled concentrated stress to simulate the metal magnetic memory (MMM) method in the reversible magnetic field. However, the MMM method could be used to qualitatively evaluate defects rather than quantitatively identify defects due to relatively large errors.

In order to solve the coupled magnetomechanical problem in defect reconstruction from MFL signals, a multiphysics FEM model is proposed in this study by interlinking the physics of mechanics and magnetics. To test the model, COMSOL Multiphysics software, a commercial FEM environment that has solid mechanics and AC/DC (i.e., magnetics) modules available is chosen. The solid mechanics module is used to calculate stress distribution of a tensioned dog-bone like rod sample including the stress concentration around a circumferential square-notch defect on the rod, while the AC/DC module is employed to simulate magnetization under stress, via Jiles-Atherton-Sablik (J-A-S) [15,16] theory incorporated into the AC/DC module. The experiments are conducted to verify the feasibility of the proposed FEM model. Finally, the quantitative prediction about the effect of stress on the MFL signal is achieved.

4.2 Analytical Model of Stress-dependent MFL [3]

4.2.1 Dipole modelling of stress-dependent MFL

4.2.1.1 Stress concentration

Before modelling the stress-dependent MFL, it is necessary to know the stress distribution around the defect. It is well known that a defect in a structural component can cause significantly greater stress around the defect than the surrounding region, which is called stress concentration. Unfortunately, there are only limited cases where the stress concentrations can be described analytically. Therefore, the stress-dependent MFL model is only suitable to limited cases, for example, the cylindrical through-hole defect in a tension plate as shown in Fig. 4.1. The cylindrical through-hole defect is located in the centre of the plate with a thickness of b. The radius (R) of the defect is assumed to be much smaller than the width (W) of the plate. The tensile stress (σ_0) is aligned to the positive direction of the *y*-axis. The top surfaces of both the plate and defect are in the *xy*-plane, and the defect is symmetric on the *xz*-plane.

Assuming the tensile stress ($\boldsymbol{\sigma_0}$) is uniform, the stress concentration induced by the defect is shown in Fig. 4.1. According to the analytical expressions reported by Timoshenko [17], in *xy*-plane, the stress distribution around the defect with a radius of *r* can be expressed as,

$$\sigma_r = \frac{\sigma_0}{2}\left(1 - \frac{R^2}{r^2}\right) - \frac{\sigma_0}{2}\left(1 + \frac{3R^4}{r^4} - \frac{4R^2}{r^2}\right) cos2\theta \qquad (4.1)$$

$$\sigma_\theta = \frac{\sigma_0}{2}\left(1 + \frac{R^2}{r^2}\right) + \frac{\sigma_0}{2}\left(1 + \frac{3R^4}{r^4}\right) cos2\theta \qquad (4.2)$$

$$\tau_{r\theta} = \frac{\sigma_0}{2}\left(1 - \frac{3R^4}{r^4} + \frac{2R^2}{r^2}\right) sin2\theta \qquad (4.3)$$

In the particular case where $r = R$, the radial stress (σ_r) and shear stress ($\tau_{r\theta}$) are zero. The angle component of the stress (σ_θ) is

$$\sigma_\theta = \sigma_0(1 + 2cos2\theta) \qquad (4.4)$$

At the direction with an angle of $\theta = 0$ or $\theta = \pi$, the angle stress is about $3\sigma_0$. When the angle is $\theta = \pi/2$ or $3\pi/2$, the stress becomes compressive with a magnitude of σ_0.

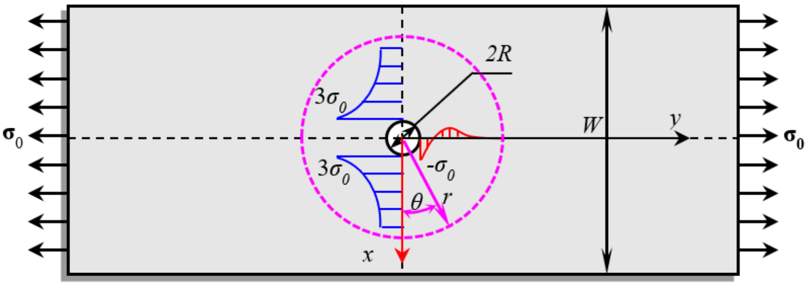

Figure 4.1. The stress distribution around the cylindrical through-wall defect [3].

4.2.1.2 Stress-dependent hysteresis

It has been discussed in chapters 2 and 3 that for the case of coaxial stress and magnetisation the effect of stress could be equivalent to a magnetic field H_σ, which resulted in the change of magnetic properties of ferromagnetic materials. Subsequently, the stress equivalent field was substituted into the effective magnetic field H_e, it arrived at

$$H_e = H + \alpha M + \frac{3\sigma}{2\mu_0}\left(\frac{\partial\lambda}{\partial M}\right) = H + \tilde{\alpha} M \tag{4.5}$$

Then the typical J-A hysteresis model was rewritten as [3]

$$\frac{dM}{dH} = \frac{(1-c)(M_{an}-M)+ck\delta\frac{dM_{an}}{dH}}{k\delta-\tilde{\alpha}(M_{an}-M)} \tag{4.6}$$

4.2.1.3 Stress-dependent MFL

The dipole model is extended based on the previous studies [6,18] to investigate the MFL field induced by a cylindrical through-hole defect in a ferromagnetic plate applying tensile stress as shown in Fig. 4.2. The surface of the defect along the negative *y*-axis is assigned with the positive magnetic charge density (i.e., north polarity), whereas the other half of the cylindrical surface is assigned with the negative magnetic charge density (i.e., south polarity).

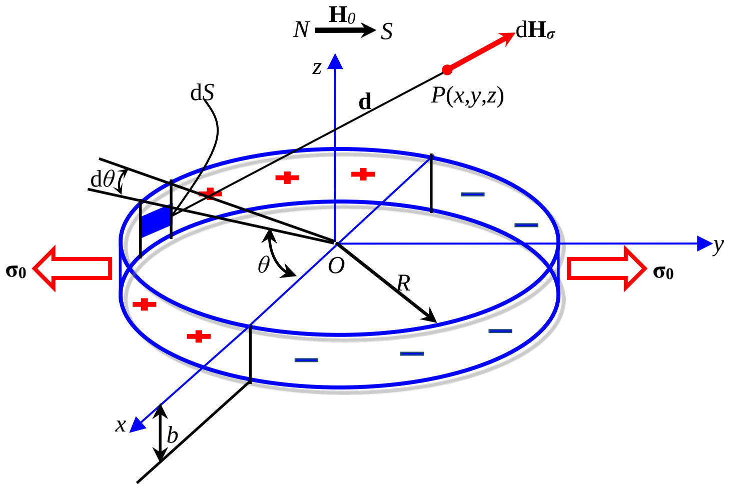

Fig. 4.2. Dipolar representation of a cylindrical through-wall defect [3].

Taking an infinitesimal element with an area of d*S* along the defect surface for instance, it is positioned at an angle of *θ* from the positive direction of the *x*-axis. The element carries a magnetic charge d*ρ*, which generates a leakage field $d\boldsymbol{H}_{\boldsymbol{MFL}}(\boldsymbol{\sigma})$ at a point *P*(*x*,*y*,*z*) in the space. The magnetic field of $d\boldsymbol{H}_{\boldsymbol{MFL}}$ is calculated by

$$d\boldsymbol{H}_{\boldsymbol{MFL}}(\boldsymbol{\sigma}) = \frac{1}{4\pi}\frac{\boldsymbol{d}}{d^3}d\rho(\sigma) \tag{4.7}$$

where $\boldsymbol{d}$ is a vector pointing from the element of dS to the point of $P(x,y,z)$ and d is the distance between the dS and the point of P. The magnetic charge density $\rho = \boldsymbol{M}_{\boldsymbol{\sigma}} \cdot \boldsymbol{n}$, where $\boldsymbol{M}_{\sigma}$ is magnetisation on the surface and $\boldsymbol{n}$ is the outward unit normal vector.

According to the previous dipole model [6], the magnetisation related to the surface magnetic charge density (ρ) could be calculated by

$$M_{\sigma}(\theta) = \left\{\frac{\mu_r(\theta)-1}{\mu_r(\theta)-N_y[\mu_r(\theta)-1]}\right\}H_e(\theta) \tag{4.8}$$

Substituting the angle component of stress σ_θ calculated by Equation (4.4) into Equations (4.5) and (4.6) of the J-A model, the magnetomechanical magnetisation along the defect surface can be determined, and the relative permeability of the element at an angle θ from the positive direction of x-axis is given by

$$\mu_r(\theta) = \frac{1}{\mu_0}\left(\frac{M(\theta)}{H} + 1\right) \tag{4.9}$$

where N_y denotes the demagnetising factor corresponding to the y-axis and is given by [19]

$$N_y = \frac{1}{2}\left[\frac{\eta}{\left(\sqrt{1-\eta^2}\right)^3} arcsin(1-\eta^2) - \frac{\eta^2}{1-\eta^2}\right] \tag{4.10}$$

where $\eta=R/b<1$. The exact value of the demagnetising factor of the infinitesimal element on a cylindrical through-hole is hard to be analytically modelled so that Equation (4.10) is an approximation. In practice, the MFL signals of different stress cases are normalised to the peak amplitude of MFL signal under free of stress so that the demagnetising factor can be avoided in the computation [6]. To investigate the change in the amplitude of MFL signal caused by the applied stress, the entire defect surface is assumed to have the same value of N_y. The magnetic charge density carrying by the surface element dS is expressed as

$$d\rho(\sigma) = \boldsymbol{M_\sigma} \cdot \boldsymbol{n} dS = M_\sigma(\theta) sin\theta dS \tag{4.11}$$

Then, the spatial leakage field generated by the magnetic charge can be solved by substituting Equations (4.8) ~ (4.11) into Equation (4.7)

$$d\boldsymbol{H_{MFL}}(\boldsymbol{\sigma}) = \frac{1}{4\pi}\frac{\boldsymbol{d}}{d^3}\left\{\frac{\mu_r(\theta)-1}{\mu_r(\theta)-N_y[\mu_r(\theta)-1]}\right\}H_e(\theta)Rsin\theta d\theta dz \tag{4.12}$$

The components of $d\boldsymbol{H_{MFL}}(\boldsymbol{\sigma})$ in the Cartesian coordinate system are arrived at

$$dH_{MFLx}(\sigma) = \frac{M_\sigma(\theta)}{4\pi}\frac{d_x}{d^3}Rsin\theta d\theta dz \tag{4.13}$$

$$dH_{MFLy}(\sigma) = \frac{M_\sigma(\theta)}{4\pi}\frac{d_y}{d^3}Rsin\theta d\theta dz \tag{4.14}$$

$$dH_{MFLz}(\sigma) = \frac{M_\sigma(\theta)}{4\pi}\frac{d_z}{d^3}Rsin\theta d\theta dz \tag{4.15}$$

Equations (4.13) ~ (4.15) can be solved by the Newton-Raphson method. The improved magnetic dipole model provides a way to investigate the effect of the stress concentration on the MFL signals analytically.

It should be noted that the precondition of the successful application of this model is that the defect size is far smaller than the sample size. Mandache and Clapham [18] have experimentally and analytically investigated the interaction between two adjacent defects. And their results showed that when the distance between the edges of adjacent defects was equal to the radius of defect, the MFL peak amplitude in the intersection dropped down to 40% of maximum value. When the distance doubled the radius, the interacting MFL peak value increased to 65% of the maximum value. If continuing to increase the distance to triple the radius, the MFL peak value would be restored to its original maximum. Therefore, the width of plate *W* should be larger than six times the radius of the cylindrical hole *R*. The widths of samples used in this chapter and chapter 5 are much larger than 15 times the corresponding radii of the cylindrical through-hole defects. The minimum distance between the defect wall and specimen edge is larger than six times the defect radius. Therefore, both of them could meet the size requirements to eliminate the edge effect.

4.2.2 Verification experiments for the analytical model

Verification experiments for the analytical dipole model have been conducted on a Q235 steel specimen with a cylindrical through-hole defect of 1mm in radius. The sizes of the specimen and defect were shown in the inset in Fig. 4.3a. The defect was centred at the centre of gravity of the specimen. A U-shaped magnetising yoke with ferrite magnets was used to provide a steady static magnetic field along the tensile direction for specimen magnetisation (Fig. 4.3b). The remanent flux density of the ferrite magnet in the magnetic circuit was around 1500 G (0.15 T). A high sensitive tunnel magnetoresistance (TMR) device of TMR2701 manufactured by the MultiDimension Technology Co., Ltd. was used to measure the surface MFL signal along the y-axis. The TMR device together with its power supply circuit was mounted onto a linear guide rail. The location of the TMR device was adjusted by moving the guide rail right above the y-axis with a lift-off distance of 0.5mm. The linear guide rail was driven by a step motor to carry the TMR device scanning the specimen surface at a speed of 10mm/s.

The specimens were annealed at 300°C for 2 hours for residual stress relief. Then, a commercial demagnetisation device was employed to demagnetise specimens. The surface magnetic field strength of the specimens was measured after the demagnetising process with a Gauss meter to make sure that the surface magnetic field strength was lower than 1 G (in free space 1G = 79.58 A/m).

Prior to verification experiments, a healthy specimen was tensioned with a stress increment of 20MPa until the stress reached 240MPa. At each stress level, the stray field along the surface was measured with the TMR device. Then the dependency of the stray field strength on the stress was used to evaluate the magnetostriction coefficients.

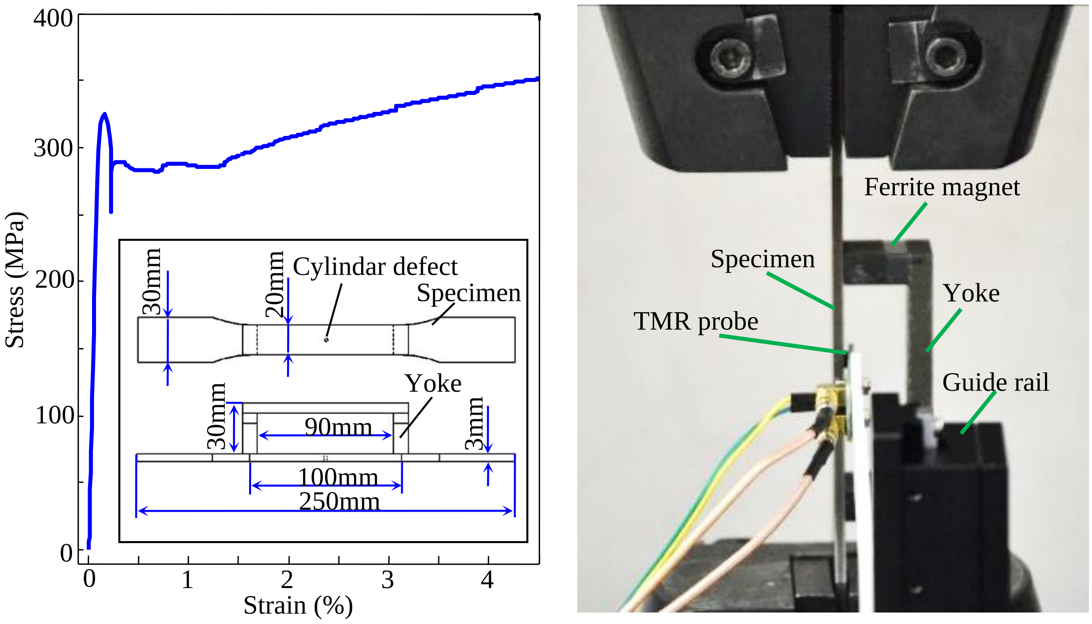

(a)

(b)

Figure 4.3. (a) Measured stress-strain curve of the Q235 steel and **(b)** the experimental setup for measuring the surface MFL in the dog-bone tensile test specimen [3].

The verification experiment for the analytical model was carried out on the specimen with defect, and the MFL signal was detected by the TMR device when the specimen was subjected to various stress levels. According to Equation (4.4), the maximum angle tensile stress along the surface of the through-hole defect was about triple the applied stress. According to the measured stress-strain curve for Q235 steel (see Fig. 4.3a), the maximum tensile stress applied on the specimens should be lower than 300MPa to ensure the Q235 steel in the elastic deformation. Therefore, to avoid the plastic deformation in the defective zone, the stress applied to the defective specimen was limited to be lower than 100MPa. The applied stress increased from 0MPa to 100MPa with an increment of 10MPa.

4.2.3 Discussion for the analytical and experimental results

The chemical composition of Q235 steel was close to 0.2% wt carbon steel, so the parameters of the J-A model for 0.2 wt.% carbon steel [20] were employed to represent the magnetic properties of Q235 steel approximately. Before calculating the hysteresis loop under different stress states, the magnetostriction coefficient should be determined. According to the Equation (4.5) for the stress equivalent effective field H_σ, the parabolic dependency of H_σ on the stress σ reached an inflexion point when the following equation was satisfied:

$$\sigma + \frac{\gamma_{11}}{2\gamma_{12}} = 0 . \tag{4.16}$$

There was a linear correlation between the stray field and the equivalent field inside the material. Hence, the measured results of the stray field strength under various tensile stresses (Fig. 4.4) were used to determine the inflexion point of Equation (4.5). The stray field along the healthy specimen surface was measured three times, and the averaged results were fitted by a parabolic equation as shown in Fig. 4.4. The symmetric axis of the fitted parabolic curve was at the stress point of 180MPa. To satisfy Equation (4.16) and the convergence conditions of the solution of the J-A model in the high stress level, the magnetostriction coefficients were selected as γ_{11} = $-1.5\times10^{-18}\text{A}^{-2}\cdot\text{m}^2$ and γ_{12} = $4.17\times10^{-27}\text{A}^{-2}\cdot\text{m}^2\cdot\text{Pa}^{-1}$. All the parameters for analytical simulation were listed in Table 4.1.

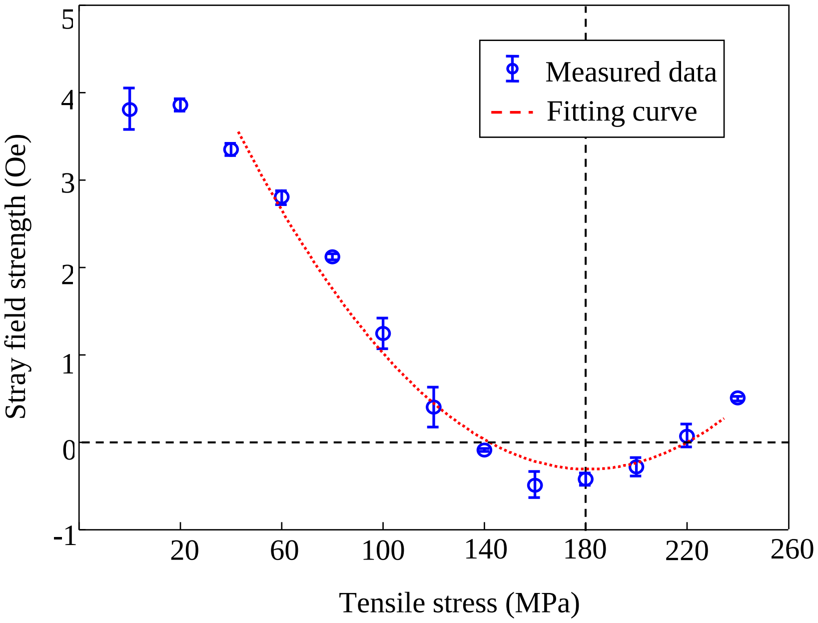

Figure 4.4. Measured stray field strength when the healthy specimen was subjected to different tensile stress levels [3].

Table 4.1. The J–A model parameters for Q235 steel

J-A parameters	Values	Sources
Reversibility parameter, c	0.0198	Fitting the hysteresis loop in [20] by using the nonlinear optimisation algorithm [21]
Pinning parameter, k	1154.6	
Domain density, a	499	
Saturation magnetisation, Ms	1.5743×10^{6}	
Coupling factor, α	7.0921×10^{-4}	
Magnetostriction coefficient, γ_{11}	$-1.5\times10^{-18}\text{A}^{-2}\cdot\text{m}^{2}$	Extracted from the fitting curve in Fig. 4.4
Magnetostriction coefficient, γ_{12}	$4.17\times10^{-27}\text{A}^{-2}\cdot\text{m}^{2}\cdot\text{Pa}^{-1}$	

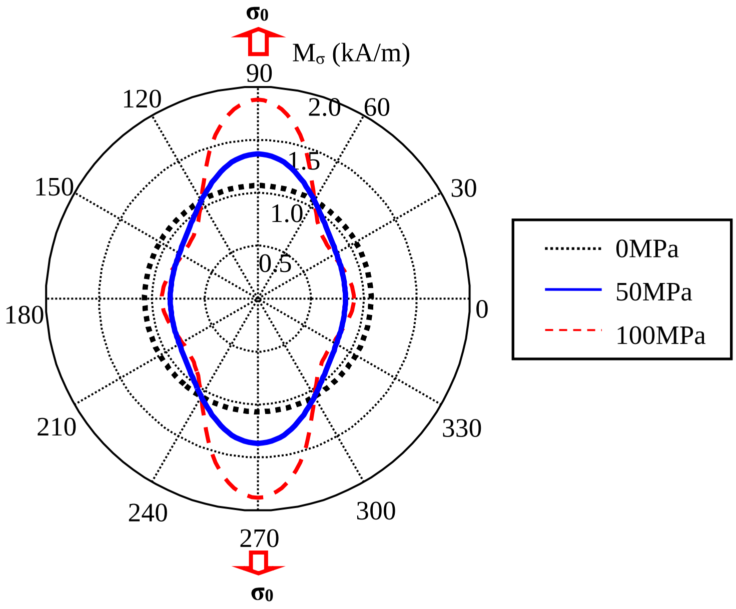

Figure 4.5. Predicted magnetisation along the defect surface when the specimen was subjected to different tensile stress levels [3].

Both the hysteresis curves and the relative permeability under different stress conditions could be predicted by Equation (4.6) of the J-A-S model. The stress-dependent relative permeability $\mu_r(\theta)$ was assessed at the static magnetic field of H = 600A/m. Then the magnetisation of $M_\sigma(\theta)$ could be evaluated with Equation (4.8) when the angle of θ varied in the range of 0~2π. Fig. 4.5 showed the predicted distribution of $M_\sigma(\theta)$ along the defect surface under the tension of 0Mpa, 50MPa and 100MPa. The magnetisation $M_\sigma(\theta)$ along the defect surface (in Fig. 4.5) was further substituted into Equation (4.11) to calculate the magnetic charge density on the surface element dS. Finally, the defect-induced MFL at a point was determined by applying the integration operation to the entire surface of the defect. The predicted MFL along the y-axis under the action of various tensile stresses was plotted in Fig. 4.6 and compared with the measurement results. All the predicted and experimental MFL signals were normalised by the maximum amplitude of the simulated and measured MFL signal under 0MPa tensile stress, respectively. It could be found that both the shape and the maximum amplitude of the predicted MFL signals were approaching the experimental results with a coefficient of determination higher than 0.98. It indicated that the proposed dipole model was adequate to predict the stress-dependent MFL with high accuracy.

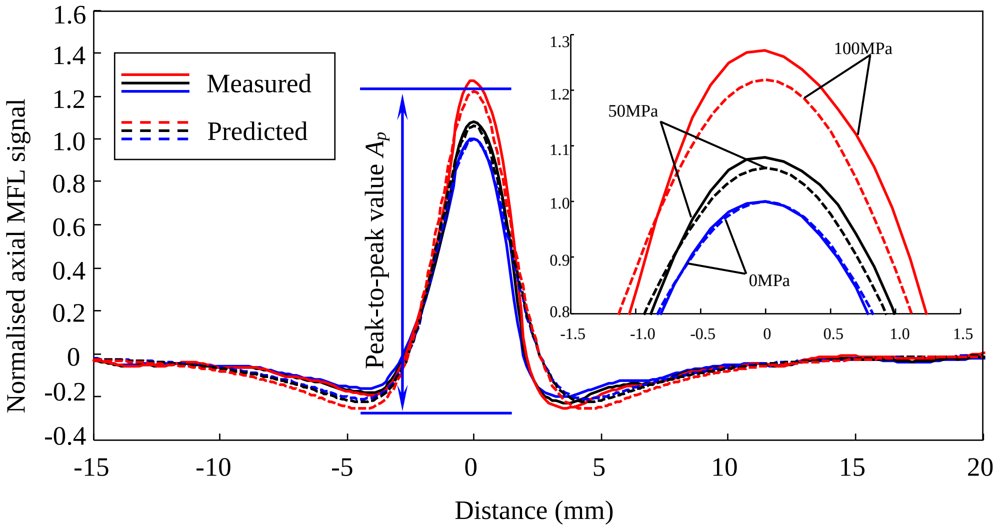

Figure 4.6. Measured (solid lines) and predicted (dashed lines) axial components of MFL along the y-axis under different stress conditions [3].

The peak-to-peak amplitudes (A_p) of the normalised MFL signals were estimated and plotted in Fig. 4.7 for quantitative evaluation. The predicted results could fit the measured data with a coefficient of determination higher than 0.99. It demonstrated that the improved dipole model was feasible to predict the effect of stress on MFL signal and also applicable to solve the inverse problem for estimating the shapes and sizes of the defects when the stress was involved. It could also be found that tensile stress of 100 MPa resulted in an increase of 23.74% and 22.04% in the measured and simulated amplitudes of MFL signals respectively. To achieve defect sizing with high accuracy, the effect of the tensile stress on the MFL signal should be considered in the calibration process. The proposed improved magnetic dipole model provided a valuable tool to evaluate the contribution of stress to the induced MFL signals and might be used to solve the inverse problem for defect sizing or stress evaluation around a defect with a given shape and size. For example, the model could predict that if the radius doubled and other geometric parameters kept the same, the peak-to-peak values of MFL signal parabolically increased by 22.52% between 0 MPa and 100 MPa. And if the radius was extended to 3 mm, this model would predict a 23.36% increase of the peak-to-peak amplitude in the tensile stress range from 0 MPa to 100 MPa. It could be concluded that tensile stress would have a noticeable influence on this kind of defect. Besides, the sizing errors that tensile stress introduced into the inverse problem of MFL would vary from defect to defect.

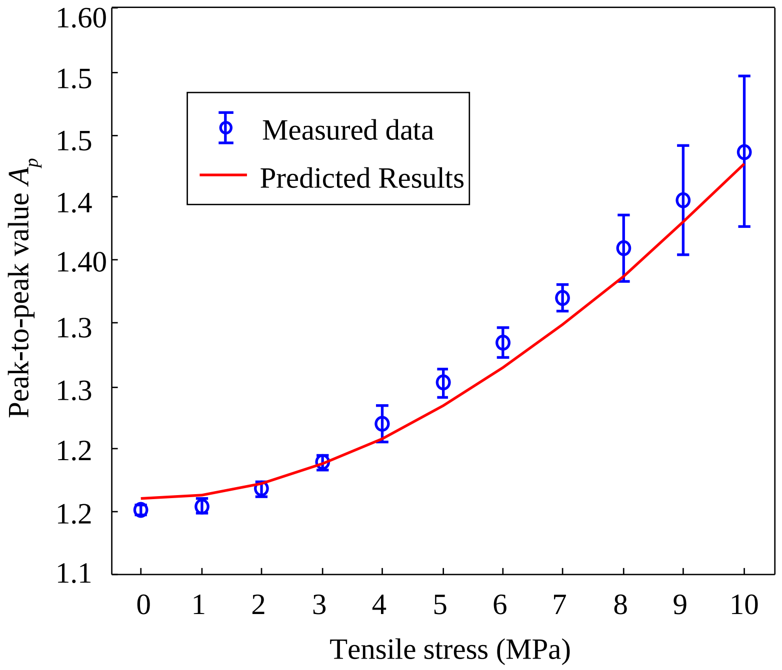

Figure 4.7. Measured and predicted peak-to-peak amplitudes of the normalised MFL signals obtained from different tension conditions [3].

However, there were several limitations of the proposed magnetic dipole model that should be stated. First, prior knowledge of the material should be grasped, such as the magnetic properties and magnetostriction. Second, only a few simple geometries where the stress concentrations could calculate analytically could be solved by this model. Last but not least, the model was not adequate to precisely deal with the defects with complex shapes due to the difficulty in calculating the demagnetising factor.

4.3 Finite Elemental Model of Stress-dependent MFL

Due to the limited applications of dipole model for stress-dependent MFL, a universal FEM used to investigate the relationship between stress and MFL signal around a defect of a geometrical complexity is further proposed. In the case of such a defect, it is hard to describe the stress distribution analytically. The dependence of magnetic hysteretic properties on stress makes the problem even more complex. Therefore, the finite element method is employed to simulate the real physical phenomenon.

4.3.1 The simulation steps of FEM for stress-dependent MFL

4.3.1.1 Step 1: Solid mechanics module

In order to simplify the formulation and presentation of the theory, a two-dimensional (2D) axisymmetric system, where geometries of sample and defect are axisymmetric, is chosen. Nevertheless, a theory for standard three-dimensional (3D) systems that lack symmetry can be formulated similarly. In addition, for the mechanics study, quasi-static conditions are assumed, i.e., the stress in the system is considered constant or varies much slower than the magnetic field. Besides, the simulation deals with elastic stress rather than plastic stress as it may lead to nonconvergence due to strong non-linearity in magnetic behaviour.

With these constraints in mind, and assuming the ferromagnetic material is a mechanically isotropic medium, the following equilibrium equation can describe the mechanical problem:

$$\mathbf{\nabla\sigma} + \mathbf{F} = \mathbf{0} \tag{4.17}$$

where $\mathbf{\nabla} = \begin{bmatrix} \frac{\partial}{\partial r} + \frac{1}{r} & -\frac{1}{r} & 0 & \frac{\partial}{\partial z} \\ 0 & 0 & \frac{\partial}{\partial z} & \frac{\partial}{\partial r} + \frac{1}{r} \end{bmatrix}$, $\boldsymbol{\sigma} = (\sigma_r, \sigma_\theta, \sigma_z, \tau_{rz})^T$ is the stress tensor, $\mathbf{F} = (f_r, f_z)^T$ is the body force. The constitutive relation:

$$\boldsymbol{\sigma} = \mathbf{D}\boldsymbol{\varepsilon} \tag{4.18}$$

is used, where **D** is the elasticity tensor of material expressed as:

$$\mathbf{D} = \frac{E(1-\upsilon)}{(1+\upsilon)(1-2\upsilon)} \begin{bmatrix} 1 & \frac{\upsilon}{1-\upsilon} & \frac{\upsilon}{1-\upsilon} & 0 \\ \frac{\upsilon}{1-\upsilon} & 1 & \frac{\upsilon}{1-\upsilon} & 0 \\ \frac{\upsilon}{1-\upsilon} & \frac{\upsilon}{1-\upsilon} & 1 & 0 \\ 0 & 0 & 0 & \frac{1-2\upsilon}{2(1-\upsilon)} \end{bmatrix} \tag{4.19}$$

where E is Young's modulus, and υ is the Poisson's ratio, and $\boldsymbol{\varepsilon} = \left(\frac{\partial u_r}{\partial r}, \frac{u_r}{r}, \frac{\partial u_z}{\partial z}, \frac{\partial u_r}{\partial r} + \frac{\partial u_z}{\partial z}\right)^T$ is the strain tensor.

Together with the geometrical constraints in the system, the solution to the mechanical problem is obtained using the standard FEM approach implemented in the solid mechanics module of COMSOL Multiphysics software. The results of these solid mechanics simulations (i.e., distribution of stress in the ferromagnetic structure) are stored and passed further as inputs for magnetic simulations.

4.3.1.2 Step 2: AC/DC magnetics module

The solid mechanics simulations are performed under quasi-static conditions, while the magnetic simulation needs to be dynamic due to the hysteretic nature of ferromagnetism where the one-to-one correspondence between states of magnetisation and the applied magnetic field is absent. Therefore, in the case of time-dependent magnetic field $\boldsymbol{H}$, the employment of hysteresis models is necessary to predict magnetisation $\boldsymbol{M}$ value at a particular moment. In this study, the ferromagnetic material of the specimen is chosen to be magnetically isotropic that follows the Jiles-Atherton-Sablik (J-A-S) magnetomechanical hysteretic theory.

A typical algorithm to solve a time-dependent magnetomechanical problem is as follows [22]:

(1) Magnetic field ($\boldsymbol{H}$) is set as a sinusoidal (or triangular) function varying with time (t). Generally, this magnetic field can be generated by feeding sinusoidal alternating current into excitation coils. In this study, the first one-fourth of the sinusoidal current is fed into Helmholtz coils to excite alternating magnetic field, and then the current is maintained at the final value so that the magnetic field and magnetisation can remain unchanged in subsequent calculations, as shown in Fig. 4.9. $\boldsymbol{H}(t)$, $\boldsymbol{B}(t)$ and $\boldsymbol{H}_e(t\text{-}\Delta t)$ start from $\boldsymbol{H}(0)$, $\boldsymbol{B}(0)$, $\boldsymbol{H}_e(0)$ and then are updated after every loop.

(2) For the given actual time step magnetic field $\boldsymbol{H}(t+\Delta t)$, the magnetisation $\boldsymbol{M}(t)$ and increment of magnetic field $d\boldsymbol{H}(t)$ can be calculated by

$$\boldsymbol{M}(t) = \boldsymbol{B}(t)/\mu_0 - \boldsymbol{H}(t) \tag{4.20}$$

$$d\boldsymbol{H} = \boldsymbol{H}(t + \Delta t) - \boldsymbol{H}(t) \tag{4.21}$$

where μ_0 is the permeability of free space. Then the effective magnetic field $\mathbf{H_e}(t)$ and the increment of effective field $\mathrm{d}\mathbf{H_e}(t)$ are computed by

$$\boldsymbol{H}_e(t) = \boldsymbol{H}(t) + (\boldsymbol{\alpha} + \frac{3\boldsymbol{b\sigma}}{\mu_0}) \cdot \boldsymbol{M}(t) = \boldsymbol{H}(t) + \widetilde{\boldsymbol{\alpha}} \cdot \boldsymbol{M}(t) \tag{4.22}$$

$$d\boldsymbol{H}_e = \boldsymbol{H}_e(t) - \boldsymbol{H}_e(t - \Delta t) \tag{4.23}$$

where $\boldsymbol{\alpha}$ quantifies the tensor of domain coupling, $\boldsymbol{\sigma}$ is the stress tensor, the coefficient $\boldsymbol{b}$ is a function of magnetostriction (λ) and magnetisation ($\boldsymbol{M}$), and $\widetilde{\boldsymbol{\alpha}}$ is the total interdomain coupling parameter.

(3) According to the J-A model [16,22,23], the differential magnetisation with respect to the magnetic field can be expressed as

$$\frac{d\boldsymbol{M}}{d\boldsymbol{H}} = \frac{\frac{\chi_f}{|\chi_f|}\cdot\boldsymbol{\chi}_f + \boldsymbol{c}\cdot\frac{d\boldsymbol{M}_{an}}{d\boldsymbol{H}_e}}{1-\widetilde{\boldsymbol{\alpha}}\left[\frac{\chi_f}{|\chi_f|}\cdot\boldsymbol{\chi}_f + c\cdot\frac{d\boldsymbol{M}_{an}}{d\boldsymbol{H}_e}\right]} \tag{4.24}$$

where $\boldsymbol{c}$ is the reversibility coefficient, $\boldsymbol{M}_{an}$ is an anhysteretic magnetisation, which is given by the Langevin function in the case of an isotropic material:

$$\boldsymbol{M}_{an}(t) = \boldsymbol{M}_{st}\left[coth\frac{\boldsymbol{H}_e(t)}{\boldsymbol{a}} - \frac{\boldsymbol{a}}{\boldsymbol{H}_e(t)}\right] \tag{4.25}$$

and $\boldsymbol{\chi}_f = (\boldsymbol{M}_{an} - \boldsymbol{M})/\boldsymbol{k}$, where $\boldsymbol{k}$ is the pinning coefficient. Equation (4.24) holds true with the condition $\boldsymbol{\chi}_f \cdot d\boldsymbol{H}_e(t) > 0$; otherwise, it changes to:

$$\frac{d\boldsymbol{M}}{d\boldsymbol{H}} = \frac{\boldsymbol{c}\cdot\frac{d\boldsymbol{M}_{an}}{d\boldsymbol{H}_e}}{1-\widetilde{\boldsymbol{\alpha}}\boldsymbol{c}\cdot\frac{d\boldsymbol{M}_{an}}{d\boldsymbol{H}_e}} \tag{4.26}$$

(4) Based on the computed results in previous steps, magnetisation $\boldsymbol{M}$ and magnetic induction $\boldsymbol{B}$ are updated by

$$\boldsymbol{M}(t+\Delta t) = \boldsymbol{M}(t) + \frac{d\boldsymbol{M}}{d\boldsymbol{H}}\cdot d\boldsymbol{H} \tag{4.27}$$

$$\boldsymbol{B}(t+\Delta t) = \mu_0[\boldsymbol{H}(t+\Delta t) + \boldsymbol{M}(t+\Delta t)] \tag{4.28}$$

Then, these renewed data are inputted into the next computing loop repeating steps (2) ~ (5), and the flow chart of the algorithm for the time-dependent AC/DC module is shown in Fig. 4.8. These procedures are not finished until the last time step is completed. In the case study, the initial hysteresis curve is used to save simulation time by feeding the first one-fourth of sinusoidal periodic current into excitation coils (see Fig. 4.9). It should be added that this algorithm can obtain all magnetisation states on the hysteresis loop by feeding relevant alternating current into excitation coils. For example, it will obtain a whole hysteresis loop by feeding 5/4 of an alternating current cycle.

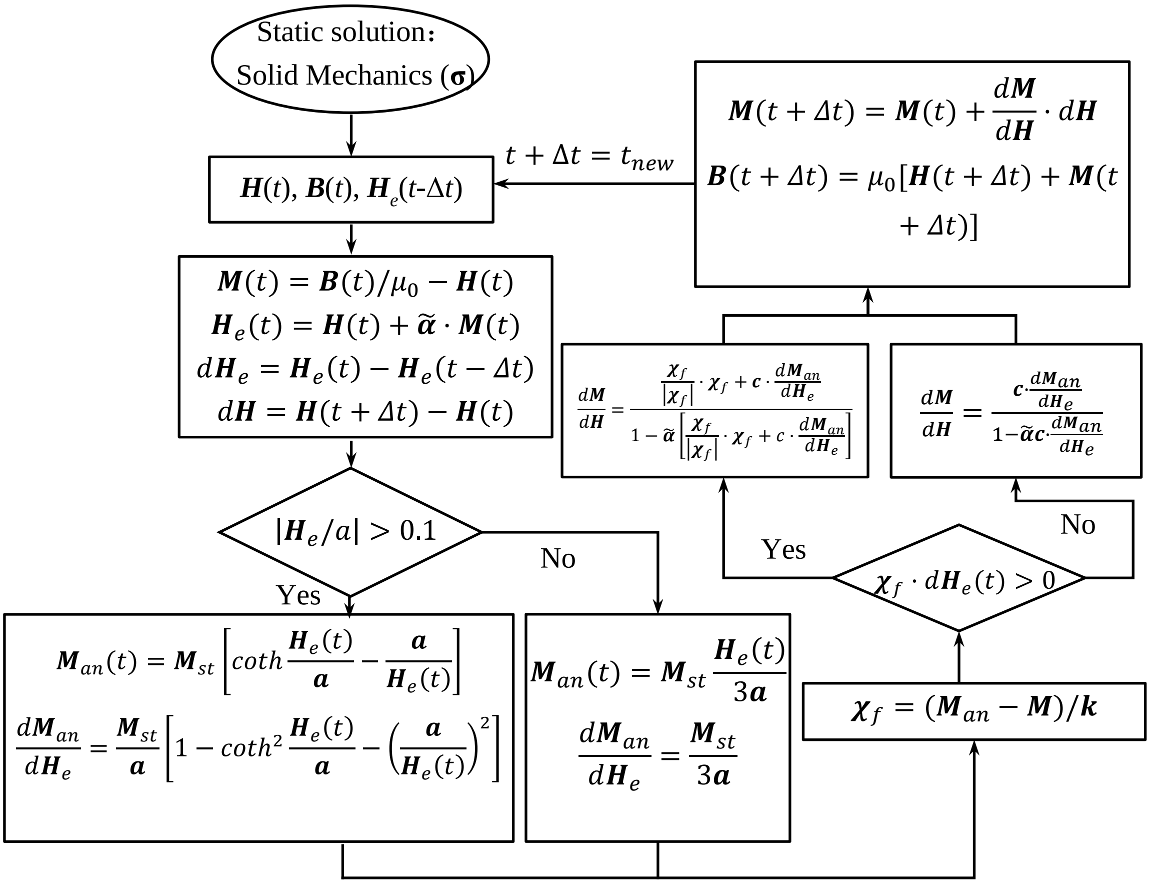

Figure 4.8. Flow chart of the time-dependent algorithm for hysteresis modelling.

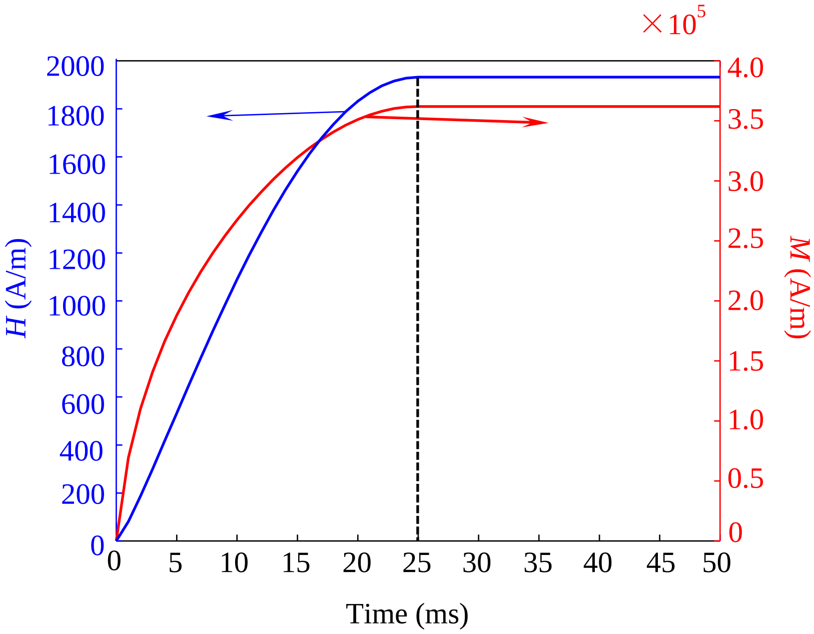

Figure 4.9. The magnetic field (H) and magnetisation (M) variations with time extracted from a point inside a specimen without defect.

Before the simulation, identification of the key parameters for the model is required. To simplify the expressions, the tensors of the J-A parameters are expressed as scalar values since the specimen is set as isotropic material, for example $\boldsymbol{M}_{st} = \begin{bmatrix} M_{st} & 0 & 0 \\ 0 & M_{st} & 0 \\ 0 & 0 & M_{st} \end{bmatrix}$ is simplified as M_{st}.

4.3.1.3 Case study: Dog-bone like rod of 1045 steel with a square-notch defect

Other than the dog-bone like plate specimen with a cylindrical through-hole used to model the stress-dependent MFL [3], in this case, a dog-bone like rod (shown in Fig. 4.10a) with a circumferential square-notch defect is studied to reveal the relation between stress and MFL signal. In the case of such a defect, it is hard to describe the stress distribution around the defect analytically.

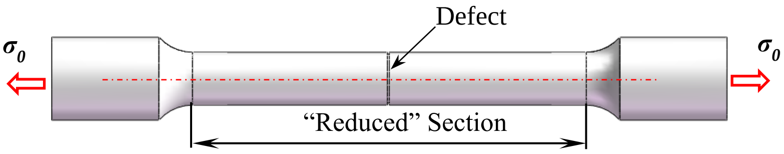

(a)

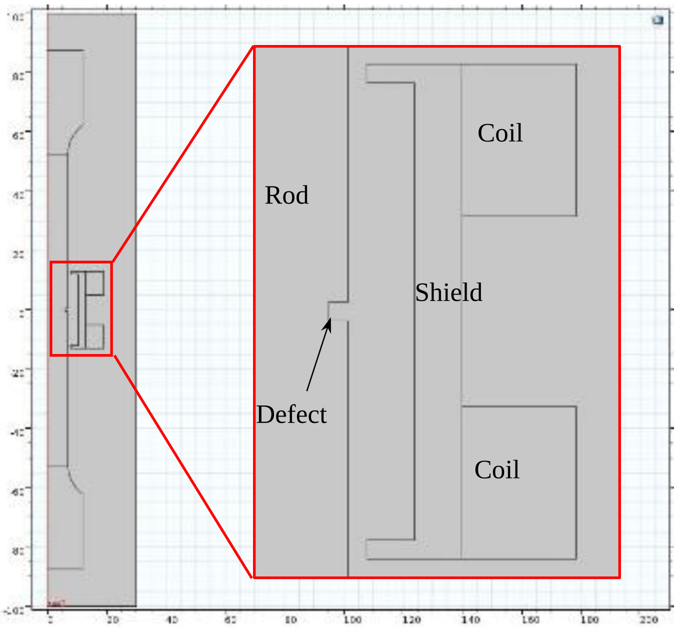

(b)

Figure 4.10. Solid mechanical analysis of a dog-bone like rod with a square-notch defect. **(a)** The tensioned test specimen, **(b)** the 2-D axisymmetric model.

Table 4.2. The geometric parameters of the modelled specimen

Geometric Parameters	Length of specimen	Length of the central part	Depth of the defect	Width of the defect	Radius of the ends	Radius of the central part
Sizes (mm)	175	105	1	1	12	7

The solid mechanics is simulated in COMSOL Multiphysics 5.2a. As shown in Fig. 4.10b, the 2-D axisymmetric model in the *r*-*z* plane is built according to the geometric structure of the dog-bone like rod specimen shown in Fig. 4.10a and the sensor optimised in the previous research [24]. The geometric parameters of the specimen and the defect are listed in Table 4.2. In the first step, when the tensile stress is applied, the mechanical problem is solved in the mechanics module. The free triangular mesh using an adaptive algorithm is applied to the specimen with predefined extremely fine element size, while element sizes are controlled to be less than 0.01 mm around the defect by adding extremely fine auxiliary lines along the periphery of the defect to obtain an accurate stress distribution around the defect.

In magnetic field simulation, i.e., AC/DC module, the results of stress distribution are inherited and used for the subsequent magnetisation calculation. In this case, the five key parameters of the J-A model for 1045 carbon steel fitted by the nonlinear optimisation algorithm are substituted into the finite elemental model to simulate the hysteresis curve. Besides, unlike the approach with the analytical model where the complex empirical equation of magnetostriction is used, in FEM simulation, the magnetostriction coefficient follows an analogous method to fit the average λ *vs* M values using a parabolic function in [25], since in this case the Equations (4.24) and (4.26) are more likely to converge and the parabolic approximation of magnetostriction may be preferable at a relative weak applied magnetic field. According to the previously measured λ *vs* M curve for 1045 carbon steel [15], coefficient b is determined as 2.2×10^{-18} (m^2/A^2) by the parabolic fitting of the λ *vs* M curve. In the following experiments, the input current is set as 3 A, and the diameter of the wire is 0.35 mm, so the input current density in the model is set as 30 A/mm^2.

4.3.2 Verification experiments for the finite elemental model

Verification experiments for FEM are conducted on a specimen of 1045 steel with a square-notch defect. The circumferential square-notch defect with both width and depth of 1 mm is machined on the surface centre of the "reduced section" as shown in Fig. 4.10a. A Helmholtz coil with magnetic shielding is used to provide a static magnetising field with a near-zero background field along the tensile direction of the specimen (see Fig. 4.11a). The TMR2701 magnetic device together with its power supply circuit is mounted onto a linear guide rail. The location of the TMR sensor is concentric with the cylindrical specimen with a lift-off distance of 1 mm. The linear guide rail is driven by a step motor to enable the TMR device to scan the specimen surface at a speed of 10 mm/s. During scanning, the MFL-induced voltage signal $U(t)$ is acquired by a TektronixMDO3024 digital oscilloscope with a sampling rate of 100 S/s.

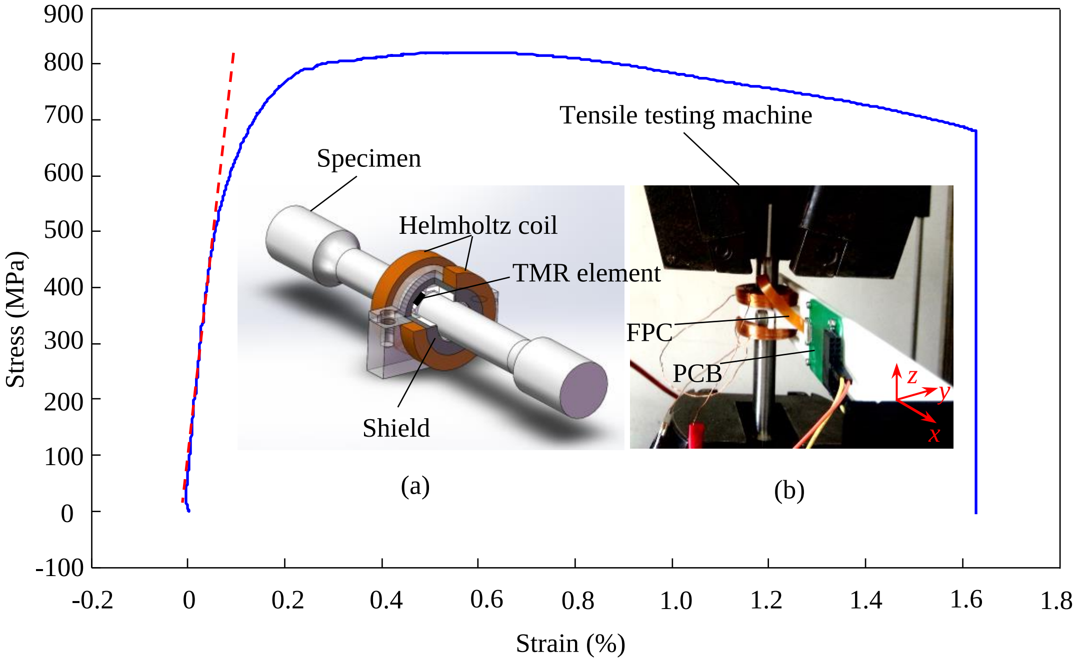

Figure 4.11. Measured stress-strain curve of the 1045 steel. Inset **(a)** sketches a prototype of the TMR-based MFL sensor; inset **(b)** shows the experimental setup to measure the surface MFL induced by the defect on the tensile test specimen.

To prove the accuracy of FEM for MFL simulation, the original data are compared. The measured data are voltage signals, which can be converted into flux leakage intensity using $H(t)= U(t)/k_s$, where k_s is the sensitivity of the TMR, 8 mV/V/Oe (100 μV/V/A·m^{-1}) fitting in the range of ±50 Oe (±3978.87 A/m), which is lower than its specification 12 mV/V/Oe (150μV/V/A·m^{-1}) in the field range of ±15 Oe (±1193.66 A/m), for this device. In the following experiments, the TMR sensor is supplied by 5 V power and used in differential mode doubling the output voltage. Hence, k_s is 1 mV/A·m^{-1} when the absolute value of the magnetic field is larger than 1193.66 A/m but lower than 3978.87 A/m. The simulated MFL results along the *z*-axis under zero stress as well as the experimental output voltage of the TMR sensor are plotted in Fig. 4.12. The maximum output voltage of 0.7224 V (±0.02 V) just above the defect corresponds to a magnetic field intensity of 722.4 A/m (±20 A/m). For comparison, the simulated maximum value of the magnetic field caused by the defect is 748.78 A/m. The relative error is less than 4%, which indicates the FEM simulation is close to the actual value. But in order to reduce the calculation error caused by demagnetisation, meshing size and other factors, the normalisation method is also adopted here, and all experimental and simulated signals are normalised to the maximum amplitude of the measured and predicted MFL signal under zero stress, respectively.

Before the experiment, the specimen is annealed at 400°C for 2 hours with furnace cooling to release the residual stress. As the simulation is conducted on the initial hysteresis stage, the specimen needs to be demagnetised before the test. Hence, a commercial demagnetisation device is employed for specimen demagnetisation. The surface magnetic field strength of the specimens is measured after the demagnetising process by a Gaussmeter to make sure that the surface magnetic field strength is lower than 80 A/m. The exciting magnetic field is supplied by the Helmholtz coil, which is fed with 3 A current.

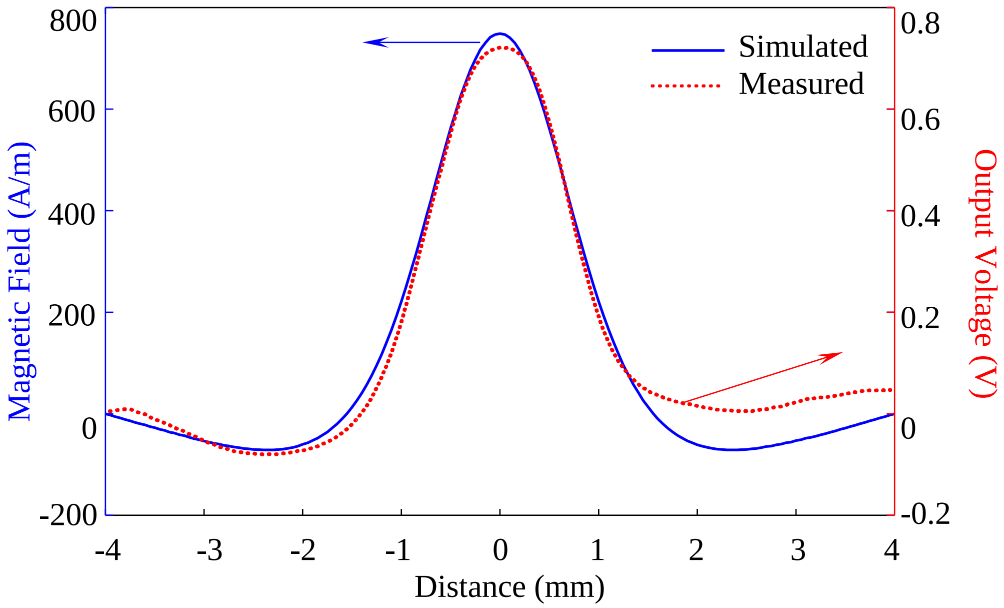

Figure 4.12. Simulation (solid lines) and experimental (dashed lines) results of the axial components of MFL along *z*-axis under 0MPa.

The experiments are carried out on the specimen with the circumferential square-notch defect, and the MFL signals are detected by the TMR sensor with the specimen subjected to various stress levels. According to the measured stress-strain curve of the 1045 steel in Fig. 4.11, to avoid plastic deformation in the defective zone, the stress applied to the specimen is limited to no more than 100 MPa. A stress increment of 10 MPa for data collection corresponds to the simulation steps. These experiments have been repeated five times to reduce measurement error.

4.3.3 Discussion for the FEM simulated and measured results

The typical result of the applied tensile stress (100 MPa) is illustrated in Fig. 4.13. In the region that is far from the defect, the stress distributes nearly uniformly, while in the vicinity of the defect the stress varies sharply, especially at the bottom of the square-notch defect. The stress along a cut-line of [(6.5, −0.5), (7.0, -0.5)] is extracted to evaluate the variation of stress along the wall of defect. The curve of the stress on the cut-line is plotted in Fig. 4.13c. It can be seen that the stress decreases to zero rapidly and then increases towards zero slowly after reaching the minimum at about

−13 MPa. Compared with stress distribution around the cylindrical defect in the analytical model [3], the stress along the vicinity of the defect is hard to be described mathematically, justifying the choice of the FEM simulations. Besides, after applying the stress, the square-notch defect, which initially had a regular and simple shape, has acquired a complex geometry as shown in Fig. 4.13b.

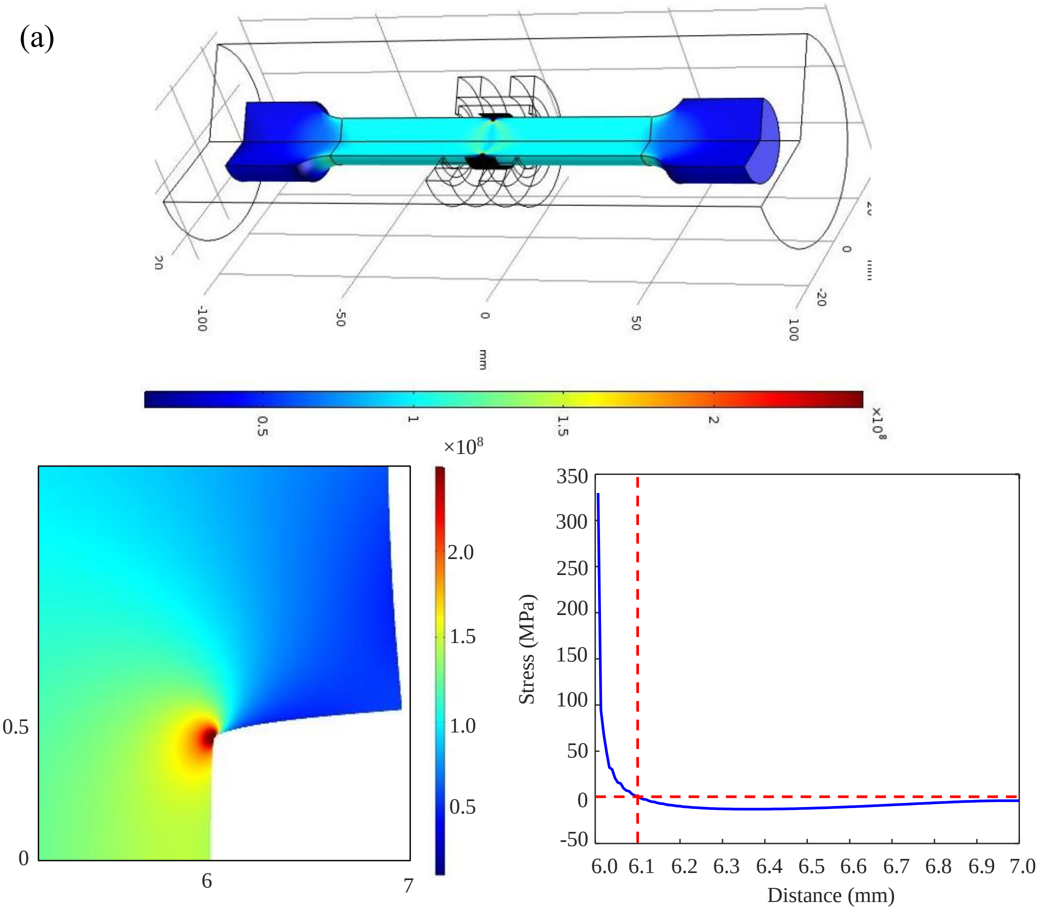

(b) (c)

Figure 4.13. (a) Solid mechanical analysis of a dog-bone like rod with a square-notch defect. **(b)** the calculated result of stress distribution around the defect (notice the change of shape of the specimen near the defect), and **(c)** stress distribution extracted along a defect wall.

The test specimen made of 1045 steel is used in this case. Its chemical components and magnetic properties are close to the 0.4%wt carbon steel so that the parameters of

0.4 wt% carbon steel fitted by nonlinear optimisation algorithm are substituted into the finite elemental model to simulate the hysteresis curve approximately. Besides, coefficient b has been determined as 2.2×10^{-18} (m^2/A^2) by the parabolic fitting of the λ vs M curve. The input current density in the model is set as 30 A/mm^2. All the parameter values of the magnetomechanical model are listed in Table 4.3.

Table 4.3. The parameters of 1045 carbon steel for FEM simulation

J-A Parameters	Value	Obtained from
Saturation magnetisation, M_s	1.5755×10^6 (A/m)	Fitting the hysteresis loop in [20] by using the nonlinear optimisation algorithm [21]
Domain density, a	1408.1 (A/m)	
Coupling factor, α	0.0024	
Pinning parameter, k	2356.5 (A/m)	
Reversibility parameter, c	0.0382	
Magnetostriction coefficient, b	2.2×10^{-18} (m^2/A^2)	Parabolic fitting the magnetostriction curve in [15]
Input current density, J_0	30 (A/mm^2)	Experiment

Fig. 4.14a and 4.14b show the simulation results of magnetisation under stresses of 0 MPa and 100 MPa at the final time step, respectively. To obtain these results, the cases of 0 MPa and 100 MPa stresses are computed using the algorithm mentioned in Section 4.3. It can be found that the magnetisation changes significantly near the bottom of the defect while varying slightly near the top of the defect. To clearly illustrate the magnetisation variations at these positions in two cases, two characteristic points on each graph are selected (marked as A_1, A_2, which are surface points on defect walls near the bottom of square-notch, and B_1, B_2, which are surface points near the top of defect wall). Figure 4.14c shows the comparison of the M-H curves at points A_1 and A_2, while Fig. 4.14d shows the comparison at points B_1 and B_2. It can be seen that the M-H curves at the points near the bottom of defect change more dramatically than that at the points near the top. This is attributed to the extent

of stress variation. As shown in Fig. 4.13c, at the bottom of the defect, i.e., point A_2, the stress concentration caused by the defect is more than threefold with respect to the applied stress (340 MPa *vs* 100 MPa), while at the top of the defect, i.e., point B_2, the stress approaches zero. Despite an apparent closeness between the *M-H* curves at the points B_1 and B_2 observed in Fig. 4.14d, the values differ slightly, and there is no overlap between those *M-H* curves. According to the analytical model, the leakage field at an off-surface point is influenced by the magnetisation states of all points along the walls of the defect (e.g., segment A_1B_1), though the closer the finite element to the surface of the specimen, the greater is the effect on MFL. Besides, the variations in magnetisation are not limited to the defect walls but also involve the neighbour area. It indicates the importance of the full-scale problem simulation and avoids any assumptions on the elemental magnetic charge distribution.

The magnetisation values at the final time step are used to calculate the MFL field with 1mm lift-off that is consistent with experiments. For example, the simulation and experimental results for stresses of 0 MPa, 50 MPa and 100 MPa normalised by the maximum amplitude of predicted and measured MFL signals under 0 MPa are shown in Fig. 4.15. The simulated MFL shapes and highest amplitudes are consistent with the measured ones. It indicates that the proposed FEM model is adequate to predict the stress-dependent MFL accurately in these conditions. The minimum values of the measured MFL signals on the left side of the defect are slightly lower than that of the simulated, while on the right side the opposite is seen. It may be caused by the slightly asymmetric shape of the defect due to the bevel angle of the machining tool.

To evaluate the relationship between the MFL signal and the applied stress quantitatively, the peak-to-peak amplitudes A_p of normalised MFL signals are plotted in Fig. 4.16. The dependence of the amplitude of MFL signal on the applied stress obtained from the experiment corresponds with the results obtained from the simulation. The value of A_p demonstrates the approximately linear decreasing trend with increasing applied stress from 0 MPa to 100 MPa. This is due to the fact that the dominant stress along the defect wall is compressive stress that increases with applied stress. The linear equation fits well with the measured results with a coefficient of determination higher than 0.99.

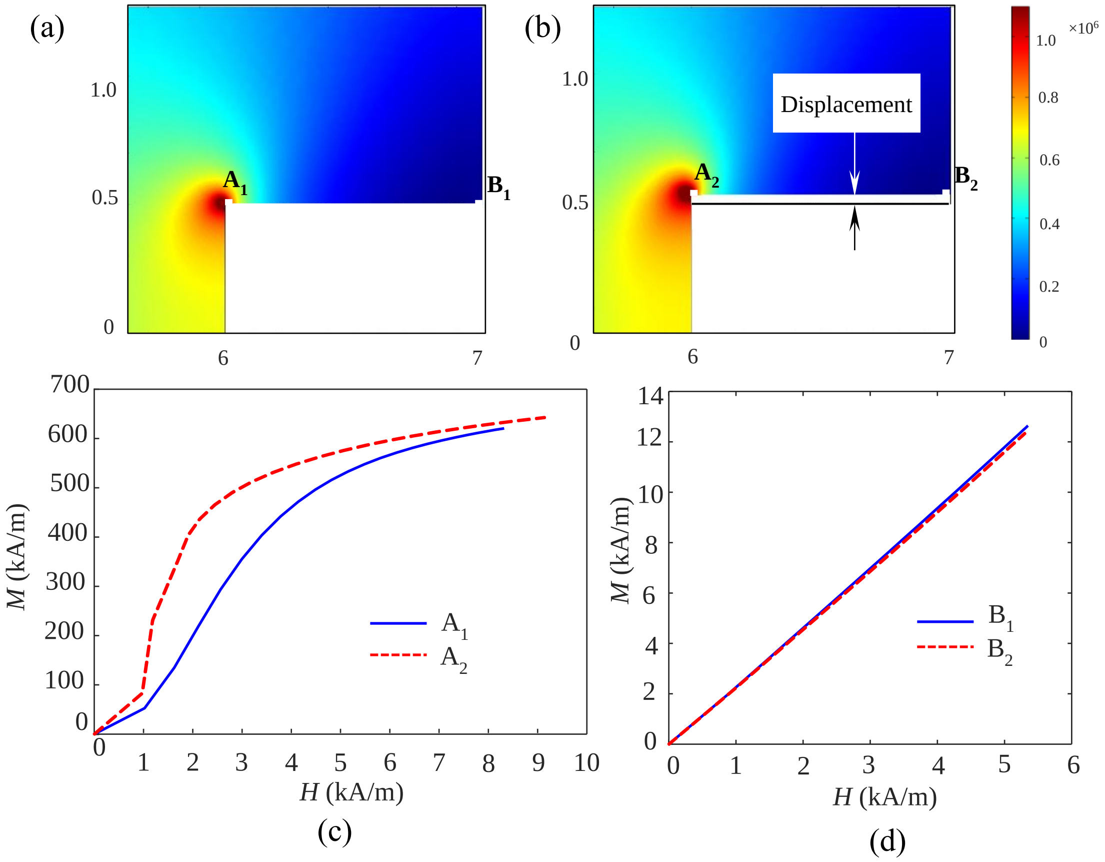

Figure 4.14. **(a)** Magnetisation distribution without stress. **(b)** Magnetisation distribution under 100 MPa tensile stress. **(c)** *M-H* curves extracted from points A_1 and A_2. **(d)** *M-H* curves extracted from points B_1 and B_2.

The applied tensile stress of 100 MPa could result in an 11.76% decrease in the peak-to-peak amplitude of the MFL signals. Compared with the analytical model, the change of the absolute value of the peak-to-peak amplitude is smaller, but it also has a significant influence when sizing the defect dimensions. The coupling FEM is proposed to provide a universal method for solving the effect of stress on the MFL signal, especially when the stress distribution around the defect is difficult to describe mathematically. Additionally, when a defect with greater stress gradients is distributed along the defect walls, it would lead to a significantly greater influence on the profile of the MFL signal. Furthermore, the percentage change will be even greater if the material has a higher relative permeability μ_r or a higher value of the magnetostriction coefficient *b*.

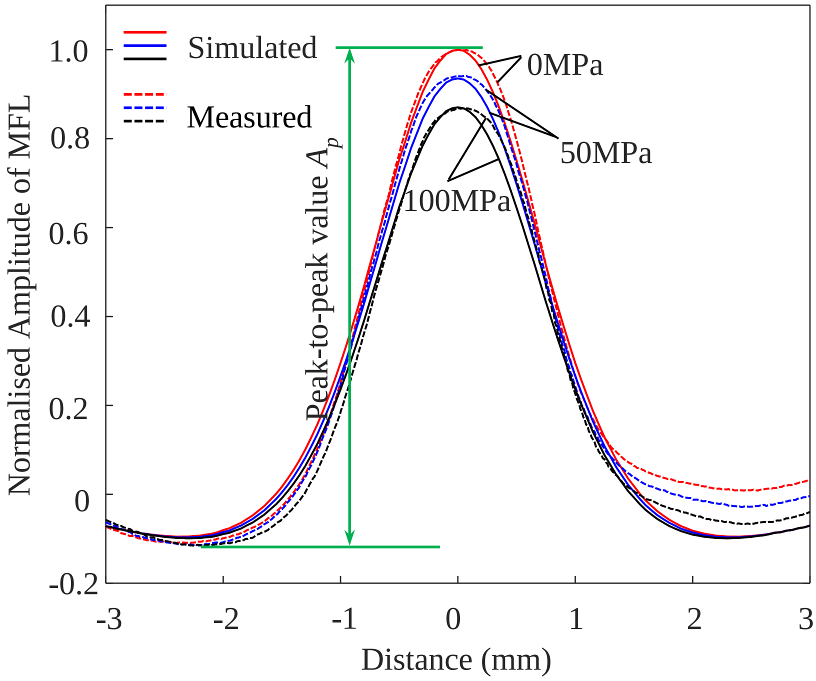

Figure 4.15. Normalised results of the axial components of MFL along the *z*-axis under various stresses.

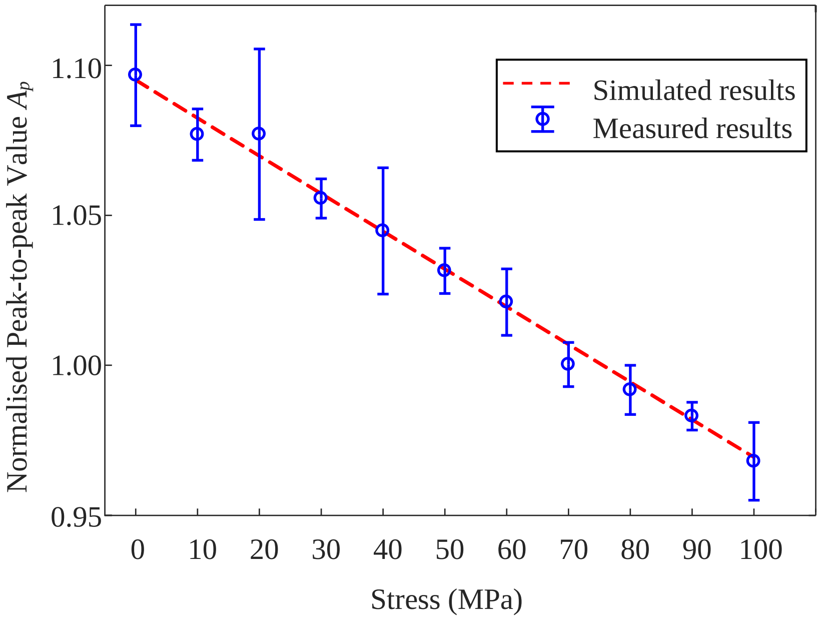

Figure 4.16. Measured and simulated peak-to-peak amplitudes of the normalised MFL signals obtained from different stress conditions.

Compared with the analytical model, FEM implements the full-scale simulation, avoids the assumption of magnetic charge, and breaks through the limitations of stress concentration and demagnetising factor computations. However, it should be noticed that there are still several limitations of the proposed FEM model. Firstly, prior to any stimulation, knowledge of certain specimen parameters is essential, including the parameters of J-A-S model and dimensions of the defect. As COMSOL uses an iterative method to solve the time-dependent problem, some parameters of the J-A-S model may result in nonconvergence, especially in the case of the magnetostriction coefficient b. If b is not properly chosen, the model will not perform well since stresses on some elements may be beyond the limits of the J-A-S model. Secondly, in this model, the material is set as isotropic steel, and the model is simplified as a 2D axisymmetric structure. Anisotropic materials can be solved via assigning various values to different components of the tensors, but only simply anisotropic problems may be solved rather than complex ones. When solving anisotropic problems, the model should be built as a 3D structure, which might also face a nonconvergence error since the magnetisation in an element is more complex than in the isotropic problem. Thirdly, during the experiments, the scanning speed may distort the MFL signal profile due to the eddy current effect. As the speed of the sensor was set to a relatively low value of 10mm/s in our experiments, the eddy current effect could be considered negligible here. In practical applications, the scanning speed may be considerably faster, and allowance for this velocity effect would need to implement.

4.4 Chapter Summary

This chapter has introduced the analytical model and proposed the FEM model for predicting the effect of stress on magnetic flux leakage. The analytical model, i.e., stress-dependent magnetic dipole model was discussed to predict the MFL signal induced by the cylindrical through-hole in the dog-bone like plate sample. The stress concentration around the defect resulting in the anisotropic distribution of magnetic properties along the defect surface was analysed and calculated using the classic

Timoshenko's theory. The J-A-S model was introduced to assess the distribution of stress-dependent magnetisation along the defect surface. Finally, the magnetic dipole model based on the stress-dependent magnetisation distribution was established to predict the dependency of the amplitude of the MFL signal on the applied stress. Verification experiments were arranged to measure the MFL under various stresses. The parabolic dependency of the measured peak-to-peak amplitude MFL on the applied tensile stress was observed, and it well fitted the results of the improved dipole model. In the case study, the tensile stress of 100MPa caused an increase of 24% in the peak-to-peak amplitude of the MFL signals. The analytical model provided a valuable tool to evaluate the contribution of stress to the induced MFL signals and could be used to solve the inverse problem for defect sizing. But the analytical model was only suitable to limited cases since only a few simple geometries where the stress concentrations and demagnetising factor could be calculated mathematically.

The multiphysics FEM method, which could deal with magnetomechanical problems, was proposed to simulate the MFL signal induced by the circumferential square-notch defect on the dog-bone shaped steel rod. The stress distribution of the specimen, especially the stress around the defect, was calculated in a solid mechanics module using a stationary solver. The results of the stress distribution were implemented as initial input values by the AC/DC magnetics module that was used to assess the distribution of stress-dependent magnetisation in the specimen based on the magnetomechanical model. Finally, the MFL fields with 1 mm lift-off were extracted in postprocessing to predict the dependency of the peak-to-peak amplitudes of the MFL signal on applied stress.

Experimental work was conducted to obtain the variation trend of the MFL signal influenced by applied stress. The measurements showed that the peak-to-peak value of MFL signal exhibited a decreasing trend with the action of increasing stress. It fitted the simulation results with a goodness of fit higher than 0.99. In this study, an increase in tensile stress of 100 MPa caused a decrease of 11.76% in the peak-to-peak amplitude of MFL signal. To size the defect accurately, the effect of stress on the MFL signal should be incorporated in the calibration process. The proposed multiphysics FEM model provided a valuable tool to evaluate the contribution of stress to the induced MFL signal and might be used to solve the inverse problem for sizing defects with a complicated stress distribution.

4.5 References for Chapter 4

[1] K. Mandal, D. Dufour, T. W. Krause, and D. L. Atherton. Investigations of magnetic flux leakage and magnetic Barkhausen noise signals from pipeline steel. *J. Phys. D. Appl. Phys.*, vol. 30, no. 6, pp. 962-973, 1997.

[2] K. Mandal and D. L. Atherton. A study of magnetic flux-leakage signals. *J. Phys. D. Appl. Phys.*, vol. 31, no. 22, pp. 3211-3217, 1998.

[3] Y. Wang, X. Liu, B. Wu, J. Xiao, D. Wu, and C. He. Dipole modeling of stress-dependent magnetic flux leakage. *NDT&E Int.*, vol. 95, pp. 1–8, 2018.

[4] V. E. Shcherbinin and N. N. Zatsepin. Calculation of the magnetostatic field of surface defects. I. Field topography of defect models. *Defectoscopy*, vol. 5, pp. 385–393, 1966.

[5] C. Edwards and S. B. Palmer. The magnetic leakage field of surface-breaking cracks. *J. Phys. D. Appl. Phys.*, vol. 19, no. 4, pp. 657-673, 1986.

[6] S. M. Dutta, F. H. Ghorbel, and R. K. Stanley. Dipole modeling of magnetic flux leakage. *IEEE Trans. Magn.*, vol. 45, no. 4, pp. 1959–1965, 2009.

[7] S. M. Dutta, F. H. Ghorbel, and R. K. Stanley. Simulation and analysis of 3-D magnetic flux leakage. *IEEE Trans. Magn.*, vol. 45, no. 4, pp. 1966–1972, 2009.

[8] M. Ravan, R. K. Amineh, S. Koziel, N. K. Nikolova, and J. P. Reilly. Sizing of 3-D arbitrary defects using magnetic flux leakage measurements. *IEEE Trans. Magn.*, vol. 46, no. 4, pp. 1024–1033, 2009.

[9] J. H. Hwang and W. Lord. Finite element modeling of magnetic field/defect interactions. *J. Test. Eval.*, vol. 3, no. 1, pp. 21–25, 1975.

[10] D. L. Atherton and M. G. Daly. Finite element calculation of magnetic flux leakage detector signals. *NDT&Int.*, vol. 20, no. 4, pp. 235–238, 1987.

[11] P.A. Ivanov, V. Zhang, C.H. Yeoh, H. Udpa, Y. Sun, S.S. Udpa and W. Lord. Magnetic flux leakage modeling for mechanical damage in transmission pipelines. *IEEE Trans. Magn.*, vol. 34, no. 5, pp. 3020–3023, 1998.

[12] V. Babbar, B. Shiari, and L. Clapham. Mechanical damage detection with magnetic flux leakage tools: modeling the effect of localized residual stresses. *IEEE Trans. Magn.*, vol. 40, no. 1, pp. 43–49, 2004.

[13] E. Altschuler and A. Pignotti. Nonlinear model of flaw detection in steel pipes by magnetic flux leakage. *NDT E Int.*, vol. 28, no. 1, pp. 35–40, 1995.

[14] L. Zhong, L. Li, and X. Chen. Simulation of magnetic field abnormalities caused by stress concentrations. *IEEE Trans. Magn.*, vol. 49, no. 3, pp. 1128–1134, 2012.

[15] D. C. Jiles. Coupled Magnetoelastic Theory of Magnetic and Magnetostrictive Hysteresis. *IEEE Trans. Magn.*, vol. 29, no. 4, pp. 2113–2123, 1993.

[16] D. C. Jiles. Theory of the magnetomechanical effect. *J. Phys. D. Appl. Phys.*, vol. 28, no. 8, pp. 1537-1546, 1995.

[17] S. Timoshenko and J. Goodier. Theory of elasticity (The third Edition). The McGraw Hill Education, 1970.

[18] C. Mandache and L. Clapham. A model for magnetic flux leakage signal predictions. *J. Phys. D. Appl. Phys.*, vol. 36, no. 20, pp. 2427-2431, 2003.

[19] J. A. Osborn. Demagnetising factors of the general ellipsoid. *Phys. Rev.*, vol. 67, no. 11–12, pp. 351-357, 1945.

[20] D. C. Jiles, J. B. Thoelke, and M. K. Devine. Numerical determination of hysteresis parameters for the modeling of magnetic properties using the theory of ferromagnetic hysteresis. *IEEE Trans. Magn.*, vol. 28, no. 1, pp. 27–35, 1992.

[21] Z. Li, Q. Li, C. Li, Q. Sun, and J. Lou. Queries on the JA modeling theory of the magnetisation process in ferromagnets and proposed correction method. *Proc. CSEE*, vol. 31, no. 03, pp. 124–131, 2011.

[22] J. P. A. Bastos and N. Sadowski. Magnetic materials and 3D finite element modeling. *CRC press*, 2013.

[23] A. J. Bergqvist. A simple vector generalization of the Jiles-Atherton model of hysteresis. *IEEE Trans. Magn.*, vol. 32, no. 5, pp. 4213–4215, 1996.

[24] B. Wu, Y. Wang, X. Liu, and C. He. A novel TMR-based MFL sensor for steel wire rope inspection using the orthogonal test method. *Smart Mater. Struct.*, vol. 24, no. 7, pp. 075007 (1-12), 2015.

[25] L. Mierczak. Evaluation of structural integrity of steel components by non-destructive magnetic methods. *Doctoral dissertation*, *Cardiff University*, 2015.

Chapter 5

Evaluation of the Effect of Temperature on Magnetic Flux Leakage

Assessing the direct effect of temperature only on magnetic flux leakage (MFL) signal is a complicated task due to the nonlinear coupling. If the temperature induces inner thermal stress, it makes the problem doubly difficult. Hence, only few models are available for predicting the MFL signal under this condition. To model the effect of temperature on MFL signal, the temperature-dependent magnetic dipole models are proposed. In the first case where the direct thermal effect is involved only, the dipole model is improved based on the modified temperature-dependent Jiles-Atherton (J-A) model. In the second case, where the combined effects of temperature and thermal stress are considered, the dipole model further introduces the magnetomechanical J-A model. The thermal stress distribution around the defect of a cylindrical through-hole is solved by thermoelastic and solid mechanics theories. The magnetomechanical theory is employed to analyse the stress-dependent magnetisation distribution, which is the key parameter in the magnetic dipole model. The experiments for verifying the direct effect of temperature are conducted on an M250-50A non-oriented (NO) grain silicon steel specimen with a cylindrical through-hole defect. In addition, the combined effects are experimentally studied on an adhesive structure of the defective NO steel and ceramic glass. The MFL signals predicted by both proposed models agree with the experimental results well. The proposed models can act as effective tools to understand the effects of the temperature and thermal stress on MFL signals, and they are also appropriate to solve the inverse problem of sizing the defects when the temperature is involved.

5.1 Introduction

In the previous chapter, the effect of stress on MFL has been investigated, while in this chapter, the effect of temperature on MFL will be studied. To the best of our knowledge, this topic has been investigated in a limited number of attempts. It is well known that most machines and structures are working at varying temperatures. Friction, Joule loss, eddy current, and so on could easily heat the devices. Besides, there are numbers of structures that are installed outdoors and experiencing various environmental temperatures, for example, railways and pipelines. The maximum value of magnetisation on the hysteresis curve has been experimentally observed to decrease more than 25% with the variation of 100 K [1–3]. According to magnetic dipole models [4,5], magnetisation, which is related to the surface magnetic charge density, could directly influence the MFL signal. Therefore, the change of temperature may significantly affect the MFL signal.

Besides, the temperature rarely independently influences on MFL signal. The thermally induced stress may also have a noticeable indirect influence on the MFL detection results. For example, the previous chapter has observed an increase of 24% in the peak-to-peak amplitude of the MFL signals caused by 100MPa tensile stress for the cylindrical hole defect in the plate. Mandal *et al.* [6] experimentally investigated the stress-dependent MFL signals in in-service oil and gas pipelines, whose amplitudes changed more than 40% caused by the line pressure stress. Under the action of an applied magnetic field, both direct and indirect effects of temperature can alter the localized magnetisation in the ferromagnetic material, further changing the MFL signal. However, it is hard to distinguish the contributions of the magnetic field, temperature, and thermal stress from the detected MFL signal due to the lack of an analytical or simulation model.

This chapter aims to propose improved magnetic dipole models considering the direct effect of temperature itself and the combined effects. The modelling object is a thin sheet specimen with a cylindrical through-hole. This chapter is organized as follows. In Section 5.2, the temperature-dependent dipole models are proposed based on the magnetothermal and magnetomechanical J-A hysteresis models. In Section 5.3, the details about the verification experiments including the specimen tempered procedure and the configuration of the MFL sensor are explained. Both the performance and limitations of the proposed model are discussed in Section 5.4. Finally, the major findings of this study are discussed in Section 5.5.

5.2 Temperature-dependent Magnetic Dipole Models

5.2.1 The model of the dependence of hysteresis on temperature

In this study, the temperature-dependent J-A model will be extended based on Raghunathan's models [1,2] using a reference temperature instead of absolute zero and developing an equation for the temperature-dependent reversibility factor, c, whose item for initial susceptibility previously was assumed to be a constant parameter. The thermal effect can be incorporated into the J-A model through five key temperature-dependent hysteresis parameters.

According to the Weiss theory of ferromagnetism, the spontaneous magnetisation M_s is the highest as the magnetic moments within a domain try to perfectly align when approaching absolute zero. As the temperature increases, it decreases until zero at the Curie point. Following an analogous argument to the spontaneous magnetisation equation given in [1,2], the dependence of saturation magnetisation, M_{st}, on temperature can be given by

$$M_{st}(T) = M_{st}(T_r) \cdot \left(\frac{T_c - T}{T_c - T_r}\right)^{\beta_1} \tag{5.1}$$

where $M_{st}(T_r)$ is the value of magnetisation at reference temperature (for example 20°C), which is more easily measured than that at 0 K, T_c is the Curie temperature, and β_1 is the material-dependent critical exponent following the mean field theory. In case $T_r = 0$ K, Equation (5.1) would turn to the original equation given in [1,2].

The domain wall pinning factor, k, is expected to exponentially decay with temperature analogous to the coercive field in a ferromagnetic material, according to the equation

$$k(T) = k(T_r) \cdot e^{\frac{1}{\beta_2} \cdot \frac{T_r - T}{T_c}} \tag{5.2}$$

where $k(T_r)$ is the pinning factor at the reference temperature, and β_2 is the critical exponent for the pinning constant.

The domain density, a, shows a similar exponential decay with temperature, which can be expressed as

$$a(T) = a(T_r) \cdot e^{\frac{1}{\beta_3} \cdot \frac{T_r - T}{T_c}} \tag{5.3}$$

where $a(T_r)$ is the domain density at the reference temperature, and β_3 is the critical exponent for domain density and is generally approximated to be equal to β_2.

The domain coupling, α, which represents the strength of magnetic interaction between domains in an isotropic material, can be expressed as

$$\alpha = \frac{3a}{M_{st}} - \frac{1}{\chi'_{an}} \tag{5.4}$$

At higher anhysteretic susceptibilities, χ'_{an}, the contribution of the second term to domain coupling is negligible and hence substituting the expression for M_{st} and a from (5.1) and (5.3) respectively yields

$$\alpha(T) = \alpha(T_r) \cdot e^{\frac{1}{\beta_3} \cdot \frac{T_r - T}{T_c}} \cdot \left(\frac{T_c - T_r}{T_c - T}\right)^{\beta_1} \tag{5.5}$$

where $\alpha(T_r)$ is the domain coupling at the reference temperature.

The reversibility factor, c, is treated in an analogous way to that of domain coupling, α, and, for isotropic materials, is expressed as

$$c = \frac{3a}{M_s} \chi'_{in} \tag{5.6}$$

The measured results in [7] showed that the initial susceptibility, χ'_{in}, also approximately exponential decayed and hence reversibility factor could be expressed as a similar equation to Equation (5.5) by substituting the expression for M_{st} and a from Equations (5.1) and (5.3), respectively

$$c(T) = c(T_r) \cdot e^{\frac{1}{\beta_3 \cdot \beta_4} \cdot \frac{T_r - T}{T_c}} \cdot \left(\frac{T_c - T_r}{T_c - T}\right)^{\beta_1} \tag{5.7}$$

where $c(T_r)$ is the reversibility factor at the reference temperature, and β_4 is the additional critical exponent by considering the temperature-dependent initial susceptibility.

Therefore, the *M-H* hysteresis model presented in Chapters 2 (Equation (2.45)) can be modified as

$$\frac{dM(T)}{dH} = \frac{\chi_M(T)}{k(T)\delta - \alpha(T)\chi_M(T)} \tag{5.8}$$

where

$$\chi_M(T) = \delta_m[M_{an}(T) - M(T)] + k(T)\delta c(T)\frac{dM_{an}(T)}{dH_e(T)} \tag{5.9}$$

5.2.2 The direct effect of temperature on MFL

In Chapter 4, the dipole model has been extended based on the previous research [4,5] to investigate the effect of stress on MFL field induced by a cylindrical through-hole defect on the carbon steel plate. Following the analogous idea, in this chapter, the dipole model is extended to study the effect of temperature on MFL field induced by a cylindrical through-hole defect in a thinner non-oriented (NO) electrical steel sheet, which could be faster and more evenly heated and cooled. The change of temperature results in overall magnetisation variation according to Equation (5.8) of the J-A model.

In this case, the element of d*S* carries a temperature-dependent magnetic charge of $d\rho_T$, which generates a magnetic field depending on the temperature, $d\mathbf{H}_T$, at a point *P*(*x*, *y*, *h*) in the space (analogous to Fig. 4.2). The formula for the calculation of the temperature-dependent magnetic field $d\mathbf{H}_T$ is

$$d\mathbf{H}_T = \frac{1}{4\pi}\frac{\mathbf{r}}{r^3}d\rho_T \tag{5.10}$$

where **r** is a vector pointing from the element of dS to the point of $P(x, y, h)$, and r is the distance between the dS and the point of P. The temperature-dependent magnetic charge density, ρ_T, on the surface element dS (see Fig. 4.2) is given by

$$d\rho_T = \mathbf{M_T} \cdot \mathbf{n} dS = M_T sin\theta dS \tag{5.11}$$

where

$$M_T = \left[\frac{\mu_{r_T}-1}{\mu_{r_T}-N_y(\mu_{r_T}-1)}\right] H_{e_T} \tag{5.12}$$

and

$$\mu_{r_T} = \frac{1}{\mu_0}\left[\frac{M(T)}{H_0}+1\right] \tag{5.13}$$

H_{e_T} is the effective magnetic field at a certain temperature, and N_y denotes the demagnetisation factor corresponding to the y-axis is given by [8]

$$N_y = \frac{\eta\pi^2-4}{4\pi\eta^2} \tag{5.14}$$

where $\eta = R/b \gg 1$. The demagnetisation factor depends on the applied magnetic field and defect shape and size.

The substitution of Equations (5.11) ~ (5.14) into Equation (5.10) the magnetic field generated by the magnetic charge can be computed from this expression:

$$d\mathbf{H}_T = \frac{1}{4\pi}\frac{\mathbf{r}}{r^3}\left[\frac{\mu_{r_T}-1}{\mu_{r_T}-N_y(\mu_{r_T}-1)}\right] H_{e_T} R sin\theta d\theta dz \tag{5.15}$$

The components of d$\mathbf{H}_T$ in the Cartesian coordinate system are given by

$$dH_{Tx} = \frac{M_T}{4\pi}\frac{r_x}{r^3} R sin\theta d\theta dz \tag{5.16}$$

$$dH_{Ty} = \frac{M_T}{4\pi}\frac{r_y}{r^3} R sin\theta d\theta dz \tag{5.17}$$

$$dH_{Tz} = \frac{M_T}{4\pi}\frac{r_z}{r^3} R sin\theta d\theta dz \tag{5.18}$$

The integration in Equations (5.16) ~ (5.18), along with Equation (5.8), can be performed using, e.g., the Runge-Kutta method. This improved magnetic dipole model provides a pathway to investigate the direct effect of temperature on the MFL signals.

5.2.3 The combined effects of temperature and thermal stress on MFL

The above presented model can calculate the direct effect of temperature itself on the MFL signal. However, the temperature gradient and variation in a sample may induce inner stress, which could significantly affect MFL results. Generally, the thermal stresses can be classified into two types: type 1 is caused by asymmetric temperature distribution in a structural component. For example, a long or sizeable structural component is exposed to gradient environmental temperatures such as railway

$$\varepsilon_{T1} = \zeta_T \cdot (T_1 - T_2) \tag{5.19}$$

And type 2 is resulted from two materials with different coefficients of thermal expansion (CTE) fixed together, such as multilayer plate

$$\varepsilon_{T2} = (\zeta_{T1} - \zeta_{T2}) \cdot (T_{ref} - T) \tag{5.20}$$

where ε_{T1} and ε_{T2} are the thermal strains induced by the types 1 and 2 respectively, and ζ_{T1} and ζ_{T2} are the larger and the smaller CTEs of two materials respectively, and T_{ref} is the reference temperature [9].

The thermal stress, σ, could be inferred from the thermal strain below elastic limitation [10]

$$\begin{bmatrix} \sigma_{xx} \\ \sigma_{yy} \\ \sigma_{zz} \\ \sigma_{xy} \\ \sigma_{xz} \\ \sigma_{yz} \end{bmatrix} = \frac{E}{(1+\nu)(1-2\nu)} \begin{bmatrix} 1-\nu & \nu & \nu & 0 & 0 & 0 \\ \nu & 1-\nu & \nu & 0 & 0 & 0 \\ \nu & \nu & 1-\nu & 0 & 0 & 0 \\ 0 & 0 & 0 & (1-2\nu)/2 & 0 & 0 \\ 0 & 0 & 0 & 0 & (1-2\nu)/2 & 0 \\ 0 & 0 & 0 & 0 & 0 & (1-2\nu)/2 \end{bmatrix} \begin{bmatrix} \varepsilon_{xx} \\ \varepsilon_{yy} \\ \varepsilon_{zz} \\ 2\varepsilon_{xy} \\ 2\varepsilon_{xz} \\ 2\varepsilon_{yz} \end{bmatrix} \tag{5.21}$$

where σ_{xx} and ε_{xx} are the *x*-axis component of thermal stress and strain, *E* is Young's modulus, and v is Poisson's ratio. Assuming there is no fixed constraint along the z-axis, for an isotropic lamination specimen, σ_{zz}, σ_{xz}, σ_{yz} are approximately equal zero, $\sigma_{xy} = \tau_{xy}$ and $\varepsilon_{xy} = \gamma_{xx}/2$, hence, Equation (5.21) can be simplified as

$$\begin{bmatrix} \sigma_{xx} \\ \sigma_{yy} \\ \tau_{xy} \end{bmatrix} = \frac{E}{(1+\nu)(1-2\nu)} \begin{bmatrix} 1-\nu & \nu & 0 \\ \nu & 1-\nu & 0 \\ 0 & 0 & (1-2\nu)/2 \end{bmatrix} \begin{bmatrix} \varepsilon_{xx} \\ \varepsilon_{yy} \\ \gamma_{xy} \end{bmatrix} \tag{5.22}$$

If there is no constraint along the *x*-axis, the sample can be considered expanding freely along the *x*-axis. Hence, the thermally induced strain along the *x*-axis approximates zero. Therefore, Equation (5.22) can be expressed as

$$\begin{bmatrix} \sigma_{xx} \\ \sigma_{yy} \\ \tau_{xy} \end{bmatrix} = \frac{E}{(1+\nu)(1-2\nu)} \begin{bmatrix} 1-\nu & \nu & 0 \\ \nu & 1-\nu & 0 \\ 0 & 0 & (1-2\nu)/2 \end{bmatrix} \begin{bmatrix} 0 \\ \varepsilon_{yy} \\ \gamma_{xy} \end{bmatrix} \tag{5.23}$$

Assuming the thermally induced inner stress of the steel sample along the *y*-axis parallel to the magnetic field, according to the analytical expressions reported by Timoshenko, the stress along the surface of the cylindrical through-hole defect can be expressed as [4,10]

$$\sigma_\theta = \sigma_{yy}(1 + 2cos2\theta) \tag{5.24}$$

According to magnetomechanical theories [4,11,12], the effective field is given by

$$H_e = H + \alpha M + \frac{3\sigma}{2\mu_0}\frac{d\lambda}{dM} = H + \tilde{\alpha}M \tag{5.25}$$

where magnetostriction

$$\lambda(\sigma, M) \approx \gamma_0 + (\gamma_{11} + \gamma_{12}\sigma)M^2 \tag{5.26}$$

Hence, the temperature-dependent *M-H* hysteresis model (5.8) can be modified as

$$\frac{dM(T)}{dH} = \frac{\chi_M(T)}{k(T)\delta - \tilde{\alpha}(T)\chi_M(T)} \tag{5.27}$$

Considering both thermal and thermal stress effects, the magnetisation, which is related to the surface magnetic charge density (ρ), along the defect wall can be expressed as

$$M_{T\sigma}(\theta)=\left\{\frac{\mu_{r_{T\sigma}}(\theta)-1}{\mu_{r_{T\sigma}}(\theta)-N_y\left[\mu_{r_{T\sigma}}(\theta)-1\right]}\right\}H_{e_{T\sigma}}(\theta) \qquad (5.28)$$

where

$$\mu_{r_{T\sigma}}(\theta)=\frac{1}{\mu_0}\left(\frac{M(T,\sigma,\theta)}{H}+1\right) \qquad (5.29)$$

and

$$H_{e_{T\sigma}}(\theta)=H+\tilde{\alpha}_T(\theta)M(T,\sigma,\theta) \qquad (5.30)$$

Hence, the spatial magnetic field generated by the magnetic charge can be modified as

$$d\mathbf{H}_{T\sigma}(\theta)=\frac{1}{4\pi}\frac{\mathbf{r}}{r^3}\left\{\frac{\mu_{r_{T\sigma}}(\theta)-1}{\mu_{r_{T\sigma}}(\theta)-N_y\left[\mu_{r_{T\sigma}}(\theta)-1\right]}\right\}H_{e_{T\sigma}}(\theta)Rsin\theta d\theta dz \qquad (5.31)$$

The components of d$\mathbf{H}_{T\sigma}$ in the Cartesian coordinate system are given by

$$dH_{T\sigma x}=\frac{M_{T\sigma}(\theta)}{4\pi}\frac{r_x}{r^3}Rsin\theta d\theta dz \qquad (5.32)$$

$$dH_{T\sigma y}=\frac{M_{T\sigma}(\theta)}{4\pi}\frac{r_y}{r^3}Rsin\theta d\theta dz \qquad (5.33)$$

$$dH_{T\sigma z}=\frac{M_{T\sigma}(\theta)}{4\pi}\frac{r_z}{r^3}Rsin\theta d\theta dz \qquad (5.34)$$

Equations (5.31) ~ (5.34), along with Equation (5.27), can be used to compute the magnetic field using the Runge-Kutta integration method. The improved magnetic dipole models explore a way to understand the effects of temperature and thermal stress on the MFL signal. Although the modified model is developed on a thin sheet sample, the applicability of the proposed model is not limited to such case only, and samples with other shapes can also be treated. For example, the stress distributions for elliptical holes and ellipsoidal inclusion in plate can be derived from the classical mathematical theory of elasticity [10]. Moreover, Trevino *et al.* [13] have improved the dipole model to simulate ellipsoidal defect shape and even more complicated defect shapes. These mathematical models provide the potential to analyse magnetic flux leakage around various shapes. Also note that the cylindrical hole used in this research is a particular case of elliptical hole defects.

5.3 Verification Experiments for Temperature-dependent MFL

5.3.1 The MFL experiments for the direct effect of temperature

The MFL experiments to study the direct effect of temperature itself on MFL are conducted on an M250-50A non-oriented (NO) grain silicon steel with 0.45mm in thickness, 30mm in width and 190mm in length. The sample with such dimensions could be fast and evenly heated/cooled the whole body. A cylindrical through-hole defect is machined at the geometric centre of the specimen with a radius of 2mm. One U-shape yoke wound by the exciting coil and the other yoke without coil are used to provide a steady static magnetic field for specimen magnetisation (as seen in Fig. 5.1). The coil is fed by 2 A direct current. According to the measurement of the Gaussmeter, it could provide about 1500 A/m magnetic field around the centre of the sample.

A Hall effect sensor (ACS70310LKTATN-010B5-C manufactured by ALLEGRO), which has ultralow thermal drift, high sensitivity and wide measurement range, is used to measure the MFL signal. A motorized XYZ linear translation stage from Thorlabs with a minimum achievable incremental movement of 0.1 µm is used to move the sensor along the sample surface in precise steps. The measurement setup is mounted on a non-magnetic breadboard located in the environmental chamber (HC4033 from Vötsch). Measurements are made by scanning the sensor across the centre of the through-hole defect, with a fixed scanning step size and sensitive element lift-off of 0.1 mm and 1.5 mm, respectively.

In the MFL experiments, the sample and the measurement set-up are refrigerated from 20℃ to -40℃ with a temperature decrement of 10 ℃ and then heated up to 60 ℃ with 10 ℃ increment. The temperatures are set step by step. At each set temperature point, such as 20 °C, 10 °C, and 0 °C, the measurement will not be implemented until the temperature is steadily for more than 10 minutes, which would allow even cooling or heating of the sample and avoid the effect of temperature variation. The measurements at each motion step are repeated 100 times, and the mean value is obtained. The entire process is repeated five times to reduce the measurement error.

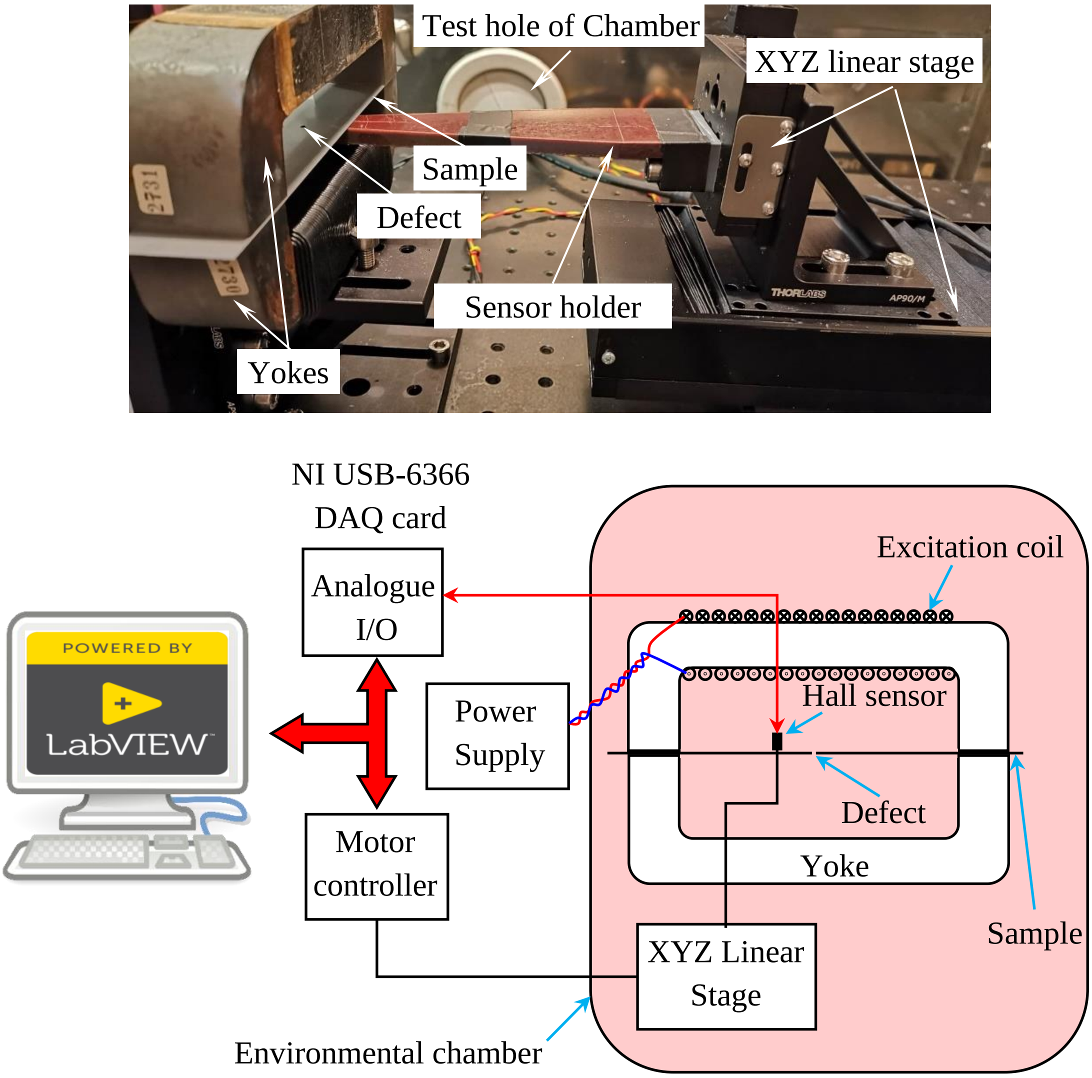

Figure 5.1. The experimental setup for the measurement of MFL induced by the defect on M250-50A NO steel.

Before the MFL experiment, the specimens were annealed at 400℃ for two hours to relieve the residual stress. Then, the hysteresis curves of the specimen without defect were measured at different temperatures by the quasi-static hysteresis measurement system (see Fig. 5.2) to determine the key parameters of the temperature-dependent J-A model. The computer-controlled system was developed in Wolfson

Centre for Magnetics, and its program was written in Labview providing high accuracy and automatic measurements.

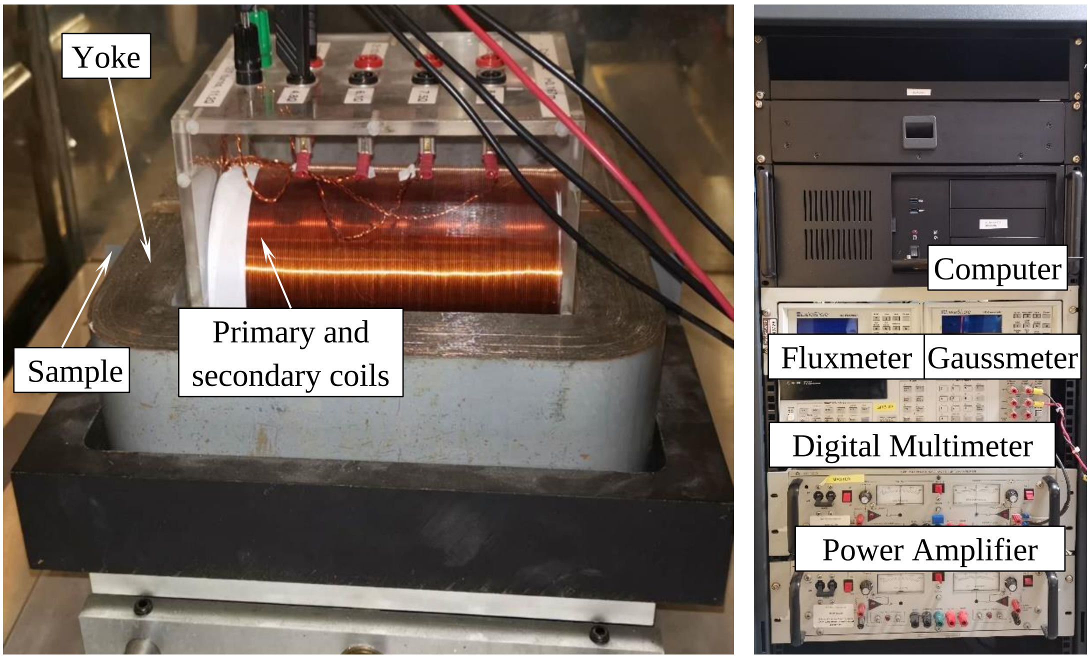

Figure 5.2. The quasi-static hysteresis measurement system.

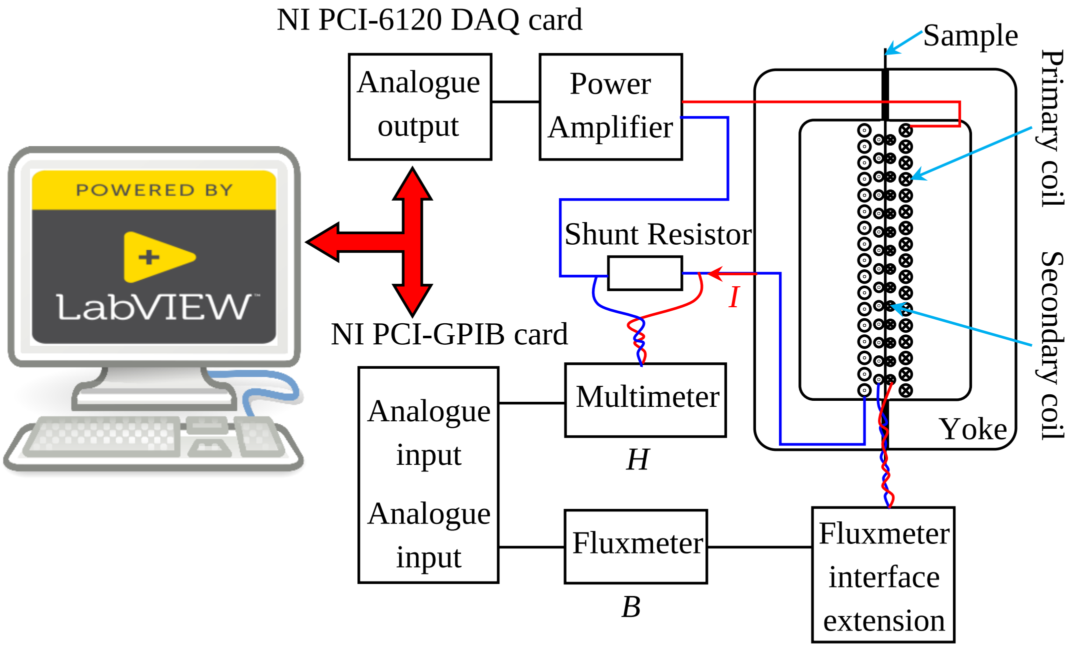

Figure 5.3. Schematic diagram of computer-controlled DC magnetic property measurement system.

Fig. 5.3 shows a schematic diagram of the system. It includes a computer with Labview, a NI PCI-6120 data acquisition (DAQ) card, a PCI-GPIB card, a power amplifier, a high precision 0.3 Ω shunt resistor, a fluxmeter and a digital multimeter, a double horizontal yoke, a primary coil and a secondary coil. During testing, the Epstein strip sample is magnetised using the primary coil and yoke composed electromagnet driven by quasi-DC current (5 mHz) supplied from NI PCI-6120 DAQ card and subsequently amplified using the power amplifier. The resulting strength of applied magnetic field H is calculated from the measured voltage on the shunt resistor V_R

$$H = \frac{N_1 V_R}{l_m R_{sh}} \tag{5.35}$$

where N_1 is the turns number of the primary coil, l_m is the mean path length, which is the distance between the inner edges of the yoke, and R_{sh} is the resistance of the shunt resistor. Simultaneously, the magnetic flux density B is picked up by GPIB linked fluxmeter integrating the voltage of secondary coil using

$$B = \frac{l \rho_m}{N_2 m} \int e dt \tag{5.36}$$

where l is the specimen length, ρ_m is the density of the sample, m is the mass of the sample, N_2 is the turns number of the secondary coil, and e is the secondary voltage.

5.3.2 The MFL experiments for the combined effects of temperature and thermal stress

In the MFL experiments that study the combined effects of temperature and thermal stress on MFL (see Fig. 5.5), the 0.45 mm NO steel is glued to the ceramic glass (Schott Zerodur), whose CTE (1×10^{-7} °C^{-1}) is much smaller than NO steel (11.9×10^{-6} °C^{-1}), at room temperature (20 °C). As the maximum thermal stress should be less than the nominal yield stress of the NO steel (344 MPa), the minimum temperature should be higher than -20 °C. Besides, when the temperature is higher than room temperature, the NO steel is compressed, and it could cause the sample bending, which makes the calculation much more complicated and uncertain. Therefore, the measurements similar to the first MFL experiment are repeated between -10 °C and 20 °C.

The experiments outside the temperature range aforementioned are also conducted. Before doing the measurements in the temperature range from 30 °C to 60 °C, the sample needs to be taped on the ceramic glass to reduce the change of lift-off caused by bending. Since in range -40 °C to -20 °C the temperature may induce plastic deformation, the experiments in this range are implemented at the last of the measurement procedure.

The experimental conditions related to this work can be described via the second type of thermal stress, where two components with different CTE are fixed together as shown in Fig. 5.4. The measurement processing is analogous to the aforementioned first kind of MFL experiments. Though the non-magnetic ceramic glass is inserted into the yoke gap, which decreases the magnetic field to around 800 A/m, it is still high enough for the soft magnetic material NO steel.

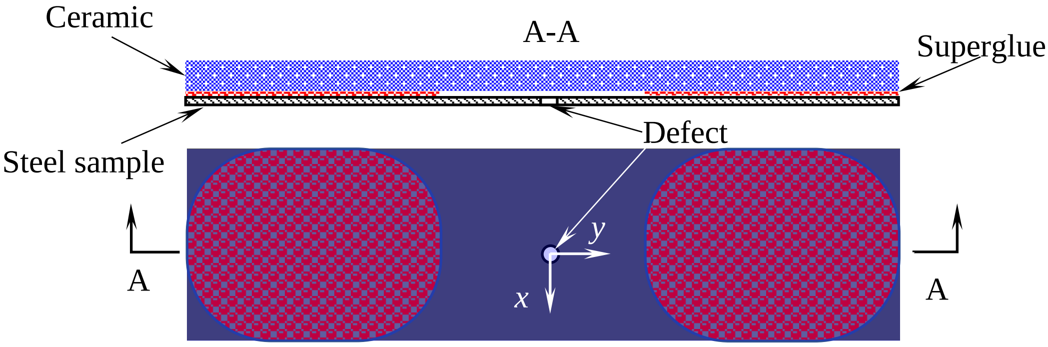

Figure 5.4. The thermally induced stress structure

Prior to the second kind of MFL experiments, the key parameters of magnetostriction are measured by the AC magnetostriction system as shown in Fig. 5.6. During testing, the large NO strip is inserted into a Polytetrafluoroethylene (PTFT) former, which is wound by the primary and secondary coils. A feedback control system is used to control the flux density and secondary induced voltage waveforms to be sinusoidal. More details about the AC measurement system will be introduced in Chapter 7. One end of the strip is fixed, and the other end is attached to an accelerometer, which is assembled on a load cell linked to a pneumatic cylinder. The system can apply a range of stress from -10 MPa to 10 MPa by controlling the pneumatic valve and compressed air pressure. When the strip is magnetised, its free end elongates or contracts due to magnetostriction. The instantaneous magnetostriction is calculated from double digital integration of the output of the accelerometer

$$\lambda(t) = \frac{1}{k_\sigma l_m} \iint V_o dt + C \tag{5.37}$$

where k_σ is the sensitivity of the accelerometer, V_o is the output voltage of the accelerometer, and C is the integration constant.

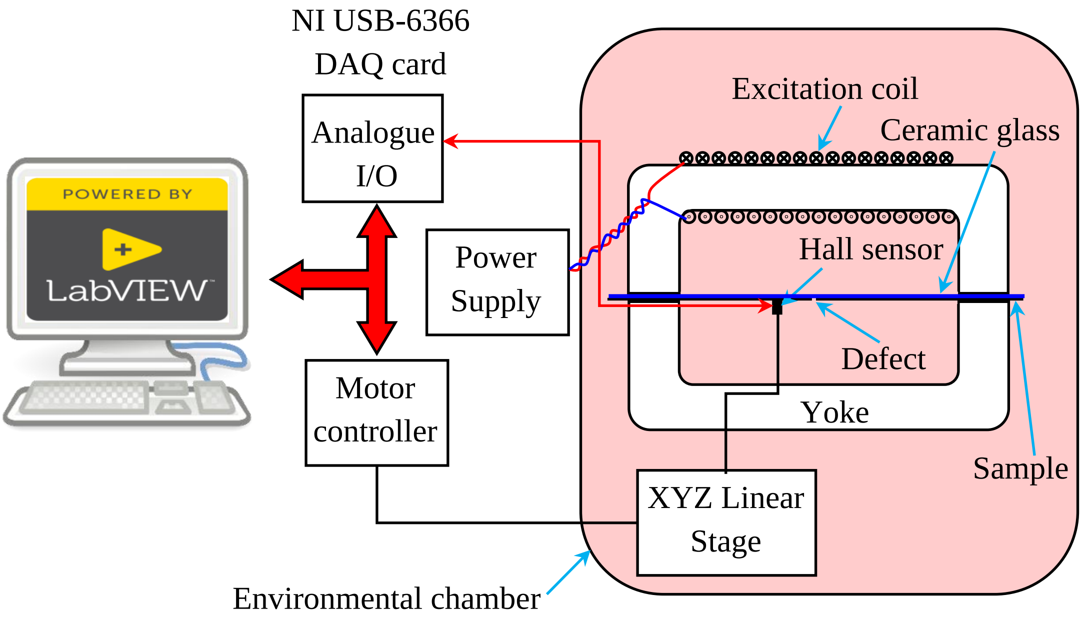

Figure 5.5. The experimental setup for the measurement of MFL induced by the defect on M250-50A NO steel.

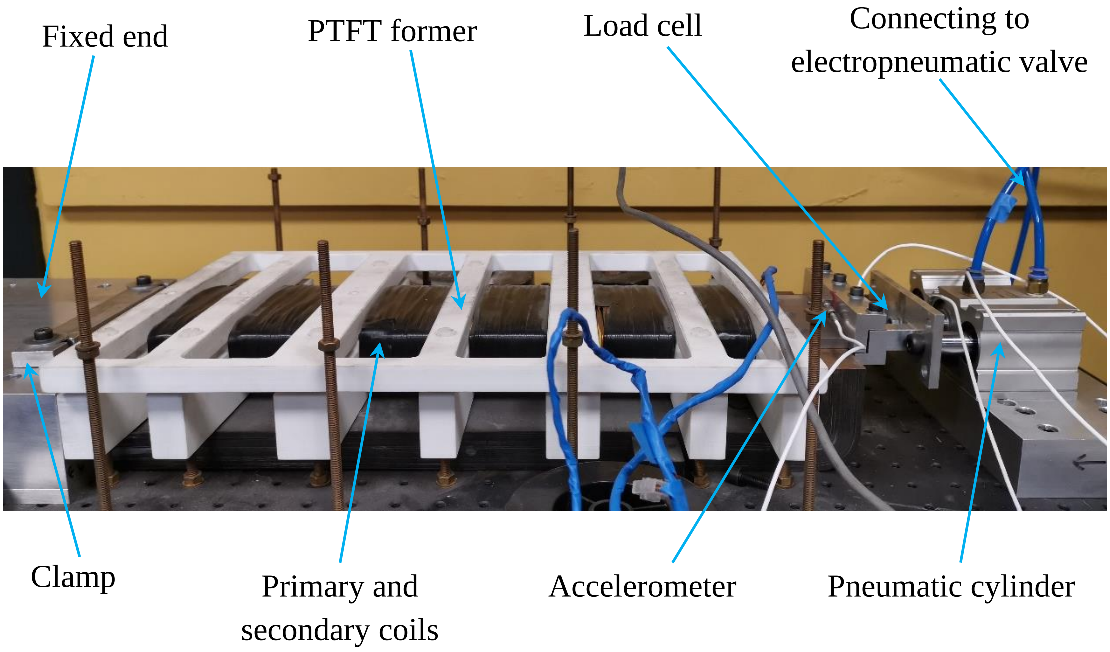

Figure 5.6. Photograph of the AC magnetostriction measurement system.

The measured magnetostriction curve is plotted in Fig. 5.12, and its values are listed in Table 5.2. Besides, Young's Modulus (E) and Poisson's Ratio (ν) are determined and listed in Table 5.2 as well.

5.4 Discussions for the Simulated and Measured MFL Results Affected by Temperature

5.4.1 The direct effect of temperature on MFL

The dipole modelling of MFL under various temperatures starts from the determination of key parameters J-A model. The tested NO steel sample is subjected to various temperatures using the environmental chamber. Magnetic hysteresis loops are obtained using a computer-controlled hysteresis loop tracer at a quasi-DC field of 5 mHz. The experimental results of hysteresis loops of M250-50A NO steel at different temperatures are illustrated in Fig. 5.7, where the maximum absolute values of induced magnetic flux density (B) decrease with the increase of temperature. It should be noted that the changes in magnetic parameters are small as shown in Figure 5.7, since the measurement temperatures are far from Curie point and the environmental temperature range is much narrower than that from 0 K to Curie point. The difference between the maximum and minimum saturation magnetic flux density is less than 0.8%. Theoretically, the change in saturation magnetic flux density should be near a linear function of temperature according to the temperature-dependent hysteresis model. But it can be found that there is an error between experimental and theoretical results. The computer-controlled hysteresis loop tracer designed for electrical steel hysteresis loop measurement has been proven to possess high accuracy and good repeatability. Besides, in the narrow region where the difference between saturation flux density is less than 0.8%, the hysteresis loop tracer can distinguish the saturation flux densities of hysteresis loops under different temperatures seriatim and clearly, as shown in Fig. 5.7. Therefore, the measurement error is acceptable. Furthermore, during the fitting process of temperature coefficient β_1~β_4 using binomial series and exponential function to the identified parameters of J-A model, the outliers will be excluded, and the values of the parameters will be reallocated to help to redress the slight measurement error.

Table 5.1. The temperature-dependent parameters of J-A model for M250-50A non-oriented electrical steel

	Parameters	value	Sources
Parameters of J-A model at 20°C	Reversibility parameter, c	0.6799	Measured and fitted using hybrid GA-PSO algorithms
	Pinning parameter, k	103.8603 (A/m)	
	Domain density, a	65.5559 (A/m)	
	Saturation magnetisation, M_s	1.7157×10^{6} (A/m)	
	Coupling factor, α	1.2493×10^{-4}	
The coefficients of the temperature-dependent J-A model	The thermal coefficient for magnetisation, β_1	0.3981	
	The thermal coefficient for pinning constant, $\beta_2\approx\beta_3$	0.2336	
	The thermal coefficient for reversibility factor, β_4	1.7220	

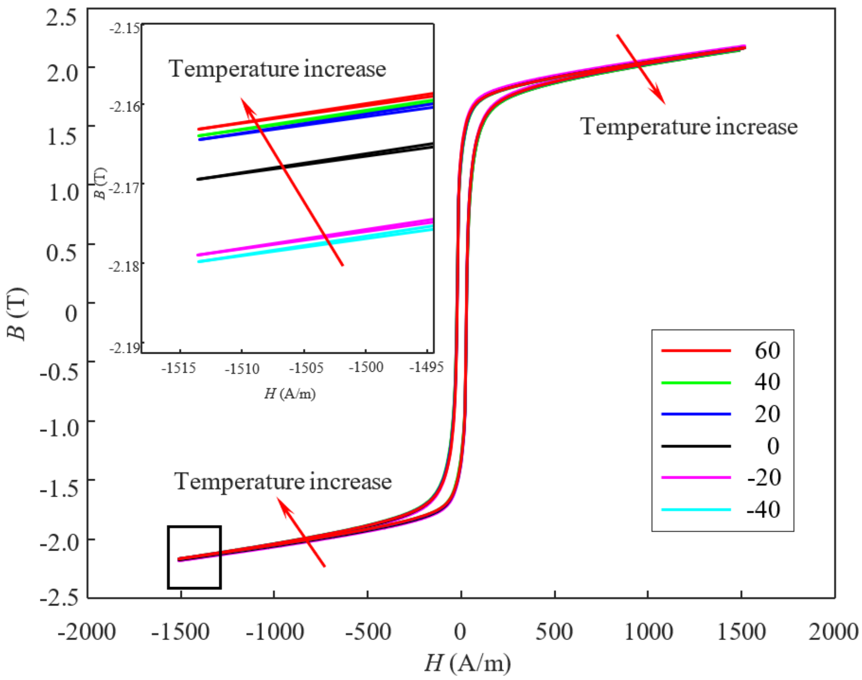

Figure 5.7. Hysteresis loops of M250-50A NO silicon steel at various temperatures.

The hybrid GA-PSO algorithm [14,15] (GA and PSO stand for Genetic Algorithm and Particle Swarm Optimisation respectively) is used to identify the parameters of the temperature-dependent J-A model, which are listed in Table 5.1. GA [16] is a stochastic optimisation technique founded on the concepts of natural selection and genetics. The algorithm starts with a set of solutions called population. Solutions from a population are used to form a new population. This is motivated by the hope that the new population will be better than the old one. Solutions that will form new solutions are selected according to their fitness: the more suitable they are, the more chances they have for reproduction. This is repeated until some condition (for example, number of generations or improvement of the best solution) is satisfied.

PSO [15] is an evolutionary computation technique developed by Kennedy and Eberhart in 1995. PSO is initialized with a population of random solutions called particles. Each particle is also associated with a velocity. Particles fly through the search space with velocities that are dynamically adjusted in a collaborative way. Therefore, particles tend to fly towards the optimal solution(s).

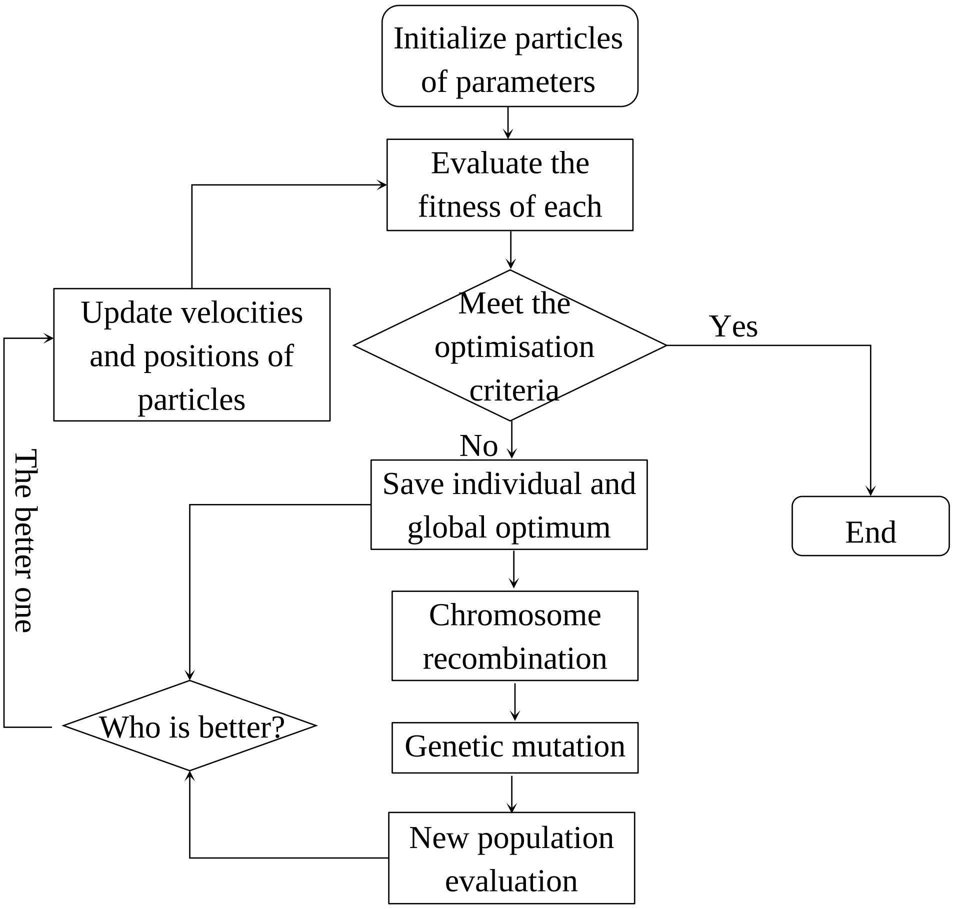

Figure 5.8. Hybrid GA-PSO optimisation procedure [14,15].

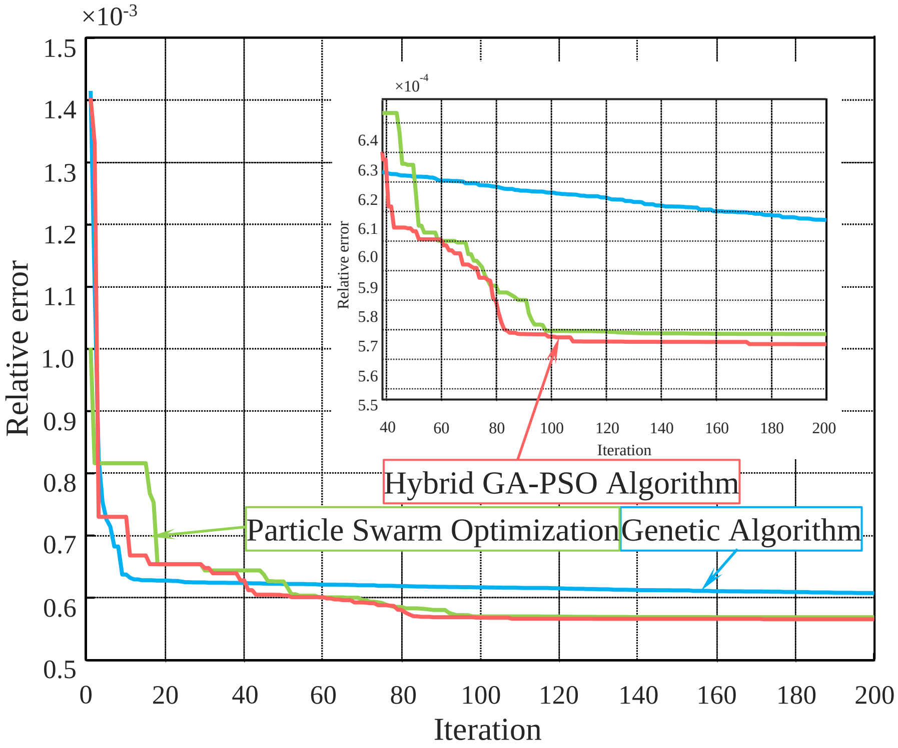

Figure 5.9. The iteration process of GA, PSO and hybrid GA-PSO algorithms.

GA can avoid traps in local minima while PSO converges rapidly. The hybrid GA-PSO algorithm combines the most appealing features of the two different algorithms. In addition, the PSO algorithm also provides appropriate initial values within a finite number of trials for their use in the other algorithm (GA), allowing it to converge rapidly towards the global minimum. Its procedure and iteration are illustrated in Figs. 5.8 and 5.9 respectively.

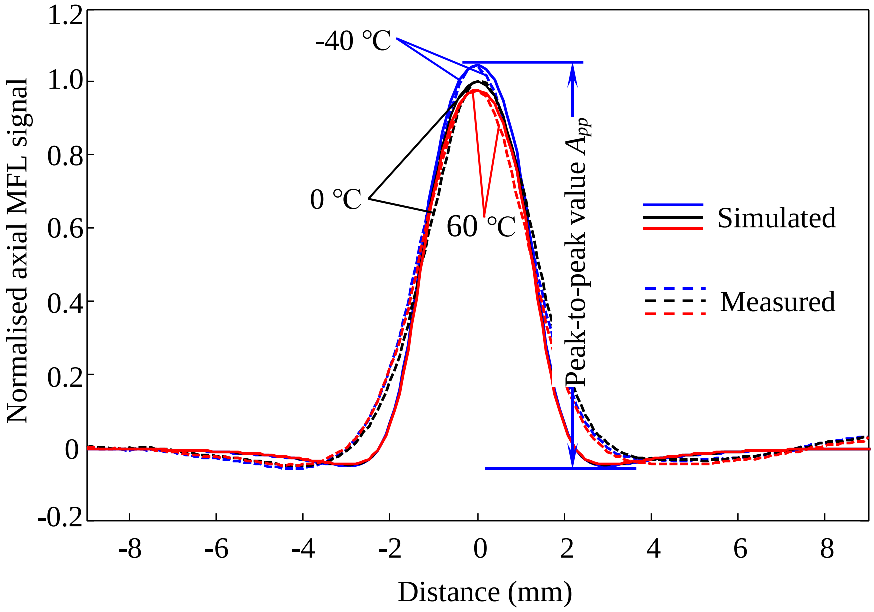

Figure 5.10. The measured (dashed lines) and simulated (solid lines) axial components of MFL along the *y*-axis under different temperature conditions.

The simulated MFL results along the y-axis at -40 °C, 20 °C and 60 °C as examples are plotted in Fig. 5.10 comparing with the results obtained from measurements. All the simulated MFL signals are normalised by the maximum amplitude of the MFL signal at 20 °C. The same operation is applied to the measured MFL signals. It can be found that both the shape and highest amplitude of the simulated MFL signals are consistent with the measured ones. It indicates that the proposed dipole model is adequate to predict the temperature-dependent MFL accurately. The distances between two minimum values of the measured MFL signals are slightly narrower than those of the simulation. It may be caused by the effect of magnetic compression [17], which is not considered in the analytical model. But this will have little influence on sizing the defect as the simulated widths of half-peak agree with the experimental ones.

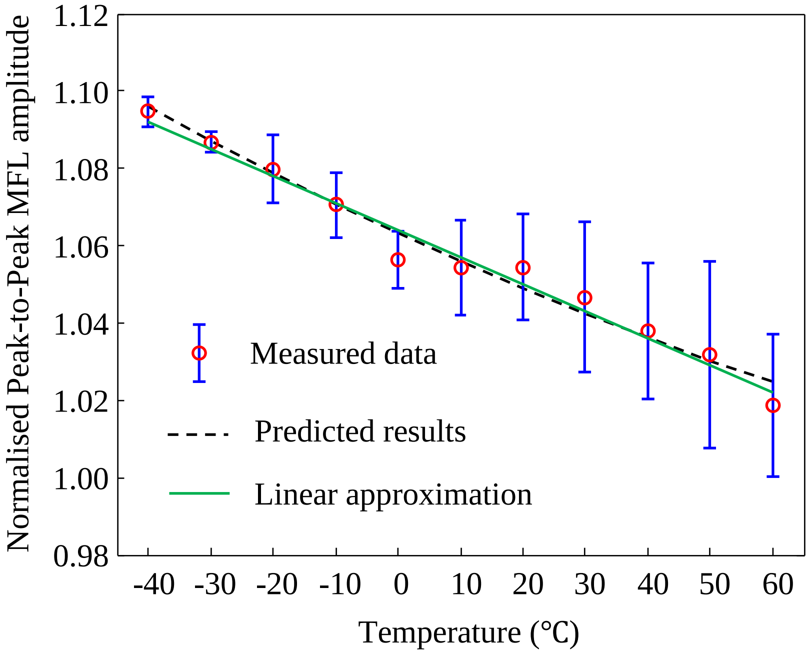

Figure 5.11. The measured and predicted peak-to-peak amplitudes of the normalised MFL signals obtained from different temperatures.

To evaluate the relationship between the MFL signal and the temperature quantitatively, the peak-to-peak amplitudes (A_{pp}) of the normalised MFL signals are estimated and plotted in Fig. 5.11. It can be found that the dependence of MFL peak-peak amplitude on the temperature obtained from the experiment corresponds with the simulated ones with a coefficient of determination (R^2) higher than 0.9. When the temperature range expands wider, an approximately exponential decrease will be demonstrated since the key parameters of J-A model exponentially decrease with the increase of temperature. Hence, though the increase of temperature from -40°C to 60°C results in the decrease of the peak-to-peak amplitude of the MFL signals by just 6.10%, it does not mean that the effect of temperature can be omitted when defect dimensions are estimated by MFL method. Besides, in the case that the environmental temperatures are far from Curie Temperature, after expanding the exponential function and binomial series using Taylor series expansion and omitting the high-order and infinitesimal items, it would show an approximately linear function. Therefore, the value of A_{pp} shows an approximately linear decrease with the increase of temperature from -40 °C to 60 °C with a goodness of fit higher than 0.9 as well.

5.4.2 The combined effects of temperature and thermal stress on MFL

Before calculating the MFL field influenced by temperature and thermal stress, the magnetostriction coefficients need to be determined. The magnetostriction (λ) *vs* magnetisation (M) butterfly loop measured at 0 MPa is plotted in Fig. 5.12. The magnetostriction butterfly loop is more complex than that measured at a low magnetic field [12,18,19] since the domain activities experience more complex processes. Taking the excursion of magnetostriction with magnetisation in the positive half of the magnetisation cycle of M250-50A NO steel that is cut parallel to the rolling direction for instance, at low magnetic field marked as region ***a***, the external field moves the domain walls leading to the increase of the volume of the domains closest to the field at the sacrifice of the other domains. In this region, the magnetostriction results from the motion of the 90° and 180° domain walls. Due to the displacement of 180° domain walls the suppression of 90° domain walls, the sample elongates slightly with the magnetisation until 1.0×10^6 A/m. Besides, the magnetostriction may also excurse a slight decrease due to the reversible magnetisation and domain rotation. With the increase of magnetisation in region ***b***, the annihilation of the 180° walls starts, and the 90° domain walls rotate towards the magnetic field direction. These result in the rapid increase of magnetostriction with magnetisation, and finally the magnetostriction reaches its saturation in region ***c***, where the domain closest to the field occupies the whole grain. But continuing to increase the magnetic field, the rotation of the domain becomes dominant in the magnetisation of the whole specimen. Since the spontaneous elongation of the domain becomes smaller or even negative when the domain magnetisation rotates from the crystal axis [20], the magnetostriction decreases with magnetisation as shown in region ***d***. When the magnetisation drops from its maximum value, the domains rotate back to its crystal axis in region ***e*** and then the 90° domain walls re-emerge in region ***f***. In region ***g***, the magnetostriction sharply decreases to zero at 8.7×10^5 A/m and with the decrease of magnetisation, the magnetostriction reaches its minimum value around -0.07 μm/m. It finally returns back to zero at $M = 0$ A/m in region ***h***. It can be found that the change of magnetostriction from saturation to zero is much faster than that from zero to saturation due to the anisotropic energy of the grain [21]. The upward and return curves of the butterfly loop follow different paths due to the irreversible magnetisation process in domains [22].

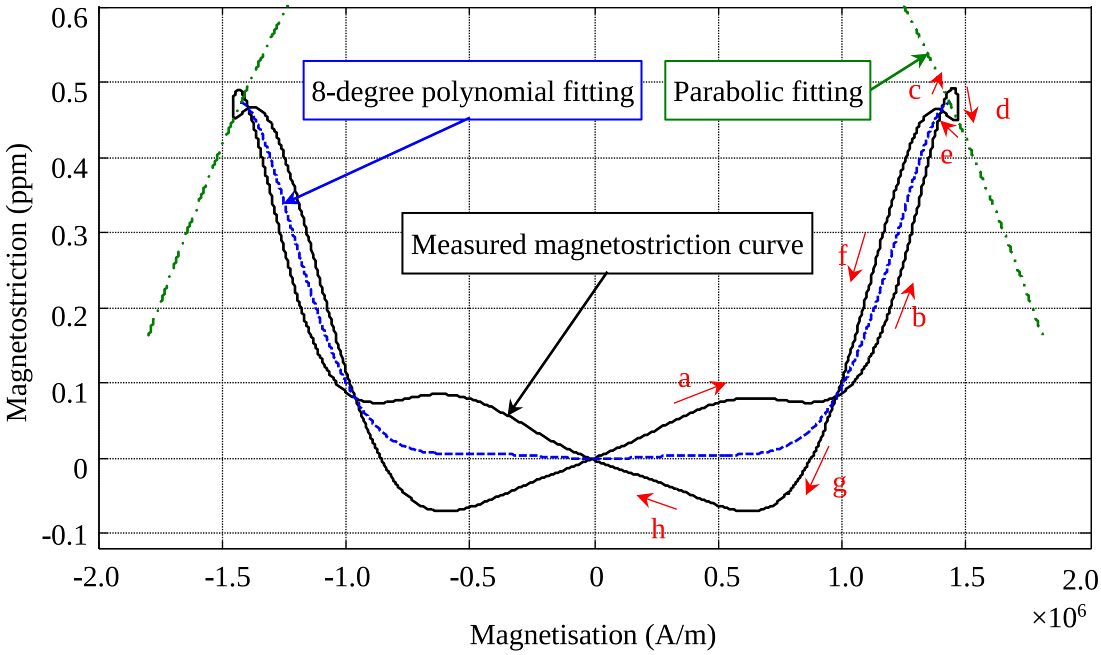

Figure 5.12. The measured magnetostriction butterfly loop for M250-50A NO steel without external stress.

To fit the complicated magnetostriction loop is not an easy task. Jiles *et al.* [23] proposed an infinite series to empirically model the relation between magnetostriction and magnetisation. For example, the eight-degree polynomial could approximate the average of magnetostriction as shown in Fig.5.12. However, it is impossible to model the stress-dependent MFL due to the infinite or massive parameters. The magnetostriction is generally simplified as a parabolic function of magnetisation as expressed in Equation (5.26). Since the sample is magnetised at high field, the parabolic approximation is fitted at high magnetisation in regions ***c*** to ***e*** of the λ *vs* M

curves, and the coefficient γ_{11} is determined as -2.58×10^{-19} ($A^{-2}\cdot m^{2}$). The determination of the coefficient γ_{12} needs the fitting to the magnetostriction measured under stress. But the value of γ_{12} is so small that the fitting result may be altered significantly with slightly different measured loops. Taking the terms $\gamma_{11}+\gamma_{12}\sigma$ in Equation (5.26) as one coefficient, it could obtain a few parabolic fitting coefficients under various stresses as shown in Fig. 5.13. The slope of the coefficient as a linear function of stress can determine the value of γ_{12}, which is around 7.37×10^{-27}($A^{-2}\cdot m^{2}\cdot Pa^{-1}$) according to the measurements.

Table 5.2. The parameters of magnetomechanical J-A model for M250-50A NO electrical steel

	Parameters	value	Sources
Magnetostriction coefficients	γ_{11}	-2.58×10^{-19} ($A^{-2}\cdot m^{2}$)	Fitting to the measured curves
	γ_{12}	7.37×10^{-27} ($A^{-2}\cdot m^{2}\cdot Pa^{-1}$)	
Coefficient of thermal expansion	CTE of ceramic glass	1.00×10^{-7} °C^{-1}	[24,25]
	CTE of NO steel	11.90×10^{-6} °C^{-1}	
The parameters of elastic mechanics	Young’s Modulus, E	205.00 (GPa)	[26]
	Poisson’s Ratio, ν	0.28	

Due to elastic limitation in tension and bending in compression, there is only a limited temperature range that is suitable for the model verification. The MFL signals simulated and measured at -10°C, 0°C, 10°C, and 20°C are respectively normalised by the maximum amplitude of the calculated and experimental MFL signal at 20°C, where the stress is 0MPa. The predicted MFL results along the *y*-axis are plotted in Fig. 5.14 comparing with the results obtained from experiments. It can be found that both the shape and highest amplitude of the predicted MFL signals approximate the experimental results, which manifests that the proposed dipole model is adequate to predict the combined effect of temperature and thermal stress on MFL with high accuracy.

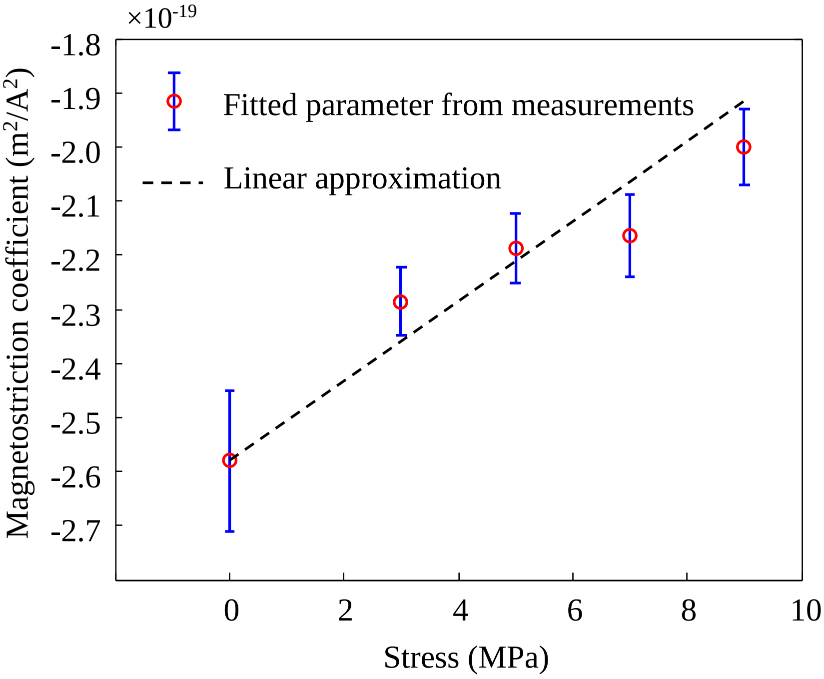

Figure 5.13. The magnetostriction coefficient of M250-50A NO steel fitted under various stresses using parabolic function.

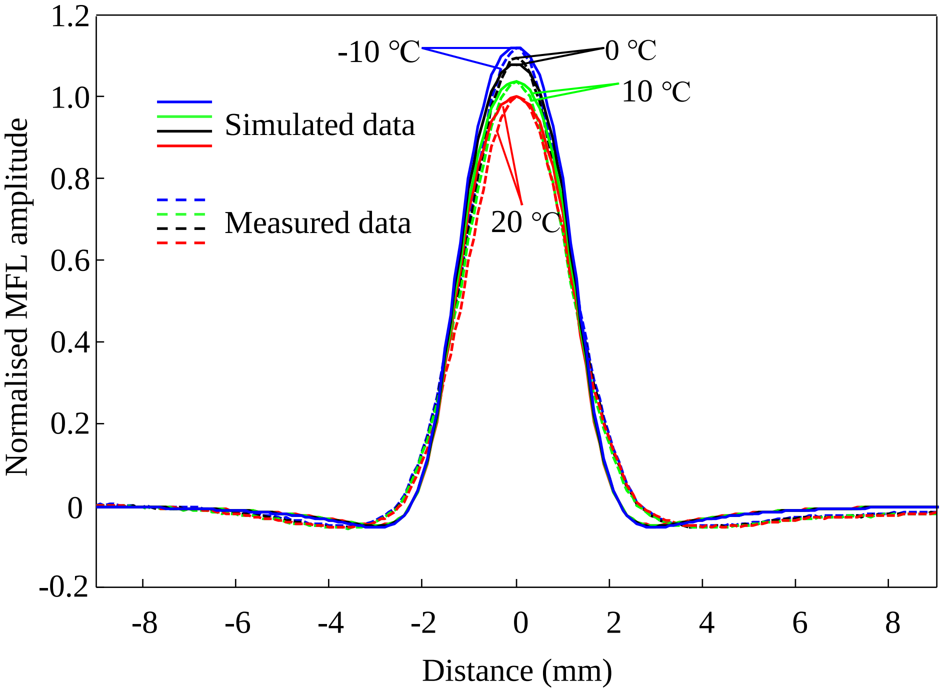

Figure 5.14. The measured (dashed lines) and simulated (solid lines) axial components of MFL along the *y*-axis under different temperature conditions.

To evaluate the relationship between the MFL signal and the temperature quantitatively, the peak-to-peak amplitudes (A_{pp}) of the normalised MFL signals are calculated and plotted in Fig. 5.15. It can be found that the dependence of A_{pp} on the temperature obtained from the experiment corresponds with the simulated ones with a coefficient of determination higher than 0.9. The value of A_{pp} demonstrates the approximately linear decreasing trend with increasing temperature from -10°C to 20°C. The temperature dropping of 30°C from room temperature results in an increase of 6.87% in the amplitude of the MFL signal, which is much larger than that considering thermal effect only (2.04%). Hence, it needs to be considered in precise defect sizing using the MFL method.

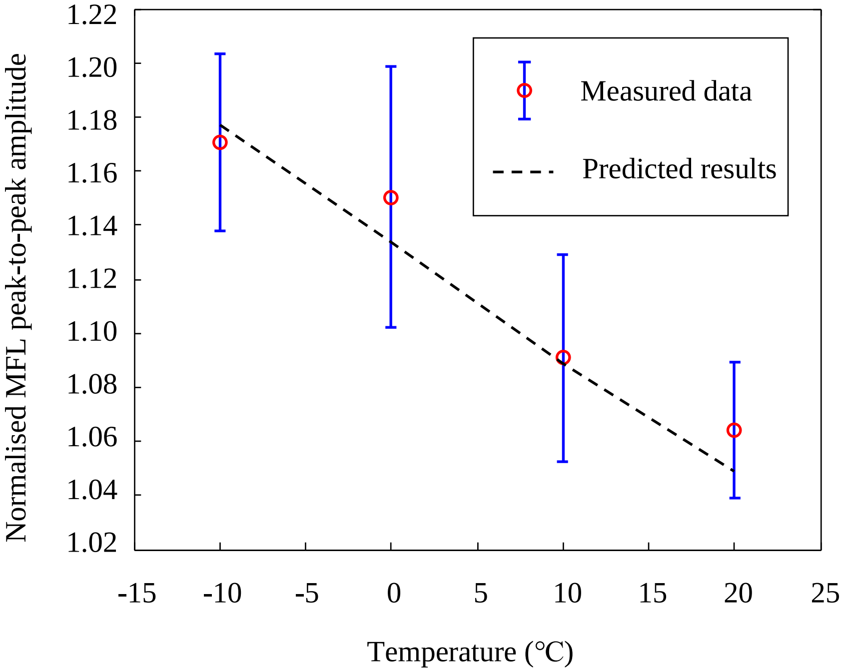

Figure 5.15. The measured and predicted peak-to-peak amplitudes of the normalised MFL signals obtained from different temperatures.

Both the shapes and the highest amplitudes of the predicted MFL signals are close to the measured results, indicating that the proposed improved dipole model is adequate to predict the effect of temperature itself and the combined effect of temperature and thermal stress on MFL with high accuracy. However, several limitations of the proposed magnetic dipole model should be stated. First of all, before the application of the temperature-dependent dipole model, prior knowledge of the material and defect should be acquired, including the hysteresis curve of the material measured at various temperatures, its magnetostriction loops obtained at different stress conditions and the stress distribution around the defect. Besides, the model is not adequate to precisely deal with the defects with complex shapes due to the difficulty in calculating the demagnetising factor. Furthermore, one of the factors that limit the applicability of the J-A magnetomechanical model using Equations (5.28) ~ (5.34) to simulate the MFL signal is the domain coupling factor α. In this case, its value is so small that it can easily become lower than zero with thermal stress using Equation (5.25). Therefore, there are a few areas on the defect wall that cannot be calculated using the dipole model when the temperature is far from the reference temperature. These blank data are filled using cubic spline interpolation since the heterogeneous distribution of magnetisation follows periodic change with angle. In the case of outliers during interpolating, the maximum and minimum interpolation values should be limited. But it is necessary to mention that the model would work better in a magnetically harder material.

For a defect with a given shape and size, since the relative permeability satisfies $\mu_r(\theta)>>1$, the differential of both sides of Equation (5.33) with respect to the temperature can be approximated to the differential with regard to thermal stress to simplify the evaluation of the effect of temperature on the MFL signal

$$\frac{\partial H_{T\sigma y}}{\partial T} \approx K\left(\frac{\partial \tilde{\alpha}}{\partial T} \cdot M + \frac{\partial M}{\partial T} \cdot \tilde{\alpha}\right) \approx K(\frac{\partial \tilde{\alpha}}{\partial \sigma_T} \cdot M + \frac{\partial M}{\partial \sigma_T} \cdot \tilde{\alpha}) \qquad (5.38)$$

where K is related to the geometrical size. Equation (5.38) has been proven to be an approximate four-order polynomial [4]. If omitting the high-order items, the dominant contribution should be owed to

$$\frac{\partial \tilde{\alpha}}{\partial \sigma_T} = \frac{(3\gamma_{11} + 6\gamma_{12} \cdot \sigma)}{\mu_0} \qquad (5.39)$$

The experiments in the cases of the temperature exceed the limited range are carefully conducted. The measured peak-to-peak values of MFL signals after normalisation are plotted in Fig. 5.16. It can be found that a parabolic approximation could well fit the measured data with a goodness of fit higher than 0.9. For the ease of visual analysis, the parabolic dependency of the amplitude of the MFL amplitude on the combined effect of temperature and thermal stress is concluded. Temperature cooling from 60 °C to -40 °C leads to an increase of 35.99% in the amplitude of MFL signals and should be considered in the inverse problem for defect sizing.

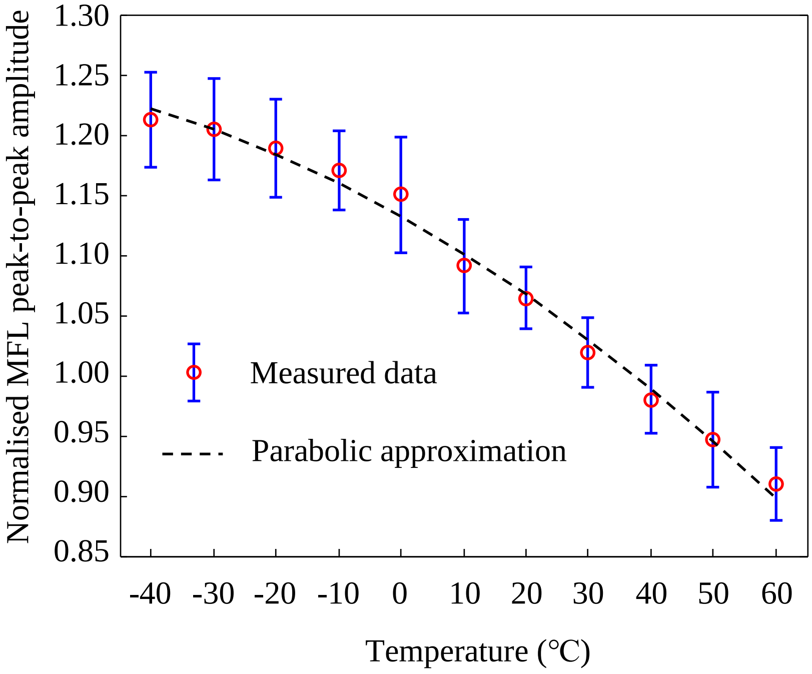

Figure 5.16. The approximation of MFL peak-to-peak amplitude as a parabolic function of temperature.

5.5 Chapter Summary

The temperature-dependent dipole models were proposed to understand and predict the effects of temperature and thermal stress on MFL field induced by a cylindrical through-hole in a NO steel sheet analytically. The temperature-dependent J-A hysteresis model has been modified by using the reference temperature (e.g., room temperature) instead of absolute zero and improving the equation for the temperature-dependent reversibility factor, c, to facilitate the use of the model in environmental temperature. The magnetic dipole model, which considered the direct effect of temperature only, was established to predict the dependency of the amplitude of the MFL signal on the temperature. Besides, the thermal stress distribution around the defect was solved by using theories of thermodynamics and solid mechanics. Subsequently, the temperature-dependent magnetic dipole model considering the combined effects of temperature and thermal stress was developed.

Temperature experiments were carefully arranged to measure the hysteresis loops of a healthy M250-50A NO silicon steel specimen with 0.45mm in thickness and detect the MFL signals induced by a cylindrical through-hole in an M250-50A NO silicon steel by using the environmental chamber. The parameters and thermal coefficients of the temperature-dependent J-A model were determined by using the GA-PSO algorithm. In the case where only the effect of temperature was involved, the temperature heating 100°C from -40°C resulted in a decrease of 6.10% in the peak-to-peak amplitude of the MFL signal, which fitted with the simulated ones well. To implement the magnetomechanical calculation, the magnetostriction coefficients were determined by parabolically fitting the measured butterfly curves. The measured data illustrated that the temperature refrigerating 30°C from room temperature (20 °C) caused an increase of 6.87% in the peak-to-peak amplitude of the MFL signal, which was much larger than that in the exclusive temperature condition (2.04%). The temperature cooling down from 60°C to -40°C altered the amplitude of the MFL signal by 35.99 %, which could significantly influence the results of defect dimension estimation by using the inverse MFL method. To size the defect accurately, the effect of temperature on the MFL signal should be considered in the calibration process. The improved magnetic dipole models could provide valuable tools to understand and evaluate the contribution of temperature and thermal stress on the induced MFL signals. Furthermore, it could be applicable for solving the inverse problem for defect sizing under multiphysics field.

5.6 References for Chapter 5

[1] A. Raghunathan, Y. Melikhov, J. E. Snyder, and D. C. Jiles. Theoretical model of temperature dependence of hysteresis based on mean field theory. *IEEE Trans. Magn.*, vol. 46, no. 6, pp. 1507–1510, 2010.

[2] A. Raghunathan, Y. Melikhov, J. E. Snyder, and D. C. Jiles. Modeling the temperature dependence of hysteresis based on Jiles-Atherton theory. *IEEE Trans. Magn.*, vol. 45, no. 10, pp. 3954–3957, 2009.

[3] H. Zhang, Y. Liu, S. Liu, and F. Lin. Application of Jiles-Atherton model in description of temperature characteristics of magnetic core. *Rev. Sci. Instrum.*, vol. 89, no. 10, pp. 104702 (1-9), 2018.

[4] Y. Wang, X. Liu, B. Wu, J. Xiao, D. Wu, and C. He. Dipole modeling of stress-dependent magnetic flux leakage. *NDT&E Int.*, vol. 95, pp. 1–8, 2018.

[5] S. M. Dutta, F. H. Ghorbel, and R. K. Stanley. Dipole modeling of magnetic flux leakage. *IEEE Trans. Magn.*, vol. 45, no. 4, pp. 1959–1965, 2009.

[6] K. Mandal, D. Dufour, T. W. Krause, and D. L. Atherton. Investigations of magnetic flux leakage and magnetic Barkhausen noise signals from pipeline steel. *J. Phys. D. Appl. Phys.*, vol. 30, no. 6, pp. 962-973, 1997.

[7] S. Hussain, V. Ghorbanian, A. Benabou, S. Clénet, and D. A. Lowther. A study of the effects of temperature on magnetic and copper losses in electrical machines. *XXII International Conference on Electrical Machines* (*ICEM 2016*), pp. 1277–1283, 2016.

[8] J. A. Osborn. Demagnetising factors of the general ellipsoid. *Phys. Rev.*, vol. 67, no. 11–12, pp. 351-357, 1945.

[9] W. Nowacki. Thermoelasticity. *Elsevier*, 2013.

[10] S. Timoshenko and J. Goodier. Theory of elasticity (The third Edition). *The McGraw Hill Education*, 1970.

[11] D. C. Jiles. Theory of the magnetomechanical effect. *J. Phys. D. Appl. Phys.*, vol. 28, no. 8, pp. 1537-1546, 1995.

[12] D. C. Jiles. Coupled Magnetoelastic Theory of Magnetic and Magnetostrictive Hysteresis. *IEEE Trans. Magn.*, vol. 29, no. 4, pp. 2113–2123, 1993.

[13] D. A. Trevino, S. M. Dutta, F. H. Ghorbel, and M. Karkoub. An improved dipole model of 3-D magnetic flux leakage. *IEEE Trans. Magn.*, vol. 52, no. 12, pp.1-7, 2015.

[14] A. M. Manasrah and H. Ba Ali. Workflow scheduling using hybrid GA-PSO algorithm in cloud computing. *Wireless Communications and Mobile Computing*, vol. 2018, pp. 1-16, 2018.

[15] A. Gálvez and A. Iglesias. A new iterative mutually coupled hybrid GA–PSO approach for curve fitting in manufacturing. *Applied Soft Computing*, vol. 13, no. 3, pp.1491-1504, 2013.

[16] M. A. Albadr, S. Tiun, M. Ayob and F. AL-Dhief. Genetic Algorithm Based on Natural Selection Theory for Optimization Problems. *Symmetry*, vol. 12, no. 11, pp. 1758 (1-31), 2020.

[17] Y. Sun and Y. Kang. A new MFL principle and method based on near-zero background magnetic field. *NDT&E Int.*, vol. 43, no. 4, pp. 348–353, 2010.

[18] L. Mierczak. Evaluation of structural integrity of steel components by non-destructive magnetic methods. *Doctoral dissertation*, *Cardiff University*, 2015.

[19] S. Somkun, A. J. Moses, P. I. Anderson, and P. Klimczyk. Magnetostriction anisotropy and rotational magnetostriction of a nonoriented electrical steel. *IEEE Trans. Magn.*, vol. 46, no. 2, pp. 302–305, 2010.

[20] T. Yamasaki, S. Yamamoto, and M. Hirao. Effect of applied stresses on magnetostriction of low carbon steel. *NDT&E Int.*, vol. 29, no. 5, pp. 263–268, 1996.

[21] F. Bohn, A. Gündel, F. J. G. Landgraf, A. M. Severino, and R. L. Sommer. Magnetostriction, Barkhausen noise and magnetisation processes in E110 grade non-oriented electrical steels. *J. Magn. Magn. Mater.*, vol. 317, no. 1–2, pp. 20–28, 2007.

[22] D. C. Jiles. Introduction to magnetism and magnetic materials. *CRC press*, 2015.

[23] D. C. Jiles and M. K. Devine. The law of approach as a means of modelling the magnetomechanical effect. *J. Magn. Magn. Mater.*, vol. 140–144, no. PART 3, pp. 1881–1882, 1995.

[24] Grain-Oriented Electrical Steel. Available online: https://www.spacematdb.com/spacemat/manudatasheets/crgo.pdf (accessed on 25 November 2020).

[25] Ultra-Low Expansion Glass-Ceramics. Available online: https://www.sydor.com/wp-content/uploads/2019/05/Ohara-CLEARCERAM-Z-Low-Expansion-Glass.pdf (accessed on 1 November 2020).

[26] S. Somkun, A. J. Moses, P. I. Anderson. Effect of Magnetostriction Anisotropy in Nonoriented Electrical Steels on Deformation of Induction Motor Stator Cores. *IEEE Trans. Magn.*, vol. 45, pp. 4744–4747, 2009.

Chapter 6

Evaluation of the Effect of Temperature on Magnetic Barkhausen Noise

The effect of temperature on magnetic Barkhausen noise (MBN) can be divided into two types: the direct effect of temperature itself and the indirect effect of thermally induced stress. The theoretical model is proposed in this study for describing these effects of temperature on the MBN signal. For the case considering the direct effect of temperature only, the analytical model allows the prediction of the effect of temperature on MBN profile, and based on the model, a simple linear calibration curve is presented to evaluate the effect of temperature on MBN amplitude quantitatively. For the case where the indirect effect of thermal stress is taken into account in addition to the direct effect, the proposed theoretical model allows the deduction of parabolic function for quantitative evaluation of the combined effect on MBN. Both effects of temperature on MBN, i.e., the direct only and the combined one, have been studied experimentally on an M250-50A non-oriented (NO) electrical steel and a NO steel adhered to a ceramic glass, respectively. The reciprocal of the measured MBN peak amplitude (1/MBNp) in the first case shows a linear function of temperature, which agrees with the proposed linear calibration curve. In the experiments considering the combined effects, 1/MBNp shows parabolic dependence on temperature, which is further simplified as piecewise functions for practical applications.

6.1 Introduction

The magnetic Barkhausen Noise (MBN) is generated by the discontinuous domain wall motion and domain transition in the ferromagnetic materials subjected to a changing magnetic field [1]. During these processes, pinning sites, local microstructural defects, and stresses (local and global) jointly contribute to the discontinuous stepwise jumps [2], which can be detected by the search coil near the surface of the sample. Such sensitivity allows the MBN technique to be applicable in various NDE fields, such as residual stress [1,3,4] and hardness [2,4].

The root-mean-square (RMS) is a widely used feature of MBN for analysis in NDT measurements. Its amplitude is found to decrease with the increase in temperature [5–7]. E.g., Wang *et al.* [5] and Guo *et al.* [6] experimentally shown a decreasing trend in the peak RMS amplitudes of MBN signals, which were measured for A3 and Q235 steels respectively, as increasing of temperature under free of applied stress. And Altpeter [7] observed that the RMS amplitude of the compact cementite specimen disappeared at its Curie temperature. Since Barkhausen noise is originated from magnetic properties of ferromagnetic material [8-11], and in turn, the magnetic properties are directly influenced by temperature, this leads to a direct influence of temperature on magnetic Barkhausen noise [12,13]. However, the temperature rarely independently affects the MBN signal. The environmental temperature may lead to thermal stress where, for example, the stress value in a seamless track of a high-speed railway could reach tens or even hundreds of MPa [14,15]. Due to the sensitivity of MBN to stress [1,3,4], thermal stress could result in a noticeable RMS change [14]. Therefore, it is necessary to understand and distinguish the mechanism of the effects caused by temperature and thermal stress as well as evaluate these effects on MBN quantitatively.

The theoretical description of the Barkhausen effect is known to be a difficult task due to its random nature. A limited number of attempts have been made to quantitatively analyse the combined effects of temperature and thermal stress on the MBN measurement. But progress has been made in recent years. The most notable attempt to mathematically describe the Barkhausen emission was made by Alessandro, Beatrice, Bertotti and Montorsi (ABBM) [16], who proposed a model of the effect based on a stochastic process. The model was extended to the entire hysteresis loop by Jiles, Sipahi and Williams (JSW) [8], who assumed the Barkhausen activity in a given time interval was proportional to the rate of change of magnetisation. Subsequently, Jiles *et al.* [17] modified the differential susceptibility dM/dH as dM_{irr}/dH to eliminate the influence of reversible magnetisation that rarely induces Barkhausen activity. Lo *et al.* [10] used an extended hysteretic–stochastic model, introducing the magnetomechanical effect, to simulate the influence of stress on Barkhausen emission. Mierczak *et al.* [9] found the linear dependency of the reciprocal peak amplitude of MBN signal on stress and proposed a method for evaluating the effect of stress. Wang *et al.* [5] and Guo *et al.* [6] investigated the temperature effect of stress detection using MBN and proposed an analytical model base on the average volume of Barkhausen jump.

In this chapter, the MBN model combined with the Jiles-Atherton (J-A) hysteresis model that has exerted latent capacity to introduce the effects of stress [18] and temperature [12,13] is adopted to study the theoretical correlations between Barkhausen emission and temperature. The methods to quantitatively evaluate the direct temperature effect and the combined effect of temperature and thermal stress on MBN are presented. The rest of this chapter organises as follows. In Section 6.2, the temperature-dependent MBN models are proposed based on the magnetothermal and magnetomechanical J-A hysteresis models. In Section 6.3, the details about the verification experiments, including the specimen tempered procedure and the MBN sensor configuration, are explained. Both the performance and limitations of the proposed model are discussed in Section 6.4. Finally, the major findings of this study are discussed in Section 6.5.

6.2 The Effect of Temperature on Magnetic Barkhausen Noise

6.2.1 The direct effect of temperature on magnetic Barkhausen noise

In Chapter 5, The thermal effect has been incorporated into the traditional J-A hysteresis model by modifying the key five parameters of J-A model (see Equations (5.1) ~ (5.9)), i.e., the saturation magnetisation M_{st}, the pinning factor k, the domain density a, domain coupling factor α, and the reversibility factor c. The previously constant values of these parameters have been modified as varying thermal parameters, which are further used to simulate the MBN.

The Barkhausen emissions caused by the discontinuous magnetisation changes inside ferromagnetic material with stochastic nature have been modelled based on the J-A model previously [8–11,17]. According to the basic model discussed in Chapter 2, the sum of Barkhausen jumps in the given period Δt is proportional to the total variation of irreversible magnetisation following the equation:

$$M_{JS} = \gamma \cdot \frac{dM_{irr}}{dt} \cdot \Delta t = \gamma \cdot \frac{dM_{irr}}{dH} \cdot \frac{dH}{dt} \cdot \Delta t \tag{6.1}$$

And the differential expression of Barkhausen jumps is given as [11,17]

$$\frac{dM_{JS}}{dt} = \frac{dM_{irr}}{dH} \cdot \frac{dH}{dt} \cdot \langle M_{disc} \rangle \cdot \frac{dN}{dM_{irr}} \tag{6.2}$$

When the temperature effect is taken into account, the thermal energy influences the magnetisation behaviour. It leads to changes in magnetic properties such as susceptibility, coercivity and hysteresis loss. And it further affects the Barkhausen jumps as

$$\frac{dM_{JS}(T)}{dt} = \frac{dM_{irr}(T)}{dH} \cdot \frac{dH}{dt} \cdot \langle M_{disc} \rangle \cdot \frac{dN}{dM_{irr}(T)} \tag{6.3}$$

where

$$\frac{dM_{irr}(T)}{dH} = \frac{M_{an}(T) - M_{irr}(T)}{k(T)\delta} \left[1 + \frac{\alpha(T) dM(T)}{dH}\right] \tag{6.4}$$

In Equation (6.3), if the rate of change of applied magnetic field dH/dt with time is consistent during the measurements under various temperatures, the Barkhausen jumps are dominated by the differential susceptibility of irreversible magnetisation $dM_{irr}(T)/dH$ as the rest part on the right-hand is represented the random behaviour of the model. It is known that the maximum value of Barkhausen noise occurs at coercivity point H_c [9,10] so that the peak amplitude of MBN can be written as

$$MBN_p = \chi'_{H_c}(\frac{dH}{dt}|_{H_c}) \cdot \gamma \cdot \Delta t \qquad (6.5)$$

where χ'_{H_c} is the differential susceptibility of irreversible magnetisation at the coercive field. It is known that in soft ferromagnetic material the maximum differential susceptibility of irreversible magnetisation χ'_{H_c} can be approximated by anhysteresis differential susceptibility χ'_{an} [9,10]. Here, γ represents the random behaviour of the model. But since the predicted and measured RMS of the MBN will be compared in this study, the stochastic fluctuation caused by Poisson distribution is replaced by the expectation after averaging. Due to

$$\alpha = \frac{3a}{M_{st}} - \frac{1}{\chi'_{an}} \qquad (6.6)$$

It could be arrived at

$$\frac{1}{\chi'_{H_c}(T)} - \frac{1}{\chi'_{H_c}(T_r)} = \frac{3a(T_r)\xi(T)}{M_{st}(T_r)\left(\frac{T_c-T}{T_c-T_r}\right)^{\beta_1}} - \alpha(T_r)\xi(T) \qquad (6.7)$$

where

$$\xi(T) = \exp\left[\frac{1}{\beta_3} \cdot \frac{T_r-T}{T_c}\right] \cdot \left(\frac{T_c-T}{T_c-T_r}\right)^{\beta_1} - 1 \qquad (6.8)$$

When the rate of change of applied field with time is determined and the random behaviour is ignored, the temperature-dependent peak values of MBN, $MBN_p(T)$, deduced from Equations (6.5) and (6.7) can be given by:

$$\frac{1}{MBN_p(T)} - \frac{1}{MBN_p(T_r)} = \kappa\left[\frac{3a(T_r)\xi(T)}{M_{st}(T_r)\left(\frac{T_c-T}{T_c-T_r}\right)^{\beta_1}} - \alpha(T_r)\xi(T)\right] \qquad (6.9)$$

where κ is a constant coefficient about the rate of applied field change and the averaged irreversible magnetisation coefficient at the coercivity point. In the case that the environmental temperatures are far from Curie Temperature, the binomial series and exponential function are expanded using the Taylor series. Omitting the high-order and infinitesimal items, Equation (6.9) can be rewritten as

$$\frac{1}{MBN_p(T)} - \frac{1}{MBN_p(T_r)} = \kappa[A + B \times T] \tag{6.10}$$

where A and B are constants since all the parameters are determined and given as

$$A = \frac{3a(T_r)}{M_{st}(T_r)\cdot\beta_3} - \frac{\alpha(T_r)}{\beta_3} \tag{6.11}$$

$$B = \frac{\alpha(T_r)}{T_c\cdot\beta_3} - \frac{3a(T_r)}{M_{st}(T_r)\cdot T_c\cdot\beta_3} \tag{6.12}$$

Equation (6.10) shows the linear tendency of the reciprocal MBN peak value, representing the effect of temperature on Barkhausen noise.

6.2.2 The combined effects of temperature and thermal stress on MBN

In the previous chapters, it has been discussed that when a ferromagnetic material was subjected to the action of elastic stress (σ) in an applied magnetic field (H), the equivalent magnetic field induced by the stress H_σ would be introduced into the effective field, H_e [10,18,19] by

$$H_e = H + \alpha M + \frac{3}{2}\frac{\sigma}{\mu_0}(\cos^2\theta - v sin^2\theta)(\frac{\partial\lambda}{\partial M}) \tag{6.13}$$

where v was the Poisson's ratio, θ was the angle between the stress axis and the direction of H_σ and λ is the bulk magnetostriction. When the strength of magnetisation was relatively weak and the direction of stress was parallel to that of magnetisation, the partial differential term with respect to magnetisation is determined by fitting $\lambda \approx a+bM^2$ [9] from experiment. Hence Equation (6.13) could be rewritten as

$$H_e = H + \alpha M + \frac{3\sigma}{\mu_0}bM = H + \tilde{\alpha}M \tag{6.14}$$

As discussed in the previous chapter, the thermal stresses were classified into two types: type 1 was caused by asymmetric temperature distribution in a structural component and type 2 resulted from different coefficients of thermal expansion (CTE) of two materials in a multilayer structure (see Equations (5.19) and (5.20)) [20].

Assuming there was no fixed constraint along the z-axis, for an isotropic lamination specimen, σ_{zz}, σ_{xz}, σ_{yz} in Equation (5.21) were approximately equal zero, $\sigma_{xy} = \tau_{xy}$ and $\varepsilon_{xy} = \gamma_{xx}/2$, hence, the thermal stress, σ, could be inferred from the thermal strain below elastic limitation [21] as

$$\begin{bmatrix} \sigma_{xx} \\ \sigma_{yy} \\ \tau_{xy} \end{bmatrix} = \frac{E}{(1+\nu)(1-2\nu)} \begin{bmatrix} 1-\nu & \nu & 0 \\ \nu & 1-\nu & 0 \\ 0 & 0 & (1-2\nu)/2 \end{bmatrix} \begin{bmatrix} \varepsilon_{xx} \\ \varepsilon_{yy} \\ \gamma_{xy} \end{bmatrix} \tag{6.15}$$

Assuming the direction of magnetisation is parallel to the y-axis, the stress along the y-axis calculated by Equation (6.15) will be substituted into Equation (6.14) for the further magnetic simulation using the following expression considering the combined effects of temperature and thermal stress

$$\frac{dM(T)}{dH} = \frac{\chi_M(T)}{k(T)\delta - \tilde{\alpha}(T)\chi_M(T)} \tag{6.16}$$

Substituting the new equation of differential susceptibility of magnetisation into Equations (6.2) ~ (6.4) would obtain Barkhausen noise expression influenced by the joint actions of temperature and thermal stress. It would represent the Barkhausen jump behaviour at a given temperature. However, the focus in this study is the extent to which the temperature and thermal stress impact Barkhausen noise. Following an analogous argument to the reciprocal MBN peak value influenced by temperature exclusively, the reciprocal MBN peak value impacted by the combined effects of temperature and thermal stress is given by the following expression

$$\frac{1}{MBN_p(T)} - \frac{1}{MBN_p(T_r)} = \kappa_1 \left[A + B \times T - \frac{3b\sigma(T)}{\mu_0} \right] \tag{6.17}$$

where κ_1 is a constant coefficient analogous to κ.

The improved MBN model, including the direct effect of temperature and the indirect effect of thermal stress, provides a way to investigate the effects of temperature on the MBN signals. The application scope of the proposed model is not limited to the case in this study. It is also appropriate to model MBN with the multiphysics problems involving temperature and stress if the magnetic properties and the magnetostrictions can be determined.

6.3 Verification Experiments for the Temperature-dependent MBN

6.3.1 The MBN experiments for the direct effect of temperature

The MBN experiments that study the direct effect of temperature itself on MBN are conducted on the lamination disc of M250-50A non-oriented (NO) grain silicon steel with 0.45 mm in thickness and 30 mm in diameter. Such specimen sizes could facilitate fast and evenly heating/cooling of the whole body of the sample. Compared with grain-oriented (GO) silicon steel, the NO specimen can be considered an isotropic material in magnetic and mechanic properties.

In this study, the Barkhausen noise measurements are carried out in the environmental chamber HC4033 from Vötsch. It uses the compressor to refrigerate and the fan to ventilate, which might introduce undesired vibration and electromagnetic interference. Hence, the S1-16-12-01 type MBN sensor supplied by Stresstech with shielding case and good stability could reduce electromagnetic interference. Besides, the sensor is assembled on a motorized XYZΘ translation stage from Thorlabs to move the sensor to the specimen centre in precise control and steadily contact the sample surface. The measurement set-up is mounted on a non-magnetic breadboard, placed on a shock mitigation frame to reduce vibration interference further. The experimental setup is cooled and heated together with the sample. There are two test holes in the chamber used to connect the experimental setup in the chamber to the control and data acquisition (DAQ) systems out of the chamber. The sensor is communicated with the computer via the Rollscan 300 MBN analyser using Microscan 600 system, which could control the start, stop, magnetising frequency, etc., and acquire the MBN data. The experimental setup and the schematic diagram of the Barkhausen sensor are presented in Fig.6.1.

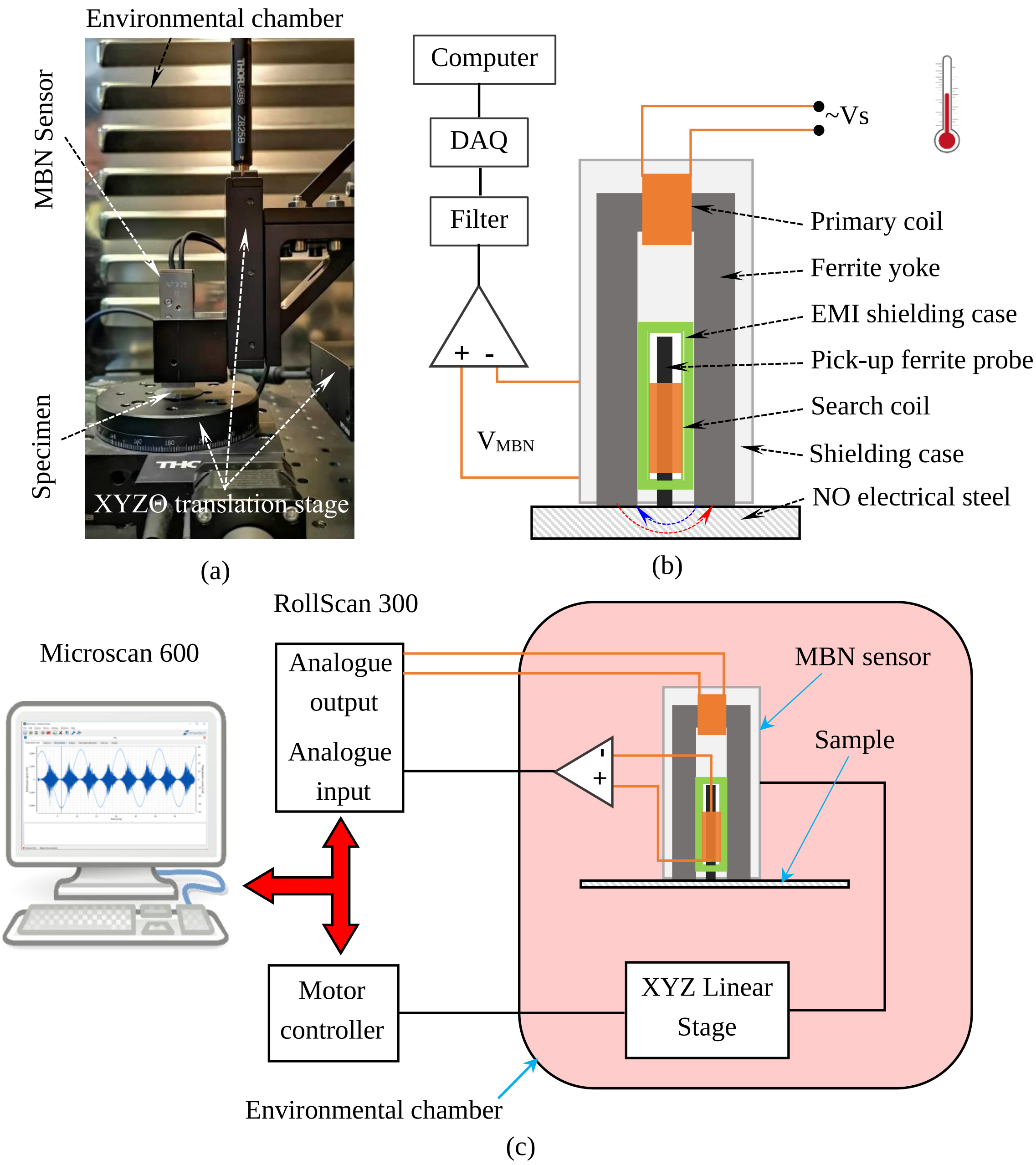

Figure 6.1. (**a**) The photograph of MBN experimental set-up inside the environmental chamber; (**b**) The schematic diagram of the MBN sensor. (**c**) The schematic diagram of the MBN experimental set-up for direct thermal effect testing.

During measurement, the sinusoidal current is fed into the primary coil to generate magnetic flux in the ferrite yoke, which forms magnetic flux closure with the test sample. The Barkhausen emissions from the magnetised section of the tested sample are detected in the form of voltage pulses induced in the searching coil winding on a ferrite probe. The magnetising frequency and voltage used in the measurements are set to 50Hz and 10V, respectively. The output voltage of the pick-up coil is subsequently amplified with the low noise AD797 operational amplifier and digitized by the Microscan 600 system with a sampling frequency of 2.5MHz.

Similar to the MFL experiments described in the previous chapter, in MBN experiments, the sample and MBN measurement set-up are also refrigerated from 20°C to -40°C with 10°C temperature interval, and then heated up to 60°C with 10°C increment step by step. At each set temperature point, the measurement will implement after the temperature being steady for more than 10 minutes. At each temperature point, eight cycles of Barkhausen noise signal are measured, and then the mean value of RMS is obtained from these cycles. The entire process is repeated five times to reduce the random behaviour of Barkhausen jumps and measurement error.

Before these MBN experiments, the specimens are annealed at 400°C for two hours to relieve the residual stress. The quasi-static hysteresis curves of an Epstein strip of M250-50A at different temperatures have been measured to determine the key parameters of the temperature-dependent J-A model in Chapter 5. The key parameters values determined by the hybrid GA-PSO algorithm in the previous chapter are listed in Table 5.1.

6.3.2 The MBN experiments for the combined effects of temperature and thermal stress

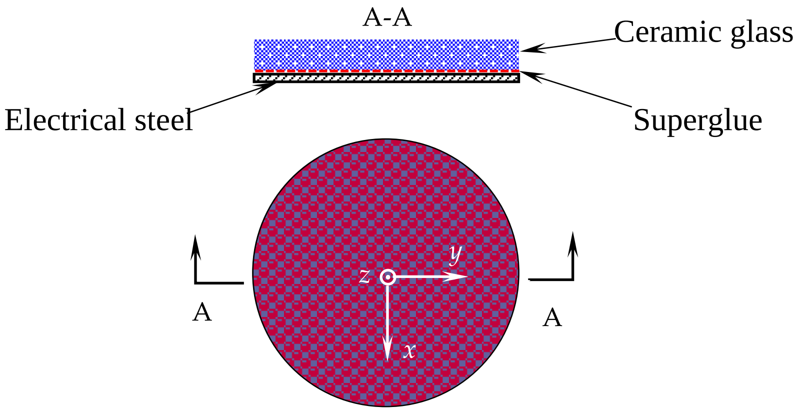

Figure 6.2. The thermally induced stress structure.

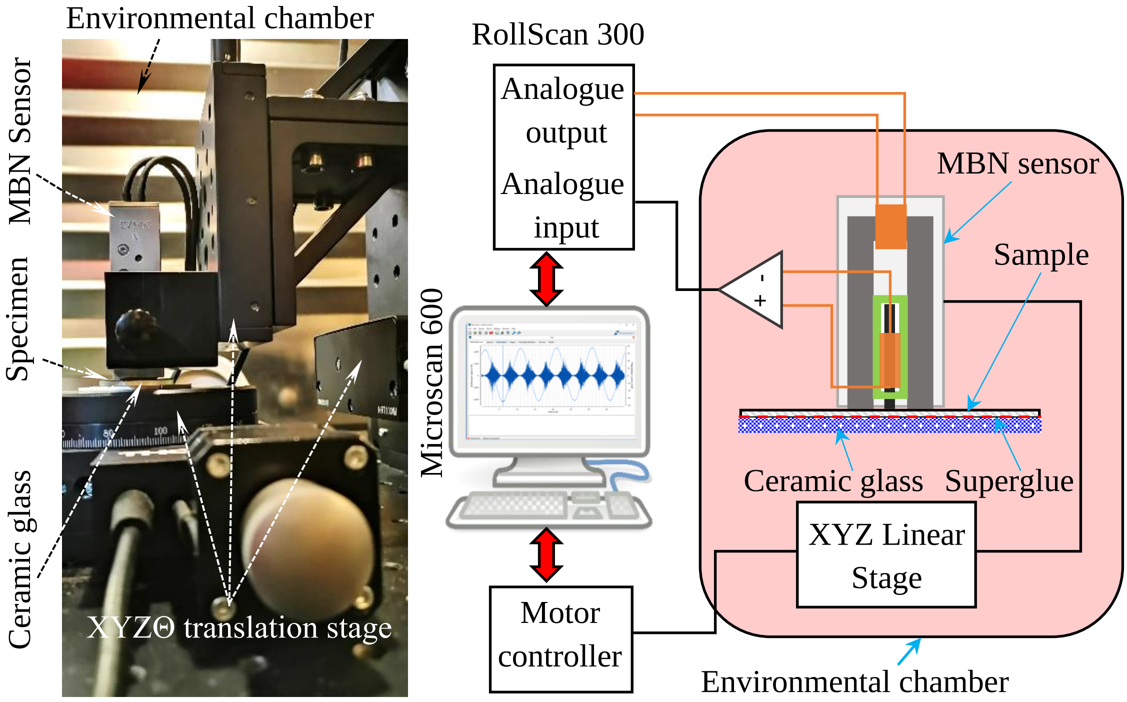

(a) (b)

Figure 6.3. (**a**) The MBN experimental setup for combined thermal effects testing; (**b**) The schematic diagram of the MBN experimental setup for combined thermal effects testing.

In the MBN experiments that study the combined direct and indirect effects on MBN, the M250-50A NO silicon steel disc is glued to a ceramic glass disc (Schott Zerodur), whose CTE (1×10-7 $°C^{-1}$) is much smaller than NO steel (11.9×10-6 $°C^{-1}$), at room temperature (20 °C). The experimental conditions related to this work can be described via the type 2 thermal stresses, where two components with different CTEs are fixed together at the reference temperature. The multilayer structure shown in Fig. 6.2 could induce thermal stress when the temperature changes due to the considerable difference in CTE between the two materials.

Similar to the experiments described above, the multilayer structure adheres to the rotation stage, and the MBN sensor is located on the centre of the NO steel disc as shown in Fig.6.3. The setup together with the multilayer is cooled from 20°C to -40°C and heated up to 60 °C with 10 °C intervals. The magnetising frequency and voltage used in the measurements are set to 50Hz and 5V, respectively. The measurement process is repeated five times as well. Before these MBN experiments, the key parameter of magnetostriction (λ) is measured and illustrated in Fig.6.4.

6.4 Results and Discussion for the Effects of Temperature on MBN

The magnetic hysteresis loops of the M250-50A NO electrical steel strip have been measured using a computer-controlled hysteresis loop tracer at a quasi-DC field of 5mHz as described in Chapter 5. The measurement system is subject to various temperatures that are controlled by the environmental chamber. The temperature-dependent parameters of J-A model have been listed in Table 5.1.

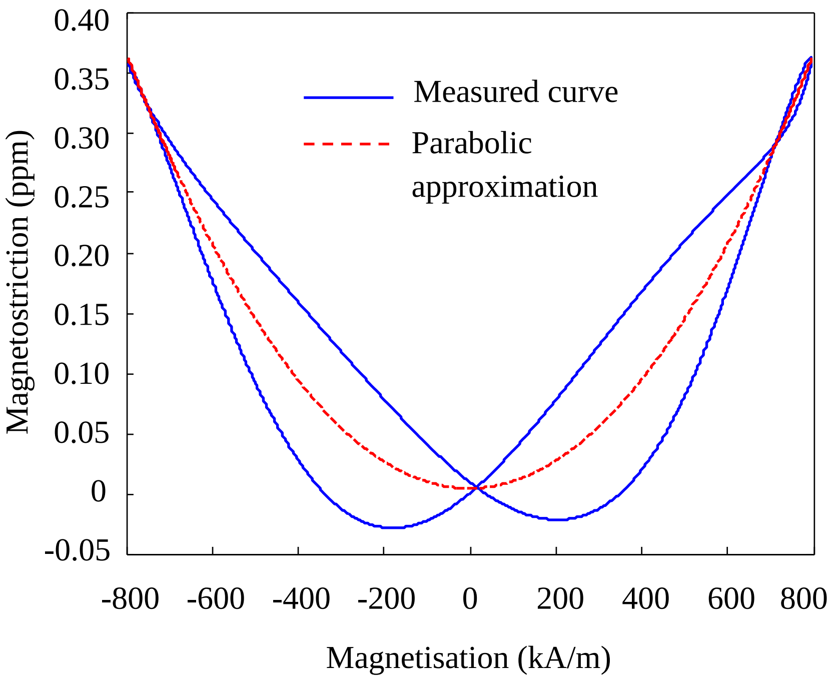

Figure 6.4. The magnetostriction as a function of magnetisation for the M250-50A NO electrical steel.

Other than the magnetostriction curve measured in the high field shown in Chapter 5, the magnetisation of MBN is generally lower than the saturation one. In this case, the magnetostriction would show a clear parabolic function of magnetisation. Fig. 6.4 shows the magnetostriction λ vs magnetisation M butterfly loop for M250-50A NO electrical steel. The parabolic function is used to fit the butterfly loop, and the obtained slope $d\lambda/dM$ of the parabolic approximation for the NO steel sample is 5.63×10^{-18} (m^2/A^2). It indicates that the stress equivalent field H_σ would be positive under applied tensile stress and negative under compressive stress. The stress-dependent parameters of J-A model could be found in Table 5.2, but the magnetostriction coefficient is replaced by $b = 5.63\times10^{-18}$ (m^2/A^2).

6.4.1 *The direct effect of temperature on MBN*

The typical raw MBN signal measured for the NO steel is plotted in Fig. 6.5. The RMS feature of MBN signal is extracted for analysis. As examples, the experimental MBN signals along the y-axis at -40 °C, -20 °C and 20 °C are shown in Fig. 6.6, and the corresponding simulated MBN signal using Equation (6.11) are plotted at the related locations of experimental ones. All the simulated and measured MBN signals are normalised by the maximum amplitudes of the simulated and measured MBN signals at 20 °C, respectively. It can be found that the highest amplitude of the simulated MBN signals is consistent with the measured ones. It indicates that the proposed temperature-dependent MBN model is adequate to predict the RMS profile of MBN under various temperatures accurately.

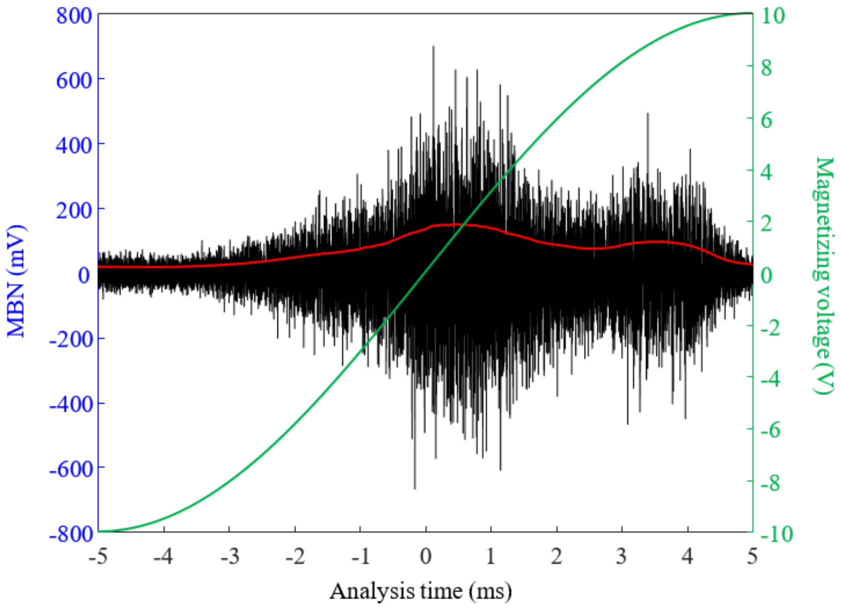

Figure 6.5. Illustration of raw Barkhausen bursts and the corresponding RMS envelope.

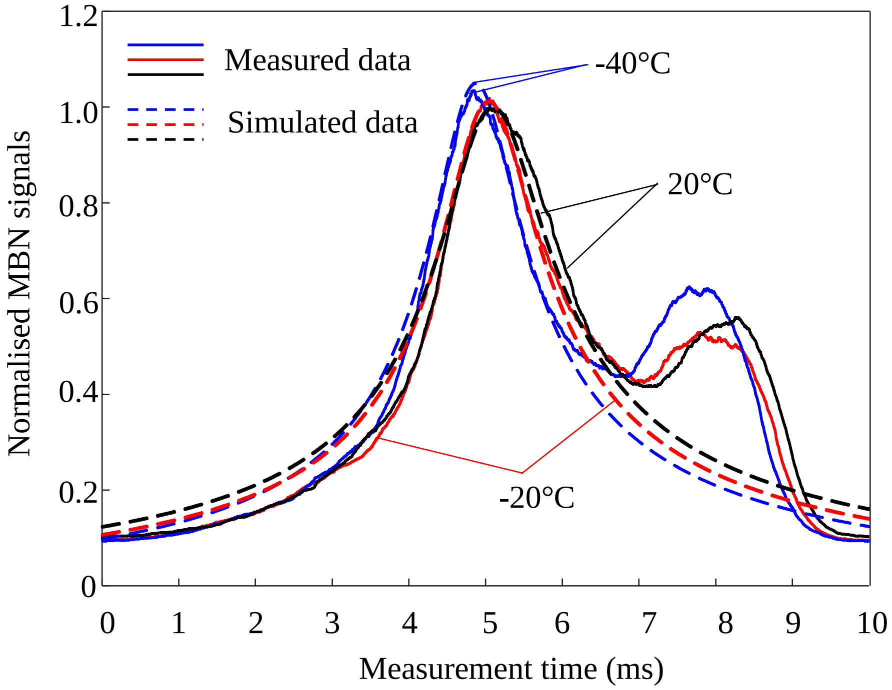

Figure 6.6. The simulated and measured MBN signal envelops for M250-50A NO electrical steel under various temperatures.

The RMSs of the measured MBN signals show one more peak than those of the simulation. Two peaks of $\mathrm{MBN}_{\mathrm{rms}}$ for NO silicon steel were not typically reported but have been observed by other investigators [22-24]. This phenomenon has also been shown in measured results for grain oriented silicon steel [25,26]. It is believed that the main peak near the coercive field is caused by the irreversible magnetisation process. Magnetic flux density decreasing from saturation results in the nucleation and growth of new domains at various sample defects and grain boundaries [23-26]. A large number of domains and the high moving velocity of domain wall near the coercive field lead to the highest level of Barkhausen emissions [8-11]. The secondary peak occurs at a higher field, where the domain annihilation and rotation gradually emerge [23-26]. Therefore, the secondary peak is possibly caused by this process. Its level is lower than the main peak. In this study, NO electrical steel is considered an isotropic material in mechanics. Its magnetic properties are modelled according to the measured hysteresis loop along its rolling direction. The maximum peak values of measured MBN signals along the rolling direction appear around the coercive field corresponding to the model (see Fig. 6.5). Therefore, the comparison of the maximum peak of simulated and measured results could be used to verify the feasibility of the model.

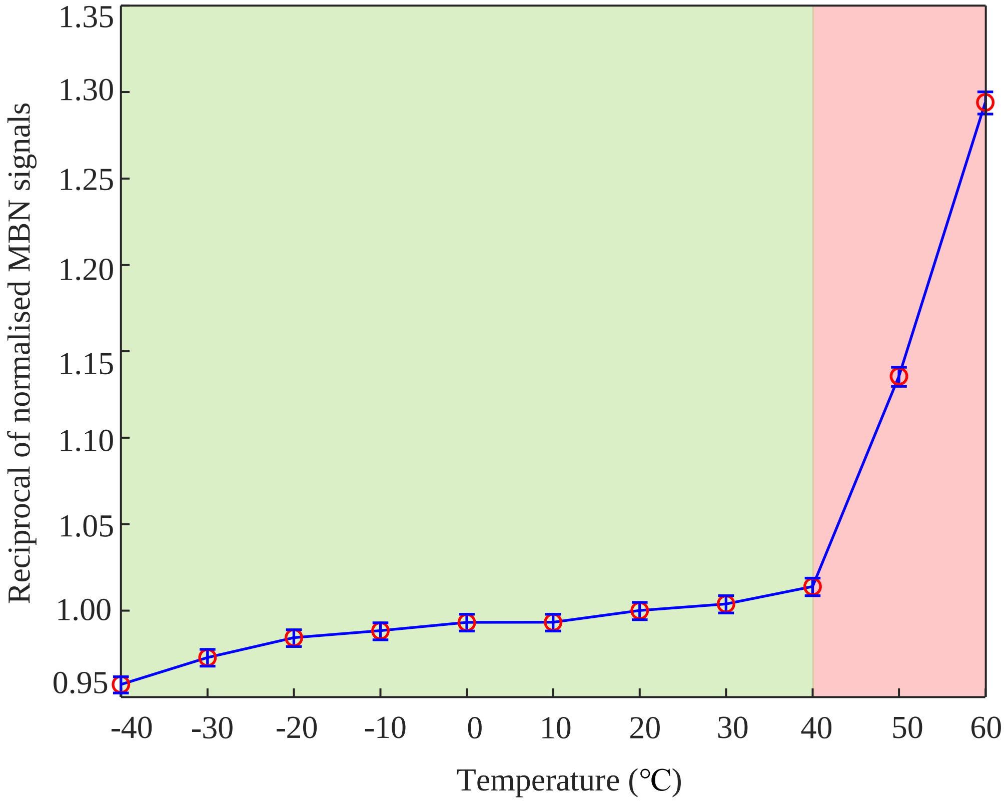

Figure 6.7. The reciprocal MBN peak amplitude as a function of temperature measured for M250-50A NO electrical steel.

To evaluate the relationship between the MBN signal and the temperature quantitatively, the reciprocal of maximum peak RMS values of the measured MBN are normalised by that at 20 °C and plotted in Fig. 6.7. It can be found that the values at 50 °C and 60 °C show an unusually steep rise. When the environmental temperature increases over 50 °C even 60 °C, the temperature inside the sensor could be higher than the operating temperature. The primary coil operation will heat the sensor and lead to an internal temperature higher than 80 °C. Generally, the Curie temperature of ferrite core (such as Mn-Cu, Mn-Zn ferrites) is not far from 100~150 °C, and its magnetic properties will sharply degrade when it is approaching its Curie point.

Besides, the maximum operating temperature of the operational amplifier inside the sensor is 80°C. Therefore, the measured MBN signals at 50 °C and 60 °C are eliminated in comparison with simulated results.

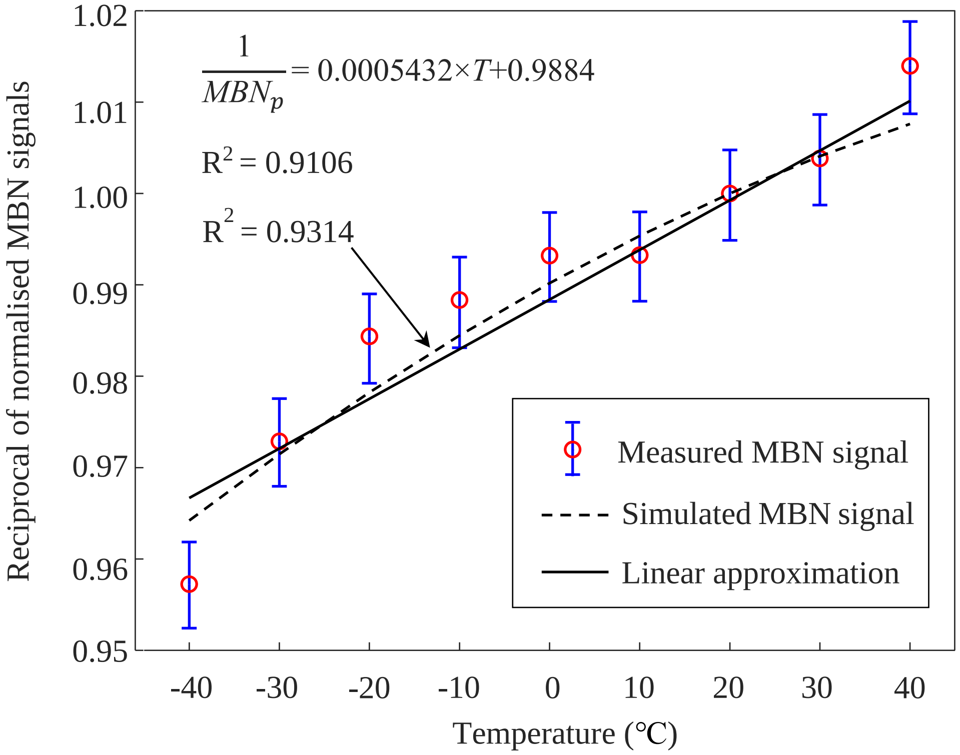

Figure 6.8. Dependence of reciprocal MBN peak value on temperature approximated with a linear function.

The predicted relation between MBN signal and temperature using Equation (6.9) is plotted in Fig. 6.8 together with the measured results. It can be found that the dependence of the reciprocal peak amplitude of the MBN signal on the temperature obtained from experiments corresponds with the simulated with a coefficient of determination higher than 0.93. For a ferromagnetic material with a much higher Curie temperature than environmental temperatures, such as for iron (Curie temperature 770°C), the reciprocal of MBN_{rms} peak amplitude increases approximately as a linear function as shown in Fig. 6.8 corresponding to the prediction of Equation (6.10). The linear approximation in the normal environmental temperature range is consistent with the experimental results (R^2 higher than 0.91).

6.4.2 The combined effects of temperature and thermal stress on MBN

One of the factors that limit the applicability of the J-A magnetomechanical model using Equations (6.13), (6.14) and (6.16) to simulate the MBN signal is the domain coupling factor α. Its value is so small that it can easily become lower than zero with stress using Equation (6.14). Therefore, there is only a limited temperature range that allows the applicability of this multiphysics MBN model. It is necessary to mention that the model will work better in a magnetically harder material. To quantitatively evaluate the effect of temperature on the MBN signal, the main concern is the extent to which the temperature and corresponding thermal stress impact Barkhausen noise. Even for those magnetically harder materials that could calculate the MBN envelopes, their peak amplitudes will be further represented as a temperature function given in Equation (6.17).

As discussed above, the reciprocal of MBN peak amplitudes influenced by the direct effect of temperature were approximated as a linear function of temperature. And hence, Equation (6.10) can be rewritten as

$$\frac{1}{MBN_p(T)} = p_1 \times T + C \tag{6.18}$$

where p_1 and C are constant coefficients. The last term of Equation (6.17) is also proportional to temperature if the coefficient b is constant. And hence, the characteristic of reciprocal MBN peak value is the linear superposition of two linear equations

$$\frac{1}{MBN_p(T)} = p_T \times T + p_\sigma \times T + C \tag{6.19}$$

where p_T and p_σ are the constant coefficients for the direct and indirect effect of temperature, respectively.

The approximated results of the reciprocal MBN signal as a linear function of temperature using Equation (6.19) are plotted in Fig. 6.9 together with the measured results. It can be seen that the reciprocal of the measured MBN peak value exhibits a clear rising trend for increasing temperature, which is consistent with the prediction of Equation (6.17) due to the positive value of magnetostriction coefficient b (5.63×10^{-18} m^2/A^2 determined by parabolic fitting measured λ-M curve as plotted in Fig. 6.4). The fitting coefficient (0.002647) is much larger than that in Fig. 6.8 (0.0005432) even with the lower excitation voltage. It indicates that the combined effect of temperature and thermal stress on the MBN signal is much more significant than the direct effect of temperature only. However, it should be noted that the fitting goodness of R^2 (0.8360) is much lower than that in Fig. 6.8. It may result from the magnetostriction coefficient b rarely being a constant.

In general, the magnetostriction curves, for example, reported for carbon steels [27] and electrical steels [28,29], have shown that the parabolic approximations of λ-M curves changed with stresses, which resulted in the different values of magnetostriction coefficient b. Considering the empirical equation of magnetostriction as a function of magnetisation [18,19]

$$\lambda \approx b_0 + (b_1 + b_2\sigma)M^2 \tag{6.20}$$

where b_0, b_1 and b_2 are magnetostriction coefficients, Equations (6.17) and (6.19) can be rewritten as

$$\frac{1}{MBN_p(T)} - \frac{1}{MBN_p(T_r)} = \kappa_1\left[A + B \times T - \frac{3b_2\sigma^2(T) + 3b_1\sigma(T)}{\mu_0}\right] \tag{6.21}$$

$$\frac{1}{MBN_p(T)} = p_1 \times T^2 + p_2 \times T + C \tag{6.22}$$

The measured reciprocal of MBN peak amplitude is parabolically approximated using Equation (6.22) as plotted in Fig. 6.9. It can be found that the dependence of the reciprocal of MBN peak amplitude on the temperature obtained from experiments corresponds with the simulated with a coefficient of determination higher than 0.97. It implies that the proposed parabolic dependency of $1/MBN_p$ on temperature can be applied to evaluate the combined effect of temperature and thermal stress on MBN quantitatively.

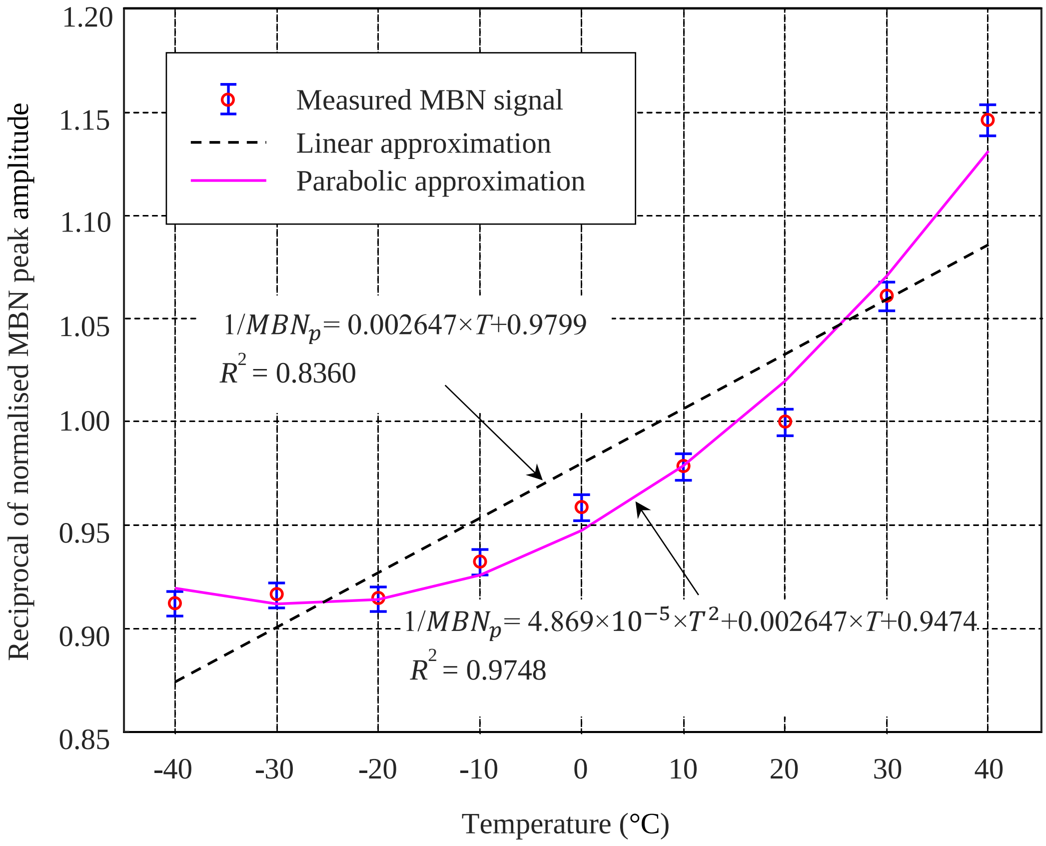

Figure 6.9. The approximation of reciprocal MBN peak amplitude as a parabolic function of temperature.

At normal environmental temperature, the thermal stress is usually in the elastic stress range of material. The dependence of MBN peak amplitude on temperature can also be approximated by parabolic function within this range. Since the quadratic equation is combined both effects of temperature and thermal stress, it leads to the difficulty in distinction of the direct and indirect effects of temperature. Besides, identifying the stress-dependent magnetostriction coefficients is a difficult task as discussed in the previous chapter. To simplify the evaluation function, the method proposed in [9] to linearly approximate the dependence of reciprocal MBN peak amplitude on temperature is adopted. But if directly eliminating the quadratic term, the coefficient of the equation degenerates to the linear approximation, which has been proven to have relatively low fitting goodness. Therefore, the parabolic fitting magnetostriction coefficient b is various rather than constant.

It has been experimentally shown [27-29] that within the elastic limitation the maximum value of magnetostriction λ at a given low magnetisation M presented approximately linear increase as the increasing compressive stress and the decreasing tensile stress, respectively. But the linear approximations show a larger slope under compression than that under tension [28,29]. According to the measured peak-to-peak amplitude of magnetostriction as a function of stress for M250-50A NO electrical steel, a piecewise linear function is used to fit the measured results under tension and compression, respectively, as shown in Fig. 6.10. The slope fitting under compression is about 4.07 times under tension, which approximately represents the ratio of magnetostriction coefficient b under compression and tension. Hence, the effect of the temperature higher than the reference temperature, for which corresponding thermal stress is compressive, and the temperature lower than the reference temperature, for which corresponding thermal stress is tensile, are evaluated separately. If the temperatures higher and lower than reference temperature are defined as high and low temperature respectively, the Equation (6.21) can be further rewritten as piecewise linear functions and calibrated with the value at reference temperature (20 °C in this study) since there is no stress involving in the measurement at the reference temperature and the measured MBN amplitude at the reference temperature is the benchmark value of normalisation. The normalised reciprocal MBN peak value passing through the reference point is given as

$$\begin{cases} \frac{1}{MBN_{pH}(T)} = (p_{H\sigma} + p_T) \times (T - T_{ref}) + 1 \quad (T \geq T_{ref}) \\ \frac{1}{MBN_{pC}(T)} = (p_{C\sigma} + p_T) \times (T - T_{ref}) + 1 \quad (T < T_{ref}) \end{cases} \tag{6.23}$$

where $p_{H\sigma}$ and $p_{C\sigma}$ are the slopes related to the thermal stresses caused by high temperature and low temperature, respectively, and p_T is the temperature coefficient similar to Equation (6.19).

The reciprocal MBN peak amplitude as linear functions of temperature using Equation (6.23) fitting to the measured results (with a fitting goodness R^2 higher than 0.98) are plotted in Fig. 6.11. It implies that the simplified practical model can be applied to evaluate the combined effect of temperature on MBN peak amplitude. The ratio of the slopes under high and low temperatures shown in Fig. 6.11 is 4.02, close to the ratio of the fitting slopes for magnetostriction under compressive and tensile stresses (4.07). The difference may owe to the direct effect of temperature in addition to the effect of thermal stress and the errors caused by fitting and measurement.

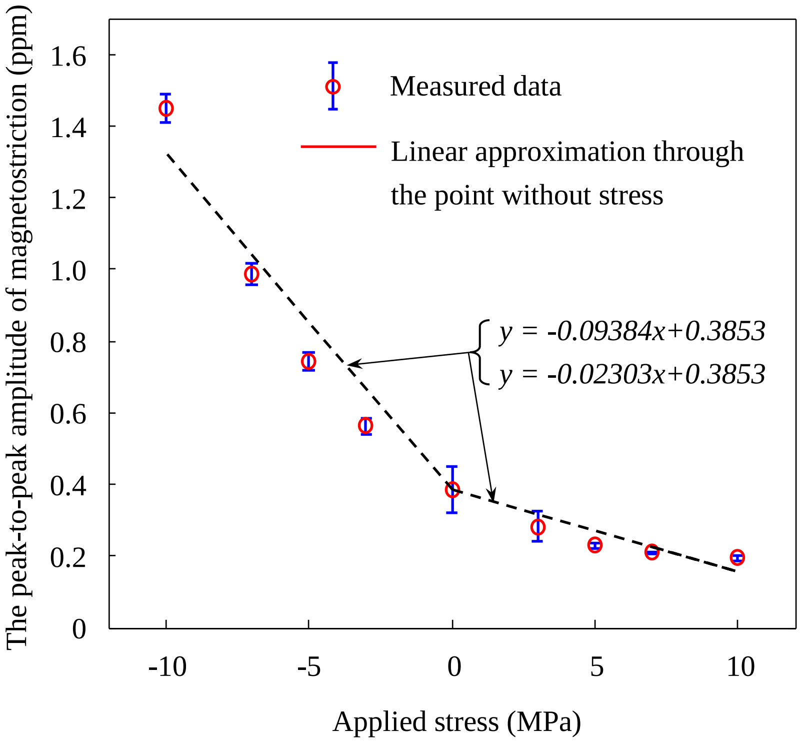

Figure 6.10. The peak-to-peak value of magnetostriction as a function of applied stress in M250-50A NO electrical steel.

For a new ferromagnetic material influenced by temperature, if the prior knowledge of the temperature-dependent hysteresis and stress-dependent magnetostriction has been obtained, the MBN profile influenced by temperature could be calculated by Equation (6.3). In practice, linear functions of temperature could be obtained by measuring two or more data points and deducing the linear function of temperature using Equations (6.10) (6.18) (6.22) and (6.23). The MBN peak amplitude at reference temperature (e.g., 20 °C) needs to be measured to determine the benchmark value at first. At least another point is needed for linear approximating the reciprocal of MBN peak value *vs* temperature. Suppose there is only the effect of temperature itself involved in the experiments. In this case, the linear fitting function could characterise the dependence of reciprocal MBN peak value on temperature and quantitatively evaluate the effect of temperature on the MBN signal. For example, as shown in Fig. 6.8, temperature heating from -40°C to 40°C results in an increase of 4.49% in the reciprocal of MBN peak value, which means the MBN peak amplitude decreases 4.60% in this temperature range.

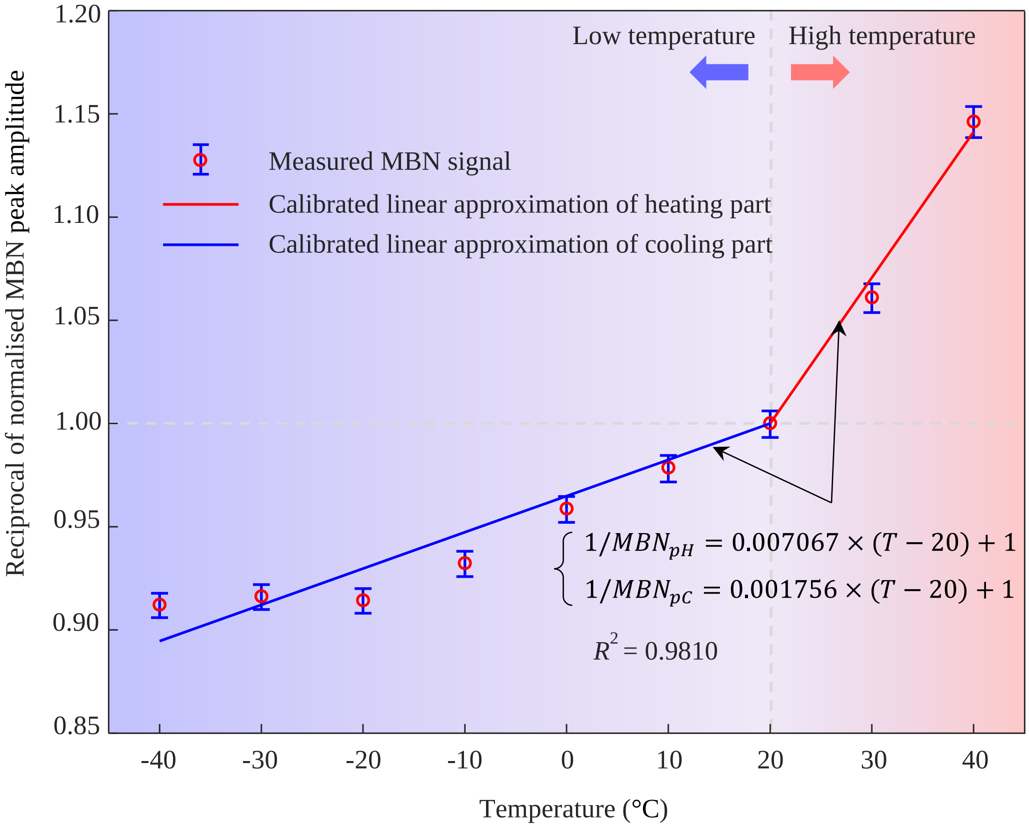

Figure 6.11. Dependence of reciprocal MBN peak value on temperature approximated with linear functions.

Regarding thermal stress involvement, one or more points apart from reference one should be measured either in high temperature range or low temperature range. Taking the points in the high temperature range shown in Fig. 6.11 for instance, a linear function passing through the reference point (20 °C) could be obtained by Equation (6.23). This linear function could represent the dependency of reciprocal MBN peak amplitude on heating temperature. There are two methods to determine the relationship between $1/MBN_p$ and temperature in the low temperature range. The simplest one is to measure one or more points in the low temperature range and use a linear function to fit them as the blue line plotted in Fig. 6.11. For another method, calculating the coefficients of thermal stress $p_{H\sigma}$ and temperature p_T is required using Equations (6.17) and (6.19). The computed coefficients caused by thermal stress and temperature are about 7.057×10^{-3} and 1.000×10^{-5}, respectively. Since the ratio of the magnetostriction coefficient b under compression and tension is around 4.07, the coefficient caused by thermal stress in the low temperature range, $p_{C\sigma}$, can be estimated as a value of 0.001742. Consequently, the linear function slope for evaluating the dependence of $1/ MBN_p$ on temperature is 1.734×10^{-3}, which is closely approaching the slope of the best linear fitting function (1.756×10^{-3}). It indicates that this method is feasible to evaluate the effect of temperature on the MBN peak amplitude quantitatively. The piecewise linear dependency of the reciprocal MBN peak amplitude on temperature is concluded.

The environmental temperature heating from -40 °C to 40 °C results in an increase of 27.54% in the reciprocal of MBN peak value. Therefore, its effect should be considered in precise evaluation using the MBN method, such as evaluating residual stress and hardness. To analyse the low and high temperature range separately, the temperature cooling from reference temperature 20 °C to -40 °C leads to a decrease of 10.54% in 1/ MBNp, representing the MBN peak amplitude increases 11.78%. While the temperature heating from 20°C to 40°C causes a sharper increase of 14.13% in $1/ MBN_p$, which means the peak amplitude of the MBN signal attenuates 12.38% quickly.

6.5 Chapter summary

This chapter considered both the direct effect of temperature and the indirect effect of thermal stress. In the case where the direct effect is involved only, the extended MBN model based on temperature-dependent hysteresis was proposed. The relationship between the reciprocal of MBN peak amplitude and temperature, which has been further simplified as the linear function to evaluate the dependence of MBN peak amplitude on temperature quantitatively, was deduced from the temperature-dependent MBN model. While considering the combined effects of temperature and thermal stress, the multiphysics MBN model has been presented, and based on this model, the parabolic dependence of the reciprocal of MBN peak value on temperature was given. Practical piecewise linear functions were then presented to approximate the dependence according to the finding that the magnetostriction coefficients under compression and tension are different.

Temperature experiments for magnetic hysteresis measurements were conducted on M250-50A NO steel before MBN experiments. The temperature-dependent parameters of the J-A model were determined by using the hybrid GA-PSO algorithm. When the direct effect of temperature itself was exclusively involved, the measured peak value of MBN signals fitted with simulated MBN envelops well, and the reciprocal of the peak amplitude of the MBN signal has been experimentally shown the linear variation with temperature corresponding with the predicted results. The linear dependency would be useful for the quantitative evaluation of temperature on the MBN signal. In this case, temperature heating from -40°C to 40°C resulted in an increase of 4.49% in the reciprocal of MBN peak value.

In addition to the direct effect, the indirect effect of thermal stress was involved. The measured reciprocal of the peak amplitude of Barkhausen emission has presented parabolic dependency on temperature, which was consistent with the predicted tendency. The parabolic relation was further simplified by piecewise linear functions at temperatures higher and lower than the reference temperature. It has been proven to be feasible to evaluate the combined effect quantitatively. The environmental temperature cooling from the reference temperature 20°C to -40°C led to a decrease of 10.54% in $1/MBN_p$. Whereas the temperature heating from 20°C to 40°C caused a sharper increase of 14.13% in $1/MBN_p$. The methods to obtain the piecewise linear function for the evaluation of the combined effects of temperature and thermal stress have been proposed. To achieve the evaluation of material and mechanical properties using the MBN method with high accuracy, the effect of temperature on the MBN signal should be considered in the calibration process of MBN measurement. Moreover, MBN is a potential method in structural health monitoring. However, the temperature compensation for the monitoring data under various temperatures is a subject remaining to be researched, and the proposed practical method would be possible to solve this problem.

6.6 References for Chapter 6

[1] J. Capó-Sánchez, J. Pérez-Benitez, and L. R. Padovese. Analysis of the stress dependent magnetic easy axis in ASTM 36 steel by the magnetic Barkhausen noise. *NDT&E Int.*, vol. 40, no. 2, pp. 168–172, 2007.

[2] X. Liu, R. Zhang, B. Wu, and C. He. Quantitative prediction of surface hardness in 12CrMoV steel plate based on magnetic Barkhausen noise and tangential magnetic field measurements. *J. Nondestruct. Eval.*, vol. 37, no. 2, pp. 1-8, 2018.

[3] H. Ilker Yelbay, I. Cam, and C. Hakan Gür. Non-destructive determination of residual stress state in steel weldments by Magnetic Barkhausen Noise technique. *NDT&E Int.*, vol. 43, no. 1, pp. 29–33, 2010.

[4] P. Žerovnik, J. Grum, and G. Žerovnik. Determination of hardness and residual-stress variations in hardened surface layers with magnetic Barkhausen noise. *IEEE Trans. Magn.*, vol. 46, no. 3 PART 2, pp. 899–904, 2010.

[5] P. Wang, X. Ji, X. Yan, L. Zhu, H. Wang, G. Tian and E. Yao. Investigation of temperature effect of stress detection based on Barkhausen noise. *Sensors Actuators A Phys.*, vol. 194, pp. 232–239, 2013.

[6] L. Guo, D. Shu, L. Yin, J. Chen, and X. Qi. The effect of temperature on the average volume of Barkhausen jump on Q235 carbon steel. *J. Magn. Magn. Mater.*, vol. 407, pp. 262–265, 2016.

[7] I. Altpeter. Nondestructive evaluation of cementite content in steel and white cast iron using inductive Barkhausen noise. *J. Nondestruct. Eval.*, vol. 15, no.

2, pp. 45–60, 1996.

[8] D. C. Jiles, L. B. Sipahi, and G. Williams. Modeling of micromagnetic Barkhausen activity using a stochastic process extension to the theory of hysteresis. *J. Appl. Phys.*, vol. 73, no. 10, pp. 5830–5832, 1993.

[9] L. Mierczak, D. C. Jiles, and G. Fantoni. A new method for evaluation of mechanical stress using the reciprocal amplitude of magnetic Barkhausen noise. *IEEE Trans. Magn.*, vol. 47, no. 2 PART 2, pp. 459–465, 2011.

[10] C. C. H. Lo, S. J. Lee, L. Li, L. C. Kerdus, and D. C. Jiles. Modeling stress effects on magnetic hysteresis and Barkhausen emission using a hysteretic-stochastic model. *IEEE Trans. Magn.*, vol. 38, no. 5, pp. 2418–2420, 2002.

[11] N. P. Gaunkar, O. Kypris, I. C. Nlebedim, and D. C. Jiles. Analysis of Barkhausen noise emissions and magnetic hysteresis in multi-phase magnetic materials. *IEEE Trans. Magn.*, vol. 50, no. 11, pp. 1-4, 2014.

[12] A. Raghunathan, Y. Melikhov, J. E. Snyder, and D. C. Jiles. Theoretical model of temperature dependence of hysteresis based on mean field theory. *IEEE Trans. Magn.*, vol. 46, no. 6, pp. 1507–1510, 2010.

[13] A. Raghunathan, Y. Melikhov, J. E. Snyder, and D. C. Jiles. Modeling the temperature dependence of hysteresis based on Jiles-Atherton theory. *IEEE Trans. Magn.*, vol. 45, no. 10, pp. 3954–3957, 2009.

[14] S. Ding, P. Wang, Y. Lin, and D. Zhu. Reduction of thermal effect on rail stress measurement based on magnetic Barkhausen noise anisotropy. *Measurement*, vol. 125, pp. 92–98, 2018.

[15] V. Damljanović and R. L. Weaver. Laser vibrometry technique for measurement of contained stress in railroad rail. *J. Sound Vib.*, vol. 282, no. 1–2, pp. 341–366, 2005.

[16] B. Alessandro, C. Beatrice, G. Bertotti, and A. Montorsi. Phenomenology and interpretation of the Barkhausen effect in ferromagnetic materials. *J. Appl. Phys.*, vol. 64, no. 10, pp. 5355–5360, 1988.

[17] D. C. Jiles. Dynamics of domain magnetisation and the Barkhausen effect. *Czechoslov. J. Phys.*, vol. 50, no. 8, pp. 893–924, 2000.

[18] D. C. Jiles. Theory of the magnetomechanical effect. *J. Phys. D. Appl. Phys.*, vol. 28, no. 8, pp. 1537-1546, 1995.

[19] Y. Wang, X. Liu, B. Wu, J. Xiao, D. Wu, and C. He. Dipole modeling of stress-

dependent magnetic flux leakage. *NDT&E Int.*, vol. 95, pp. 1–8, 2018.

[20] W. Nowacki. Thermoelasticity. *Elsevier*, 2013.

[21] S. Timoshenko and J. Goodier. Theory of elasticity (The third Edition). *The McGraw Hill Education*, 1970.

[22] O. Stupakov. Local non-contact evaluation of the ac magnetic hysteresis parameters of electrical steels by the Barkhausen noise technique. *Journal of Nondestructive Evaluation*, vol. 32, no. 4, pp.405-412, 2013.

[23] J. Pal'a and J. Bydžovský. Barkhausen noise as a function of grain size in non-oriented FeSi steel. *Measurement*, vol. 46, no. 2, pp.866-870, 2013.

[24] F. Bohn, A. Gündel, F. Landgraf, A.M. Severino and R.L. Sommer. Magnetostriction, Barkhausen noise and magnetization processes in E110 grade non-oriented electrical steels. *J. Magn. Magn. Mater.*, vol. 317, no. 1-2, pp.20-28, 2007.

[25] F. Qiu, M.J. Klug, G. Tian, P. Hu and J. McCord. Influence of magnetic domain wall orientation on Barkhausen noise and magneto-mechanical behavior in electrical steel. *J. Phys. D. Appl. Phys.*, vol. 52, no. 26, p.265001 (1-13), 2019.

[26] D.G. Hwang, C.G. Kim, K.H. Lee and H.C. Kim. The retarding field model of Barkhausen noise and permeability in conventional and highly grain-oriented 3% Si-Fe polycrystals. *J. Magn. Magn. Mater.*, 125(1-2), pp.129-137, 1993.

[27] T. Yamasaki, S. Yamamoto, and M. Hirao. Effect of applied stresses on magnetostriction of low carbon steel. *NDT&E Int.*, vol. 29, no. 5, pp. 263–268, 1996.

[28] P. Klimczyk. Novel techniques for characterisation and control of magnetostriction in GOSS. *Doctoral dissertation*, *Cardiff University*, 2012.

[29] S. Somkun, Magnetostriction and magnetic anisotropy in non-oriented electrical steels and stator core laminations. *Doctoral dissertation*, *Cardiff University*, 2010.

Chapter 7

Evaluation of the Effect of Microstructure-induced Anisotropy in Non-oriented Silicon Steel on Magnetic Barkhausen Noise

The effect of magnetic anisotropy correlated with the crystallographic structure of non-oriented (NO) silicon steel on Magnetic Barkhausen Noise (MBN) is evaluated. The theoretical model is proposed for describing the effect of anisotropy on the MBN signal. Meanwhile, the effect of excitation frequency is also considered in the model. The proposed model predicts the amplitude increasing and envelope broadening with the increase of excitation frequency accurately. Besides, it anticipates the decrease in the amplitude of the MBN envelope and the increase in width as the angle between the tested direction and rolling direction (RD) increases. The analytical model allows the deduction of a trigonometric function for quantitative evaluation of the anisotropic effect on MBN. The effect of anisotropy on MBN has been investigated experimentally on M330-35A NO silicon steel under excitation frequencies of 50 Hz and 100 Hz, respectively. Under both excitation frequencies, the measured MBN peak amplitudes (MBN_p) show cosine dependences on the angle, which approach the proposed trigonometric calibration curves.

7.1 Introduction

In the previous chapters, the non-oriented (NO) silicon steel is treated as an isotropic material. However, there could be a significant anisotropy in magnetic characteristics in some NO steels [1]. The NO steels are usually manufactured under two-stage cold rolling with intermediate annealing. After the first cold rolling, the annealing could recrystallize and decarburize the steel. After the second cold rolling, the annealing can remove residual stress and obtain the desired random grain growth orientation [2]. Due to the cold rolling processing, inherent anisotropy in its magnetic characteristics depends on the angle to rolling direction but is much less pronounced than in grain oriented steel [2,3]. The anisotropic magnetostriction [4] and hysteresis [5,6] have been experimentally observed in NO steel. In electrical machines applications, it also has been reported that the magnetic anisotropy in NO steel could lead to the increase of core losses [7–9], flux harmonics [5] and cogging torque [10]. Besides, it has been found that both the crystallographic structure and machining process related to the rolling of the tested material is associated directly with magnetic anisotropy [11–14]. Therefore, the evaluation of the magnetic anisotropy would be correlated with assessing the anisotropic mechanical properties and crystallographic structure.

MBN has been proven to be the most efficient and fast method to evaluate the directional magnetic properties [12–16]. The MBN is originated from the discontinuous magnetic domain wall motion and domain transition in the ferromagnetic material occurring under alternating magnetic fields [15,17]. The discontinuous stepwise jumps are attributed to defects in the crystallographic structure of the material, such as dislocations, second-phase and grain boundaries [16,18]. The texture of NO steel after rolling and annealing presents directionality [11,12], which directly affects the pinning sites distribution. Hence, MBN signal could be significantly influenced by the anisotropy at different testing directions. And in turn, MBN is also a preferable solution for the evaluation of the anisotropy of the magnetic material.

It is well known that the Barkhausen jumps of ferromagnetic material are sensitive to various factors such as the microdefect, stress and inclusion. Besides, the anisotropy of material is attributed to a number of factors depending on its microstructure, shape, and mechanical deformation. As a result, the global magnetic anisotropy is influenced by all the factors affecting heterogeneous magnetic properties in different directions of a given material [13]. Therefore, it is an interesting and important topic to analytically evaluate and distinguish the contributions of different factors on MBN. A few studies have investigated the stress anisotropy associated with the magnetomechanical effect [19,20]. The impact of metallographic structure on magnetic anisotropy using MBN activity has been experimentally observed [13,21]. However, few attempts were made to analytically study the anisotropic MBN induced by the microstructure of the material. Hence, in this chapter, an MBN model is proposed to distinguish and evaluate the contribution of microstructure-induced anisotropy.

In this chapter, the MBN model combined with the directional Jiles-Atherton (J-A) hysteresis model that considers the effect of frequency is adopted to study the theoretical correlations between Barkhausen emission and anisotropy. The rest of this chapter is organized as follows. In Section 7.2, the anisotropic MBN models are proposed based on the angular dependent dynamic J-A hysteresis model. In Section 7.3, the details about the verification experiments, including the specimen tempered procedure and the MBN sensor configuration, are introduced. Both the performance and limitations of the proposed model are discussed in Section 7.4. Finally, the major findings of this study are discussed in Section 7.5.

7.2 The Directional Modeling of Magnetic Barkhausen Noise

7.2.1 The frequency-dependent hysteresis model

In previous chapters, the static J-A model was used to solve the problems. But the frequency of excitation may alter the shape and amplitude of the Barkhausen noise

[22] since the excitation frequency could influence the velocities of magnetic domain wall motion and domain transition in the ferromagnetic material resulting in the change of Barkhausen emission level.

According to the conservation of energy, the magnetic energy supplied to an initially demagnetised material (anhysteresis magnetisation M_{an}) can appear either as a change in magnetostatic energy or be dissipated due to hysteresis loss (irreversible magnetisation M_{irr}) [23]

$$\mu_0 \int M_{an} dH_e = \mu_0 \int M dH_e + \mu_0 \delta k(1-c) \int \frac{dM_{irr}}{dH_e} dH_e \tag{7.1}$$

where $H_e = H + \alpha M$, k is the pinning parameter determining the amount of dissipated energy, $\delta = +1$ when $dH/dt>0$ and $\delta = -1$ when $dH/dt<0$, and c is a parameter representing the amount of reversible change in magnetisation.

To consider the effect of frequency in conducting material, the static J-A hysteresis model could be extended by introducing the eddy current losses (classical eddy current loss and anomalous loss) [23].

The classical eddy current (macroscopic) instantaneous power loss per unit volume is proportional to the square of the rate of change of flux density [23]

$$\frac{dW_{cls}}{dt} = \frac{d^2}{2\rho\beta}\left(\frac{dB}{dt}\right)^2 \tag{7.2}$$

where d, ρ and β are the lamination thickness, resistivity and geometrical factor, respectively.

And the anomalous loss or excess loss (microscopic) originated from the domain wall motion is given as [24,25]

$$\frac{dW_{exc}}{dt} = \left(\frac{GdwH_0}{\rho}\right)^{1/2} \delta \left(\left|\frac{dB}{dt}\right|\right)^{3/2} \tag{7.3}$$

where $(GdwH_0/\ \rho)^{1/2}$ can be treated as a constant k_{exc} as it is a fitting parameter regardless of the meaning of G, w and H_0. Therefore, Equation (7.2) can be simplified as

$$\frac{dW_{exc}}{dt} = k_{exc}\delta\left(\left|\frac{dB}{dt}\right|\right)^{3/2} \tag{7.4}$$

Incorporating the eddy current losses into the energy balance Equation (7.1) allows the total loss W (J/m^3) decomposed into hysteresis loss (static hysteresis W_{hys}), classical eddy current loss (W_{cls}) and excess loss (W_{exc})

$$W_{tot}(t) = W_{hys}(t) + W_{cls}(t) + W_{exc}(t) \tag{7.5}$$

$$\mu_0 \int M_{an} dH_e = \mu_0 \int M dH_e + \mu_0 \delta k(1-c) \int \frac{dM_{irr}}{dH_e} dH_e$$

$$+ \int \frac{d^2}{2\rho\beta}\left(\frac{dB}{dt}\right)^2\ dt + \int k_{exc}\delta\left(\left|\frac{dB}{dt}\right|\right)^{3/2}\ dt \tag{7.6}$$

In soft magnetic materials, the flux density B approximates to $\mu_0 M$. Ignoring the reversible magnetisation during irreversible magnetising, the differentiation of Equation (7.4) can be given as

$$M_{an} = M_{irr} + \delta k \frac{dM_{irr}}{dH_e} + k'\left(\frac{dM_{irr}}{dH_e}\right) \tag{7.7}$$

where

$$k' = \frac{d^2}{2\rho\beta}\frac{dB}{dt} + k_{exc}\delta\left(\left|\frac{dB}{dt}\right|\right)^{1/2} \tag{7.8}$$

And the differential susceptibility relation given in [25,26] is employed here

$$\frac{dM}{dH} = \frac{\chi_M}{k\delta + k' - \alpha\chi_M} \tag{7.9}$$

where

$$\chi_M = \delta_m(M_{an} - M) + k\delta c \frac{dM_{an}}{dH_e} \tag{7.10}$$

where

$$\delta_m = \begin{cases} 0: \frac{dH}{dt} < 0 \; and \; M_{an}(H_e) - M(H) > 0 \\ 0: \frac{dH}{dt} > 0 \; and \; M_{an}(H_e) - M(H) < 0 \\ 1: otherwise \end{cases} \tag{7.11}$$

In Equation (7.9), the dynamic hysteresis model is driven by the excitation magnetic field *H* and the magnetic flux density *B* or magnetisation *M* is the dependent variable.

If the magnetic flux density *B* is the independent variable and the magnetic field *H* is the dependent variable, the modified J-A model, i.e., inverse J-A model, allows calculating eddy current losses described above more easily. The procedure in Refs. [25,27] was given to obtain *H*

$$\frac{dM}{dB} = \frac{dM/dH}{\mu_0(1+dM/dH)} \tag{7.12}$$

Substituting it into Equation (7.9), it arrived at

$$\frac{dM}{dB} = \frac{\chi_M}{\mu_0[k\delta+k'+(1-\alpha)\chi_M]} \tag{7.13}$$

where

$$\chi_M = \delta_m(M_{an} - M) + k\delta c\frac{dM_{an}}{dH_e} \tag{7.14}$$

and

$$\delta_m = \begin{cases} 0: \frac{dB}{dt} < 0 \; and \; M_{an}(H_e) - M(B) > 0 \\ 0: \frac{dB}{dt} > 0 \; and \; M_{an}(H_e) - M(B) < 0 \\ 1: otherwise \end{cases} \tag{7.15}$$

Hence, the dynamic magnetic field could be obtained by

$$\frac{dH}{dt} = \frac{1}{\mu_0} \cdot \frac{dB}{dt} - \frac{dM}{dB} \cdot \frac{dB}{dt} \tag{7.16}$$

7.2.2 The angular dependent magnetic hysteresis model

The J-A model usually deals with isotropic problems. But a few attempts have been made to introduce anisotropy into the J-A model [6,28,29]. The NO steel usually experiences two annealings after cold rolling, one for recrystallization and the other for residual stress relief. After the cold rolling, the equiaxed grains are heavily deformed and elongated in the rolling direction. Though the residual stress is gradually released and the microstructure recrystallized after annealing, the recrystallized grains are small in size and amount. In contrast, the main grains are still deformed crystals. These result in the inherent anisotropy of NO steel [12]. The deformation of grains increases the anisotropic energy along the rolling direction, and hence the magnetocrystalline anisotropy energy depends on the rolling direction angle.

Since the anisotropy depends on the angle, the widely used fitting function is a trigonometric function [6,30,31], though the formulas are different. Following an analogous formula of anisotropy energy, the angular dependent parameters of the J-A model that could well fit the measurements is proposed as

$$x(\theta) = x_{RD} cos^2\theta + x_{TD} sin^2\theta \tag{7.17}$$

where x can be M_{st}, a, k, α and c. θ is the angle between the tested direction and the rolling direction. x_{RD} and x_{TD} represent the identified parameters of J-A model in the rolling direction (RD) and transverse direction (TD), respectively.

Therefore, Equations (7.9) and (7.12) can be rewritten as

$$\frac{dM(\theta)}{dH} = \frac{\chi_M(\theta)}{k(\theta)\delta + k' - \alpha(\theta)\chi_M(\theta)} \tag{7.18}$$

$$\frac{dM(\theta)}{dB} = \frac{\chi_M(\theta)}{\mu_0[k(\theta)\delta + k' + (1 - \alpha(\theta))\chi_M(\theta)]} \tag{7.19}$$

7.2.3 The angular dependent magnetic Barkhausen noise

In the previous chapter, the formula of Barkhausen emissions modelled on the J-A model was given by

$$M_{JS} = \gamma \cdot \frac{dM_{irr}}{dt} \cdot \Delta t = \gamma \cdot \frac{dM_{irr}}{dH} \cdot \frac{dH}{dt} \cdot \Delta t \tag{7.20}$$

where

$$\gamma = \frac{d(N\langle M_{disc}\rangle)}{dM_{irr}} \tag{7.21}$$

$$\frac{dM_{irr}}{dH} = \frac{M_{an}-M_{irr}}{k\delta} \cdot \left(1 + \frac{\alpha \cdot dM}{dH}\right) \tag{7.22}$$

where γ was a coefficient with respect to the irreversible magnetisation, and $\langle M_{disc}\rangle$ was the average size of discontinuous jumps.

And the differential expression of Barkhausen jumps was given by

$$\frac{dM_{JS}}{dt} = \frac{dM_{irr}}{dH} \cdot \frac{dH}{dt} \cdot \langle M_{disc}\rangle \cdot \frac{dN}{dM_{irr}} \tag{7.23}$$

When the effects of frequency and anisotropy are taken into account, using the frequency-dependent and angular dependent J-A model, the Barkhausen jumps model could be modified as

$$\frac{dM_{JS}(f,\theta)}{dt} = \frac{dM_{irr}(f,\theta)}{dH} \cdot \frac{dH}{dt} \cdot \langle M_{disc}\rangle \cdot \frac{dN}{dM_{irr}(f,\theta)} \tag{7.24}$$

where

$$\frac{dM_{irr}(f,\theta)}{dH} = \frac{M_{an}(f,\theta)-M_{irr}(f,\theta)}{k(f,\theta)\delta+k'(f,\theta)}\left(1 + \frac{\alpha(f,\theta)dM(f,\theta)}{dH}\right) \tag{7.25}$$

In Equation (7.24), if the rate of change of applied magnetic field dH/dt with time is determined, the Barkhausen jumps are dominated by the differential susceptibility of irreversible magnetisation $dM_{irr}(f,\theta)/dH$ as the rest part on the right-hand is represented the random behaviour of the model. Since the predicted and measured MBN_{rms} will be compared in this study, the stochastic fluctuation caused by the

Poisson distribution is replaced by the expectation after averaging. Equation (7.24) can be further modified as

$$\frac{dM_{JS}(f,\theta)}{dt}|_{rms} = A \cdot \frac{dM_{irr}(f,\theta)}{dH} \cdot \frac{dH}{dt} \tag{7.26}$$

If *dB*/*dt* is an independent variable, using the dynamic inverse J-A model, the Barkhausen jumps model could be expressed by

$$\frac{dM_{JS}(f,\theta)}{dt}|_{rms} = A' \cdot \frac{dM_{irr}(f,\theta)}{dB} \cdot \frac{dB}{dt} \tag{7.27}$$

where

$$\frac{dM_{irr}(f,\theta)}{dB} = \frac{M_{an}(f,\theta)-M_{irr}(f,\theta)}{\mu_0(k(f,\theta)\delta+k'(f,\theta))}\left(\alpha(f,\theta) + \frac{\mu_0 dH(f,\theta)}{dB}\right) \tag{7.28}$$

Furthermore, it is known that the maximum value of Barkhausen noise occurs at the coercive field H_c [32,33], as discussed in the previous chapter

$$MBN_p = \chi'_{H_c}(\frac{dH}{dt}|_{H_c}) \cdot \gamma \cdot \Delta t \tag{7.29}$$

where χ'_{H_c} is the differential susceptibility of irreversible magnetisation at the coercivity point. It is known that in soft ferromagnetic material the maximum differential susceptibility of irreversible magnetisation χ'_{H_c} can be approximated by anhysteresis differential susceptibility χ'_{an} [32,33]. According to the expression of differential susceptibility χ'_{an} in Equation (6.14), it could be obtianed

$$MBN_p(\theta) = \frac{1}{\Gamma(\theta)} \tag{7.30}$$

where

$$\Gamma(\theta) = \kappa\left[\frac{3a(\theta)}{M_{st}(\theta)} - \frac{3a_{RD}}{M_{st_{RD}}} + (\alpha_{RD} + \alpha_{TD})sin^2\theta\right] + \frac{1}{MBN_p(0)} \tag{7.31}$$

where κ is a constant coefficient about the rate of applied field change and the averaged irreversible magnetisation coefficient at the coercivity point. When the parameters along the rolling direction are determined, Equation (7-31) can be further simplified as

$$\Gamma(\theta) = \kappa \left[\frac{3a(\theta)}{M_{st}(\theta)} - \alpha(\theta)\right] + \kappa' \tag{7.32}$$

where κ' is a constant coefficient, and the angular dependent parameters a (θ), M_{st} (θ) and α (θ) follows Equation (7.17).

7.3 Verification Experiments for the Effect of Anisotropy on MBN

According to the directional J-A model, the angular dependent parameters could be represented by those in RD and TD. Hence, the Epstein sheets of M330-35A non-oriented (NO) grain silicon steel cut along RD and TD are used to identify the parameters of J-A model. The specimens are annealed at 400°C for two hours to relieve the residual stress. The quasi-static hysteresis measurement system described in the previous chapters is used to measure the hysteresis loops without the effect of frequency. The key parameters values in RD and TD are determined by the hybrid GA-PSO algorithm, and the results are listed in Tables 7.1 and 7.2, respectively.

When the frequency is involved, the computer-controlled AC system is used to measure the hysteresis loop by controlling magnetic induction as a sinusoidal waveform. Fig. 7.1 shows the schematic diagram of the system, which includes a personal computer (PC) with the installed National Instrument software package Labview, a NI PCI-6120 DAQ card, a power amplifier, a mutual inductor, a single strip tester (SST) and a shunt resistor. The SST comprises two vertical yokes, primary and secondary coils, and the plastic carrier. One of the mutual inductors is connected to the primary coil in series, while the other is connected to the secondary winding in the opposite series to compensate for air flux.

The magnetising voltage is generated by PC via Labview and DAQ card. The voltage waveform is fed through a low-pass filter to SST *via* the power amplifier. The magnetising current passing through the shunt resistor allows magnetic field H measurement. The secondary voltage read by the DAQ card is used to calculate the magnetic flux density B.

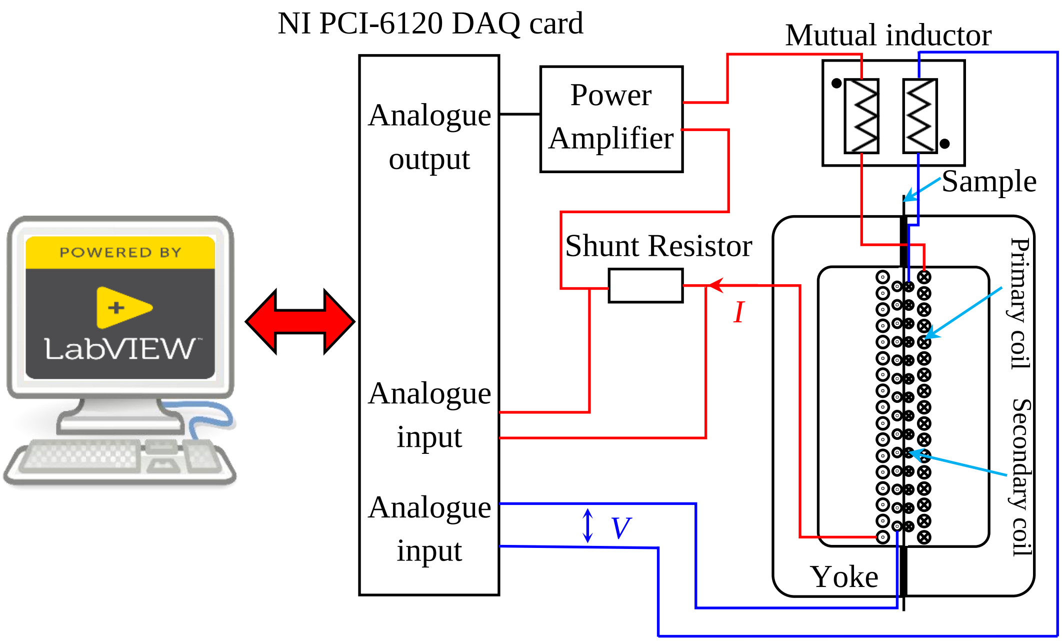

Figure 7.1. The schematic diagram of the AC measurement system.

The instantaneous magnetic field strength (*H*) is calculated following the expression

$$H(t) = \frac{N_1 \cdot V_R(t)}{l \cdot R} \tag{7.33}$$

where N_1, V_R, l, R are the turns number of the primary coil, voltage drop across the shunt resistor, the distance between the inner edges of the yoke and the resistance of shunt resistor, respectively.

The instantaneous magnetic flux density (*B*) originated from the secondary voltage can be expressed as

$$B(t) = \frac{l_s \cdot \rho}{N_2 \cdot m} \int_t^{t+\Delta t} V dt \tag{7.34}$$

where l_s, ρ, N_2, m, V are the sample length, the density of the sample, the turns number of the secondary coil, the mass of the sample and the inducing voltage, respectively.

The block diagram of the feedback system used for the control of flux density waveform is presented in Fig. 7.2. At first, a reference sinusoidal waveform of flux density *B* is given according to the setting, and a first magnetising waveform is applied to SST. Then, the relative difference between reference waveform B_{ref} and the measured flux density waveform B_m is computed. If the criteria, which are generally

0.02% error of the peak value of B and 0.02% error of the ideal form factor, are met, the *B* and *H* waveforms will be saved and recorded to a file. Otherwise, the output voltage waveform is continuously adapted and modified by the feedback algorithm [34] in every subsequent iteration until it meets the criteria.

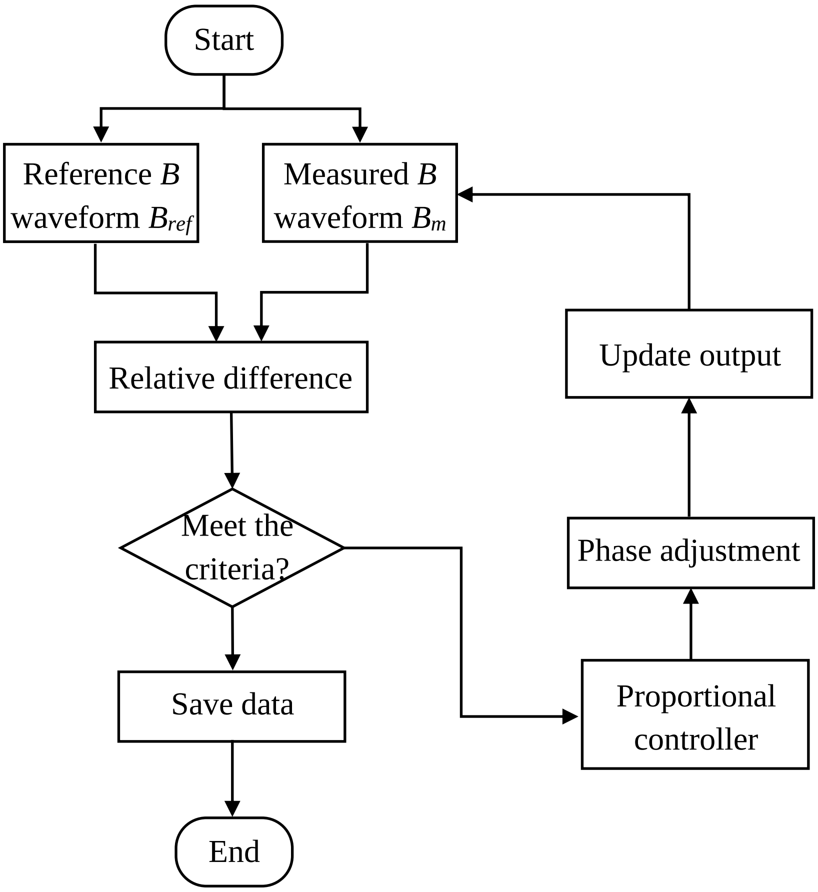

Figure 7.2. Block diagram of the adaptive feedback system.

To test the effect of frequency on MBN, the magnetising frequencies 25Hz, 50Hz, 75Hz, 100Hz and 200Hz are used. During anisotropy measurements, the magnetising frequencies 50Hz and 100Hz are applied. The voltage used in all measurements is set to 10V. The pick-up coil output voltage is subsequently amplified with the low noise AD797 operational amplifier and digitized by the Microscan 600 system with a sampling frequency of 2.5MHz.

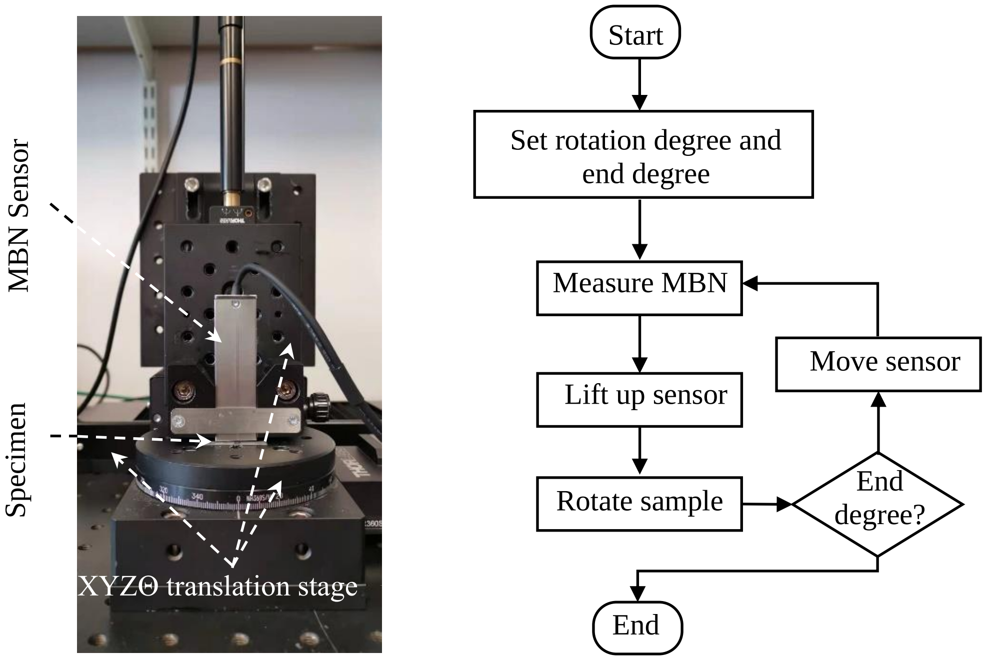

(a) (b)

Figure 7.3. (**a**) The MBN experimental set-up; (**b**) The schematic diagram of the Barkhausen sensor.

7.4 Results and Discussion for the Effects of Frequency and Anisotropy on MBN

7.4.1 The effect of frequency on MBN signal

The typical MBN_{rms} signals measured along the rolling direction of M330-35A NO steel at different frequencies are plotted in Fig. 7.4. Since the MBN originates from the abrupt irreversible motion of the magnetic domain walls, which is proportional to the rate of change of magnetisation in the material, the increase in the rate of magnetisation with the increase in excitation frequency will lead to the increase in the peak height of MBN [35,36]. It can be observed from Fig. 7.4 (a) to (d) that the height of the MBN profile increase with the excitation frequency. However, simultaneously, the increase of excitation frequency will decrease penetration depth and increase the eddy current losses. Due to the skin effect, the increasing excitation frequency decreases the magnetised depth, resulting in a decreased number of domain walls and pinning sites. Besides, the increase of eddy current losses will reduce the internal potential to drive the domain walls and further decrease the extent of displacement. Therefore, at high frequency, the height of MBN may decrease with excitation frequency as shown in Fig. 7.4 (e). Those factors jointly influence the level of MBN signal.

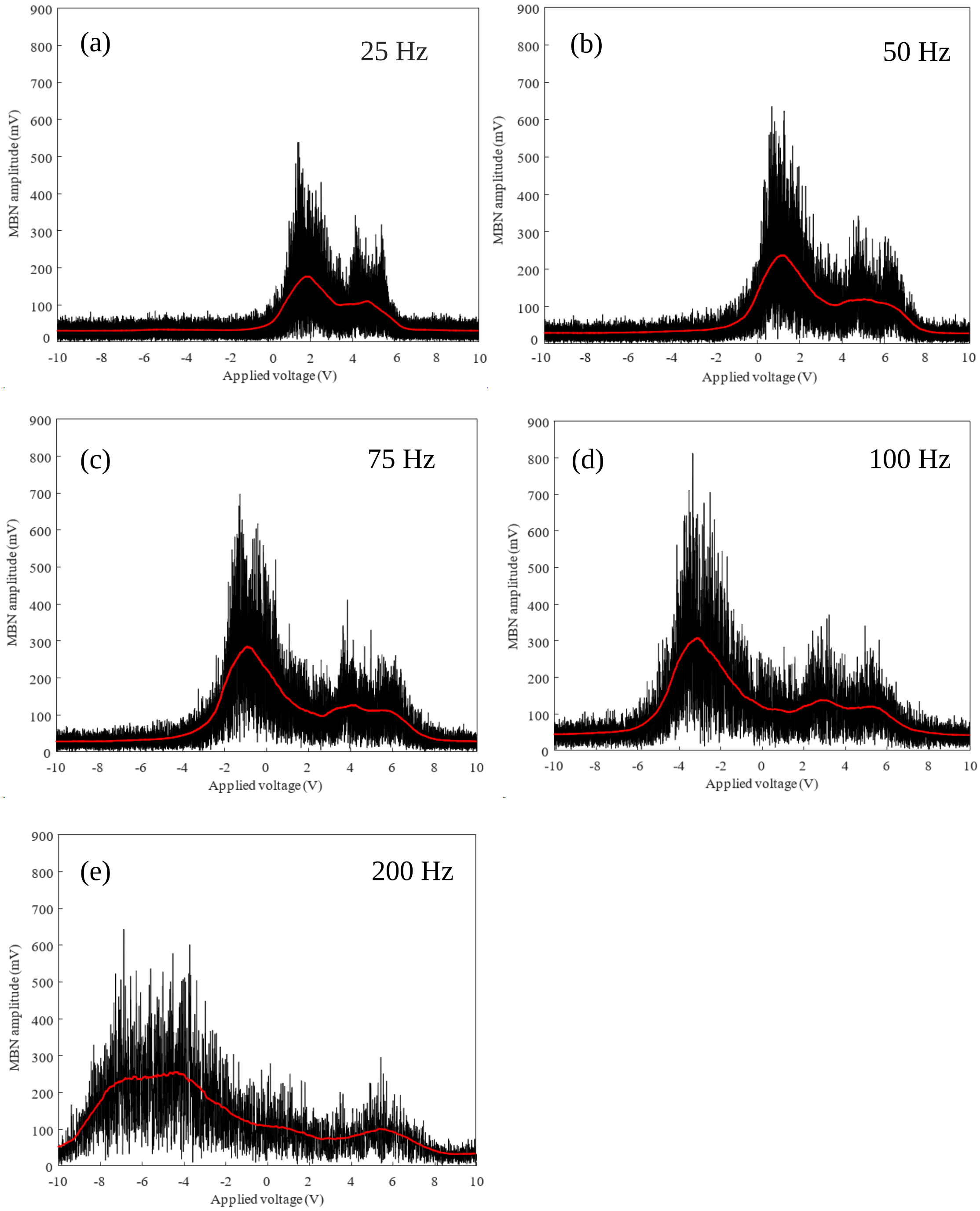

Figure 7.4. MBN profiles measured along RD of M330-35A NO steel under various excitation frequencies.

At low frequency (e.g., less than 100 Hz), the level of MBN is dominated by the rate of change of magnetisation in the material. The height of MBN signal is proportional to the excitation frequency. While at high frequency (e.g., higher than 100 Hz), the combined effects of skin and eddy current losses surpass the effect of the rate of change of magnetisation. The height of MBN signal is inversely proportional to the excitation frequency. This conclusion can be observed in Fig. 7.5. In most studies, the excitation frequencies are less than 100 Hz, i.e., low frequency. Since the analysis at high frequency is complicated and unnecessary, the magnetisation on MBN at low frequency is mainly considered in this study.

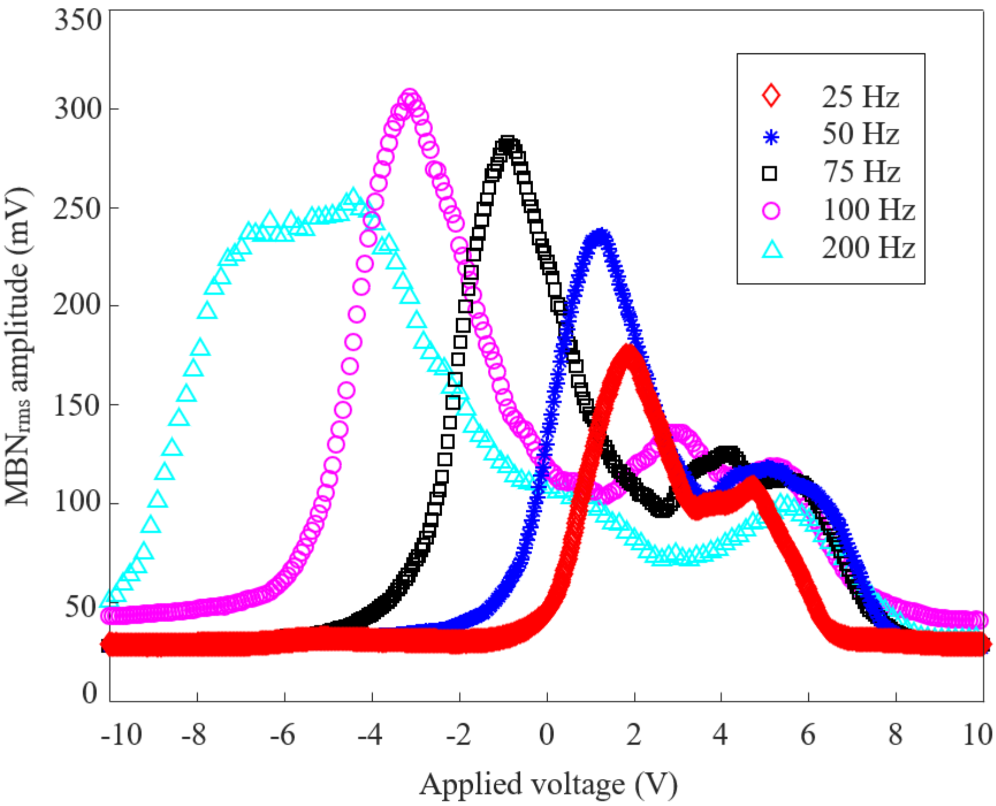

Figure 7.5. The effect of excitation frequency on MBN envelopes for M330-35A NO steel.

It can be seen in Fig. 7.5 that the MBN profile is broadening with the increase of excitation frequency. It mainly attributes to the eddy current losses caused by dynamic magnetisation. Due to the energy losses, the domain walls need more intensive magnetic potential to overcome the pinning sites. Hence, a higher excitation frequency would cause a higher coercive field and a wider distribution range of Barkhausen activities in a magnetisation period (experimentally observed in [36] as well). The hysteresis loops obtained for M330-35A NO steel at various frequencies in Fig. 7.6 can also indicate that the excitation frequency would broaden the loops leading to the increase of coercive field.

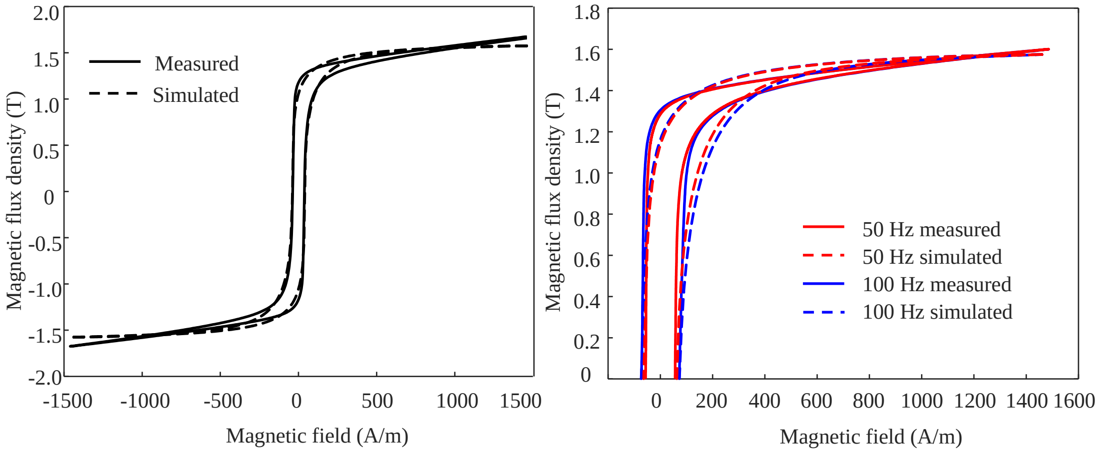

(a) (b)

Figure 7.6. (a) The measured and fitted hysteresis loops for M330-35A NO steel along the rolling direction at quasi-static frequency. **(b)** The measured and fitted hysteresis loops for M330-35A NO steel along rolling direction at 50 Hz and 100 Hz.

It can also be observed from Figs. 7.4 and 7.5 that the secondary peak of MBN envelope is increasingly obscure with the increase of excitation frequency. It has been explained in the previous chapter that the secondary peak is originated from the domain annihilation and rotation at a higher field. The increase of eddy current losses leads to the decrease of internal magnetic potential. For the softer phase, the effect of energy losses is the secondary factor at a low frequency, while for the harder phase, the influence is comparable to the effect of magnetisation change. Therefore, the secondary peak of MBN envelope increases slower at low frequency. Since the prominent peak of the MBN envelope is clearer and more sensitive to characterise the effects of excitation frequency and material anisotropy at low frequency, the one peak model for the softer phase is considered in this chapter only.

To model the effect of frequency on MBN, the key parameters of J-A model for M330-35A NO steel need to be determined. The hysteresis loop for the M330-35A NO silicon steel strip cut along the rolling direction is measured by a computer-controlled hysteresis loop tracer at a quasi-DC field of 5mHz as shown in Fig. 7.6a. The hybrid GA-PSO algorithm is used to fit the measured hysteresis loop without consideration of frequency. The best fitting parameters are listed in Table 7.1. The hysteresis loops shown in Fig. 7.6b are measured at 50 Hz and 100 Hz by controlling the magnetic induction *B* as a sinusoidal waveform. They can also be fitted using the hybrid GA-PSO algorithm using Equation (7.13). During the MBN measurements, the excitation magnetic field is sinusoidal, so the values of magnetic field *H* are independent variables, and the values of magnetic induction *B* are dependent variables. Hence, the parameters of J-A model fitted at quasi-DC are substituted into Equation (7.9) to fit the loops at different frequencies by introducing the eddy current losses. The best frequency coefficient is determined and listed in Table 7.1.

Table 7.1. The key parameters of the J-A hysteresis model for M250-50A NO electrical steel along the rolling direction (RD) and transverse direction (TD)

J-A parameters	Values (RD)	Values (TD)	Sources
Saturation magnetisation, M_{st}	1.2961×10^6 (A/m)	1.4195×10^6 (A/m)	Measured and identified by hybrid GA-PSO algorithm
Pinning parameter, k	80.0055 (A/m)	189.6829 (A/m)	
Domain density, a	53.3297 (A/m)	266.3804 (A/m)	
Coupling factor, α	1.3992×10^{-4}	4.8642×10^{-4}	
Reversibility parameter, c	0.4223	0.6725	
Frequency coefficient, k_{exc}	41.2491	25.4512	

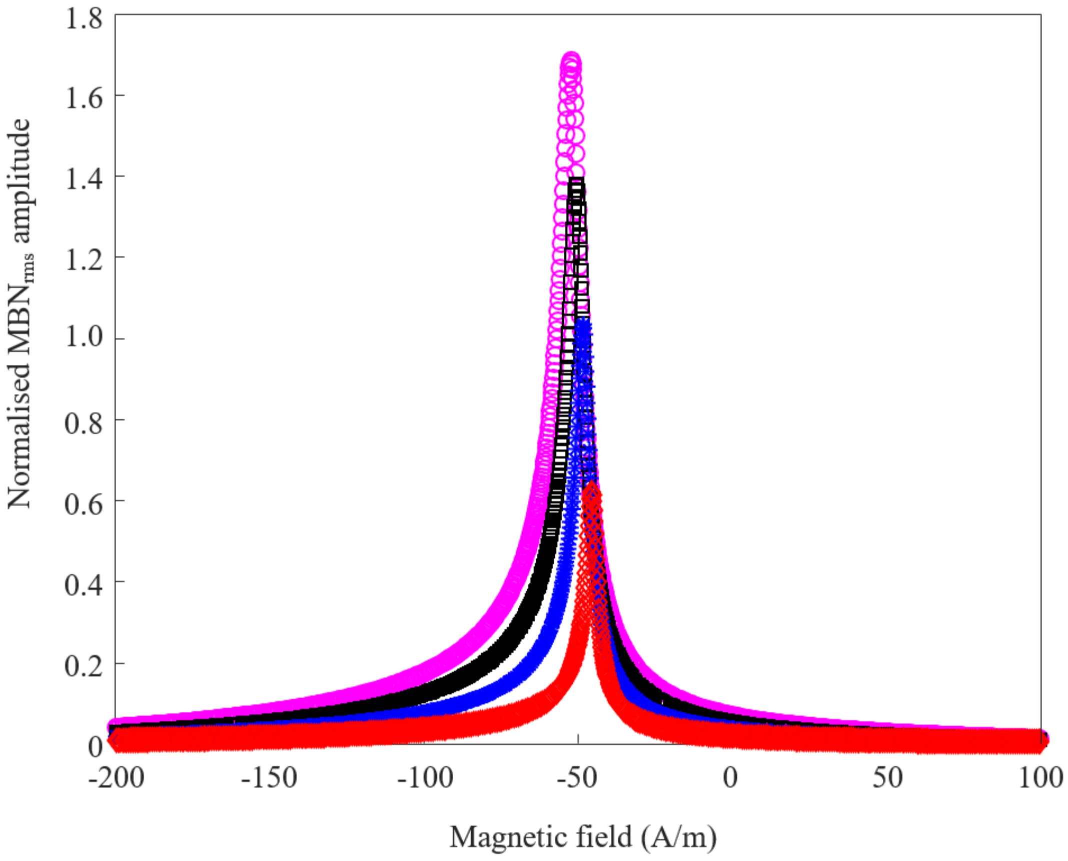

Figure 7.7. The simulated MBN envelopes for M330-35A NO steel at various frequencies.

Based on the best fitted parameters, the profiles of MBN$_{rms}$ simulated at 25 Hz, 50 Hz, 75 Hz and 100 Hz are plotted in Fig. 7.7. It can be seen that the height of MBN profile also increases with the excitation frequency and the width of MBN profile broadens with the excitation frequency. It indicates that the correctness of the mechanism and the proposed model.

7.4.2 The effect of anisotropy on MBN

The key parameters of J-A model for M330-35A NO steel along the transverse direction are also obtained following an analogous procedure. The hysteresis loop for the M330-35A NO steel strip cut along the transverse direction is measured at a quasi-DC field of 5mHz as well (see Fig. 7.8a). The hybrid GA-PSO algorithm is used to determine the parameters. The hysteresis loops of M330-35A NO steel along transverse direction measured at 50 Hz and 100 Hz by controlling the magnetic induction *B* as sinusoidal waveform are shown in Fig. 7.8b. The parameters of J-A model fitted at quasi-DC are employed to fit the loops further and determine the frequency coefficient. The fitted J-A parameters and the frequency coefficient for M330-35A NO steel along the transverse direction are listed in Table 7.1.

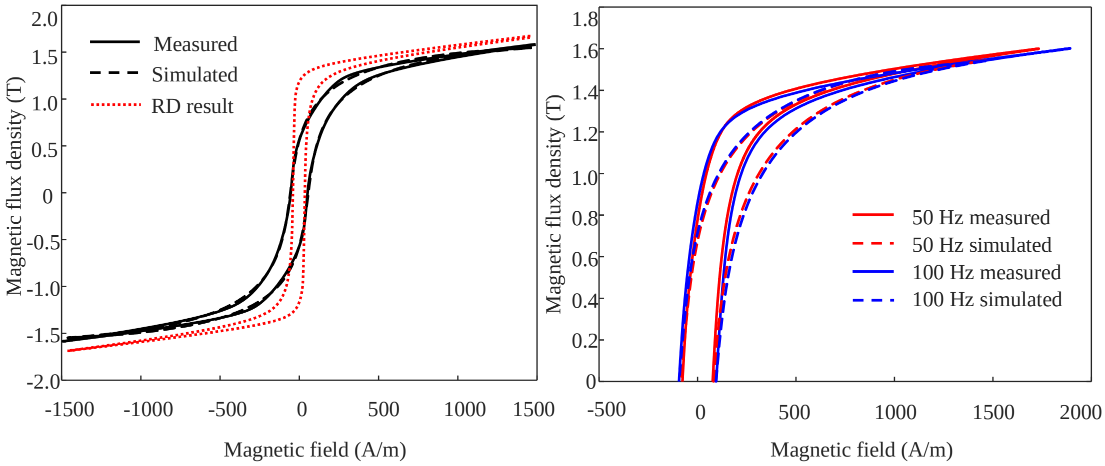

(a) (b)

Figure 7.8. (a) The measured and fitted hysteresis loops for M330-35A NO steel along the transverse direction at quasi-static frequency comparing with the measured hysteresis loop for M330-35A along rolling direction. **(b)** The measured and fitted hysteresis loops for M330-35A NO steel along the transverse direction at 50 Hz and 100 Hz.

Comparing the hysteresis loops presented in 7.8a, it can be seen that M330-35A NO silicon steel is magnetically anisotropic. Hence, the optimised parameters of RD are significantly different from those of TD. It is well known that the pinning parameter *k* is related to the coercive field strength H_c and the coercive field is widely used to characterise the magnetic hardness. The pinning parameter of RD k_{RD} is much smaller than that of TD k_{TD}. It indicates that the RD is magnetically soft, i.e., easy direction, whereas the TD is the hard direction. Besides, according to the formula of anhysteresis Equation (2.40), the domain density parameter *a* could control the smoothness of the '*s*' shape. Therefore, the larger the value of *a*, the smoother the shape of hysteresis loop is. Since the domain density parameter, *a*, of TD is much larger than that of RD, the rate of change of magnetisation of TD should be lower than that of RD, especially at the coercive field point. It has been known that the maximum value of Barkhausen noise usually is proportional to the differential susceptibility of irreversible magnetisation at the coercive field point χ'_{H_c}. Hence, the peak value of MBN envelope of TD should be smaller than that of RD.

The representative experimental MBN signals measured for the M330-35A NO silicon steel in monotonically increasing angle within the range from 0^o to 90^o under 50 Hz sinusoidal excitation are illustrated in Fig. 7.9. These acquired bursts indicated the effect of anisotropy on MBN. The increasing angle between measurement direction and rolling direction results in the increase in magnetic hardness, which decreases the Barkhausen activities generating lower MBN emissions. Moreover, it can be seen that with the increasing angle the Barkhausen emissions gradually increase in width of the primary MBN bursts, whereas the secondary bursts gradually vanish in the primary. The smoothed $\mathrm{MBN_{rms}}$ envelopes are shown in Fig. 7.9h. These envelopes demonstrate the progressive decreasing and broadening of the MBN bursts as the increasing angle.

Based on the optimised parameters of J-A model for RD and TD of M330-35A NO silicon steel, the simulated MBN envelopes in monotonically increasing angle within the range from 0^o to 90^o under 50 Hz sinusoidal excitation using Equations (7.9), (7.17) and (7.26) are plotted in Fig. 7.10. The simulated MBN envelopes are normalised by the maximum amplitudes of the simulated MBN envelope of RD. It can be found that the highest amplitude and the width of the simulated MBN envelopes decrease and broaden with increasing angle, respectively. It corresponds to the observation in experiments, which indicates that the proposed MBN model could explain the effect of anisotropy on MBN profiles. However, it should be noted that the rate of change of the amplitude of the simulated MBN envelope is larger than the measured. It can be attributed to the following reasons.

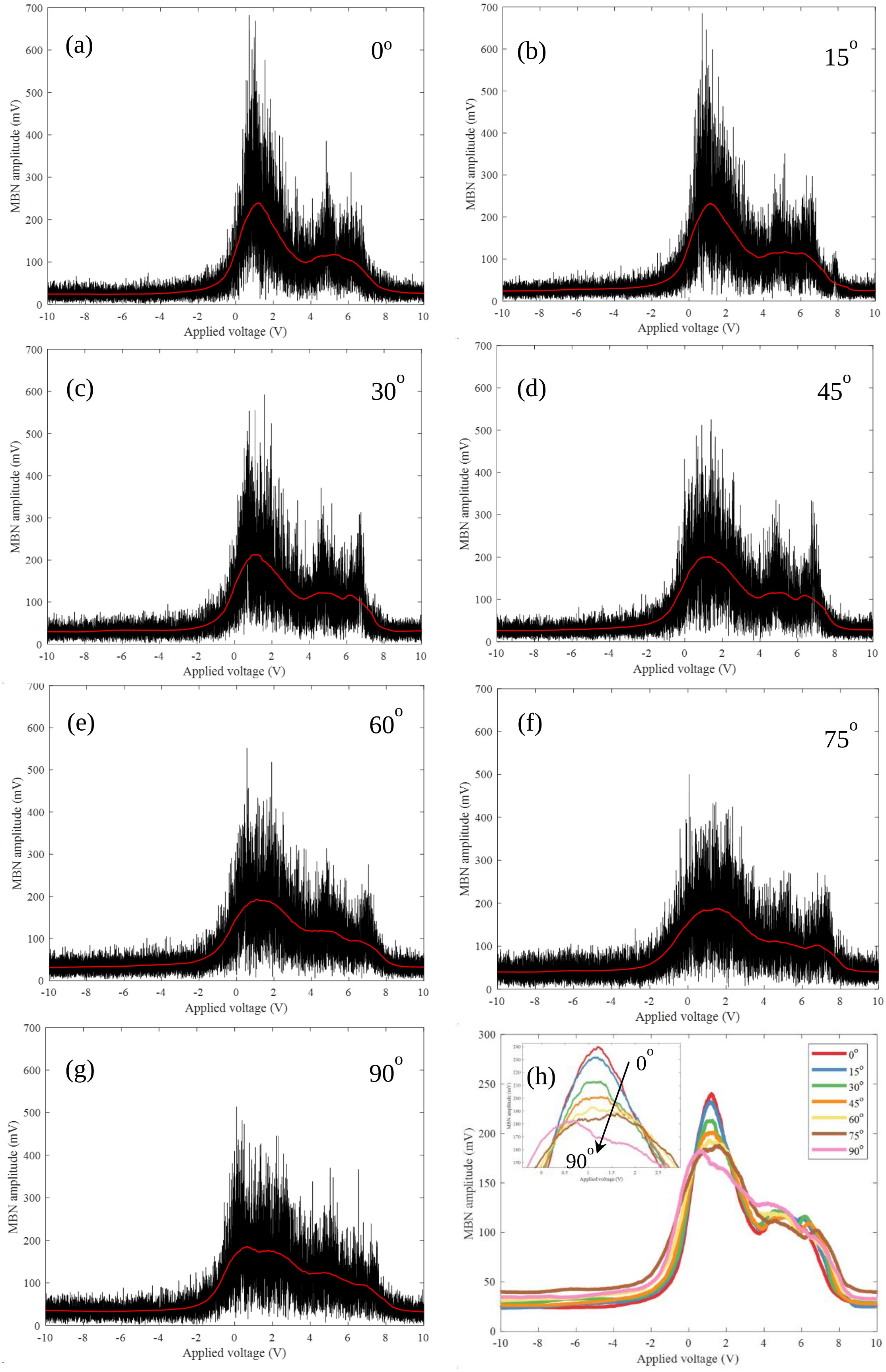

Figure 7.9. MBN profiles measured for M330-35A NO steel in various directions.

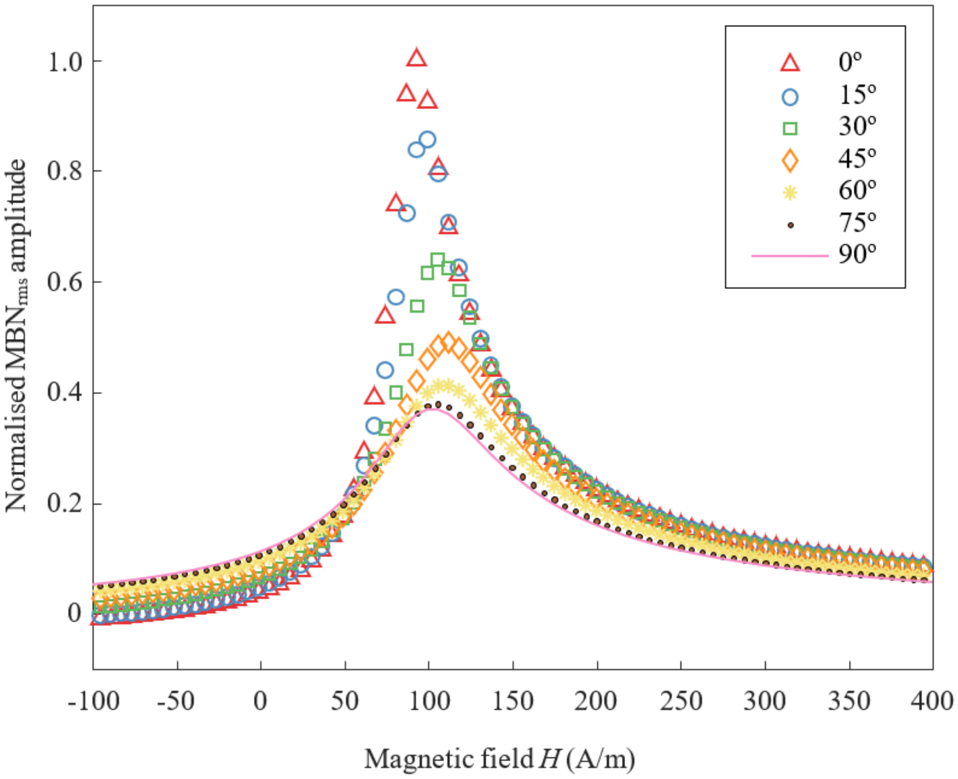

Figure 7.10. Simulated magnetic Barkhausen Noise signal envelopes for M330-35A NO silicon steel sample in various directions.

According to the MBN model, the maximum amplitude of MBN envelope emerges around the coercive field, where the differential irreversible susceptibility χ'_{irr} reaches its largest value χ'_{H_c}. As seen in Fig. 7.6a, the hysteresis curve of the rolling direction sample at coercive field is approximately perpendicular to the *x*-axis, which means the slope of susceptibility at coercivity may approach infinity or a considerable value. The slope of susceptibility is usually calculated by $\Delta M/\Delta H$, which can be considered as a tangent function. When the angle decreases from π/2 to 0, the value of tangent function sharply decreases and then smoothly. Therefore, when the simulated direction rotates from RD to TD, the peak values of MBN envelopes experience a sharp and smooth decrease. In comparison, the reality is that the measured direction may not that significantly influence the Barkhause activities. The domains randomly distribute in NO silicon steel after annealing, though there is magnetic anisotropy due to rolling.

Hence, in any tested directions, there are considerable numbers of Barkhausen activities.

Besides, considering the magnetic field *H* non-coaxial with the easy axis, to simplify the analysis, Fig. 7.11 shows the change of domains in a crystal grain with the increase of magnetic field *H* that is not coaxial with the 180^{o} domain wall. At a low magnetic field (Fig. 7.11a), the external field moves the domain walls leading to the increase of the volume of the domains closest to the field at the sacrifice of the other domains. With the increase of applied field as shown in Fig. 7.11b, the annihilation of the 180° walls starts and the 90° domain walls rotate towards the magnetic field direction. These result in the rapid movement of domain walls, which causes the main Barkhausen activities. Finally, the domain closest to the field occupies the whole grain (Fig. 7.11c). Continuing to increase the external field, when the field energy overcomes the anisotropy energy, the moments will rotate from the original easy axis to the new one closest to the applied field direction. The Barkhausen emissions mainly occur in the stage shown in Fig. 7.11b, where a relatively low external field would implement this procedure. Since the excitation field is high enough, even its component along the easy axis would provide sufficient energy to drive the movement and rotation of domain walls in a range of angle, like 15^{o} and 30^{o}. Therefore, the measured MBN envelopes decrease with increasing angle more slowly than the simulated ones.

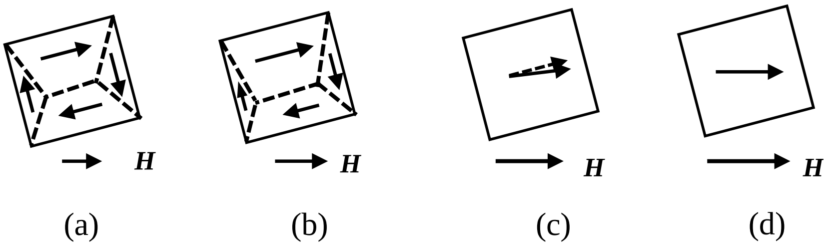

Figure 7.11. Schematic diagram of the change of domain structure during magnetisation with a non-coaxial external magnetic field.

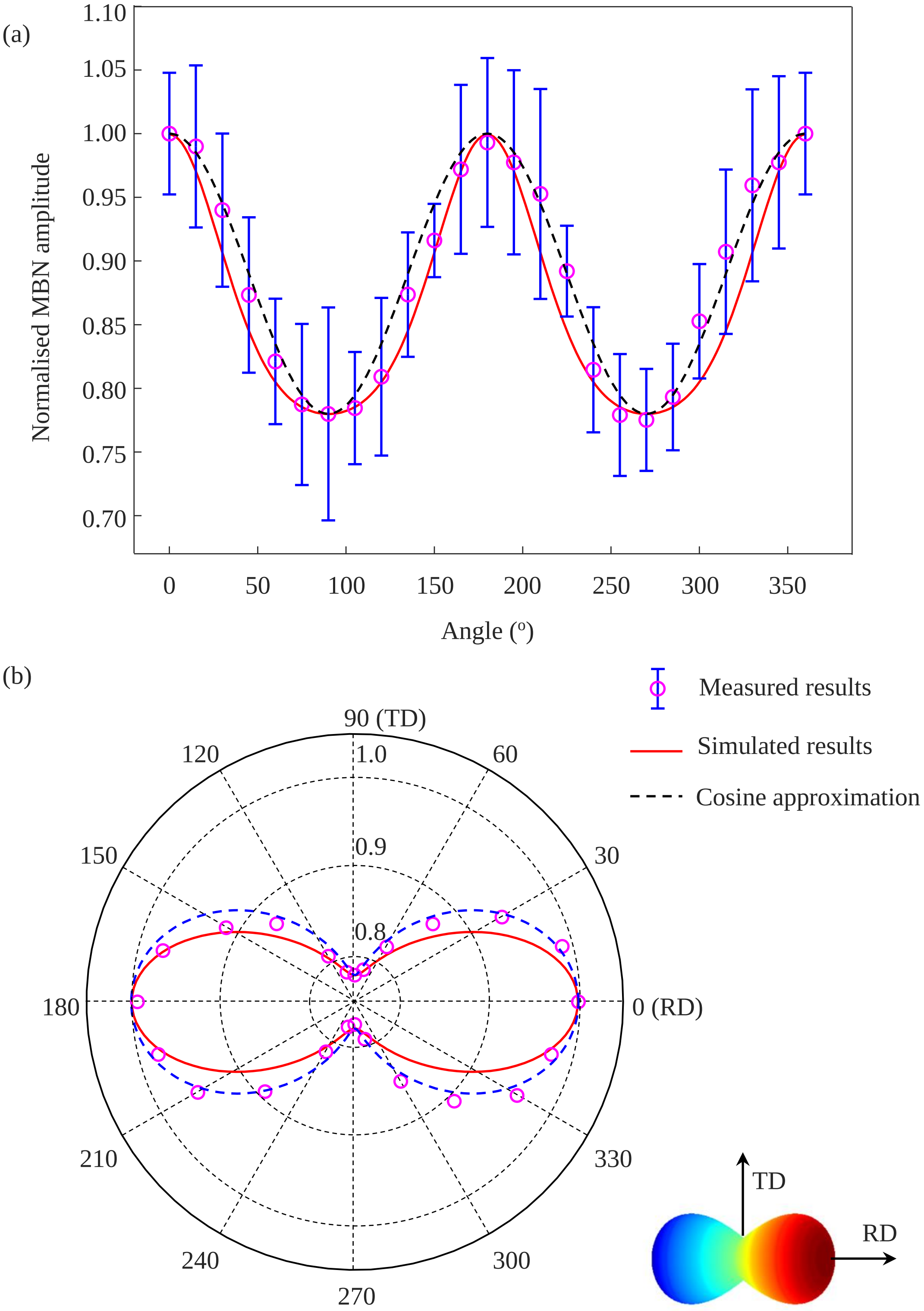

Figure 7.12. **(a)** The comparison of measured and predicted MBN peak values as a function of angles under 50 Hz excitation. **(b)** Comparison of the MBN_p in polar plot.

To quantitatively evaluate the effect of anisotropy on the MBN signal, the main concern should be the extent to which the measured direction impact Barkhausen noise.

The peak value of MBN envelope is used to characterise the influence. Its changing trend is described in Equation (7.32). The practical formula could avoid the calculation of differential susceptibility but remain the anisotropic characteristics. The predicted angular dependent MBN peak amplitude using Equation (7.32) is plotted in Fig. 7.12a together with the measured results and its cosine approximations. The measured and predicted results are normalised by the maximum amplitudes of the experimental and simulated MBN envelopes of RD, respectively.

It can be found that the dependence of the peak amplitude of the MBN signal on the tested direction obtained from experiments corresponds with the simulated and cosine approximated with coefficients of determination R^2 higher than 0.90 and 0.97, respectively. It indicates that both the proposed MBN_p model and the cosine dependency of MBN_p on angle can be applied to evaluate the effect of anisotropy of MBN quantitatively. The simulation model could fit the measured points in angles near RD and TD better than cosine approximated, whereas the cosine approximation could better fit the experimental results when the angles between tested direction and RD or TD are larger than 15°. The tested angle rotating from RD to TD results in a decrease of 22.24% in the MBN peak value. Therefore, its influence should be considered in precise evaluation using the MBN method, especially residual stress evaluation, since stress could also induce magnetic anisotropy.

The comparison of MBN peak amplitude in polar coordinates is further plotted in the polar diagram (Fig. 7.12b). It is well known that the anisotropic magnetic behaviour is related to the magnetocrystalline anisotropy energy (MAE), which is the intrinsic characteristic of ferromagnetic material caused by the crystal structure, stress, grain size and shape. It reflects in the structure of texture that macroscopically influences the anisotropy of ferromagnetic material and subsequently impacts MBN signals [37]. Therefore, the polar plot of the MBN peak value may be used to indicate the MAE of M330-35A NO steel. According to the MBN experimental results, the inferred MAE distribution is depicted on the right-hand plot of Fig. 7.12b.

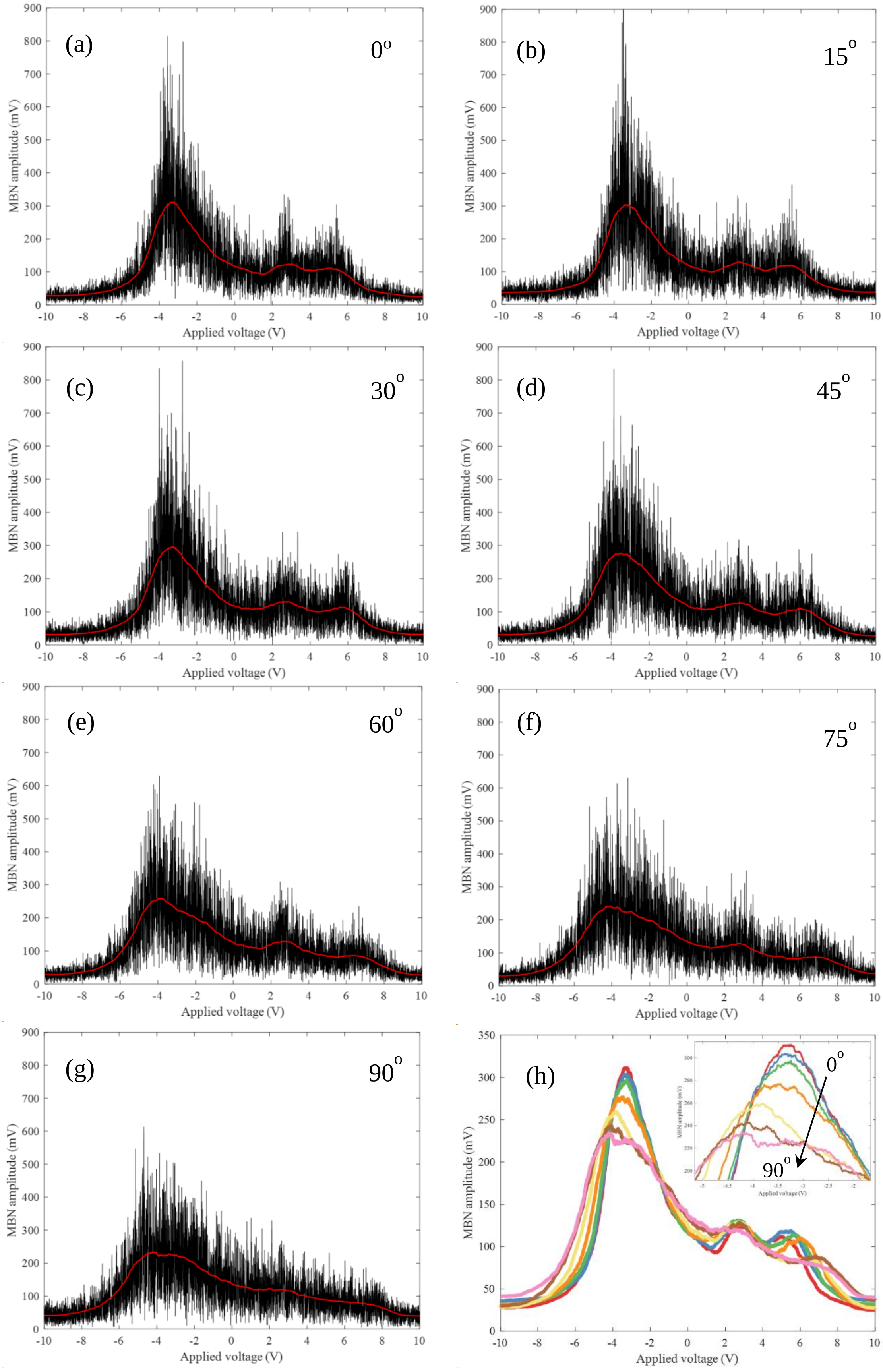

Figure 7.13. MBN profiles measured for M330-35A NO steel in various directions under excitation of 100 Hz.

The quantitative evaluation of the effect of anisotropy on MBN emissions in M330-35A NO steel sample under 100 Hz sinusoidal excitation is analysed through the smoothed MBN signal envelopes shown in Fig. 7.13. It can also be seen that with the increasing angle from RD to TD the Barkhausen envelopes of the primary MBN bursts gradually broaden, whereas the secondary bursts gradually vanish in the primary. It is also demonstrated the progressive decrease of the MBN peak value as the increase of angle as shown in Fig. 7.13h. Comparing with the results of 50 Hz, both the values of height and width of the MBN envelopes under 100 Hz excitation are larger.

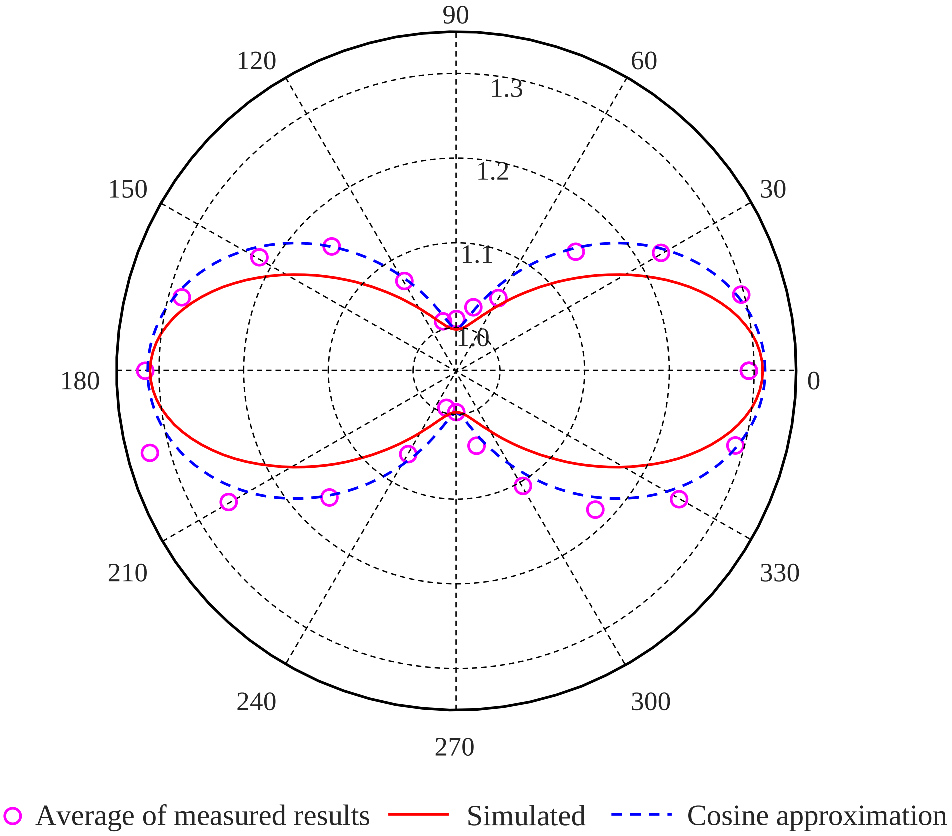

Figure 7.14. Angular dependence of MBN peak amplitude under 100 Hz excitation.

Based on the optimised parameters of J-A model for RD and TD of M330-35A NO silicon steel, the MBN peak values calculated within the range angle from 0^o to 90^o under 100 Hz sinusoidal excitation using Equation (7.32) are plotted in polar Fig. 7.14 together with the measured results and its cosine approximations. All the results are normalised by the maximum amplitudes of the corresponding MBN envelopes of RD under 50 Hz excitation. It is obvious that under 100 Hz excitation the MBN peak value in each angle is larger than the corresponding value under 50 Hz excitation. In this case, the peak values of MBN envelopes decrease by 23.87% with the increasing angle from 0^o to 90^o. It indicates that the effect of anisotropy on Barkhausen emission is more significant with the increase of excitation frequency. Both the predicted model and cosine approximation show a good fitting to the measured results with coefficients of determination R^2 higher than 0.85 and 0.96, respectively, though they are slightly smaller than that under 50 Hz excitation. It indicates that both the proposed MBN_p model and the cosine dependency of MBN_p on angle can be appropriate for evaluating the effect of anisotropy on MBN under various excitation frequencies.

It is interesting that He *et al*. [38,39] experimentally found that the thermomechanical processing steps such as hot rolling, cold rolling and annealing would significantly influence the angular dependency of $\mathrm{MBN_{rms}}$. The peak values of $\mathrm{MBN_{rms}}$ of hot rolling and cold rolling showed an opposite trend with the angle between testing and rolling directions [38]. Moreover, the $\mathrm{MBN_{rms}}$ amplitudes of different final annealing temperatures presented different or even opposite dependency on the angle between measuring and rolling directions [38,39]. Since the final annealing temperature and annealing time of NO steel in this study are likely different from the cases in [38,39], it is hard to compare those results. But it should be noted that MBN signal is sensitive to stress and a number of microstructural features such as phases, grain size, crystallographic texture, *etc*. During thermomechanical processing of NO silicon steel, the stress state, microstructure and crystallographic texture of the steel change significantly leading to substantial variations of the MBN signal [38]. Therefore, though previous investigations [40,41] have observed that the MBN signals for some kinds of commercial NO silicon steel were the strongest along the rolling direction, it is important to determine the macromagnetic easy and hard axes before using the model proposed in this study.

7.5 Chapter summary

This chapter evaluated the effect of anisotropy induced by the microstructure in NO electrical steel on the MBN signal. The extended MBN model based on anisotropic hysteresis was proposed. Meanwhile, the effect of excitation frequency was introduced into the MBN model based on dynamic hysteresis. The dependency of MBN peak amplitude on angle between tested direction and rolling direction was deduced from the analytical model and further simplified as a trigonometric function to evaluate the effect of anisotropy on MBN quantitatively.

Angle and frequency experiments for magnetic hysteresis loops were conducted on M330-35A NO electrical steel. The angular dependent parameters of the J-A model were determined by using the hybrid GA-PSO algorithm. The analytical model predicted the increase in amplitude and width of MBN envelope with increasing excitation frequency based on the optimised parameters. It also calculated the peak value decreasing and envelope broadening with the increase of the angle. Those simulated results could agree with the measured ones, but the simulated MBN peak value changed more sharply. The peak amplitude of the MBN envelope has experimentally shown the cosine variation with angle corresponding with the proposed practical trigonometric function under the excitation frequency of 50 Hz. The proposed trigonometric function and the cosine approximation of MBN peak value could evaluate the anisotropy of NO silicon steel since their coefficients of determination R^2 were both higher than 0.9. The tested direction rotating from RD to TD would decrease 22.24% in the MBN peak value. When the excitation frequency was 100 Hz, the proposed practical model and the cosine approximation could agree with the measured results as well. But the peak values of MBN envelopes decreased by 23.87% with the increasing angle from 0^{o} to 90^{o}.

It proved that the MBN technique was capable of evaluating the anisotropy of NO electrical steel. Besides, to achieve the evaluation of material and mechanical properties using the MBN technique with high accuracy, the effect of microstructure-induced anisotropy on the MBN should be considered in the calibration process of MBN measurement. Moreover, MBN is sensitive to stress anisotropy, but the discrimination of different kinds of anisotropy remains to be studied further.

7.6 References for Chapter 7

[1] N. Nencib, S. Spornic, A. Kedous-Lebouc, and B. Cornut. Macroscopic anisotropy characterization of SiFe using a rotational single sheet tester. *IEEE Trans. Magn.*, vol. 31, no. 6, pp. 4047–4049, 1995.

[2] A. J. Moses. Electrical steels: past, present and future developments. *IEE Proc. A* (*Physical Sci. Meas. Instrumentation, Manag. Educ.*), vol. 137, no. 5, pp. 233–245, 1990.

[3] S. Somkun. Magnetostriction and magnetic anisotropy in non-oriented electrical steels and stator core laminations. *Doctoral dissertation*, *Cardiff University*, 2010.

[4] S. Somkun, A. J. Moses, P. I. Anderson, and P. Klimczyk. Magnetostriction anisotropy and rotational magnetostriction of a non-oriented electrical steel. *IEEE Trans. Magn.*, vol. 46, no. 2, pp. 302–305, 2010.

[5] I. Zagradisnik and B. Hribernik. Influence of anisotropy of magnetic material on the saturation harmonics in the three-phase induction motor. *IEEE Trans. Magn.*, vol. 24, no. 1, pp. 491–494, 1988.

[6] B. Upadhaya, L. Perkkiö, P. Rasilo, A. Belahcen, P. Handgruber, and A. Arkkio. Representation of anisotropic magnetic characteristic observed in a non-oriented silicon steel sheet. *AIP Adv.*, vol. 10, no. 6, pp. 065222 (1-10), 2020.

[7] K. M. Lee, S. Y. Park, M. Y. Huh, J. S. Kim, and O. Engler. Effect of texture and grain size on magnetic flux density and core loss in non-oriented electrical steel containing 3.15% Si. *J. Magn. Magn. Mater.*, vol. 354, pp. 324–332, 2014.

[8] F. N. Isaac, A. A. Arkadan, and A. El-Antably. Magnetic field and core loss evaluation of ALA-motor synchronous reluctance machines taking into account material anisotropy. *IEEE Trans. Magn.*, vol. 34, no. 5, pp. 3507–3510, 1998.

[9] O. Hamrit, O. de la Barrière, M. LoBue, and F. Mazaleyrat. Anisotropy of losses in non-oriented iron silicon sheets: Influence on electrical machine applications. *IEEE Trans. Magn.*, vol. 52, no. 2, pp. 1–7, 2015.

[10] S. Yamaguchi, A. Daikoku, and N. Takahashi. Cogging torque calculation considering magnetic anisotropy for permanent magnet synchronous motors. *COMPEL-The Int. J. Comput. Math. Electr. Electron. Eng.*, 2004.

[11] J. J. Sidor, K. Verbeken, E. Gomes, J. Schneider, P. R. Calvillo, and L. A. I. Kestens. Through process texture evolution and magnetic properties of high Si non-oriented electrical steels. *Mater. Charact.*, vol. 71, pp. 49–57, 2012.

[12] Y. He, M. Mehdi, E. J. Hilinski, and A. Edrisy. Through-process characterization of local anisotropy of Non-oriented electrical steel using magnetic Barkhausen noise. *J. Magn. Magn. Mater.*, vol. 453, pp. 149–162, 2018.

[13] Y. He, M. Mehdi, E.J. Hilinski, A. Edrisy, S. Mukundan, A. Mollaeian and N.C. Kar. Evaluation of Local Anisotropy of Magnetic Response from Non-oriented Electrical Steel by Magnetic Barkhausen Noise. *2018 IEEE International Magnetics Conference* (*INTERMAG*), 2018, pp. 1-5.

[14] P. Martínez-Ortiz, J. A. Pérez-Benitez, J. H. Espina-Hernández, F. Caleyo, and J. M. Hallen. On the estimation of the magnetic easy axis in pipeline steels using magnetic Barkhausen noise. *J. Magn. Magn. Mater.*, vol. 374, pp. 67–74, 2015.

[15] J. Capó-Sánchez, J. Pérez-Benitez, and L. R. Padovese. Analysis of the stress dependent magnetic easy axis in ASTM 36 steel by the magnetic Barkhausen noise. *NDT&E Int.*, vol. 40, no. 2, pp. 168–172, 2007

[16] M. Maciusowicz and G. Psuj. Time-Frequency Analysis of Barkhausen Noise for the Needs of Anisotropy Evaluation of Grain-Oriented Steels. *Sensors*, vol. 20, no. 3, pp. 768 (1-16), 2020.

[17] S. Ding, G. Tian, G. Dobmann, and P. Wang. Analysis of domain wall dynamics based on skewness of magnetic Barkhausen noise for applied stress determination. *J. Magn. Magn. Mater.*, vol. 421, pp. 225–229, 2017.

[18] X. Liu, R. Zhang, B. Wu, and C. He. Quantitative prediction of surface hardness in 12CrMoV steel plate based on magnetic Barkhausen noise and tangential magnetic field measurements. *J. Nondestruct. Eval.*, vol. 37, no. 2, pp. 1-8, 2018.

[19] M. S. Amiri, M. Thielen, M. Rabung, M. Marx, K. Szielasko, and C. Boller. On the role of crystal and stress anisotropy in magnetic Barkhausen noise. *J. Magn. Magn. Mater.*, vol. 372, pp. 16–22, 2014.

[20] Y. Wang, X. Liu, B. Wu, J. Xiao, D. Wu, and C. He. Dipole modeling of stress-dependent magnetic flux leakage. *NDT&E Int.*, vol. 95, pp. 1–8, 2018.

[21] M. Caldas-Morgan and L. R. Padovese. Fast detection of the magnetic easy axis on steel sheet using the continuous rotational Barkhausen method. *NDT&E Int.*, vol. 45, no. 1, pp. 148–155, 2012.

[22] A. Stupakov, O. Perevertov, and V. Zablotskii. Dynamical properties of magnetic Barkhausen noise in a soft microalloyed steel. *IEEE Trans. Magn.*, vol. 51, no. 1, pp. 2–5, 2015.

[23] D. C. Jiles. Frequency dependence of hysteresis curves in conducting magnetic materials. *J. Appl. Phys.*, vol. 76, no. 10, pp. 5849–5855, 1994.

[24] G. Bertotti. Hysteresis in magnetism: for physicists, materials scientists, and engineers. *Gulf Professional Publishing*, 1998.

[25] S. E. Zirka, Y. I. Moroz, R. G. Harrison, and K. Chwastek. On physical aspects of the Jiles-Atherton hysteresis models. *J. Appl. Phys.*, vol. 112, no. 4, pp. 043916 (1-7), 2012.

[26] K. Chwastek and J. Szczygłowski. An alternative method to estimate the parameters of Jiles-Atherton model. *J. Magn. Magn. Mater.*, vol. 314, no. 1, pp. 47–51, 2007.

[27] N. Sadowski, N. J. Batistela, J. P. A. Bastos, and M. Lajoie-Mazenc. An inverse Jiles-Atherton model to take into account hysteresis in time-stepping finite-element calculations. *IEEE Trans. Magn.*, vol. 38, no. 2, pp. 797–800, 2002.

[28] A. J. Bergqvist. A simple vector generalization of the Jiles-Atherton model of hysteresis. *IEEE Trans. Magn.*, vol. 32, no. 5, pp. 4213–4215, 1996.

[29] J. V Leite, N. Sadowski, P. Kuo-Peng, N. J. Batistela, J. P. A. Bastos, and A. A. De Espindola. Inverse Jiles-Atherton vector hysteresis model. *IEEE Trans. Magn.*, vol. 40, no. 4, pp. 1769–1775, 2004.

[30] A. Ramesh, D. C. Jiles, and J. M. Roderick. A model of anisotropic anhysteretic magnetisation. *IEEE Trans. Magn.*, vol. 32, no. 5, pp. 4234–4236, 1996.

[31] S. Higuchi, T. Nakao, Y. Takahashi, T. Tokumasu, K. Fujiwara, and Y. Ishihara. Modeling of two-dimensional magnetic properties based on one-

dimensional magnetic measurements. *IEEE Trans. Magn.*, vol. 48, no. 11, pp. 3486–3489, 2012.

[32] C. C. H. Lo, S. J. Lee, L. Li, L. C. Kerdus, and D. C. Jiles. Modeling stress effects on magnetic hysteresis and Barkhausen emission using a hysteretic-stochastic model. *IEEE Trans. Magn.*, vol. 38, no. 5, pp. 2418–2420, 2002.

[33] L. Mierczak, D. C. Jiles, and G. Fantoni. A new method for evaluation of mechanical stress using the reciprocal amplitude of magnetic Barkhausen noise. *IEEE Trans. Magn.*, vol. 47, no. 2 PART 2, pp. 459–465, 2011.

[34] S. Zurek, P. Marketos, T. Meydan, and A. J. Moses. Use of novel adaptive digital feedback for magnetic measurements under controlled magnetising conditions. *IEEE Trans. Magn.*, vol. 41, no. 11, pp. 4242–4249, 2005.

[35] A. Stupakov. Dynamic normalization of the Barkhausen noise signal. *J. Magn. Magn. Mater.*, vol. 482, pp. 135–147, 2019.

[36] V. Moorthy. Important factors influencing the magnetic Barkhausen noise profile. *IEEE Trans. Magn.*, vol. 52, no. 4, pp. 1–13, 2015.

[37] B. Ducharne, Y. A. T. Deffo, P. Tsafack, and S. H. N. Kouakeuo. Directional magnetic Barkhausen noise measurement using the magnetic needle probe method. *J. Magn. Magn. Mater.*, vol. 519, pp. 167453 (1-10), 2021.

[38] Y. He, M. Mehdi, E.J. Hilinski and A. Edrisy. Through-process characterization of local anisotropy of Non-oriented electrical steel using magnetic Barkhausen noise. *J. Magn. Magn. Mater.*, vol. 453, pp.149-162, 2018.

[39] Y. He, M. Mehdi, E.J. Hilinski, A. Edrisy, S. Mukundan, A. Mollaeian and N.C. Kar. Evaluation of local anisotropy of magnetic response from non-oriented electrical steel by magnetic Barkhausen noise. *IEEE Trans. Magn.*, vol. 54, no. 11, pp.1-5, 2018.

[40] A.A. Samimi, T.W. Krause, L. Clapham, M. Gallaugher, Y. Ding, P. Ghosh, R. Chromik and A.M. Knight. Correlation between ac core loss and surface magnetic Barkhausen noise in electric motor steel. *J. Nondestruct. Eval.*, vol. 33, no. 4, pp.663-669, 2014.

[41] L. Wang, C. He and X. Liu. Evaluation of the Magnetocrystalline Anisotropy of Typical Materials Using MBN Technology. *Sensors*, vol. 21, no. 10, p.3330 (1-18), 2021.

Chapter 8

Evaluation of Carbon Content in Steel using Magnetic Techniques

Barkhausen jumps are usually acquired by a Magnetic Barkhausen Noise (MBN) sensor with the sensing element of a pick-up coil. The resonant frequency characteristics of the pick-up coil may significantly influence the MBN profile. To improve the performance of MBN sensor, the pick-up coil is optimised using analytical models of inductance and parasitic capacitance for the hexagonal winding coaxial coil. Furthermore, the coil is manufactured according to the optimised size. Its inductance, capacitance and resonant frequency are found to be close to the designed. A multifunctional measurement system using the optimised coil is employed to measure both magnetic hysteresis loops and MBN signals. The peak-to-peak value of MBN envelope, coercive field and remanence of hysteresis loop are used to characterise carbon content in various steels.

8.1 Introduction

In this chapter, the effect of microstructure in carbon steel on magnetic NDE methods is further investigated. In turn, the correlations could be used to evaluate the microstructure of steel. The most common phases or constituents in commercial carbon steel are ferrite, pearlite and cementite. The volumes of these phases are determined by the carbon content. Ferrite is iron containing an extremely minimal amount of carbon. The amount of carbon dissolved in ferrite practically is zero at room temperature, and the solubility increases to only a maximum of 0.02% at 723℃ [1]. At room temperature ferrite shows high ductility and low mechanical strength and also low magnetic hardness in terms of coercive field [2]. In contrast, cementite also known as iron carbide, which is formed by the combination of iron and carbon containing 6.67% carbon [1], shows high mechanical and magnetic hardness and is much more brittle [2]. In carbon steel, which generally contains less than 2% carbon in weight, the mixture of ferrite and cementite turns to a lamellar (thin plate like layers) microstructure referred to as pearlite [1]. The relative volume fraction of the ferrite, pearlite and cementite phases gives rise to the final mechanical and magnetic properties of the steel. Thus, the knowledge of the amount of carbon content in steel is crucial.

As described in previous chapters, magnetic Barkhausen noise (MBN) method was sensitive to the microstructure of ferromagnetic material. Thus, the metallographic phase of steel related to carbon content would influence the Barkhausen emission, and inversely, MBN could be used to evaluate the amount of carbon in steel. However, since various MBN sensors were used to assess the carbon contents in steel, the comparison of results reported by different investigators appeared to conflict with each other. For example, Batista *et al.* [2] inserted the tested steels inside an electromagnet for MBN measurements and found the existence of two peaks of MBN profile. One of the peak amplitudes decreased with increasing amount of carbon from 0 wt% to 1.5 wt%, while the other one increased. But Samimi *et al.* [3] used a flux-controlled MBN system and located the MBN sensor on top of the surface of tested steels. They experimentally observed just one peak of MBN envelope in half excitation cycle, and the peak amplitude increased with the increase in the amount of carbon, but it abruptly dropped when the carbon content excessed 0.65 wt%. Either one peak or two peaks of MBN envelope for carbon steel evaluation were found by other investigators [4]–[6], but the height of peaks was not correlated with the carbon content in steel.

Besides, MBN signal is the voltage pulses induced in the pick-up coil by the change of discrete micromagnetic flux caused by the irreversible movement of magnetic domain walls during the cyclic magnetisation process. The applications and signal processing of MBN signals were paid more attention by researchers, while the improvement of MBN system performance, especially the optimisation of a pick-up sensor was insufficiently considered. Besides, it has been observed that the MBN signal strongly depended on the measurement parameters such as maximum magnetic field strength [7–9], magnetising frequency [7–9], and the resonant frequency of pick-up coil [9,10], which widely varied from one MBN system to another. It resulted in an inconsistent correlation between microstructural variations and MBN signals in different investigations. As one of the main elements of the MBN measurement, the pick-up coil could strongly impact the MBN profile. Capó-Sánchez *et al.* [10] and Moorthy *et al.* [8,9] experimentally investigated the influence of the pick-up coils' turns and constructive characteristics of MBN sensors. They could control the frequency response behaviour, sensitivity, and signal-to-noise ratio (SNR). Therefore, it is considerable to optimise the MBN pick-up coil for the assessment of the relative amount and contributions of the carbon in steels.

In the previous chapter, it has been experimentally seen that increasing excitation frequency would increase the MBN signal level but would also decrease the range of magnetisation. This led to the reduction in the ability to magnetise harder phases in material and the weakening interaction of magnetic domain walls within harder metallurgical phases such as pearlite and carbides [8] so that the harder phases might not be activated and detected in the MBN bursts. Besides, the measured results showed that the MBN signal level turned round to decrease when the excitation frequency continued to increase higher than 100 Hz. Moorthy [8] pointed that a higher MBN level did not always mean maximum MBN profile since the applied magnetic field and the tangential magnetic field might not achieve their maximum value. Therefore, Moorthy [8] and Batista *et al.* [2] preferred to magnetise the sample at low frequencies such as 0.2 Hz, 0.8 Hz [8], 0.1 Hz and 0.5 Hz [2]. Hence, the low excitation frequency (typically <2 Hz) is beneficial to perform the advantage of the optimised pick-up coil and enrich the information in the Barkhausen emission.

The hysteresis loop is another widely used magnetic technique for the microstructure characterisation of ferromagnetic materials [2,3,11,12]. Hysteresis measurements could provide reproducible and reliable results. But it is only appropriate for the samples with a special shape like cylinder that could be wound coils to measure the magnetic induction [2]. There are various magnetic properties that can be extracted from the hysteresis loop, like the coercive field, remanence, and differential permeability. Samimi *et al.* [3] Jiles *et al.* [11], and Thompson *et al.* [12] found that the coercive field of the hysteresis loop increased linearly with the increasing carbon content in steel. Therefore, the parameters of the hysteresis loop may have the potential to evaluate the carbon content quantitatively.

This chapter is organized as follows. In Section 8.2, the formulas for the accurate evaluation of the total inductance and parasitic capacitance are introduced. The equivalent circuit of the pick-up coil and optimisation method are discussed. The measurement system, tested samples and experiments are introduced in Section 8.3. In Section 8.4, the experimental results, the advantages and disadvantages of different magnetic NDE techniques for evaluating the carbon content in steel are proposed. Finally, the summary of this chapter is given in Section 8.5.

8.1 The optimisation of MBN pick-up coil

MBN pick-up coil, generally composed of a solenoid coil with a ferromagnetic core, is usually made of enamelled wire, which introduces inductance (L), parasitic capacitance (C) and resistance (R) to the measurement system. These parasitic elements will determine the resonant frequency, sensitivity, and signal-to-noise ratio (SNR) of MBN sensor. There are various models to simulate the aforementioned elements. The Rosa-Nagaoka method [13–15] was the early attempt to solve the inductance of the solenoid. Maxwell pioneered to compute self- and mutual-inductance using the summation method [16]. With the increase of computer performance, the filamentary method was widely used in inductance calculation for various inductors [17–20]. The method is used for the optimisation of coil inductance by considering a ferromagnetic core inside in this study.

8.1.1 Inductance model

The diagram of a rectangular cross-section coil with length *l*, the inner diameter D_i and the outer diameter D_0 is shown in Fig. 8.1 with half of the coil depicted due to symmetry. This inductor is formed by a discrete wire array of N_T turns per layer and N_L number of layers. In Fig. 8.1, the deep orange outline and orange filled circles are enamelled coating and copper centre, respectively. It shows the widely used and relatively reasonable distribution of wires, i.e., the hexagonally winding. To evaluate the inductance accurately, the formulas are given as a function of N_T, N_L, ξ_T, ξ_L, and d_0. ξ_T is the gap between turns to avoid twisting and overtighten the turns, while ξ_L is the offset between layers caused by decentration and the gap between turns. ξ_T is always positive, which means distance added to the width of coil. While ξ_L can be positive to shorten the height of coil and negative to add the height of coil. It can be seen from the figure that the width *w* and the height *h* of the hexagonal winding are

$$w = N_T d_0 + (N_T - 1)\,\xi_T \tag{8.1}$$

and

$$h = \frac{\sqrt{3}N_L d_0}{2} - (N_L - 1)\,\xi_L \tag{8.2}$$

Maxwell [16] gave an expression for the mutual inductance of hypothetical filaments, which had finite length but zero cross-sectional area and were spaced at the Geometric Mean Distance (GMD), in complete elliptic integrals. It was further improved by [14,18–20]:

$$M = \sum_{i=1}^{N_{tot}} \sum_{j=1, j\neq i}^{N_{tot}} M_{ij} = \mu_c \sum_{i=1}^{N_{tot}} \sum_{j=1, j\neq i}^{N_{tot}} \sqrt{\left(r_i + r_j\right)^2 + s_{ij}^2}\left[\left(1 - \frac{\epsilon_{ij}^2}{2}\right)F\left(k_{ij}\right) - E\left(k_{ij}\right)\right] \tag{8.3}$$

where μ_c was the relative magnetic permeability of the core. If it was air core, $\mu_c = \mu_0$,

$$N_{tot} = N_T \times N_L \tag{8.4}$$

$$r_i = \frac{D_i}{2} + \frac{d_0}{2} + (i-1)\left(\frac{\sqrt{3}d_0}{2} + \xi_L\right) \quad (i = 1, 2,3, \dots, N_L) \tag{8.5}$$

$$s_{ij} = \sqrt{(z_i - z_j)^2} \tag{8.6}$$

$$z_j = \begin{cases} jd_0 + (j-1)\xi_T & i \text{ even} \\ \frac{(2j-1)d_0}{2} + (j-z)\xi_T & i \text{ odd} \end{cases} \quad (j\text{=}1, 2, 3, \dots, N_T) \tag{8.7}$$

The elliptic integral modulus ϵ was given by

$$\epsilon_{ij} = 2\sqrt{\frac{r_i r_j}{(r_i+r_j)^2+s_{ij}^2}} \tag{8.8}$$

F and *E* were complete elliptical integrals of first and second kinds, respectively.

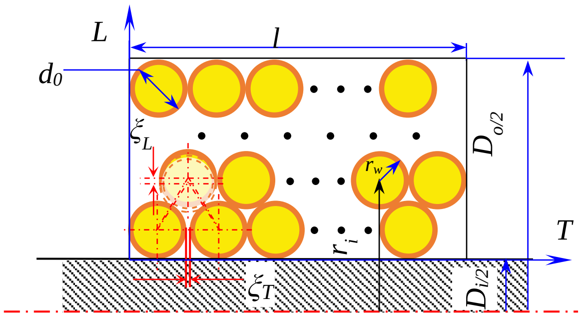

Figure 8.1. Schematic diagram of half cross-section of coil (*l* — length of the coil, D_o —outer diameter of the coil, D_i — inner diameter of the coil, d_0 — diameter of the wire, ξ_T — gap between turns in horizon and ξ_L — offset between layers in vertical).

The self-inductance could be calculated by either placing two notional filaments parallelly at an axial separation of r_w, which was the radius of a wire, or placing one filament inside the other centrically at zero axial distance. The parallel filament pair was more realistic, but the difference was slight when $r \gg r_w$. In the case of parallel filament pair, $s = 0$, $r_i = r_i$, r_j=r_i-r_w, and the self-inductance was given by

$$L_s = \mu_c \sum_{i=1}^{N_{tot}} (2r_i - r_w)\left[\left(1-\frac{\epsilon_i^2}{2}\right)F(k_i)-E(k_i)\right] \tag{8.9}$$

And the total inductance of a coaxial coil was obtained by the superposition of L_s and M contributions as

$$L = L_s + M \tag{8.10}$$

8.1.2 Capacitance model

Many attempts have been made to model the parasitic capacitance induced by electromagnetic interaction of adjacent turns [20–25]. These studies reported more and more accurate results concerning practical constitute of stay capacitance, such as turn-to-turn [22], interlayer [23,24], winding types and fringing effect of peripheral wire [20,24,25].

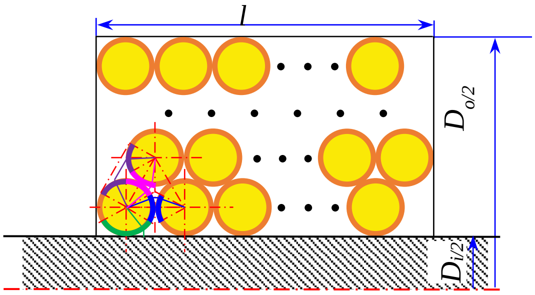

Figure 8.2. Schematic diagram of the hexagonal winding coil (blue pair line represents the turn-to-turn capacitance, magenta pair line represents the layer-to-layer capacitance, purple pair line represents the outer-layer capacitance and green pair line represents the turn-to-core capacitance).

The self-capacitance of the widely used and reasonable hexagonally winding is analysed in this chapter. The total value of the self-capacitance in multi-layer coaxial coils with ferromagnetic core includes the following four parts: the turn-to-turn capacitances between adjacent coil pair in the same layer (C_{tt}), the layer-to-layer capacitances induced by adjacent coil pair in different layers (C_{ll}), the outer-layer capacitances between the adjacent coils in the outer layers (C_{ol}) and the turn-to-core capacitances between the innermost coil and the ferromagnetic core (C_{tc}) as shown in Fig. 8.2. The analytical solution for the self-capacitance of coil with an improved model for the hexagonal winding case is described as follows.

Fig. 8.2 shows the arrangement of turns in the hexagonal winding coil. There are two kinds of winding, i.e., standard and flyback windings. Their basic analysis cells are the same as shown in Figs. 8.3 and 8.4. In this study, the more common standard winding is adopted. In the four components of self-capacitance, the turn-to-turn capacitance C_{tt} and layer-to-layer capacitance C_{ll} are dominant due to their large quantities. Assuming that a conductor surface carries an equal potential and the propagation of electric field always travels along the shortest path, for the path along an angle θ as shown in Fig. 8.3a, the electric field passes through the insulation coating of a turn, the air gap between two adjacent turns and the insulation coating of the other turn successively. On this path, these three insulation elements compose three series-connected capacitance, which are two capacitances induced by the insulation layer dC_i and capacitance caused by the air gap dC_g. These series-connected components constitute the infinitesimal turn-to-turn capacitance dC_{tt}, as shown in Fig. 8.3b.

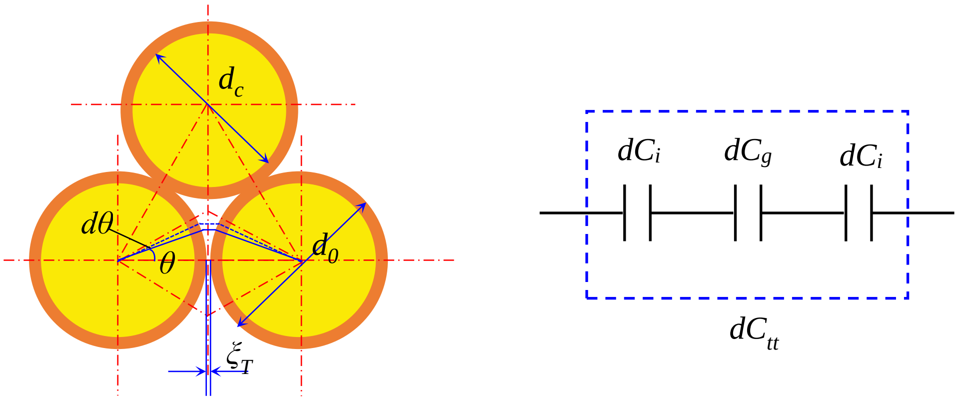

(a) (b)

Figure 8.3. Model of turn-to-turn capacitance for the hexagonal winding coil.

The inner surface and the external surface of coating form a dielectric capacitance. The elementary capacitance related to the cylindrical coating shell dC_i is given by [20,21,22,25]

$$dC_i = \varepsilon_r \varepsilon_0 d\theta \int_0^{l_t} dl \int_{d_0/2}^{d_c/2} \frac{r}{dr} = \frac{\varepsilon_r \varepsilon_0 l_t}{\ln \frac{d_0}{d_c}} d\theta \qquad (d_0 > d_c) \qquad (8.11)$$

where ε_0 is the vacuum permittivity, ε_r is the relative permittivity of the insulation coating, d_0 is the diameter of the wire, d_c is the copper core of the wire, and l_t is the length of a turn, but it is usually simplified as mean length $l_t = \pi(D_i+D_o)/2$.

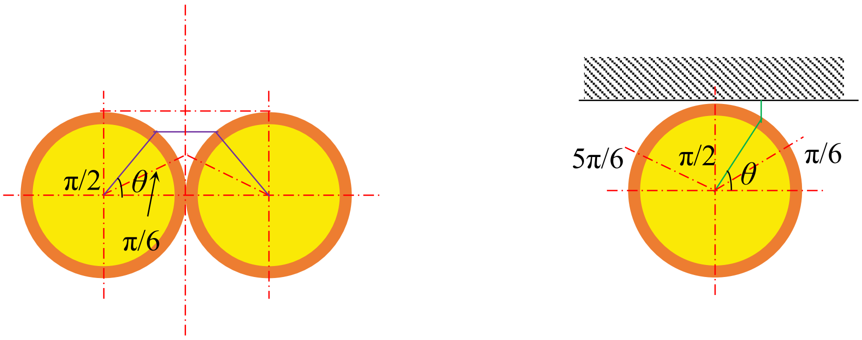

(a) (b)

Figure 8.4. Schematic diagram of **(a)** outer layer and **(b)** turn-to-core capacitances for the hexagonal winding coil.

The assumed air gap length l_g as a function of θ is given by

$$l_g = d_0(1 - \cos\ \theta) + \xi_T \qquad (8.12)$$

Similarly, the elementary capacitance induced by the air gap dC_g per unit angle can be calculated by

$$dC_g = \frac{\varepsilon_0 d_0 l_t d\theta}{2l_g} = \frac{\varepsilon_0 d_0 l_t d\theta}{2(d_0(1 - \cos\ \theta) + \xi_T)} \qquad (8.13)$$

For dense winding coil, the gap between turns ξ_T is zero, while for sparse coil the effect of ξ_T should be taken into account. The capacitance analysis in this chapter focuses on the dense winding coil, and hence the air gap induced capacitance can be simplified as

$$dC_g = \frac{\varepsilon_0 l_t d\theta}{2(1 - \cos\theta)} \qquad (8.14)$$

The series combination of three elementary capacitances can be given by

$$dC_{tt} = \frac{dC_i dC_g}{dC_i + 2dC_g} = \frac{\varepsilon_0 l_t d\theta}{2\left(1 + \frac{1}{\varepsilon_r}\ln\frac{d_0}{d_c} - \cos\theta\right)} \tag{8.15}$$

The angle *θ* is limited in a range from -6/π to 6/π since the electric field out of this range will follow the layer-to-layer path. Besides, Fig. 8.2 shows that the electric field between the adjacent turns in different layers would go through a similar path to turn-to-turn. The same expressions will be obtained through rotating the coordinates. Therefore, the turn-to-turn capacitance C_{tt} is equal to the layer-to-layer capacitance C_{ll}.

$$C_{tt} = C_{ll} = \int_{-\frac{\pi}{6}}^{\frac{\pi}{6}} \frac{\varepsilon_0 l_t}{2\left(1 + \frac{1}{\varepsilon_r}\ln\frac{d_0}{d_c} - \cos\theta\right)} d\theta \tag{8.16}$$

Following an analogous argument, the outer-layer capacitance C_{ol} shown in Fig.8.4a can be expressed as

$$C_{ol} = \int_{\frac{\pi}{6}}^{\frac{\pi}{2}} \frac{\varepsilon_0 l_t}{2\left(1 + \frac{1}{\varepsilon_r}\ln\frac{d_0}{d_c} - \cos\theta\right)} d\theta \tag{8.17}$$

And the turn-to-core capacitance C_{tc} shown in Fig.8.4b is given by

$$C_{tc} = \int_{\frac{\pi}{6}}^{\frac{\pi}{2}} \frac{2\varepsilon_0 l_t}{1 + \frac{1}{\varepsilon_r}\ln\frac{d_0}{d_c} - \sin\theta} d\theta \tag{8.18}$$

Supposing that an electric potential (*U*) is applied on two terminals of the winding, the potential of the *k*th turn is given by

$$dU_k = \frac{(k-(k-1))U}{N} = \frac{U}{N}, \ \ k = 1, 2, 3, \ldots, N \tag{8.19}$$

The potential between two adjacent turns can be calculated by

$$\Delta U_{ij} = (j - i)dU \text{ , } i \text{ adjoins } j \text{ and } j > i \tag{8.20}$$

And the electrical energy stored between the turns are

$$\Delta E_{ij} = \frac{1}{2} C_{ij} \Delta U_{ij}^2 \tag{8.21}$$

According to the conservation of total energy, the energy calculated by total stray capacitance should equal the summation energy computed by four capacitance components (i.e., C_{tt}, C_{ll}, C_{ol}, and C_{tc}). Therefore, the total stray capacitance of the hexagonal winding coil is given by

$$\begin{aligned} C_s = \frac{1}{N_{tot}^2} \Bigg[&(N_T - 1) N_L C_{tt} + \sum_{i=1}^{2N_t - 1} i^2 (N_L - 1) C_{ll} + (N_L + N_T - 2) C_{ol} \\ &+ (2N_T - 1)^2 (N_L - 1) C_{ol} + \sum_{j=1}^{N_t} j^2 C_{tc} \Bigg] \end{aligned} \tag{8.22}$$

8.1.3 Optimisation of MBN pick-up coil

It is known that the MBN profile strongly depends on the resonant frequency characteristics of the pickup coil. Vashista *et al.* [9] found that a larger number of turns of pick-up coil would result in better sensitivity and response in the lower frequency range. Capó-Sánchez *et al.* [10] experimentally observed that MBN signals reached their maximum value of power spectrum at the corresponding resonant frequencies. As a result, the coil resonant frequency decreased, but the resonant peak amplitude increased as the number of turns increased. Therefore, measurement of magnetic Barkhausen signal using optimised coil could be the basis for studying microstructure in ferromagnetic material like metallographic phases in steel.

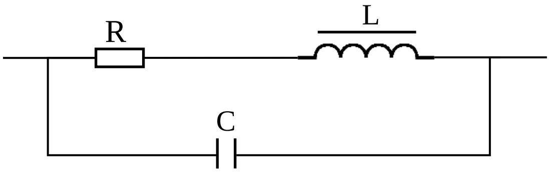

Figure 8.5. Equivalent circuit of pick-up coil.

The equivalent electric circuit of a pick-up coil is presented in Fig. 8.5. Its resonant frequency can be given by [26]

$$f_0 = \frac{1}{2\pi\sqrt{LC}}\sqrt{1-\left(\frac{R^2C}{4L}\right)} \tag{8.23}$$

where the resistance R is given by

$$R = \frac{4\rho}{d_c^2}N\{D_i + (N_L - 1)\sqrt{3}r_w - (N_L - 1)\xi_L\} \tag{8.24}$$

where ρ is the resistivity of the wire.

To obtain an intensive output signal and good signal-to-noise ratio (SNR), the outer diameter of coil D_o and length of coil l is recommended to be about four times the ferromagnetic core and 0.7~0.9 of the length of the core, respectively [27]. Additionally, the analogous measurement system described in [2] is employed in this study for activating the domain activities in both soft and hard phases of carbon steel. The lengths and diameters of all tested samples are the same and determined as 50 mm and 8 mm, respectively. Moorthy [8] found that it was important to use an MBN sensor with a good response in a low frequency range of less than 10 kHz to detect MBN signals from the deep subsurface effectively. Under these limited conditions, three Standard Wire Gauge (SWG) grades 25, 29 and 35 wires with 0.48 mm, 0.33 mm and 0.200 mm diameters of copper cores respectively are used to optimise the pick-up coil size. The sizes of these kinds of wires are listed in Table 8.1.

Since the MBN measurement system used in [2], where the pick-up is wound on the tested cylindrical samples, is employed in this study, the pick-up coil is a ferromagnetic core sensor. The relative permeability for carbon steel is set as 100, and the relative permittivity of the coil coating for polyurethane is set as 4.2. The sizes of different wires listed in Table 8.1 are substituted into the equations mentioned above to simulate the resonant frequencies of pick-up coils.

Table 8.1. The sizes of wires for pick-up coil optimisation

Grade	Wire diameter (mm)	Diameter of copper core (mm)
SWG-35	0.2134	0.2000
SWG-29	0.3450	0.3300
SWG-25	0.5080	0.4800

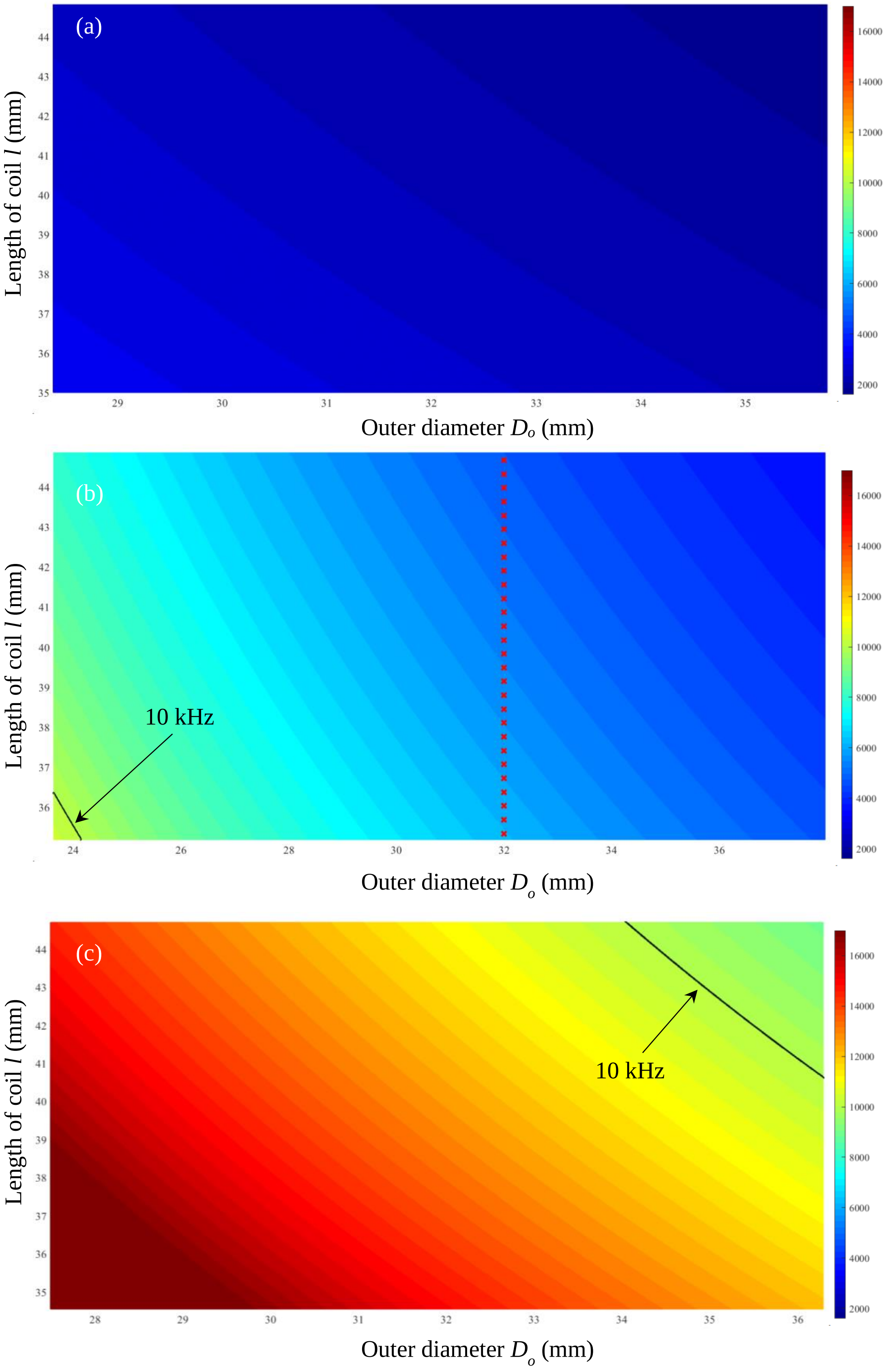

Figure 8.6. The simulated relation between sizes of coils and their resonant frequencies. **(a)** SWG-35 wire, **(b)** SWG-29 wire and **(c)** SWG-25 wire.

Fig. 8.6 shows the relation between the sizes of coils made by different grades of wires and their resonant frequencies. Due to the small diameter of SWG-35 wire, it requires large amounts of turns to meet the limited conditions of coil sizes. The resonant frequencies of all defined size coils made by SWG-35 wire are much lower than 10 kHz as presented in Fig. 8.6a. This may lead to the loss of key information near 10 kHz. For SWG-25 wire, the reverse applies. As it does not need abundant turns to wind the coil in defined sizes, the resonant frequencies of the coils made by SWG-25 wires are much higher than 10 kHz as illustrated in Fig. 8.6 (c). These coils that either has much higher resonant frequencies or lower frequencies than the demand cannot meet the design requirements.

If the wire diameter is an intermediate value of SWG 25 and 35, such as SGW-29, it is possible to optimise a qualified MBN pick-up coil. Fig. 8.6b shows the simulation resonant frequencies of SGW-29 made coils with ferromagnetic core. A few coils may be suggested that are in compliance with the design requirements. They are marked as red crosses in Fig. 8.6b. Finally, the optimised sizes of the pick-up coil are determined as 8 mm in inner diameter, 32 mm in outer diameter, and 35.2 mm in length, respectively, for saving turns, weight and closing to the required resonant frequency.

8.2 MBN and Hysteresis Loop Experiments on Carbon Steels

8.2.1 Magnetic Barkhausen noise experiments

There are various samples examined in this study, including a high purity iron (iron content > 99.99%) and different kinds of carbon steels containing carbon from 0.085% to 0.81% in weight as listed in Table 8.2. These samples are machined into cylindrical shapes with the same diameter and length of 8 mm and 50 mm, respectively. Then, they are annealed at 400°C for two hours to relieve the residual stress. Since all these commercial steels were as-received materials and annealed under the same condition, their grain sizes are assumed to be similar in this research.

It has been reported that the shape of the MBN profile strongly depends on maximum magnetic field strength and excitation frequency [8,9]. They synergistically affect the amplitude of MBN and the activities of domains in hard phases of carbon steel. Therefore, it is important that the magnetic excitation unit can provide an adequately strong magnetic field with sufficiently low frequency. The laboratory C-core with tapered poles electromagnet can generate an intense magnetic field with low frequency as shown in Fig.8.7. The electromagnet can excite tens of kA/m strength magnitude with water cooling. It can work on quasi-static frequency by being fed in correlative current from a computer-controlled bipolar power supply. The tapered poles can be driven by an adjustable lever to match the length of sample.

Table 8.2. Carbon and sulphur analysis results

Samples	Carbon [%]	Sulphur [%]
Pure Iron	<0.001	<0.001
230M07	0.085	0.330
1015	0.190	0.041
080M40	0.460	0.011
1045	0.480	0.008
1055	0.600	0.030
1075	0.810	0.006

In MBN measurements, the shaped carbon steel samples are inserted into the optimised pick-up coil. The samples and pick-up coil are placed between tapered poles of the electromagnet and clamped by twirling the adjustable lever. A sinusoidal voltage waveform of 0.5Hz generated by the computer is amplified by the bipolar power supply (manufactured by Kepco). The feeding current from the bipolar power supply into the electromagnet generates the corresponding magnetic field. The pick-up coil can detect the MBN emissions generated in the magnetised material. The detected signals are filtered by a bandpass filter in the range from 1 kHz to 20 kHz. A National Instruments manufactured data acquisition (DAQ) card USB-6366 is used to measure MBN signals with a sampling rate of 1 MS/s. The dedicated software is developed for exciting magnetic field and processing the MBN signals.

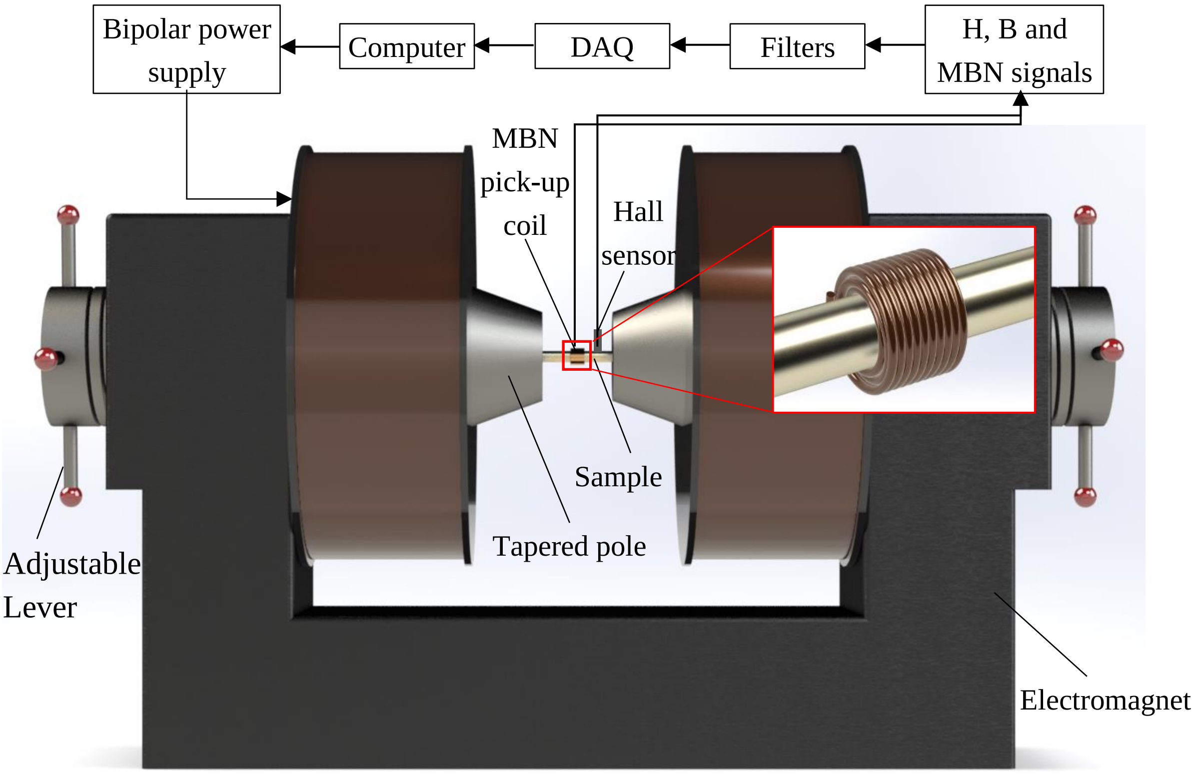

Figure 8.7. Schematic diagram of C-core electromagnet for hysteresis loop and MBN measurements.

The MBN measurement results of pure iron, 1015, 080M40, 1055, and 1075 are used to investigate the effect of carbon level in steel on the root mean square (RMS) of MBN. In addition, the 230M07 and 1045 samples are employed to verify the inverse application of the correlation.

8.2.2 Magnetic hysteresis loop experiments

The experimental set-up used for magnetic hysteresis loop measurements is similar to that for MBN measurements as shown in Fig. 8.7. During the hysteresis loop measurements, the carbon steel samples are magnetised by the electromagnet driven by quasi-DC (5 mHz) current that is generated by the computer and subsequently amplified by the Kepco amplifier. The strength of applied magnetic field *H* is measured at the surface of the sample by a transverse Lakeshore Hall probe connecting to a gaussmeter that communicates with the computer via GPIB link. Simultaneously the values of magnetic flux density *B* are acquired by GPIB linked Lakeshore fluxmeter integrating the voltage of pick-up coil wound around the sample. The measurement procedure is similar to the related description in Chapter 5.

Following an analogous procedure, samples 230M07 and 1045 are used to verify the dependency of the parameters of hysteresis loop on carbon content in pure iron, 1015, 080M40, 1055 and 1075.

8.3 Results and Discussion for the MBN and Hysteresis Loop Measurements

The optimised MBN pick-up coil is tailored by Anstee Coil Technology Ltd using self-bonding enamelled copper wire SWG-29. The comparison between the designed and manufactured coils is listed in Table 8.3. Agilent 4294A precision impedance analyser with the 16089B Kelvin clip attachment is used to measure the tailored coil. The value of induction calculated by the introduced model for air core coil is close to the manufactured. The relative error of the induction for the designed coil to the manufactured is estimated as 9.81%. Besides, the capacitances and the resonant frequency of designed and tailored coils are also compared. Their relative errors are 2.04% and 6.40%. In addition, the electrical parameters of the manufactured coil are simulated using the induction and capacitance models. The results are also listed in Table 8.3. It can be found that the relative errors of the simulated coil using the geometric parameters of the real coil are smaller than that of the designed one. The comparison results indicate that the induction and capacitance models for hexagonal winding can predict the induction and capacitance of circular-section multi-layer coils with high precision. Hence, the analytical model can be an effective tool to design or optimise the desired pick-up coils.

Table 8.3. Comparison of the designed coil with the manufactured coil.

Parameters	Designed coil	Manufactured coil	Simulated coil
Turns	4080	4225	4223
Length (mm)	35.2000	35.5000	35.5000
Inner diameter (mm)	8.0000	8.1000	8.1000
Outer diameter (mm)	32.0000	33.8000	32.7000
Induction (mH)	98.2138	108.8930	107.9141
Capacitance (pF)	66.6091	67.9956	66.9512
Resonant frequency(kHz)	6.2225	5.8490	5.9211

8.3.1 Magnetic Barkhausen noise measurements

The cylindrical samples are magnetised along their axial direction by a sinusoidal magnetic field maximum strength of 11,000 A/m at excitation frequencies of 0.5 Hz. Fig. 8.8 shows the MBN signal envelopes for pure iron, 1015, 080M40, 1055 and 1075 grades steels. To evaluate the performance of the optimised pick-up coil, the short-time Fourier transform (STFT) spectrum of the MBN signal for pure iron as an example is also plotted in Fig. 8.8f. It can be found that the energy mainly distributes in the time range from 0.4 s to 0.7 s corresponding to the raw signal in Fig. 8.8a, and in the frequency range from 0 kHz to 9 kHz consist with the designed frequency range (< 10 kHz). It indicates that the optimised pick-up coil for low frequency MBN signal can acquire the main energy of Barkhausen emissions originating from carbon steels.

The MBN envelopes in Figs. 8.8a ~ 8.8e are smoothed by the moving average method to highlight data variations within half cycle of the excitation field. It can be seen that the peak heights of MBN envelopes increase with carbon content increasing. The amplitudes of background noise increase as well with the increase in carbon level. Therefore, in order to reduce the influence of background noise, the peak-to-peak values of MBN envelopes (MBN_{pp}) are used for the evaluation of the dependency of MBN signals on carbon contents in steel.

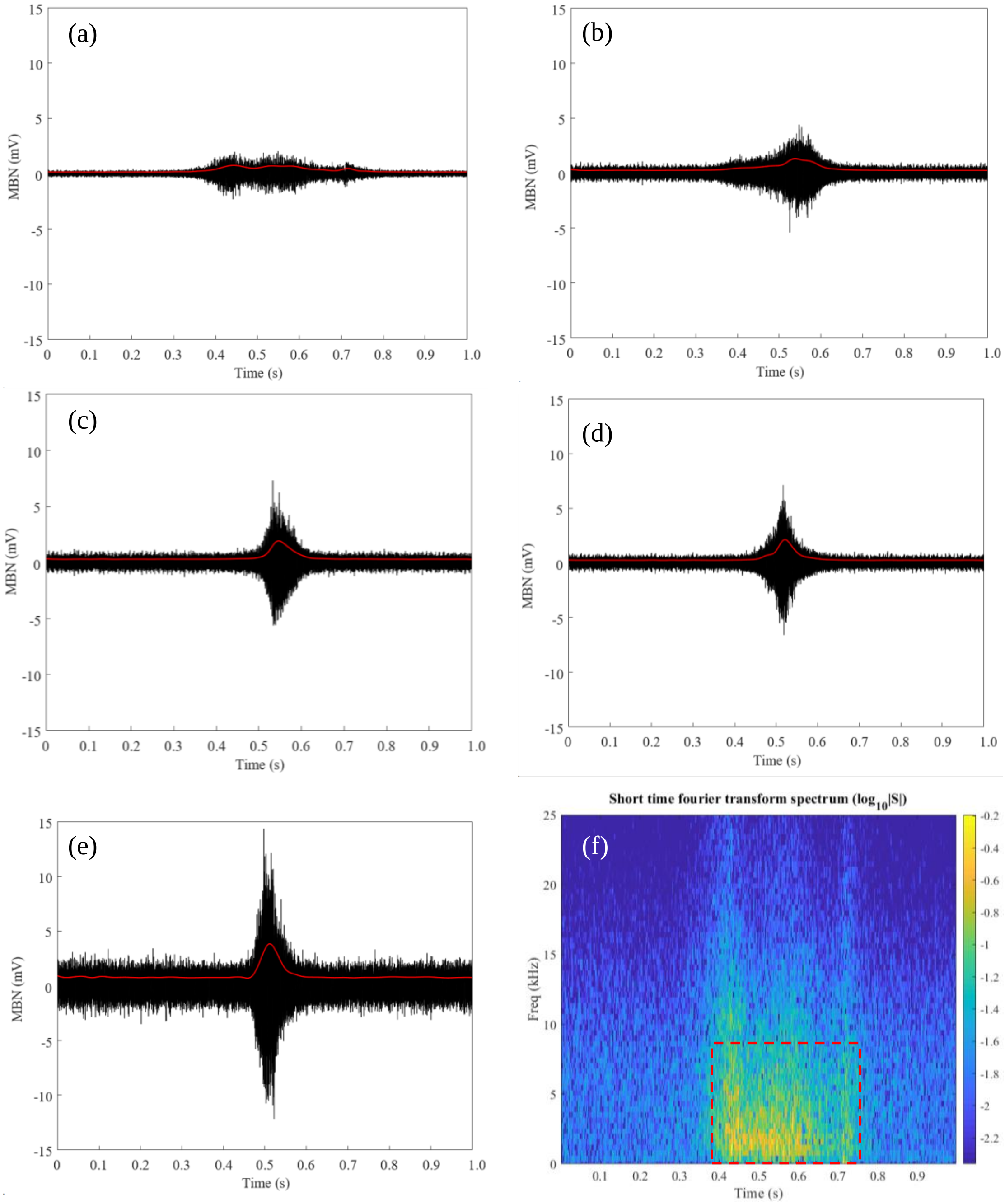

Figure 8.8. Barkhausen voltage bursts acquired for **(a)** pure iron, **(b)** 1015, **(c)** 080M40, **(d)** 1055, **(e)** 1075 and **(f)** the STFT spectrum for MBN signal of pure iron.

Fig. 8.9 plots the peak-to-peak value of MBN envelope as a function of carbon content. The peak-to-peak value presents a clear increasing trend. Therefore, the larger Barkhausen jumps in higher carbon content steel are believed to be associated with the increase of pearlite volume fraction relative to ferrite [28].

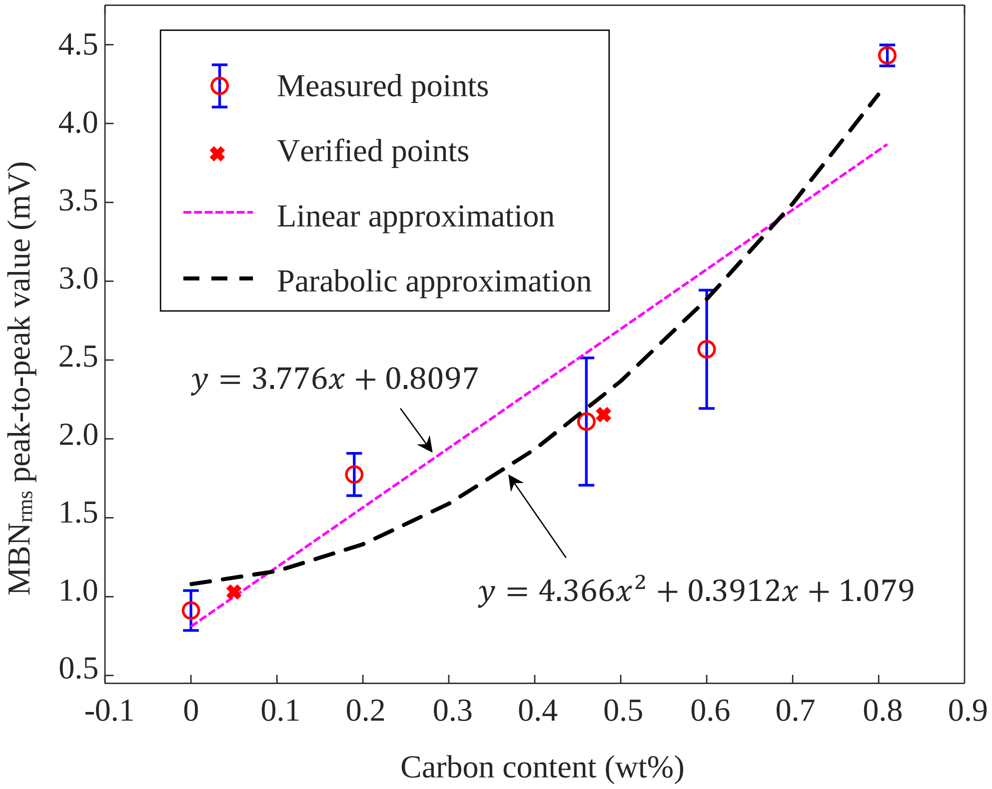

Figure 8.9. The peak-to-peak value of MBN envelope as a function of carbon content.

To quantitatively evaluate the correlation between MBN_{pp} and carbon content in steels, linear and parabolic functions are used to fit the measured results as shown in Fig. 8.9. It can be found that the parabolic function could better approximate the experimental results with fitting goodness R^2 higher than 0.94. The 230M07 and 1045 carbon steel samples are used to verify the parabolic approximation. Their peak-to-peak values after averaging are plotted as crosses in Fig. 8.9. It can be seen that the measured result of 230M07 sample is closer to linear correlation with a relative error of 2.97% than parabolic with a relative error of 7.81%. While the result of 1045 shows the parabolic correlation (relative error 5.51%) is more appropriate to characterise the carbon content using MBN technique than linear function (relative error 22.66%). But it should be pointed out that the measured values of low carbon steel may deviate from the parabolic prediction. Hence, the parabolic dependency of MBN_{pp} on carbon content could be concluded in steels containing carbon higher than 0.3% in weight. The parabolic function may also be an appropriate parameter for the evaluation of carbon amount in steels containing carbon higher than 0.3% in weight.

It should be noted that the carbon steels investigated in this study contain carbon mostly less than 0.8%, where the ferrite is not fully altered to pearlite, i.e., hypoeutectoid steel (see Fig. 3.32). When the carbon content in steel is higher than 0.8% in weight, the main phases of steel are pearlite and hypereutectoid cementite (Fe_3C_{II}). Samimi *et al.* [3] and Koo *et al.* [29] experimentally observed that the peak height of MBN envelope increased with the increasing carbon content in hypoeutectoid steel while decreased in hypereutectoid steel. The maximum MBN amplitude is believed to be obtained in a steel closest to the eutectoid composition (0.8 wt% C), where the volume fraction of pearlite is largest. Therefore, the peak value of the MBN signal measured on 1075 steel sample should be approaching to the maximum Barkhausen jumps among various steels, and the parabolic approximation aforementioned is only appropriate for evaluate the carbon content in hypoeutectoid steels.

8.3.2 Magnetic hysteresis loop measurements

The hysteresis loop measurements are performed inside the electromagnet driven by quasi-DC current (5 mHz) supplied from computer and subsequently amplified by the bipolar power amplifier. The magnetic tangential field strength H is measured by the transverse Lakeshore Hall probe. The value of magnetic flux density B is measured by the pick-up coil. The magnetic hysteresis loops of pure iron, 1015, 080M40, 1055 and 1075 grades of steel are plotted in Fig. 8.10. It is clearly shown that the hysteresis loop is broadening with the increasing carbon content of steel. With the increasing amount of carbon in the form of pearlite and cementite precipitates in the ferrite matrix, the obstruction of domain wall motion is enhanced due to interaction with different phases and the influence of interstitial carbon atoms. Besides, the pearlite and cementite phases contribute to the increase of the magnetic hardness of the steel. Therefore, the hysteresis loop is observed to widen with the increase of magnetically hard phases caused by increasing carbon content.

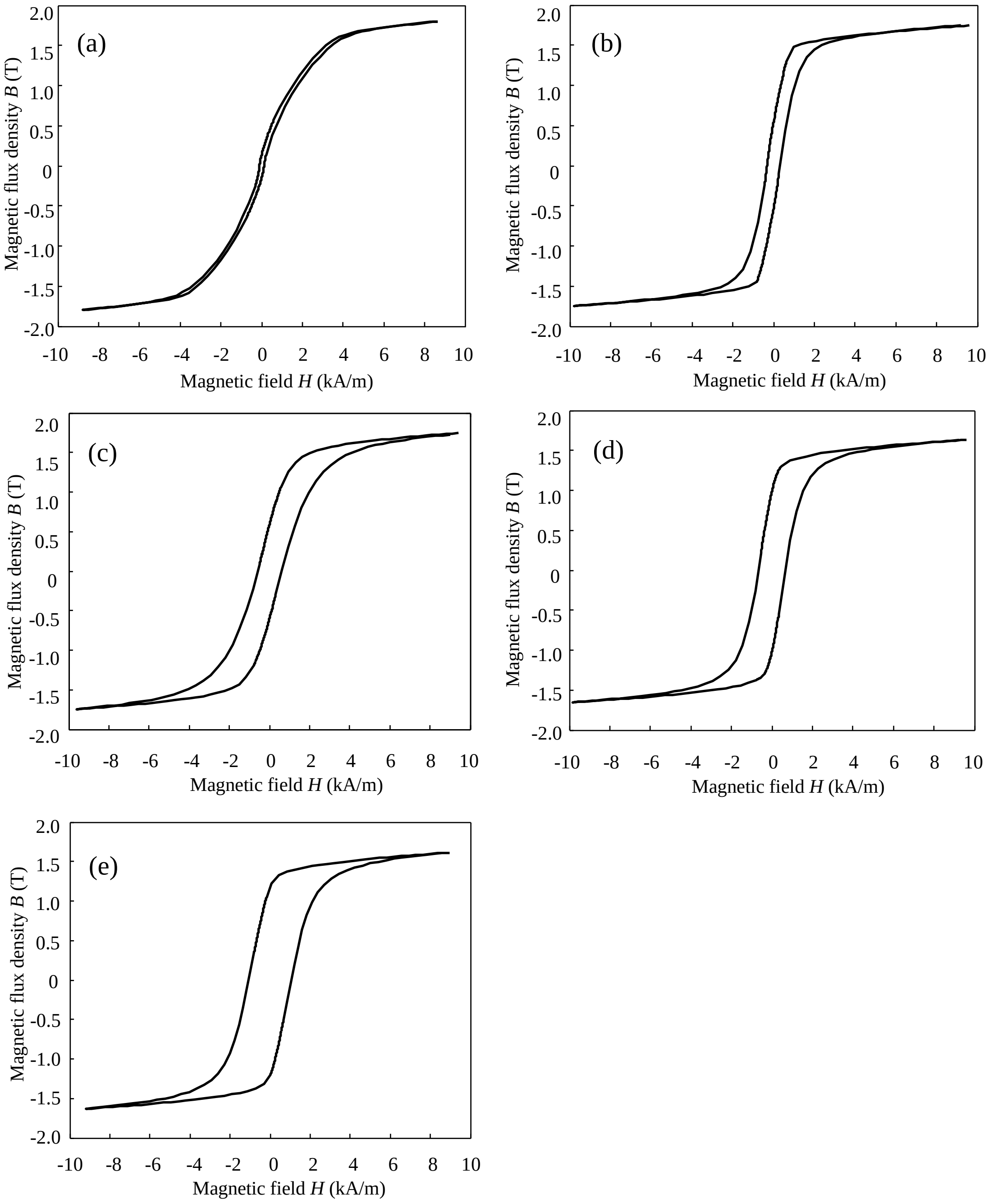

Figure 8.10. DC hysteresis loops obtained for **(a)** Pure iron, and carbon steels **(b)** 1015, **(c)** 080M40, **(d)** 1055 and **(e)** 1075

The dependency of the coercive fields of hysteresis loop H_c on carbon content in steels is shown in Fig. 8.11. It can be seen that the coercive field increases as a linear function of carbon content with a coefficient of determination higher than 0.97. The coercive fields of 230M07 and 1045 grades of steel are used to verify the linear approximation marked as crosses in Fig.8.10. The relative error between measured results and predicted results for 230M07 and 1045 samples are 30.06% and 6.32%, respectively. It indicates that the coercive field could be a potential parameter to evaluate the carbon content in steels, but it may present a relatively large error in a few cases.

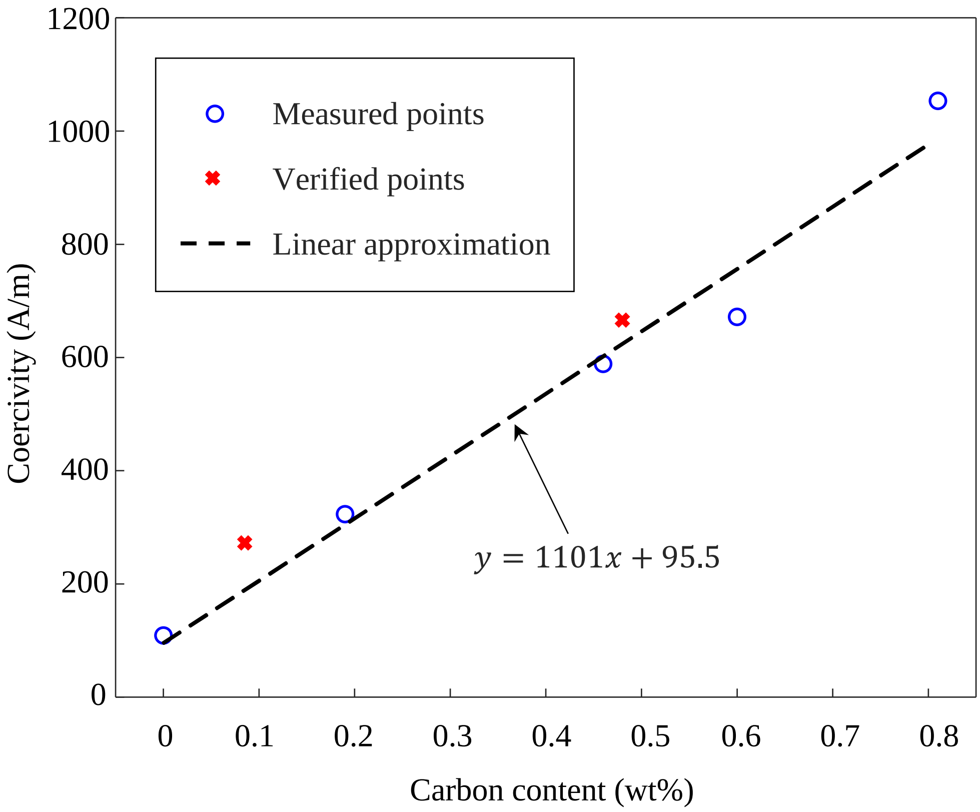

Figure 8.11. The coercivity H_c of carbon steel as a function of carbon content.

Besides, the parameter remanence B_r is plotted against the carbon content in Fig. 8.12. The remanence B_r also presents a linear correlation with carbon content. But it is not suitable to predict carbon level in medium carbon steels since the measured results of medium carbon steels 080M40 and 1045 deviate from the linear fitting function. Eliminating the outlier value of 080M40 steel, the linear correlation between remanence B_r and carbon content could fit the measured results well with a coefficient of determination R^2 higher than 0.98. The remanence of 230M07 is marked as crosses in Fig.8.12. The relative error between the measured result and the fitting line is 18.03% which is much lower than that of coercive field. It also can be found in Fig. 8.12 that the relative error between experimental results and linear approximation for higher carbon steels like 080M55 and 1075 is much lower than that of MBN_{pp} and coercivity. It indicates that the remanence B_r could be a potential parameter to evaluate the carbon content in mild and higher carbon steels.

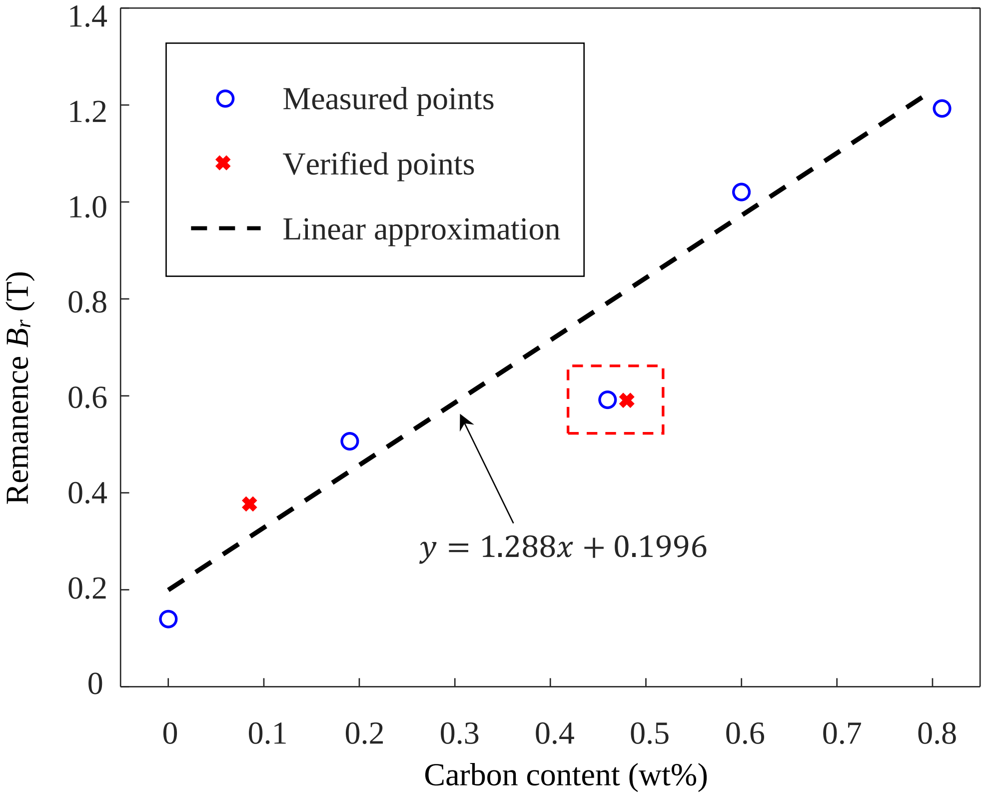

Figure 8.12. The remanence B_r of carbon steel as a function of carbon content.

A single parameter may not be appropriate to evaluate the amount of carbon in steels since the parameters of peak-to-peak value of MBN envelope (MBN_{pp}), coercive field (H_c) and remanence (B_r) of hysteresis loop have their advantages and disadvantages in carbon content evaluation. To quantitatively estimate the amount of carbon in steel, the multi-parameter should be comprehensively considered. In this study, the carbon levels in hypoeutectoid and eutectoid steels are exclusively evaluated since the MBN_{pp} may no longer be a monotonic function of carbon content if hypereutectoid steels are included. The hypoeutectoid and eutectoid steels can be divided into three kinds: low carbon steel (0~0.3 wt% C), medium carbon steel (0.3~0.6 wt% C) and high carbon steel (0.6~0.8 wt% C). If the measured values of MBN_{pp}, coercive field and remanence for carbon steel are all lower or at least two of them are lower than the corresponding values of the 0.3 wt% carbon content on the fitting curves, this steel can be determined as low carbon steel. Its carbon content can be further estimated using coercive field and remanence linear functions. Following an analogous method, it can also determine medium and high carbon steels. However, to further evaluate the carbon level in medium carbon steel, MBN_{pp} and coercive field H_c are the preferable parameters since the remanence B_r measured in medium carbon steel may vary from the predicted value.

8.4 Chapter summary

This chapter discussed the optimisation steps for the MBN pick-up coil based on the inductance and stray capacitance models. The comparison of the designed coil and the manufactured coil according to optimised size verified the feasibility of the optimisation method. Furthermore, the power spectral density of the MBN signal measured by the optimised pick-up coil concentrating in the design frequency range proved the reliability of the designed coil.

The MBN and hysteresis loop experiments were conducted to analyse the dependency of these magnetic signals on the amount of carbon in steel. For the MBN measurements, the frequency and strength of the applied field were crucial in the detection of the hard phases. The maximum amplitude of 11 kA/m sinusoidal magnetic field at 0.5 Hz was chosen to measure Barkhausen jumps using the multifunctional measurement system. The peak-to-peak value of MBN envelope was experimentally observed as a parabolic function of carbon content. The multifunctional measurement system was also used to obtained magnetic hysteresis loops of various steels. Both the coercive field and remanence presented linear dependence on the amount of carbon in steel. Therefore, these parameters of MBN and hysteresis loop could be inversely used for the evaluation of carbon content in steels.

However, the MBN_{pp} might no longer increase as a function of carbon content if the carbon content in steel was higher than 0.8 wt%. Hence, in this study, the carbon level in hypoeutectoid and eutectoid steels were exclusively evaluated. Besides, it was experimentally observed that the parameters of MBN_{pp}, coercive field and remanence might be inappropriate to evaluate the amount of carbon in steels alone due to their disadvantages. Therefore, the multi-parameter was comprehensively considered.

8.5 References for Chapter 8

[1] H. Okamoto. The C-Fe (carbon-iron) system. *J. Phase Equilibria*, vol. 13, no. 5, pp. 543–565, 1992.

[2] L. Batista, U. Rabe, I. Altpeter, S. Hirsekorn, and G. Dobmann. On the mechanism of nondestructive evaluation of cementite content in steels using a combination of magnetic Barkhausen noise and magnetic force microscopy techniques. *J. Magn. Magn. Mater.*, vol. 354, pp. 248–256, 2014.

[3] A. A. Samimi, T. W. Krause, and L. Clapham. Multi-parameter Evaluation of Magnetic Barkhausen Noise in Carbon Steel. *J. Nondestruct. Eval.*, vol. 35, no. 3, pp. 1–8, 2016.

[4] S. Zhang, X. Shi, L. Udpa, and Y. Deng. Micromagnetic measurement for characterization of ferromagnetic materials' microstructural properties. *AIP Adv.*, vol. 8, no. 5, pp. 056614 (1-7), 2018.

[5] J. A. Pérez-Benitez, J. Capó-Sánchez, J. Anglada-Rivera, and L. R. Padovese. A model for the influence of microstructural defects on magnetic Barkhausen noise in plain steels. *J. Magn. Magn. Mater.*, vol. 288, pp. 433–442, 2005.

[6] I. Altpeter. Nondestructive evaluation of cementite content in steel and white cast iron using inductive Barkhausen noise. *J. Nondestruct. Eval.*, vol. 15, no. 2, pp. 45–60, 1996.

[7] A. Dhar and D. L. Atherton. Influence of magnetising parameters on the magnetic Barkhausen noise. *IEEE Trans. Magn.*, vol. 28, no. 6, pp. 3363–3366, 1992.

[8] V. Moorthy. Important factors influencing the magnetic Barkhausen noise profile. *IEEE Trans. Magn.*, vol. 52, no. 4, pp. 1–13, 2015.

[9] M. Vashista and V. Moorthy. Influence of applied magnetic field strength and frequency response of pick-up coil on the magnetic Barkhausen noise profile. *J. Magn. Magn. Mater.*, vol. 345, pp. 208–214, 2013.

[10] J. Capó-Sánchez and L. Padovese. Magnetic Barkhausen noise measurement by resonant coil method. *J. Magn. Magn. Mater.*, vol. 321, no. 18, pp. L57–L62, 2009.

[11] D. C. Jiles, J. B. Thoelke, and M. K. Devine. Numerical determination of hysteresis parameters for the modeling of magnetic properties using the theory of ferromagnetic hysteresis. *IEEE Trans. Magn.*, vol. 28, no. 1, pp. 27–35, 1992.

[12] S. M. Thompson and B. K. Tanner. The magnetic properties of pearlitic steels as a function of carbon content. *J. Magn. Magn. Mater.*, vol. 123, no. 3, pp. 283–298, 1993.

[13] H. Nagaoka. The inductance coefficients of solenoids. *J. Coll. Sci.*, vol. 27, no. 3, pp. 1-33, 1909.

[14] D. W. Knight. Solenoid inductance calculation. available online: *http//www. g3ynh. info/zdocs/magnetics/Solenoids. pdf* (accessed on 20 February 2021)

[15] E. B. Rosa and F. W. Grover. Formulas and tables for the calculation of mutual and self-inductance. *US Government Printing Office*, no. 169, 1948.

[16] J. C. Maxwell. A treatise on electricity and magnetism. *Oxford: Clarendon Press* vol. 1., 1873.

[17] Z. Luo and X. Wei. Mutual inductance analysis of planar coils with misalignment for wireless power transfer systems in electric vehicle. *2016 IEEE Vehicle Power and Propulsion Conference (VPPC)*, pp. 1–6, 2016.

[18] A. K. RamRakhyani, S. Mirabbasi, and M. Chiao. Design and optimisation of resonance-based efficient wireless power delivery systems for biomedical implants. *IEEE Trans. Biomed. Circuits Syst.*, vol. 5, no. 1, pp. 48–63, 2010.

[19] S. R. Khan, S. K. Pavuluri, and M. P. Y. Desmulliez. Accurate modeling of coil inductance for near-field wireless power transfer. *IEEE Trans. Microw. Theory Tech.*, vol. 66, no. 9, pp. 4158–4169, 2018.

[20] J. Martínez, S. Babic, and C. Akyel. On evaluation of inductance, DC resistance, and capacitance of coaxial inductors at low frequencies. *IEEE Trans. Magn.*, vol.

50, no. 7, pp. 1–12, 2014.

[21] A. Massarini and M. K. Kazimierczuk. Self-capacitance of inductors. *IEEE Trans. power Electron.*, vol. 12, no. 4, pp. 671–676, 1997.

[22] A. Massarini, M. K. Kazimierczuk, and G. Grandi. Lumped parameter models for single-and multiple-layer inductors. *27th Annual IEEE Power Electronics Specialists Conference*, vol. 1, pp. 295–301, 1996.

[23] L. Dalessandro, F. da Silveira Cavalcante, and J. W. Kolar. Self-capacitance of high-voltage transformers. *IEEE Trans. power Electron.*, vol. 22, no. 5, pp. 2081–2092, 2007.

[24] M. Aghaei and S. Kaboli. On the effect of disorder on stray capacitance of transformer winding in high-voltage power supplies. *IEEE Trans. Ind. Electron.*, vol. 64, no. 5, pp. 3608–3618, 2017.

[25] B. Wu, X. Zhang, X. Liu, and C. He. An analytical model for predicting the self-capacitance of multi-layer circular-section induction coils. *IEEE Trans. Magn.*, vol. 54, no. 5, pp. 1–7, 2018.

[26] R. L. Boylestad. Introductory circuit analysis. *Pearson Education*, 2010.

[27] W. Richter. Induktionsmagnetometer für biomagnetische Felder. *Exp. Tech. Phys*, vol. 27, pp. 235–243, 1979.

[28] L. Clapham, C. Jagadish, and D. L. Atherton. The influence of pearlite on Barkhausen noise generation in plain carbon steels. *Acta Metall. Mater.*, vol. 39, no. 7, pp. 1555–1562, 1991.

[29] K. M. Koo, M. Y. Yau, D. H. L. Ng, and C. C. H. Lo. Characterization of pearlite grains in plain carbon steel by Barkhausen emission. *Mater. Sci. Eng. A*, vol. 351, no. 1–2, pp. 310–315, 2003.

Chapter 9

Conclusions and Future work

This chapter concludes the findings and contributions of the investigation regarding the effect of stress, temperature and microstructure on magnetic NDE methods. Also, the possible future directions for this work are presented with respect to the multiphysics simulation and deep learning in magnetic flux leakage and Barkhausen noise techniques.

9.1 Conclusions

The major contribution of this thesis was the development of magnetic NDE techniques for the accurate evaluation of mechanical properties and monitoring the health status of ferromagnetic materials by considering the effects of stress, temperature and microstructure. In this research, the mainly concerned magnetic NDE techniques were magnetic flux leakage (MFL) and magnetic Barkhausen Noise (MBN).

9.1.1 Evaluation of the effect of stress on MFL

To evaluate the effect of stress on MFL signal, a universal FEM method, which could deal with magnetomechanical problems, was proposed for overcoming the geometric limitation of the analytical model. The FEM model predicted a linear relationship between the peak-to-peak value of MFL signal and stress for the circumferential square-notch defect on a dog-bone shaped steel rod.

The anticipated linear behaviour of peak-to-peak amplitude of MFL signal with stress based on the model was validated by experimental results obtained for 1045 steel. The measurements showed that the peak-to-peak value of MFL signal decreased linearly with the increase of external stress, which fitted the simulation results well with a coefficient of determination higher than 0.99.

An increase in tensile stress of 100 MPa caused a decrease of 11.76% in the peak-to-peak amplitude of MFL signal. Therefore, to size the defect accurately, the effect of stress on the MFL signal should be incorporated in the calibration process. The proposed multiphysics FEM model provides a valuable tool to evaluate the contribution of stress to the induced MFL signal and may be used to solve the inverse problem for sizing defects with a complicated stress distribution.

9.1.2 Evaluation of the effect of temperature on MFL

Since temperature might induce thermal stress inside tested specimens, new analytical dipole models for predicting both the direct effect of temperature and combined effects of temperature and thermal stress on MFL were proposed. The temperature-dependent magnetic dipole model exclusively considering the direct effect predicted the linear dependency of the amplitude of the MFL signal on the temperature for the cylindrical through-hole defect in a ferromagnetic sheet. Besides, the magnetic dipole model considering the combined effects of temperature and thermal stress anticipated the parabolic relation between the peak-to-peak value of MFL signal and temperature.

The model for evaluating the direct effect of temperature was verified by measurement results for the M250-50A non-oriented (NO) grain silicon steel specimen with a cylindrical through-hole defect. Besides, the model for the combined effects was experimentally validated on an adhesive structure of the defective NO steel and ceramic glass.

When the direct effect of temperature itself was involved, the temperature heating 100 ℃ from -40 ℃ resulted in a decrease of 6.10% in the peak-to-peak amplitude of the MFL signal, which agreed with the simulated well with a goodness of fit higher than 0.9. Under the combined actions of temperature and thermal stress, the temperature cooling 30℃ from room temperature (20 ℃) to -10 ℃ caused an increase of 6.87% in the amplitude of the MFL signal, which was much larger than that in the exclusive temperature condition (2.04%).

The temperature cooling down from 60 ℃ to -40 ℃ altered the amplitude of the MFL signal by 35.99%, which could significantly influence the results of defect dimension estimation by using the inverse MFL method. To size the defect accurately, the effect of temperature on the MFL signal should also be considered. The improved magnetic dipole models could pave paths to understand and evaluate the contribution of temperature and thermal stress on the induced MFL signals.

9.1.3 Evaluation of the effect of temperature on MBN

Analogous to temperature-dependent MFL models, new models describing the dependence of magnetic Barkhausen noise peak amplitude on temperature have been developed. The extended MBN model based on temperature-dependent hysteresis was proposed to predict the direct effect of temperature itself on MBN signal. The exponential relationship between the reciprocal MBN peak amplitude and temperature, which has been further simplified as the linear function to evaluate the dependence of MBN peak amplitude on temperature quantitatively, was deduced from the temperature-dependent MBN model.

Considering the combined effects of temperature and thermal stress, a multiphysics MBN model was presented, and based on this model, the parabolic dependence of the reciprocal MBN peak value on temperature was given. Practical piecewise linear functions were then presented to approximate the dependence according to the finding that the magnetostriction coefficients under compression and tension are different.

The verification experiments for those models were conducted on M250-50A NO silicon steel and the adhesive structure of the NO steel and ceramic glass, respectively. When the direct effect of temperature itself was exclusively involved, the measured peak value of MBN signals could agree with simulated MBN envelops, and the reciprocal of the peak amplitude of the MBN signal has been experimentally shown the linear variation with temperature corresponding with the predicted results. In this case, temperature heating from -40°C to 40°C results in an increase of 4.49% in the reciprocal of MBN peak value.

In addition to the direct effect, the indirect effect of thermal stress was involved. The measured reciprocal of the peak amplitude of Barkhausen emission has presented parabolic dependency on temperature, which was consistent with the predicted tendency. The parabolic relation was further simplified by piecewise linear functions at temperatures higher and lower than the reference temperature. It has been proven to be feasible to evaluate the combined effect quantitatively. The environmental temperature cooling from the reference temperature 20 °C to -40 °C led to a decrease of 10.54% in $1/MBN_p$. Whereas the temperature heating from 20 °C to 40 °C caused a sharper increase of 14.13% in $1/MBN_p$. To achieve the evaluation of material and mechanical properties using the MBN method with high accuracy, the effect of temperature on the MBN signal should be considered in the calibration process of MBN measurement.

9.1.4 Evaluation of the effect of microstructure-induced anisotropy in non-oriented silicon steel on MBN

An extended MBN model for evaluation of the anisotropy induced by microstructure in NO silicon steel was developed. Besides, the effect of excitation frequency was introduced into the MBN model. The analytical model predicted the increase in amplitude and width of MBN envelope with increasing excitation frequency. It also calculated the MBN peak value decreasing and envelope broadening with the increase of the angle. The relationship between the MBN peak amplitude and angle between the tested direction and rolling direction of NO silicon steel was deduced from the analytical model and further simplified as a trigonometric function to evaluate the dependence of MBN peak amplitude on angle quantitatively.

The model has been verified by experimental results for M330-35A NO silicon steel. The measured results for different frequencies could agree with the simulated ones, but the simulated MBN peak value changed more sharply than the measured. The peak amplitude of the MBN envelope has experimentally shown the cosine variation with angle corresponding with the proposed practical trigonometric function at the excitation frequency of 50 Hz. The proposed trigonometric function and the cosine approximation of MBN peak value could evaluate the anisotropy of NO silicon steel since their coefficients of determination R^2 were both higher than 0.9. The tested direction rotating from RD to TD would decrease 22.24% in the MBN peak value.

When the excitation frequency increased to 100 Hz, both coefficients of determination of the proposed practical model and the cosine approximation decreased, but they were still higher than 0.85. It proved that the MBN technique was capable of evaluating the anisotropy of NO electrical steel in low excitation frequency. Besides, the peak values of MBN envelopes decreased by 23.87% with the increasing angle from 0^o to 90^o. To achieve the evaluation of material and mechanical properties using the MBN technique with high accuracy, the effect of microstructure-induced anisotropy on the MBN should be considered in the calibration process of MBN measurement. Moreover, MBN is sensitive to stress anisotropy, but the discrimination of different kinds of anisotropy remains an important research issue to be studied further.

9.1.5 Evaluation of carbon content in steel using magnetic techniques

The optimisation steps for MBN pick-up coil based on the inductance and stray capacitance models have been discussed, and the effect of carbon content in steel on hysteresis loop and MBN signals has been experimentally investigated.

The comparison of the designed coil and the manufactured coil according to optimised size verified the feasible optimisation method. The power spectral density of the Barkhausen signal measured by the optimised pick-up coil concentrated in the design frequency range, proofing the reliability of the designed coil.

For the MBN measurements, the peak-to-peak value of MBN envelope was experimentally observed as a parabolic function of carbon content. For the magnetic hysteresis loops measurements, both the coercive field and remanence presented linear dependence on the amount of carbon in steels. Therefore, these parameters of MBN and hysteresis loop were the potential methods to estimate the carbon level in steels. In this study, the carbon levels in hypoeutectoid steels were mainly evaluated. Besides, it was experimentally observed that the parameters of MBN_{pp}, coercive field and remanence might be inappropriate to evaluate the amount of carbon in steels alone due to their disadvantages. Therefore, the multi-parameter should be comprehensively considered.

9.2 Future Work

Though the combined effect of temperature and thermal stress has been investigated in this thesis, the practical application, where the environmental temperature changes and the external stress is applied, has not been considered yet. For example, the seamless track for the high-speed train is usually suffering from the ambient temperature and the pressure from the wheels of train. Besides, in practical inspection, another important factor that cannot be ignored is the velocity effect. Taking the high-speed railway for instance, the practical inspection speed using MFL sensor is much faster than the experimental in this thesis. Therefore, to obtain the defect dimension accurately using the inverse MFL method, the multiple effects including stress, temperature and inspection speed on the MFL signal should be considered in the calibration process. As a continuation of this research, the difficulties are the development of multiphysics MFL model and implementation of the verified experiments.

It is well known that MBN is sensitive to stress. Hence, it is widely used to evaluate the residual stress in ferromagnetic material. However, the temperature may also induce thermal stress as discussed in this thesis. The identification of thermal stress and external stress would be a difficulty in future research. Besides, stress will result in anisotropy in the magnetic properties of a material in addition to the microstructure induced anisotropy investigated in this thesis. For example, MBN is used to assess the residual stress in an anisotropic ferromagnetic material. In this case, the distinction between stress-induced anisotropy and microstructure-induced anisotropy will be an important problem to be solved. Besides, MBN is a potential method in structural health monitoring. However, the temperature compensation for the monitoring data under various temperatures is a subject remaining to be researched, and the proposed practical method in this thesis might be possible to solve this problem.

In this thesis, the amount of carbon in steel has been evaluated by various MBN and hysteresis loop parameters. It is possible to classify a tested sample as a carbon steel grade by using the fitting functions. But it is far from evaluation of the exact amount of carbon. Besides, the samples were tested in their as-received state. The steel used in engineering structures is usually produced by thermal treatment, which will alter the microstructure of material, leading to the change of magnetic properties. Therefore, it needs a large number of experiments on various grades of steel and different thermal treatments. To determine the grade of steel also requires establishing a database and using deep learning to build the connection between magnetic signal and carbon content in steel.

Appendix

The hybrid GA-PSO algorithm code

```
% %%%%%%%%%% Main code %%%%%%%%%%
clc;
clear;
close all;

global Bmeas Hmeas Para_range

BH=xlsread('D:\research documents\2021.03\50_RD_1.6T.xlsx');
Bmeasraw=BH(1:50:end,2);
Hmeasraw=BH(1:50:end,1);

% %%%%%%%%%% intensify local grids if needed%%%%%%%

Hmeas=Hmeasraw; % use interpolating methods if needed
Bmeas=Bmeasraw;
figure(1)
plot(Hmeas,Bmeas,'-o')

%% JA parameters definition
Para_range.a=[3.5 35];
Para_range.k=[1.4 35];
Para_range.c=[0.001 0.999];
Para_range.Ms=[1.2e6 2e6];
Para_range.alpha=[1e-8 1e-4];

%% Problem Definiton

problem.CostFunction = @(x) JAcostFun(x);  % Cost Function
problem.nVar = 5;       % Number of Unknown (Decision) Variables
problem.VarMin =  0;  % Lower Bound of Decision Variables   0
problem.VarMax =  10;   % Upper Bound of Decision Variables  10

%% Parameters of PSO
params.MaxIt = 100;        % Maximum Number of Iterations  100
params.nPop = 50;           % Population Size (Swarm Size)  50
params.w = 1;               % Intertia Coefficient
params.wdamp = 0.99;        % Damping Ratio of Inertia Coefficient
params.c1 = 2;              % Personal Acceleration Coefficient
params.c2 = 2;              % Social Acceleration Coefficient
params.ShowIterInfo = true; % Flag for Showing Iteration Informatin
params.px=0.8;              % The probability of Crossover
params.pm=0.05;             % The probability of Mutation
params.GGAP=0.95;           % The generation gap

%% JA parameters range
aMin=Para_range.a(1);
aMax=Para_range.a(2);
```

```
kMin=Para_range.k(1);
kMax=Para_range.k(2);

cMin=Para_range.c(1);
cMax=Para_range.c(2);

MsMin=Para_range.Ms(1);
MsMax=Para_range.Ms(2);

alphaMin=Para_range.alpha(1);
alphaMax=Para_range.alpha(2);

%% Calling Hybird GA-PSO

[out, particle]= GAPSO_JA(problem, params);

BestSol = out.BestSol;
BestCosts = out.BestCosts;

%% Results

figure(2)
semilogy(BestCosts, 'LineWidth', 2);
xlabel('Iteration');
ylabel('Best Cost');
grid on;

%%    Read the best result
SolverType=4;
x=out.BestSol.Position;

a=x(1)/10*(aMax-aMin)+aMin;
k=x(2)/10*(kMax-kMin)+kMin;
c=x(3)/10*(cMax-cMin)+cMin;
Ms=x(4)/10*(MsMax-MsMin)+MsMin;
alpha=x(5)/10*(alphaMax-alphaMin)+alphaMin;
BsimT =  JAn_loops(a,k,c,Ms,alpha,Hmeas,SolverType);

figure(3)
plot(Hmeas, Bmeas,'-k',Hmeas, BsimT,'-r')


%%%%%%%%%%%% GAPSO_JA function%%%%%%%%%%

function [out, particle] = GAPSO_JA(problem,params)

global Bmeas Hmeas Para_range

%% Problem Definiton

CostFunction = problem.CostFunction;  % Cost Function
nVar = problem.nVar;        % Number of Unknown (Decision) Variables
VarSize = [1 nVar];         % Matrix Size of Decision Variables
VarMin = problem.VarMin;    % Lower Bound of Decision Variables
VarMax = problem.VarMax;    % Upper Bound of Decision Variables

%% Parameters of PSO
```

```
MaxIt = params.MaxIt;    % Maximum Number of Iterations
nPop = params.nPop;      % Population Size (Swarm Size)
w = params.w;            % Intertia Coefficient
wdamp = params.wdamp;    % Damping Ratio of Inertia Coefficient
c1 = params.c1;          % Personal Acceleration Coefficient
c2 = params.c2;          % Social Acceleration Coefficient
px= params.px;            % The probability of Crossover
pm= params.pm;            % The probability of Mutation
FieldD=[VarMin*ones(1,nVar);VarMax*ones(1,nVar)];

% The Flag for Showing Iteration Information
ShowIterInfo = params.ShowIterInfo;
MaxVelocity = 0.2*(VarMax-VarMin);
MinVelocity = -MaxVelocity;

%% Initialization

%% The Particle Template
empty_particle.Position = [];
empty_particle.Velocity = [];
empty_particle.Cost = [];
empty_particle.Best.Position = [];
empty_particle.Best.Cost = [];
% Create Population Array
particle = repmat(empty_particle, nPop, 1);

% Initialize Global Best
GlobalBest.Cost = inf;

% Initialize Population Members
for i=1:nPop

% Generate Random Solution
        particle(i).Position = unifrnd(VarMin, VarMax, VarSize);
% Initialize Velocity
        particle(i).Velocity = zeros(VarSize);
 % Evaluation
        particle(i).Cost=CostFunction(particle(i).Position);
% Update the Personal Best
        particle(i).Best.Position = particle(i).Position;
        particle(i).Best.Cost = particle(i).Cost;
 % Update Global Best
        if particle(i).Best.Cost < GlobalBest.Cost
            GlobalBest = particle(i).Best;
        end
end

% Array to Hold Best Cost Value on Each Iteration
BestCosts = zeros(MaxIt, 1);

%% Main Loop of PSO

for it=1:MaxIt

    for i=1:nPop

            % Update Velocity
particle(i).Velocity = w*particle(i).Velocity ...
```

```
                + c1*rand(VarSize).*(particle(i).Best.Position -
particle(i).Position) ...
                + c2*rand(VarSize).*(GlobalBest.Position -
particle(i).Position);

% Apply Velocity Limits
particle(i).Velocity = max(particle(i).Velocity, MinVelocity);
particle(i).Velocity = min(particle(i).Velocity, MaxVelocity);

% Update Position
particle(i).Position = particle(i).Position + particle(i).Velocity;
% Apply Lower and Upper Bound Limits
particle(i).Position = max(particle(i).Position, VarMin);
particle(i).Position = min(particle(i).Position, VarMax);
Chrom(i,:)=particle(i).Position ;
% Evaluation
particle(i).Cost=CostFunction(particle(i).Position);
ObjV(i)=particle(i).Cost;
% Update Personal Best
      if particle(i).Cost < particle(i).Best.Cost

        particle(i).Best.Position = particle(i).Position;
        particle(i).Best.Cost = particle(i).Cost;
% Update Global Best
        if particle(i).Best.Cost < GlobalBest.Cost
           GlobalBest = particle(i).Best;
        end

      end

   end

%% GA optimiser %%

    [m,n]=size(ObjV);
    if n~=1
       ObjV=ObjV';
    else
       ObjV=ObjV;
    end
    FitnV=ranking(ObjV);                        %Fitness
    SelCh=select('sus',Chrom,FitnV,1);          %Select parant
    SelCh=recombin('xovsp',SelCh,px);           %Crossover
    SelCh=mutbga(SelCh,FieldD);                 %mutation
    for Chx=1:size(SelCh,1)
        ObjVSel(Chx)=CostFunction(SelCh(Chx,:));    %evaluation
offspring
    end
    [m1,n1]=size(ObjVSel);
    if n1~=1
      ObjVSel=ObjVSel';
    else
      ObjVSel=ObjVSel;
    end
    [Chrom,ObjV]=reins(Chrom,SelCh,1,[1 0.5],ObjV,ObjVSel);
    for Chxi=1:size(Chrom,1)
        ObjVCh(Chxi)=CostFunction(Chrom(Chxi,:));    %evaluation new
population
    end
    [Y,I]=min(ObjVCh);
```

```
    if Y>GlobalBest.Cost
       BestCosts(it)=GlobalBest.Cost;
    else
       BestCosts(it)=Y;

    for i=1:nPop
        particle(i).Position=Chrom(i,:);
        particle(i).Position = max(particle(i).Position, VarMin);
        particle(i).Position = min(particle(i).Position, VarMax);
        particle(i).Cost=CostFunction(particle(i).Position);
      if particle(i).Cost < particle(i).Best.Cost
            particle(i).Best.Position = particle(i).Position;
            particle(i).Best.Cost = particle(i).Cost;
        if particle(i).Best.Cost < GlobalBest.Cost
                    GlobalBest = particle(i).Best;
        end
      end

    end
  end
% Display Iteration Information
   if ShowIterInfo
      disp(['Iteration ' num2str(it) ': Best Cost = '
num2str(BestCosts(it))]);
   end
         % Damping Inertia Coefficient
   w = w * wdamp;

%%%%%%%% this is the accuracy I add
   if BestCosts(it)<1e-4
            break
    end

  end

    out.pop = particle;
    out.BestSol = GlobalBest;
    out.BestCosts = BestCosts;

end

%%%%%% Due to the limitation of coverage, the function of JAn_loops
and its related functions are not attached.
```